PROCEEDINGS OF THE
NATIONAL CONFEENMCE
ON
"RECENT ADVANCES IN APPLIED NANO MATERIALS"
(NCRAANM-2016)

March 4-5, 2016

Editors

Dr. V. Nathanial

Dr. Guntha Aravind

Dr. B. Ramaiah

Dr. Ch. Venkateshwarlu

Organised by

DEPARTMENT OF PHYSICS

UNIVERSITY COLLEGE OF SCIENCE, SAIFABAD

Masab Tank, Osmania University, Hyderabad – 500 004. TS

PROCEEDINGS OF THE NATIONAL CONFEENMCE ON
"RECENT ADVANCES IN APPLIED NANO MATERIALS"

DISCLAIMER

The authors are solely responsible for the contents of the papers compiled in this volume. The publishers or editors do not take any responsibility for the same in any manner. Errors, if any, are purely unintentional and readers are requested to communicate such errors to the editors or publishers to avoid discrepancies in future.

ISBN : 978-93-5258-222-8

PREFACE

In the globalization era material science has become more advanced in many aspects. I tried my level best to organize a two day national conference at our University College of Science, Sifabad, Masab Tank, Osmania University, Hyderabad. In this occasion, I invited the eminent Resource persons like Prof. Ashok Kumar Ganguli, Director, INST, New Delhi, Prof.K.V.Ramanuja Chary, Rowan University, USA, Prof. M. Lakshmi Kantam, IICT, Mumbai, Dr.Tata Narsing Rao, ARCI, Hyderabad, Prof.Subhash Kondawar, RTM University Nagpur, Prof .D.Suresh Babu, Head, Dept Of Physics, Osmania University, Hyderabad, Prof. D.Ravinder, Dept of Physics Osmania University Hyderabad, Prof. K.V.R.Murthy, University of Baroda, Gujarat,etc.

All these Resource persons spoke on various topics, new ideas and suggestions. On behalf of this conference, I extend my regards to them. I thank to our College Principal Prof. B. Laxmaiah and Faculty Members for their support and encouragement in conducting this academic activity in the college to make this event a grand success. In this first attempt, I tried my level best to bring out proceedings of full papers of the conference in the form of a book with ISBN No 978-93- 5258-222-8.

This two day national conference acted as a major forum for the presentation of innovative ideas, approaches, developments and research projects in the area of material science by incorporating different preparation methods in order to fulfill the dreams of sustainable development into reality for the society.

The NCRAANM 2016 committee invited original submissions from the students, researchers, faculties and scientists that illustrate the analytical research results, review works and industrial experiences describing significant advances in the areas related to the relevant themes and tracks of the conference. All the submissions underwent a strenuous peer-review process which comprised expert reviewers. The papers were reviewed based on their technical matter, clarity and originality. The entire process which includes the submission, review & acceptance processes was done electronically.

We extend our thanks to UGC, SERO, Hyderabad, CANARA BANK, Masab Tank Branch and VISHAKA TRUST, Hyderabad for their financial assistance for conducting two day national conference. Finally I thank all the authors who contributed to the success of conference. I also sincerely wish that all attendees will get benefitted academically from the conference and wish them every success in their research endeavor.

Dr. V. Nathanial

Convener and Organising Secretary

NCRAANM - 2016

INDEX

Synthesis of TiO_2 Nanoparticles and Their Application in Waste Water Treatment

Annapoorna Avula[1], Kaleem Ahmed Jaleeli[2], Adeel Ahmad[2]

[1]Asst Prof, Dept of Physics, Al-Habeeb College of Engg and Tech, Chevella, India

[2]Biophysics Research Laboratory, Department of Physics, Nizam College (Autonomous), Osmania University, Hyderabad – 500 001, India

ABSTRACT:

The main objective of this paper is to determine the photo catalytic degradation efficiency for refinery effluent from wastewater by using new generation photo catalytic TiO2 Nanoparticles synthesized using Green synthesis. The obtained TiO2 nanoparticles have been characterized by X-ray diffractometer (XRD). In the present work, photo catalysis has been used as tertiary treatment for petroleum refinery wastewaters in order to reduce the amount of pollutants to the level of the regulatory discharge limits and to oxidize persistent compounds that had not been oxidized in the biological treatment .The potential use of nanotechnology improves access to clean water and basic sanitation.

Keywords: Green Synthesis, Photo catalytic, TiO2 Nanoparticle and Wastewater.

INTRODUCTION:

Water pollution is a major environmental issue in India. Rivers, lakes and surface water in India are polluted. Drinking water pollution is most important; as such pollution is directly connected with human health. The main source of freshwater pollution can be attributed to the discharge of untreated waste, dumping of industrial effluent, and run-off from agricultural fields. By always increasing pollution it becomes more difficult to guarantee the fundamental right to water. Water has a self-cleaning capacity that ensures the natural break of a number of substances. Water is however too much polluted, and then the self-cleaning capacity is damaged (1). In terms of wastewater treatment, nanotechnology is applicable in detection and removal of various pollutants. Heavy metal pollution poses as a serious threat to environment. Various methods such as Photolysis, Nano filtration, Adsorption and Electrochemical oxidation involve the use of TiO2,ZnO, ceramic membranes,

nanowire membranes, polymer membranes, carbon nanotubes, submicron Nanopower, metaloxides, magneti nanoparticles, nanostructured boran doped diamond are used to resolve or greatly diminish problems involving water quality in natural environment(2). Photo catalysis is being applied for the elimination of several pollutants (e.g., alkenes, alkenes, phenols, aromatics, pesticides) with great success. In many cases, total mineralization of the organic compounds has been observed. The wastewaters of an oil refinery are the waters resulting from washing the equipments. These effluents have high oil and grease contents, besides other organic compounds in solution. These pollutants form a residual COD that may pose serious toxic hazards to the environment. Composition for these effluents is troublesome. In the present work, photo catalysis has been used as tertiary treatment for petroleum refinery wastewaters in order to reduce the amount of pollutants to the level of the regulatory discharge limits (3). Photo catalyst TiO2 is synthesized using Orange fruit peel extract using Green synthesis. Titanium dioxide is a white colour metal oxide, which have advanced properties like hydrophobic, non-wet ability, high surface to volume ratio and large band gap. Hence, it can be used in the different types of applications self-cleaning devices, dye sensitized solar cell, photo catalysis, electrochemistry, anti bacterial products and textiles. The green synthesis process is environmental friendly technique, due to it uses the extracts of plant parts such as peels, leaves, flowers, roots, stem and seed. It is a one of the best method among physical and chemical methods as it does not require any high end equipments, hazardous chemicals and high temperatures. Orange peel acts as reducing agent for synthesis of TiO2 because it contains Citric acid as main source. Orange peel can be used in bath oil, room freshen air, face creams, mosquito repellent and weight loss

MATERIALS AND METHODS:

Make Orange peel into small pieces. A 50 g of orange peel was directly taken into the beaker and extracted with 150 ml of water for 2 hrs at 90 C. The extract was filtered using what man filter paper. The filtrate was stored for the further synthesis of nanoparticle (4).Dissolve 1.5 N of titanium tetra iso prop oxide in 100 ml of distilled water for synthesis the TiO2 nanoparticles. Added extract drop wise under constant stirring up to achieve pH of solution became 7. The mixture was subjected

to constant stirring for 3 hours continuously at room temperature. In this process formation of nanoparticles were occurred, these nanoparticles were separated using what man filter paper and washed the materials with distilled water repeatedly to remove the by-products. The obtained wet nanoparticles were dried at 80 C for overnight. Finally particles were calcined at 600 C for 3 hours for obtaining Rutile phase (5).

CHARACTERIZATION TECHNIQUE:

The crystal structure and average crystalline size was measured by Bruker D8 X-ray diffractometer.

PHOTO CATALYTIC EXPERIMENTS:

The wastewater was collected at the exit pipe of a series of aerated lagoons and stored at 4ºC with a pH<2. The wastewater characterization, along with the pollutant limits, are presented in Table 1

Parameters	Average Concentration of Wastewater(mg/L)	Concentration
pH	6.7	6
COD(filtrated)	250	200
DOC	28	
Oil and grease	27	15
Ammonia	26	5
Phenol	3.7	0,2

Table 1 The wastewater characterization

The experiment was carried out with, a Pyrex® annular reactor containing 550 mL of wastewater. The reaction mixtures inside the reactors were maintained in suspension by magnetic stirring. In the experiment, air was continuously bubbled through the suspensions. A 250 W Phillips HPL–N medium pressure mercury vapor lamp was used as the UV-light source. The lamp was inserted into the well; The experiment was performed at 25± 1°C. The catalyst concentration ranged from 0.5

to 5.5 g/L and the initial pH from 3.5 to 9. In order to remove photo catalyst particles before analyses, samples were filtered through 0.45 µm pore size cellulose acetate filters.

RESULTS AND DISCUSSION:

X-RAY DIFFRACTOMETER:

The XRD pattern of TiO2 nanoparticles obtained from green synthesis were as shown in Figure 1. The result showed that the structure was in tetragonal structure and these results were good agreement with JCPDS card number 87-0920. Peaks were absorbed at 27°, 36°, 39°, 41°, 44°, 54°, 56°, 62°, 64° and 69° along with miller indices values (1 1 0), (1 0 1), (2 0 0), (1 1 1), (2 1 0), (2 1 1), (2 2 0), (0 0 2), (3 1 0) and (1 1 2) respectively. As the width of the peak increases size of particle size decreases, which resembles that present material in nano range.

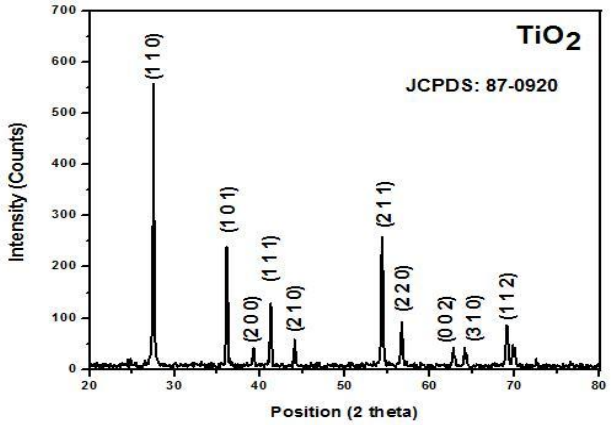

Fig: 1XRD Pattern of TiO2 Nanoparticles

The lattice parameters were obtained a=b=0.4594 nm and c=0.2958 nm. The average crystallite size was measured by Debye-Schereer's equation

$$D = \frac{K\lambda}{L\cos\theta}$$

Where D is the average crystallite size of the particles, K- is Debye Scherer's constant (=0.94), λ- is the wavelength of the CuKα-radiation (=0.154 nm), L is the full width half maximum (FWHM) of the peak, θ is the Bragg's angle. The average crystallite size was measured as 19 nm using the above formula.

FINAL WASTEWATER CHARACTERIZATION:

After photo catalytically treatment of the wastewater in the Pyrex® annular reactor, under the optimized conditions, its general quality was significantly improved. The results are summarized in Table 2. It is noteworthy that phenol and oil and grease contents, which had been above the legislated limits, were reduced to discharge levels. Also, more than half of the DOC was removed from the wastewater. Finally, an insignificant amount of ammonia was removed (not more than 10%).

TiO2	Degradation% UV Area	Phenols,mgr/L
pH	6.7	7
DOC	20	10
Oil and grease	23	<10
Ammonia	70	50
Phenols	3.7	0.5

Table 2-Wastewater Photo catalytic treatment

CONCLUSION:

The TiO2 nanoparticles can be synthesized successfully in green synthesis method using Orange peel and XRD analysis of the sample was obtained 19 nm with the Tetragonal structure. . Undoubtedly, the TiO2 was the most active photo catalyst. . Moreover, it offers two other advantages: less photo catalyst can be used and the pH is already near the effluent discharged, requiring no adjustment of pH. The use of TiO2 /UV (photo catalysis) resulted in a significant increase in phenol removal (93%). 56% of the DOC was removed. This is probably due to the fact that photo catalysis is a much more oxidative process than H2 O2 /UV, so the reactions that take place are much faster. Therefore, the use of helio-photocatalysis with this wastewater would be feasible.

REFERENCES:

1. Ijoer vol.3. S3, 2015, issn: 2321-7758 ncerfm-2015
2. Nanotechnological methodology for treatment of waste water l. Nageswara rao
3. & Table 2 Brazilian journal of chemical engineering-vol. 23, no. 04, pp. 451 - 460, October - December, 2006
4. P. Balashanmugam, R. Nandhini, V. Vijayapriyadharshini, P.T Kalaichelvan; (2013) Biosynthesis of Silver Nanoparticles from Orange Peel Extract and its Antibacterial Activity against Fruit and Vegetable Pathogens, International Journal of Innovative Research in Science & Engineering, 1(2): 6 page
5. Synthesis of tio2 nanoparticles from orange fruit waste international journal of multidisciplinary advanced research trends issn : 2349-7408 volume ii, issue I, February 2015
6. Table 1 limits imposed by the Iran Department of Environment (DOE).

Fabrication of Hybrid Gel Nanofibrous PVdF/PMMA Polymer Electrolyte for Lithium-Ion Battery

Rozi D. Thalal[#], Monali V. Bhute, Subhash B. Kondawar*
Dept. of Physics, Rashtrasant Tukadoji Maharaj Nagpur University,
Nagpur - 440033, India
*Corresponding Author Email: sbkondawar@yahoo.co.in
[#]Presenting Author Email: thalalrosy@gmail.com

ABSTRACT

In this paper, hybrid gel polymer electrolyte (HGPE) based on PVdF/PMMA nanofibrous membranes were prepared by electrospinning technology. The microstructure of the nanofibrous membranes, the physical and electrochemical performances of the activated HGPEs were studied systematically by scanning electron microscopy (SEM), Fourier transform infrared spectroscopy (FTIR), X-ray diffraction (XRD), Linear sweep voltammetry (LSV) and electrolyte uptake. The properties of the nanofibrous membranes and the corresponding HGPEs were found to be varied with the relative weight ratio of the blending polymers. The thickness of the nanofibrous membrane was found to be around 100μm via the controlled procedure parameters. The polymer electrolytes from electrospun nanofibrous membranes were prepared by soaking the membranes in 1 M $LiPF_6$ (lithium hexaflurophosphate) in ethylene carbonate : diethelyne carbonate (EC:DEC) in 1:1 (v/v) ratio. For HGPE, the most important character is its electrochemical performance. When the weight percentage of PVdF/PMMA was 15%, the maximum ionic conductivity of the prepared HGPE was found to be 3.51×10^{-3} S/cm with electrochemical stability up to 3.8 V versus Li^+/Li at room temperature indicate the good suitability of the polymer electrolyte membranes for polymer lithium-ion battery.

Keywords: Electrospinning; Polymer electrolyte; Electrochemical performance; Lithium-ion battery.

1. Introduction

Polymer electrolytes have attracted great interest compared to traditional liquid electrolytes, which provide the advantages to develop lighter and safer batteries with long shelf life, leak proof construction and easy fabrication into desired shape and size [1]. Electrospinning technique is a very unique and useful way to prepare Polymer electrolyte with superior performance. Electrospinning is an efficient fabrication process that gives fibrous and porous membranes with an average diameter ranging from 100 nm to 5 μm [2, 3]. Poly(vinylidene fluoride) (PVdF) is a well-known semi-crystalline thermoplastic polymer with excellent film-forming ability and thermal stability . Due to the high dielectric constant and strong chemical and electrochemical resistance, it has become a favorable polymer matrix for porous polymer electrolytes in lithium-ion batteries [4, 5] .The crystalline domains of PVdF hinder the penetration of liquid electrolytes and the migration of lithium ions, and hence the high-crystalline PVdF becomes one of the major factors to give the low ionic conductivity of polymer electrolytes [6].For the purpose of tackling the aforementioned problems, several attempts have been carried out, one of the best way to introduce other blending polymers like polyacrylonitrile (PAN), poly(methyl methacrylate)(PMMA), and thermoplastic polyurethane (TPU) into electrospun PVdF membranes. PMMA is a common thermoplastic polymer with well known chemistry. Its amorphous structure is beneficial to ionic conduction. PMMA based polymer electrolytes exhibit high electrolyte uptake, ionic conductivity and good electrochemical stability. Also, PMMA has ability to increase the mechanical strength and the electrolyte solution retention ability of the polymer electrolytes [7]. The characterizations and measurement of porosity, electrolyte uptake and ionic conductivity of the electrospun PVdF–PMMA membrane were investigated. These results showed that PVdF–PMMA composite nanofibrous membrane prepared by electrospinning had a good prospect as PE for lithium-ion batteries.

2. Experimental

Materials

Poly(vinylidene fluoride) (PVdF), poly (methylmethacrylate) PMMA, hexafluro-phosphate (LiPF6,battery grade, dry 99.99%) and plasticizers ethylene carbonate: diethelyne carbonate (EC:DEC) were purchased from Sigma-Aldrich.

Synthesis of PVdF/PMMA composite nanofibrous membrane

Poly(vinylidene fluoride) PVdF and PMMA were used as the starting materials for the preparation of fibrous nanocomposite polymer membranes by electrospinning technique. A 15% solution of PVDF/PMMA (8/2,w/w) in DMF/acetone (2/6, v/v) was prepared by magnetic stirring for 12 hr. The resultant optimized viscous solution was taken into a 10 ml syringe and loaded in a syringe pump to form nanocomposite fibers by setting the electrospinning parameters. The following electrospinning parameters are used for all the compositions: solution feed rate 0.6 ml/hr, applied voltage between spinneret and collector is 18 kV. Nanofibers were collected on aluminum foil wrapped on rotating collector which was grounded .The electrospun fibrous membranes were collected and dried in vacuum oven at 60^{o}C for 24 h to remove the solvent for further use.

3. Results and discussion

Fig.1 shows the surface morphology of electrospun pure PVdF (Fig. 1a) and nanocomposite fibrous polymer membrane with PMMA (Fig.1b). It can be seen that the membranes exhibit a three dimensional web structure with fully interconnected pores of ultrafine multi-fibers with bead free morphology. The interlaying of multi-fiber layers generates a porous structure between the fibers in the electrospun membrane, which can good absorb and retain the liquid electrolyte effectively.

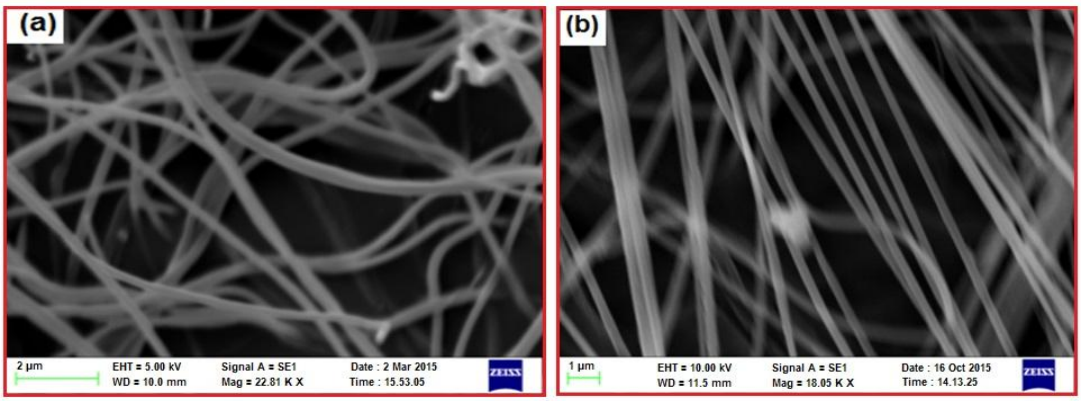

Fig.1: SEM images of electrospun (a) PVdF and (b) PVdF-PMMA nanofibrous membrane

Fig. 2 shows the FT-IR spectra of electrospun pure PVdF and PVdF–PMMA nanofibrous membranes. The bands appearing at 1397, 1275, 840 cm^{-1} are assigned to CF stretching, CF_2 stretching, and characteristic frequency of vinylidene compound respectively in PVdF.The characteristic absorption peaks of PMMA (692, 879, 1729 cm^{-1}) are found in the composite nanofibrous membrane. An absorption peak appears at 1729 cm^{-1}, which is related to C=O stretching vibration of PMMA. The appearance of new peaks along with changes in the existing peaks in the FTIR spectra confirms the miscibility of PMMA with PVdF in the composite PVdF-PMMA fibrous membrane. The XRD pattern of PVdF and PVdF-PMMA nanofibrous membranes are shown in **Fig. 3.** The presence of crystalline peaks and amorphous humps indicates the semi crystalline nature. There are two broad diffraction peaks at $2\theta = 18.5^{o}$ and 27.2^{o} corresponding to the crystal diffraction peaks of PVdF. The intensity of the crystalline peaks is decreased due to incorporation of PMMA in composite.

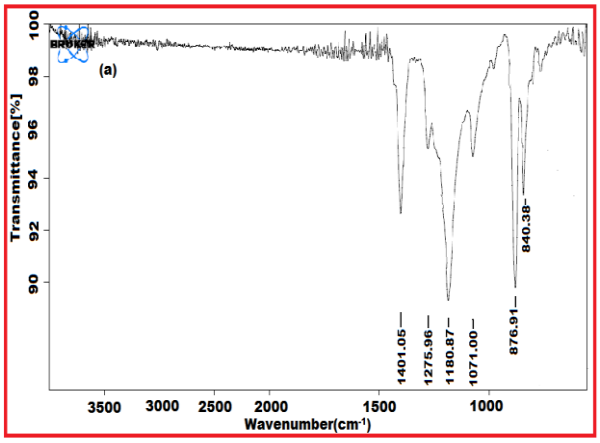

Fig. 2(a): FTIR spectrum of PVdF nanofibrous membrane

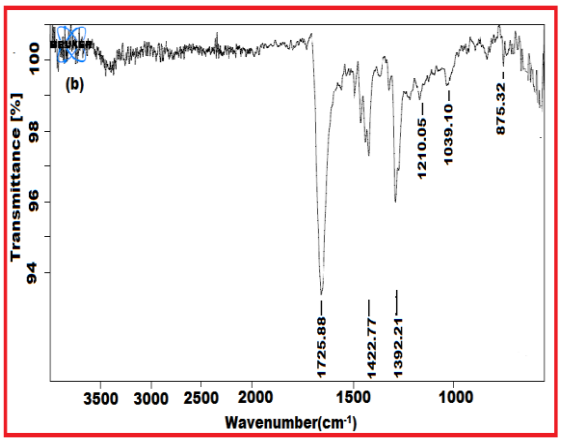

Fig. 2(b): FTIR spectrum of PVdF–PMMA nanofibrous membrane

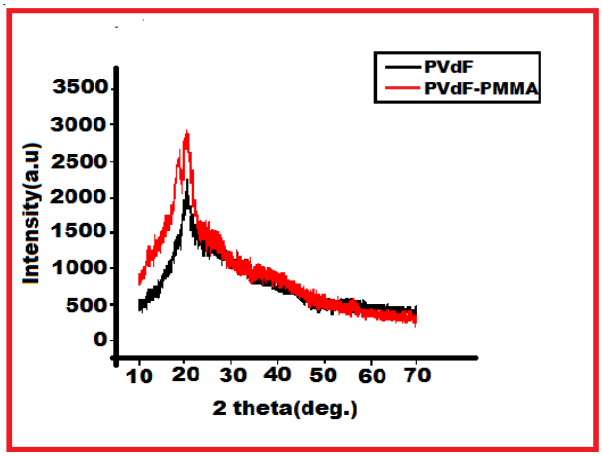

Fig 3: XRD patterns of membranes

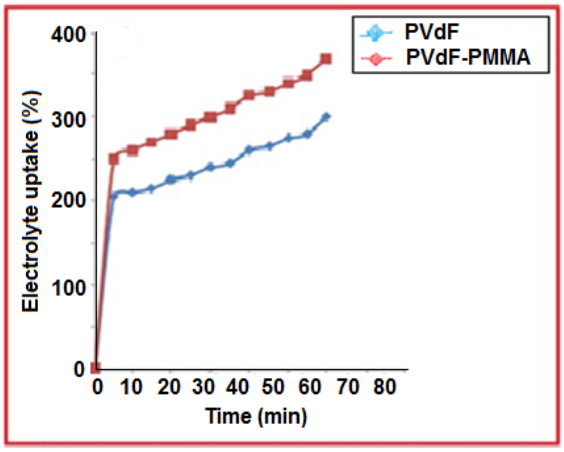

Fig. 4: Electrolyte uptake of membranes

The electrochemical measurements of the PEs were obtained by immersing the electrospun nanofibrous membrane in 1 M $LiPF_6$ - EC:DEC (volume 1:1) solution for 60 minute at 25 ^oC in a dry glove box [8]. The ionic conductivity was calculated by AC impedance measurement using Zahner Zennium electrochemical analyzer. The frequency of testing ranged from 100 mHz to 100 kHz at AC amplitude of 5mV. **Fig.4** represents the electrolyte uptake behavior of the electrospun PVdF and PVdF–PMMA membranes. It has been calculated by soaking the membrane in the liquid electrolyte 1M $LiPF_6$ - EC:DEC (volume 1:1) solution for 60 min [9]. The unique fibrous structure of this membrane induces fast liquid penetration into the membranes to form the polymer electrolyte with interpenetrating polymer network within 30 minute. The higher electrolyte uptake can make an improvement of ionic conductivity. The ionic conductivities of the polymer electrolyte were determined at room temperatures by ac impedance spectroscopy **(Fig. 5).** The ionic conductivity of pure PVDF-based GPE was found to be 3.07×10^{-3} S/cm and increased with the addition of PMMA for PVdF-PMMA nanofibrous membrane of about 3.51×10^{-3} S/cm. Good ionic conductivity of PVdF-PMMA nanofibrous membrane shows the most stable performance with the temperature.

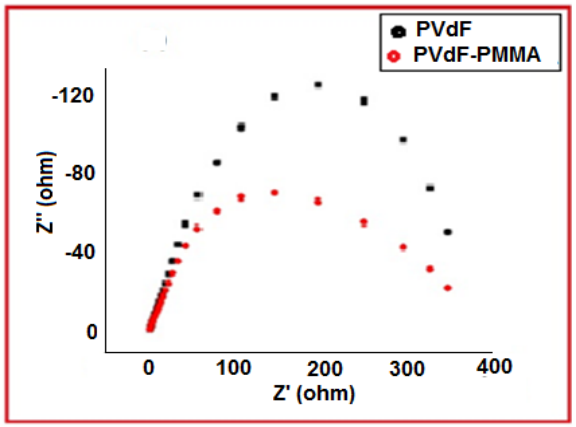

Fig. 5: Impedance spectra of polymer electrolytes

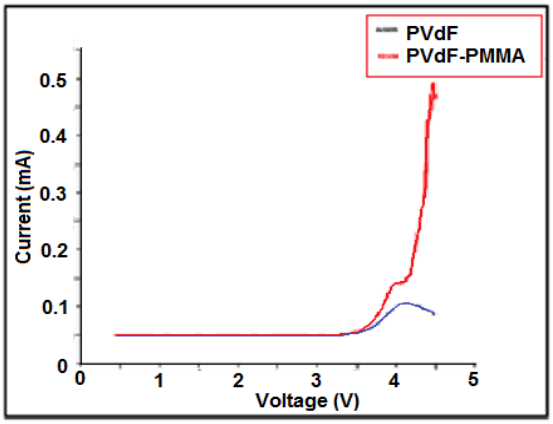

Fig 6: Linear sweep voltammetry of polymer electrolytes

The results of electrochemical stability tests of the polymer electrolytes by linear sweep voltammetry are shown in **Fig. 6.** The linear sweep voltammetry was applied for Li/polymer electrolyte/ SS cell at room temperature. The electrochemical stability was found to be 3.5 V for the PVdF polymer electrolyte and with the addition of the addition of PMMA, the stability was further enhanced to 3.8 V.

4. Conclusion

Electrospun PVdF and PVdF-PMMA composite nanofibrous polymer electrolyte membranes were successfully prepared by electrospinning method. The ionic conductivity, impedance and electrolyte uptake were found to be improved after the addition of PMMA in PVdF. Thus, PVdF–PMMA composite nanofibrous membranes prepared via electrospinning is a good candidate compared to that of pure PVdF as the polymer electrolyte for polymer lithium-ion batteries.

References

1. Xi.Y. J., Qiu.P. X., Tang. Z. X., Zhu.T.W and Chen. Q. L, *Journal of Power Sources*, (2006), 157(1), 501-506.
2. Hwang. J.Y., Nahm. S. K, Kumar. P.T and Stephan.M. A, *Journal of Membrane Science*, (2008), 310, 349–355.
3. Muniyandi. N., Kalaiselvi.N., Periyasamy.P.,Thirunakaran R., Babu.R.B., Gopukumar .S, Renganathan. G.N, Raghavan .M., *Journal of Power Sources*, (2001), 96, 14–19.
4. Liu, F., Hashim, N.A., Liu, Y.T., Abed, M.R.M., Li, K., *Journal of Membrane Science*, (2011), 375, 1-27.
5. Stephan, M.A . *Europium Polymer Journal*, (2006), 42, 21–42.
6. Li, X.Y, Cao, Q, Wang, X.Y, Jiang, S.H, Deng, H.Y, Wu, N., *Journal of Applied Polymer Science*, (2011), 122, 2616-2620.
7. Tatsuma, T., Taguchi, M., Oyama, N., *Electrochimica Acta*, (2001), 46, 1201-1207.
8. Chung, S.H., Wang, Y., Persi , L. Croce , F.S, Greenbaum, G,. Scrosati, B. and Plichta, E., *Journal of Power Sources*, (2001), 97, 644-648.
9. Wu, N., Qi, C., Wang, X., Li, S., Li, X., Deng, H., *Journal of Power Sources*, (2011), 196, 9751–9756.

Ethnobotanical studies of Peddagattu and Sherepally area, a proposed site for uranium Mining project, Nalgonda District, Telangana State, India

A. Baleeshwar Reddy[1], V. Vasudeva Rao[2] and A. Vijaya Bhasker Reddy[1*]
[1] Department of Botany, University College of Science, Osmania University, Saifabad, Hyderabad-500 004, Telangana State, India.
[2] AINP on Vertebrate Pest Management, Prof. Jayashankar Telangana State Agricultural University, Rajendranagar, Hyderabad- 500030, Telangana State, India.
*Corresponding author e-mail: avijayabhaskerreddy@gmail.com

ABSTRACT

The present study aimed to record the information of medicinal plants used by tribal groups in the study area. 83 medicinal plants used as a cure for 47 ailments were recorded. They are distributed across 78 genera and 41 families. Of these 83 species, the maximum contribution was recorded for herbs (32.5%) and trees (32.5%) followed by shrubs (23%) and climbers (12%). Among these species, parts used wise contribution was maximum recorded for leaf (42 %) followed by root (13 %), bark (12%), fruits (10%), whole plant (9%), and seed (7%). The large numbers of remedies were used to treat external injuries, skin diseases, and snake bite.

Key words: Ethnobotany, external injuries, Peddagattu, Sherepally, uranium project.

INTRODUCTION

The first human beings were food gathers and hunters of food, but subsequently concentrated on plants that are useful for other purposes, such as shelter and health care etc. They understood the use of various plant parts for different purposes such as food, resins, beverages and medicines since immemorial time. This knowledge was passed through orally from generation to the next generation. The indigenous people of various regions have developed their own way of using plants for their health care and following their own culture, customs and food habits (Ramakrishna et al., 2014).

Indians herbal knowledge base is very diverse and it consists of many streams like Ayurveda, Unani, Siddha and other systems. In India ethnobotany was initially well cited in different folklore practiced for curing various ailments similarly in other parts of the world like China, Africa and South America were

highlighted the importance of herbal uses. People of the world are still dependent on traditional plant based healing practices as it is cheap and easily available. The World Health Organization has estimated that over 80% of the world populations rely chiefly on traditional medicine (Akerele., 1992). It was officially recognized that 2500 plant species have medicinal value over 6000 plant species are estimated to be explored in traditional, folk and herbal medicine (Huxley., 1984).

Different workers have documented the uses of medicinal plants from different parts of Telangana and Andhra Pradesh states (Kapoor., 1980, Singh et al., 1981, Hemdri et al., 1987 a & b, Raja Reddy et al., 1989, Venkanna., 1990., Basi Reddy et al., 1991, Ravishanker &Herny.,1992, Chandra et al., 2010, Murthy.,2012 and Ramakrishna et al., 2014, Saynasi Rao and Varma., 2014). The literature revealed that there are only few attempts on ethnobotanical studies of this region (Reddy., 2013). The main focus of the present study is to ascertain the detailed information on the use of the ethnomedicinal plants mostly used by tribals such as Sugalis, Yerukali and Chenchus of the study area.

MATERIALS AND METHODS

The present study area (Peddagattu and Sherepally area) is a part of the Nalgonda District covering of 4781.35km^2 (Fig 1). Peddagattu and Sherepally area was explored during the 2010- 2013. The tribals, Sugali (Lambadi) is the highest population followed by Chenchu and Yerukala are living in the study area. Local informants with the knowledge of medicinal plants were selected based on the experience in the preparation of medicines, the way they acquired knowledge on the medicinal plants and their ability to treat a specific disease. The data was collected through questionnaires, discussions among the tribal people. The information on useful plants species, parts used, local names and mode of utilization was collected. Plants used in their traditional medicine were identified with the help of regional floras (Gamble & Fischer 1915-1935., Jain S.K., 1991, Pullaiah et al. 1997 a, b and c., Rao et al. 2001 & Pullaiah et al. 2000). The plants specimens were pressed and deposited in the Deccan Regional Center, Botanical Survey of India (BSI), Hyderabad.

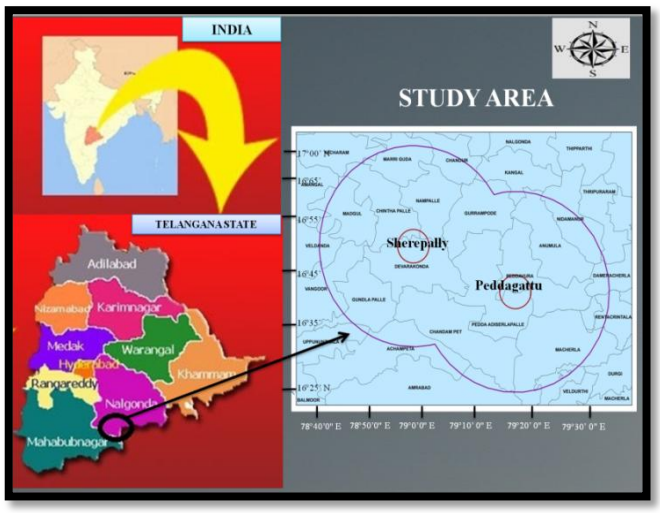

Figure 1. Location map of the study area

RESULTS AND DISCUSSION

A total of 83 medicinal plants belonging to 78 genera and 41 families were recorded. Asteraceae has the highest number of species (7 species) followed by Asclepiadeaceae (6 species), Euphorbiaceae (6 species), Caesalpiniaceae (5 species), Lamiaceae (4 species), Fabaceae, Liliaceae, Mimosaceae (3 species each), Acanthaceae, Amaranthaceae, Capparidaceae, Lythraceae, Menispermaceae, Moraceae, Rubiaceae, Rutaceae, Sapindaceae, Simarubaceae, Solanaceae, Sterculiaceae, and Verbenaceae (2 species each) and rest of the families (21 families) contain one species each (Table 1). Out of these 83 species, the maximum contribution was recorded for herbs 27 (32.5%) and trees 27 (32.5%) followed by shrubs 19 (23%) and climbers 10 (12%) (Fig 2). Among these species, parts used wise contribution was maximum recorded for leaf (42 %) followed by root (13 %), bark (12%), fruits (10%), whole plant (9%), seed (7%), stem (2%) and Flowers, Gum, Latex and Wood (1% each) (Fig 3).

A total of 47 diseases are known to cure by using 83 medicinal plant species. A maximum of 14 plant species are used for cure wounds healing. Seven species are recorded to cure skin diseases, cut injuries and snake bite. Five species have diabetes control properties and four species are recorded for cure cold and cough. Burns, Eczema and Mosquitoes control are known to cure individually by using of 3 species. Two species are used to cure aphrodisiac, bone fracture, relieve from headache, jaundice, rheumatism, anti helminthes and diuretic. Astringent, abdominal

pain, bladder stones melt, blood purification, boils, broken limbs, bronchitis, whooping cough, cleaning teeth, constipation, dyspepsia, fever, hair health, hernia, indigestion, joint pains, kidney stones melts, pustules, rejuvenate, respiratory diseases, ring worm, scabies, rheumatic swellings, rubefacient, toothache and ulcers are known to cure individually by usage of single species (Table 1).

Whole plant powder of *Aerva lantana* is mixed with milk and small amount of sugar is used for kidney stones melts. Branches of *Dodonaea viscosa* used for dentifrice and relief from dental diseases. Root paste of *Echinops echinatus* is applied to externally on wounds. Seed powder of *Abrus precatorius,* root bark power of *Alangium salviifolium,* dry root paste of *Dregea volubilis,* seed paste of *Strychnos nux-vomica* and root paste of *Aristolochia indica, Calotropis gigantea* and *Pergularia daemia* applied on snake bite used as antidote against snake bite. Leaf juice of *Datura metal* is applied over the affected areas of ring worm. Leaves of *Andrographis paniculata* is chewed with betel leaf for control diabetes and fever. Stem of *Senna auriculata* used as tooth brush and leaf paste with egg albumen used for bone fracture. Leaf paste of *Lawsonia inermis* used for hair dye, wound healing and other beautification purpose. Root paste of *Hemidesmus indicus* used as cooling agent and root powder with milk is used for blood purification. The stem bark of *Holoptelea grandis* make into paste form used for healing wounds. Leaf juice of *Leucas aspera* is mixed with milk then taken orally for cure skin diseases and rheumatic swellings. The juice of *Oxystelma esculentum* leaves externally applied on cut and wounds. Juice of *Parkinsonia aculeata* stem bark and fruit juice of *Solanum pubescens* are used to treat indigestion. Leaf smoke of *Vitex negundo, Azadirachta indica, Hyptis suaveolens and Chloroxylon swietenia* are used for control of mosquitoes and mites in houses. Fresh stem bark of *Morinda pubescense* and Leaf juice of *Phyllanthus amarus* used for cure jaundice. Wood paste of *Vitex leucoxylon* is applied on externally to cuts, burns and wound healing. Leaf juice of *Xanthium strumarium, Albizia amara, Cocculus hirsutus* and *Ageratum conyzoides* are applied to cure cut and wounds healing. Juice of *Croton bonplandianus* whole plant is applied to treat cut and wound healing. Latex of *Euphorbia hirta* is applied on cut and injuries twice a day until healed. Leaf paste of *Ziziphus oenopolia* is used to cure wound healing. Leaf smoke of *Azadirachta indica* is used for control of

mosquitoes and leaf paste is used for anti helminthes and skin diseases. Leaf juice of *Caesalpinia bonduc* used as anti helminthes and raw leaves used for hernia. The leaf paste of *Cassia fistula* mixed with turmeric used for cure skin diseases. Leaf juice of *Ficus mollis* is used on externally to cure eczema and skin diseases. Fresh bark paste of *Acacia nilotica* is used for skin diseases and burns. Succulent leaf paste of *Aloe vera* is applied in skin diseases and cure diabetes. Fresh leaves of *Ammannia baccifera* used in skin diseases. Fruit decoction of *Syzygium cumini* and leaf juice of *Ficus hispida* used for control diabetes. *Terminalia arjuna* bark extraction is used relief from urinal problems and decoction of leaves cures diabetes. Raw leaves of *Tinospora cordifolia*, succulent leaf of *Aloe vera* and leaves of *Andrographis paniculata* are used for control diabetes. Fresh leaves *Anisochilus carnosus* squeezed and inhaled for relieve cold and cough. Fruit powder of *Balanites aegyptiana* is given with milk once in a day for cough and cold cure. Seeds of *Pongamia pinnata* used for cure bronchitis and whooping cough. The stem bark of *Acacia leucophloea* is crashed and inhaled to relieve cough and cold. Leaf paste of *Leonotis nepetifolia,* Wood paste of *Vitex leucoxylon,* Fresh bark paste of *Acacia nilotica are* applied on the burns. Fruits of *Sapindus trifoliatus and* Leaf juice of *Ficus mollis* and *Senna occidentalis* are used for eczema. Whole plant extraction of *Cleome gynandra* used to cure peptic ulcers. Leave juice of *Persicaria glabra* and leaf paste of *Senna auriculata are* applied for setting of fractured bones. Root extraction of *Coccinia grandis* and flower paste of *Pandanus odorifer* used to relief and cure headache. Fruits of *Cordia dichotoma* and *Diospyros chloroxylon* are taken internally for diuretic. Juice of whole plant of *Flueggea leucopyrus* is used for cure joint pains and rheumatism. Tubers of *Gloriosa superba* make to paste and applied over boils. Root juice of *Asparagus racemosus* and seeds of *Spermacoce neohispida* are used for aphrodisiac. Leaf extraction of *Tinospora cordifolia* is given orally once in a day for the removal of bladder stones. Dried root of *Tephrosia purpurea* is burned and the smoke inhaled to cure respiratory diseases. Leaf extraction of *Eclipta prostrata* mixed with coconut oil and applied on head for hair health. Leaf paste of *Annona squamosa* applied to hair and on the pustule. It is noted that the tribals use most of the medicinal plants to cure their day to day health problems like fever, snake bite,

skin diseases, wound healing, jaundice, ring worm, joint pains and mosquitoes control (Table 1).

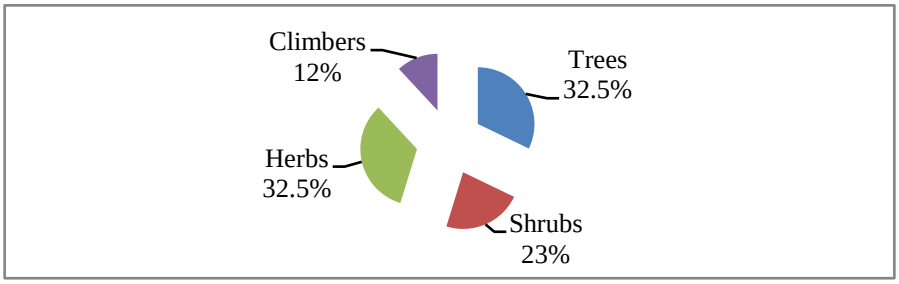

Figure 2. Growth form pattern of plant species

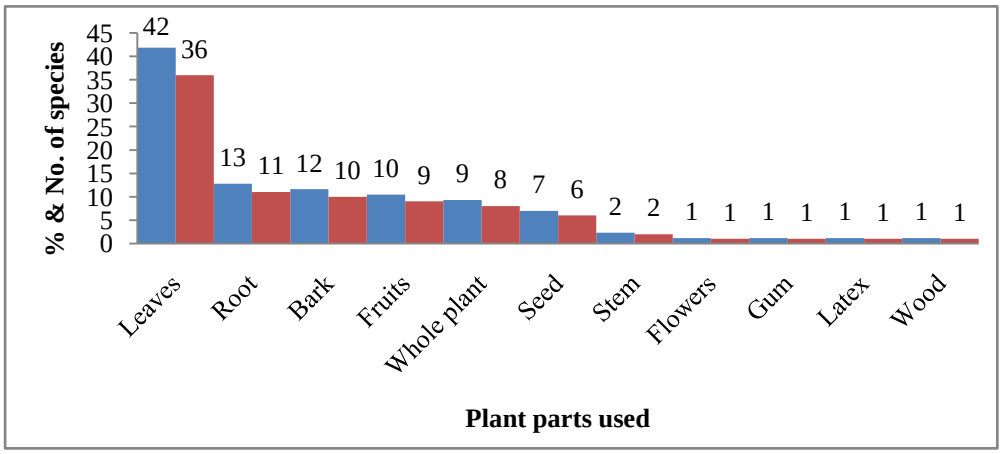

Figure 3. Showing percentage of organoleptic part used in medicines

Table 1. Showing Ethnomedicinal plants and their medicinal importance.

S. No	Family / Species name	Growth form	Vernacular name	Parts used	Medicinal importance
1	**Acanthaceae**				
1	*Andrographis paniculata* (Burm.f.) Nees	H	Nelavemu	Leaves	Leaves are chewed with Betel leaf for control diabetes.
2	*Elytraria acaulis* (L.f.) Lindau	H	Eddu adugu	Leaves	Leaf paste is applied on wounds twice in a day until cured.
2	**Alangiaceae**				
3	*Alangium salviifolium* (L.f.) Wangerin	T	Uduga chettu	Root bark	Root bark is used as an antidote for snake bites.

3	**Amaranthaceae**				
4	*Achyranthes aspera* L.	H	Uttareni	Roots	Fresh root is used for tooth cleaning and toothache.
5	*Aerva lantana* (L). Juss.	H	Telanga pindi	Whole plant	Whole plant powder mixed with milk is used for kidney stones.
4	**Annonaceae**				
6	*Annona squamosa* L.	T	Sitaphalamu	Leaves	Leaf paste applied joint pains.
5	**Apocynaceae**				
7	*Wrightia tinctoria* R.Br.	T	Palakudise	Leaves	Extraction of leaves and roots relieve tooth pain and wounds.
6	**Aristolochiaceae**				
8	*Aristolochia indica* L.	C	Thella usiri	Roots	Root paste is applied to cure snake bite.
7	**Asclepiadaceae**				
9	*Calotropis gigantea* (L.) Dryand.	S	Tella jilledu	Root	Root paste is used externally and given orally as an antidote for snake bite.
10	*Decalepis hamiltonii* W ight & Arn.	C	Nannari	Root	Root extract is taken orally to rejuvenate the body and it is the popular health tonic for rural people.
11	*Dregea volubilis* (L.f.) Benth. ex Hook.f.	SS	Pala teega	Root, leaves	Dry root paste is used as an antidote for snake bite. Leaf extraction used for wounds.
12	*Hemidesmus indicus* (L.) R.Br.ex Schuult.	H	Sughandhi pala	Roots	Root paste used as cooling agent and root powder with milk is used for blood purification.
13	*Oxystelma esculentum* (L. f.) Sm.	C	Dudipala teega	Leaves	Leaf juice applied on cut and wounds.
14	*Pergularia daemia* (Forssk.) Chiov.	C	Dushtapu teega	Root	Root paste is used for snake bite.
8	**Asteraceae**				

15	*Ageratum conyzoides* (L.) L.	H	Pumpulla	Leaves	The leaf paste is externally used for cuts.
16	*Cyanthillium cinereum* (L.) H.Rob.	H	Kalupumokka	Whole plant	Whole plant extraction used to cure urinary infection and abdominal pain.
17	*Echinops echinatus* Roxb.	H	Bramha danthi	Roots	Root paste is applied on wounds.
18	*Eclipta prostrata* (L.) L.	H	Guntaguragura	Leaves	Leaf extraction mixed with coconut oil used as hair tannic.
19	*Lagascea mollis* Cav.	H	Nallagada	Leaves	The juice of fresh leaves used for bleeding control.
20	*Tridax procumbens* (L.) L.	H	Allammokka	Leaves	Leaf paste used for wound healing.
21	*Xanthium strumarium* L.	US	Pallaru	Leaves	Leaf juice is applied to cut and wounds.
9	**Boraginaceae**				
22	*Cordia dichotoma* G.Forst	T	Banka iriki	Fruits	Fruits are taken internally as an astringent and diuretic.
10	**Caesalpiniaceae**				
23	*Caesalpinia bonduc* (L.) Roxb.	S	Gachhakaya	Leaves	Leaf juice used as anthelmentic and raw leaves used for hernia.
24	*Cassia fistula* L.	T	Rela	Leaves	Leaf paste and turmeric is used for skin diseases.
25	*Parkinsonia aculeata* L.	T	Seemathumma	Stem bark	Stem bark is used to treat indigestion.
26	*Senna auriculata* (L.) Roxb.	S	Thangedu	Stem, Leaf	Stem used as tooth brush and leaf paste with egg albumen used for bone fracture.
27	*Senna occidentalis* (L.) Link	US	Kasivinda	Leaves	Leaf juice is applied externally to treat eczema.
11	**Capparidaceae**				

28	*Cadaba fruticosa* (L.) Druce.	S	Vuttarasi chettu	Leaves	Leaf paste used to cure skin diseases (leucoderma).
29	*Cleome gynandra* L.	H	Talake	Whole plant	Whole plant extraction used to cure peptic ulcers.
12	**Combretaceae**				
30	*Terminalia arjuna* (Roxb. ex DC.) Wight & Arn.	T	Tellamaddi	Bark	Bark extraction gives relief from urinal problems and decoction of leaves cures diabetes.
13	**Convolvulaceae**				
31	*Rivea hypocrateriformis* Choisy.	TH	Boddikura	Whole plant	Plant juice used for cure of fever.
14	**Cucurbitaceae**				
32	*Coccinia grandis* (L.) Voigt.	TH	Donda	Root, Fruit	Root extract is applied to relief and cure headache.
15	**Ebenaceae**				
33	*Diospyros chloroxylon* Roxb.	T	Ullinda	Stem bark, Fruits	Bark powder is applied on wounds and fruits used for diuretic and constipation.
16	**Euphorbiaceae**				
34	*Jatropha curcas* L.	S	Adavi amudam	Twigs	The tender twigs are used for cleaning teeth.
35	*Croton bonplandianus* Baill.	H	Verrimirapa	Whole plant	Juice of whole plant is applied to treat cuts and wound healing.
36	*Euphorbia hirta* L.	H	Alumu	Latex	Latex is applied for cut and injuries twice a day until healed.
37	*Flueggea leucopyrus* Wild.	S	Tellapulichettu	Leaves	Juice of whole plant is used for joint pains and rheumatism.
38	*Phyllanthus amarus* Schumach. & Thonn.	H	Nela usiri	Leaves	Leaf juice is administered for

					Jaundice.
39	*Phyllanthus reticulatus* Poir.	S	Pulichari	Root	Root or stem with coconut oil is applied on joint pains.
17	**Fabaceae**				
40	*Abrus precatorius* L.	C	Guruvinda	Seed	Seed powder is used as antidote for snake bite
41	*Pongamia pinnata* (L.) Pierre	T	Kanuga	Seeds	Seeds are used for bronchitis and whooping cough.
42	*Tephrosia purpurea (L.) Pers.*	H	Vempali	Root	Dried root is burned and the smoke inhaled to cure respiratory diseases.
18	**Lamiaceae**				
43	*Anisochilus carnosus* (L .f.) Wall.	H	Karpuravalli	Leaves	Fresh leaves squeezed and inhaled for cold and cough.
44	*Hyptis suaveolens* (L.) Poit.	US	Danthitulasi	Whole plant	Plant smoke is used for mosquitoes control.
45	*Leonotis nepetifolia* (L.) R.Br.	H	Ranabheri, Seeranta	Leaves	Leaf paste is applied on the burns.
46	*Leucas aspera* (Willd.) Link	H	Thummi	Leaves	Leaf juice mixed with milk is taken orally for skin diseases and rheumatic swellings.
19	**Lauraceae**				
47	*Cassytha filiformis* L.	C	Pachiteega	Stem	The stem with sugar, make in to powder used for heat.
20	**Liliaceae**				
48	*Aloe vera* (L.) Burm.f.	H	Chinna kalbandha	Leaves	Succulent leaf paste is applied in skin diseases, cool agent and cure diabetes.
49	*Asparagus racemosus* Willd.	SS	Pillipeechari gaddalu	Tubers	Root juice is mixed with honey used for dyspepsia. Root powder is taken with

					milk as aphrodisiac.
50	*Gloriosa superba* L.	C	Konda Nabhi	Tubers	Tubers paste applied over boils.
21	**Loganiaceae**				
51	*Strychnos nux-vomica* L.	T	Vishamushti	Seed	Seed paste used for snake bite.
22	**Loranthaceae**				
52	*Dendrophthoe falcata* (L.f) Ett.	C	Bhajanaka	Stem	Stem paste is used as an external application to cure wounds.
23	**Lythraceae**				
53	*Ammannia baccifera* L.	H	Agnivendra paku	Leaves	Fresh leaves are used in skin diseases.
54	*Lawsonia inermis* L.	T	Gorinta	Leaves	Leaf paste used for hair dye, wound healing.
24	**Meliaceae**				
55	*Azadirachta indica* A.Juss.	T	Vepa	Leaves	Leaf smoke is used for control of mosquitoes and leaf paste is used for anti helminthes and Skin diseases.
25	**Menispermaceae**				
56	*Cocculus hirsutus* (L.) W.Theob.	C	Dusari teega	Leaves	Leaves crushed and applied to cut and wounds.
57	*Tinospora cordifolia* (Willd.) Miers	SC	Tippatheega	Leaves	2or 3 raw leaves eaten for Diabetes.
26	**Mimosaceae**				
58	*Acacia leucophloea* (Roxb.) Willd.	T	Tellathumma	Stem bark	The stem bark is squeezed and inhaled to relieve from cold and cough.
59	*Acacia nilotica* (L.) Delile	T	Nallathumma	Bark	Fresh bark paste is used for Skin diseases and Burns.
60	*Albizia amara* (Roxb.) B.Boivin	T	Narlinga	Leaves	Leaf juice is applied externally on cut and

					wounds.
27	**Moraceae**				
61	*Ficus hispida* L.f.	T	Bramha mamedi	Leaves, Fruits	Leave juice is applied to treat boils and fruit and root is used for diabetes.
62	*Ficus mollis* Vahl	T	Juvvi	Leaves	Leaf juice is used externally to cure eczema and skin diseases.
28	**Myrtaceae**				
63	*Syzygium cumini* (L.) Skeels	T	Allaneredu	Seeds	Fruit decoction used for diabetes.
29	**Pandanaceae**				
64	*Pandanus odorifer* (Forssk.) Kuntze	S	Mogali	Flowers	Flower paste is applied for headache.
30	**Polygonaceae**				
65	*Persicaria glabra* (Willd.) M.Gómez	H	Neetiganneru	Leaves	Leaf juice is applied for setting of fractured bones.
31	**Rhamnaceae**				
66	*Ziziphus oenopolia* (L.) Mill.	S	Pariki	Leaves	Leaf paste is used wound healing.
32	**Rubiaceae**				
67	*Morinda pubescense* Sm.	T	Maddi	Stem bark	Fresh stem bark is crushed and the infusion given orally for jaundice.
68	*Spermacoce neohispida* Govaerts	H	Madana chettu	Seed	Seeds are intensifying sexual desires (aphrodisiac).
33	**Rutaceae**				
69	*Atalantia monophylla* DC.	S	Adavi nimma	Fruits	Berries yield oil used externally on joints pains.
70	*Chloroxylon swietenia* DC.	T	Billudu	Leaves	Leaf smoke is used for mosquitoes control.

34	**Sapindaceae**				
71	*Sapindus trifoliatus* L.	T	Kunkudu	Fruit	Fruits are used for eczema.
72	*Dodonaea viscosa* (L) Jacq.	S	Bandaru	Branch stem	Branches are good dentifrices.
35	**Simarubaceae**				
73	*Ailanthus excelsa* Roxb	T	Peddamanu	Stem bark	The stem bark paste is used to cure skin diseases.
74	*Balanites aegyptiana* (L.)	T	Garachettu	Fruit	Fruit powder is given with milk once in a day for cough and cold.
36	**Solanaceae**				
75	*Datura metal* L.	H	Ummentha	Leaves	Leaf juice is applied over the affected areas of ring worm.
74	*Solanum pubescens*.Willd.	S	Usintha	Fruit, seed	Fruit juice about 10 ml, 2 times for day for two days for indigestion.
37	**Sterculiaceae**				
77	*Firmiana simplex* (L.) W.Wight	T	Tapsi	Gum	Gum used for constipation.
78	*Helicteres isora* L.	T	Gubatada	Fruits	Fresh fruits made into paste and prepared a pills, given ones a day for 10days to cure scabies.
38	**Ulmaceae**				
79	*Holoptelea grandis* (Hutch.) Mildbr.	T	Tharisa	Stem bark	Stem bark paste used for healing wounds.
39	**Verbenaceae**				
80	*Vitex leucoxylon* L. f.	T	Konda vavili	Leaves	Leaf paste is applied to cuts, burns.
81	*Vitex negundo* L.	S	Vavili	Leaves	Leaf smoke used for removal of mosquitoes and mites.
40	**Vitaceae**				

82	*Cissus quadrangularis* L.	C	Anduatukula teega	Whole plant	Plant paste is for broken limbs.
41	**Zygophyllaceae**				
83	*Tribulus terrestris* L.	H	Palleru kaya	Leaves	Leaf extract is given orally once in a day for the removal of bladder stones.

C= Climber; H= Herb; S= Shrub; T= Tree; US= under shrub; TH= Twining herb; SC= Shrubby climber; SS= straggling shrub.

CONCLUSION

The present study clearly indicates the presence of rich diversity of medicinal plants. The use of herbal remedies among the tribal people in study area reflects the revival of interest in traditional medicine. This data provides basic source for future studies aimed at conservation, cultivation, improvement of ethnic traditional medicines and economic welfare of rural and tribal population of region. The ethnic knowledge has been rapidly eroded due to various factors such as lack of proper documentation, lack in transmission of knowledge to next generation, modernization and loss of floral diversity. Hence, conservation of floral diversity will be important tool to sustain and carry such important knowledge to the future generation.

ACKNOWLEDGMENTS

The Authors thank to the tribal people who shared their traditional knowledge and extend our grateful to Board of Research on Nuclear science (BRNS), BARC, Government of India, for funding the project.

REFERENCES

Akerele. O (1992). WHO guidelines for assessment of herbal medicines. Fitoterapia 63: 99-118.

Basi Reddy M. Raja Reddy K. & Reddy M.N. (1991). Ethnobotany of Cuddappah District, Andra Pradesh, India. Int. Journal of Pharmacognosy, 29: 1-8.

Chandra Babu N.M. Tarakeswar Naidu & Venkaiah (2010). Ethnobotanical plants of Kotia hills of Vijayanagaram District, Andrapradesh, India. *Journal of Phytology*. 2(6): 76-82.

Gamble J.S. & Fischer C. E. C. (1915-1935). Flora of the Presidency of Madras (repr. ed. 1957. Calcutta).

Harshberger J.W. (1895). The purpose of ethnobotany-1. Botanical Gazette, 21: 146-154.

Hemdri K. Shara C.R.R & Rao S.S. (1987 a). Medicinal plants of Andra Pradesh, Part –I. Ancient Science of life. 6: 167 – 186.

Hemdri K. Shara C.R.R & Rao S.S. (1987 b). Medicinal plants of Andra Pradesh, Part –II. Ancient Science of life. 7 (5): 5- 64.

Huxley. (1984). Green inheritance: The World wildlife Fund Book of India. (Collins/ Harvel, London).

Jain S.K. (1991). Dictionary of Indian folk medicine and Ethnobotany. Deep publications, New Delhi.

Murthy, E.N (2012): Ethno medicinal plants used by gonds of Adilabad District, Andhra Pradesh, India. International journal of Pharmacy & life sciences. Vol 3 (10): 2034-2043.

Kapoor S.L. and Kapoor L.D. (1980). Medicinal plantwealth of Karimnagar District of Andhra Pradesh. Bull. Med. Ethnobot. Res. 7: 120-144.

Pullaiah T. (1997a.) Flora of Andhra Pradesh. Vol.III, Monocotyledons, Scientific Publishers, Jodhpur.

Pullaiah T. & Ali Moulali D. (997b). Flora of Andhra Pradesh, Vol .II. Rubiaciae-Urticaceae. Scientific Publishers, Jodhpur.

Pullaiah, T. & Chennaiah E.(1997c). Flora of Andhra Pradesh, *Vol. I.* Ranunculacea-Alangiaceae. Scientific Publishers, Jodhpur.

Pullaiah T. Ramakrishnaiah V. Sadhya Rani S. & Rao P. N. (2000). Flora of Guntur district, Andhra Pradesh, India. Regency Publications.

Raja Reddy K.G. Sudarsanam & Gopala Rao. (1989). Plant drugs of Chittoor District, Andra Pradesh, India. Journal of Crude drugs Research. 27: 41-54.

Rama Krishna N. Varma Y.N.R. and Saidulu Ch. (2014). Ethnobotanical studies of Adilabad District, Andhra Pradesh, India. Journal of pharmacognosy and Photochemistry. 3 (1). 18-36.

Rao P.N. Raghava Swamy. & Pullaiah T. 2001. Flora of Nalgonda district, Andhra Pradesh. Shipra publication, Delhi.

Ravisanker T and Herny A.N. (1992). Ethnobotany of Adilabad District, Andhra Pradesh, India. Ethnobotany 4: 45-52.

Reddy N.M. (2013). Ethno botanical Study of Medicinal Plants in and around NAR Agriculture Farms area of Appannapeta village at Nalgonda district, Telangana, India. Journal of Medicinal Plants Studies. Vol. 1: 27-29.

Sanyasi Rao M. L. and Varma Y.N.R (2014): Folklore traditional knowledge on digestive disorders of domestic animals (cattle, sheep and goats) in the Medak District, Telangana, India. Biolife, Vol 2(3): 858-865.

Singh K.K. Palvi S.K and Singh H.B. (1981). Survey and biological activity of some medicinal plants of Mannanur forest, Andhra Pradesh. Indian Journal of forestry 4: 115-118.

Venkanna P. (1990). Medicinal plant wealth of Krisna District, Andhra Pradesh. A preliminary survey. Ancient Science of life. 102: 137-140.

Structural Characterization of Nano Crystalline Ni $Sm_xFe_{2-x}O_4$ferrites

Gopal boda[1], Nehru boda[2], G. Aravind[2], A. Panasa Reddy[1*], D.Ravinder[2*]
[1]Department of chemistry, college of Engineering, Osmania University, Hyderabad,
[2]Department of physics, Osmania University, Hyderabad, 500007, Telangana, India
[*]Correspondence author email: ravindergupta28@rediffmail.com.

ABSTRACT: Nano crystalline Samarium doped Nickel ferrites having compositional formula $NiSm_xFe_{2-x}o_4$where(x=0.00 to 0.10 with a step of 0.01) were synthesized by the citrate-gel auto combustion method. Synthesized powders were sintered at 500^0C for four hours in air and characterized by XRD, SEM, and EDS. X-ray diffraction analysis of the investigated samples showed cubic spinel structure of the ferrites without any impurity peak and the values of lattice parameter(a)and X-ray density(d_x) increases with the increase of Sm content. Scanning Electron Microscope (SEM) studies revealed morphology of the Nano crystalline samples. An elemental composition of the sample was studied by Energy Dispersive spectroscopy (EDS). The observed results can be explained on the basis of composition.

1. Key Words:-Ni-Sm Nano ferrites, citrate-gel auto combustion method, XRD, SEM and EDS.

1. Introduction:-Ferrites have diverged practical applications as high density magnetic data storage, Microwave absorbing materials. Magnetic resonance imaging contract agents and targeted release of drugs preparation conditions influence the cation distribution. Which in term reflects In the chemical and physical of ferrites to a great extend [1]

Properties of ferrites are highly sensitive to the substitution of different metal ions in its tetrahedral and octahedral sites

Substitution of large rare earth ions In place of small ions will result in strain which induce structural distribution and there by modify the properties of samples in Nano-region

The properties of ferrites are dependent on several factors, chemical composition, method of preparation, grain size, sintering temperature and atmosphere [2]

2. Experimental Details: The Nickel-Samarium nano ferrites having the chemical formula $NiSm_xFe_{2-x}O_4$ were synthesized by citrate gel auto combustion method using the below raw materials

2.1 Raw Materials:

- Nickel nitrate 99%pure(AR Grade)[$Ni(NO_3)_2$]
- Samarium nitrate 99.9% sigma Aldrich [$Sm(NO_3)_3$] $6H_2O$
- Ferric nitrate –99.9%pure(AR Grade) ($Fe(NO_3)_3$ $9H_2O$
- Citric acid –99%pure(AR Grad) ($C_6H_8O_7.H_2O$)
- Ammonia Solution -99%pure(AR Grade)(NH_3)

2.2. The flow chart of synthesis of Ni-Sm Nano ferrites:

The calculated quantities of metal nitrates were dissolved in minimum amount of distilled water to get clear homogeneous solution an aqueous solution of citric acid was added to the metal nitrate solution. The molar ratio of citric acid to the total moles of citric acid to the total moles of nitrate ions was adjusted to 1:3 the flow chart shown in fig ;(1)

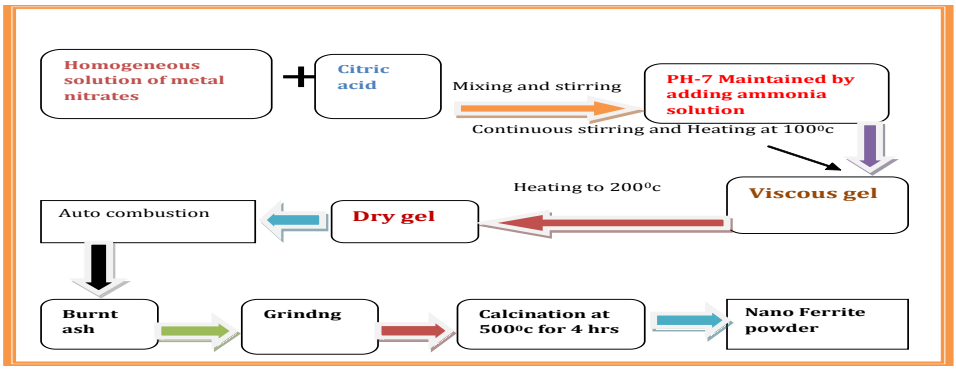

Fig(1): The flow chart for synthesis

2.3 Structural characterization by XRD:

The structural characterization was done by X-Ray Diffract meter were recorded using Regakumaniplex powder X-ray diffractometer (Cu-Kα λ=1.5406A°)with

diffracted mono chromatic beam with radiation of wave length (1.5405A^0) the diffraction pattern of Ni-Sm between brag Angles 10^o to 80^o in the steps of 0.04º/sec. nano ferrites particles Were shown in fig.

The crystalline size was calculated for the sample using the high intensity 311 peak and using Debay Scherrer formula **[**3**]** while taking into account the intensity broadening [4].

Crystalline size of the sample $\boldsymbol{D = \frac{0.91\lambda}{\beta \cos\theta}}$

Where λthe wavelength of X-ray is used [5]. βis the width of diffraction peak i,e. full width Half Maximum(FWHM) , θ is the peak position.

Lattice parameter (a) of the sample was calculated by the formula. $\boldsymbol{a = d * \sqrt{h^2 + k^2 + l^2}}$[6] Where a=Lattice constant, (hkl) are the Miller indices, d is the inter planner space The X-ray density of the prepared sample was calculated using the relation $\boldsymbol{dx = \frac{8M}{a^3 N}}$ (g/cm^3) [7] where **M**= molecular weight of the sample, **a** is the lattice parameter and **N** is the Avogadro number.

3. Result and Discussion;-

3.1. XRD Analysis:

A phase analysis using X-ray diffraction technique was performed to confirm the formation of single-phase cubic spinel structure as shown in **fig-(2)**.With no extra lines corresponding to any other crystallographic phase. The results obtained from XRD pattern for all the samples of $NiSm_xFe_{2-x}O4$ with the (hkl) values corresponding to the diffraction peaks of different planes (220), (311), (400), (422), (511), and (440) are spinel cubic phase

The calculated values of crystalline size for the different compositions are given in the table (1).It can be seen from the table that the values of the crystal size varies from 28.53nm to 39.45nm of the various Sm concentrations

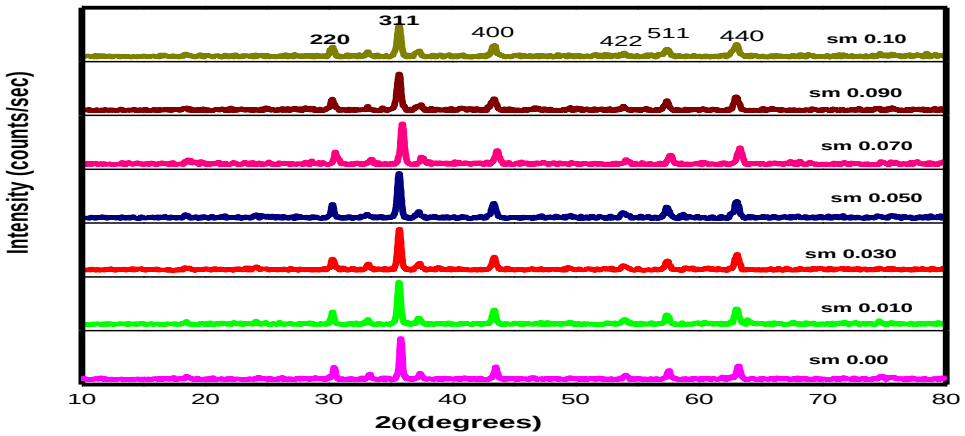

Fig (2): XRD pattern of Ni-Sm Nano ferrites

The lattice parameter values of all the composition of Samarium doped Iron ferrites have been calculated from the d- spacing and are given in the table.(1)

A plot is drawn between the lattice parameter vs Samarium composition is shown in Figure (3) variation of lattice constant with Sm^{+3} content in $NiSm_xfe_{2-x}O_4$is (x=0.00 to 0.10 with a step of 0.01)is observed that the Lattice parameter increases with increase in Sm content. This is attributed to replacement of smaller ionic radii Ni (0.78A°) by larger ionic radii Sm^{+3} (A°) ions. This linear variation indicates that the Ni-Sm ferrite system obeys vegard's law [8] and table1 shown below

Ferrite composition	**Crystalline size(D)nm**	**Lattice parameter(a)A^0**	**X-ray density(d_x)[gm/cc]**
$NiFe_2O_4$	**39.45**	**8.307**	**5.432**
$NiSm_{0.010}Fe_{1.99}O_4$	**33.37**	**8.338**	**5.393**
$NiSm_{0.030}Fe_{1.97}O_4$	**30.72**	**8.061**	**6.162**
$NiSm_{0.050}Fe_{1.95}O_4$	**30.74**	**8.329**	**5.679**
$NiSm_{0.070}Fe_{1.93}O_4$	**31.65**	**8.281**	**5.638**
$NiSm_{0.090}Fe_{1.91}O_4$	**28.53**	**8.458**	**5.332**
$NiSm_{0.10}Fe_{1.9}O_4$	**29.53**	**8.334**	**5.596**

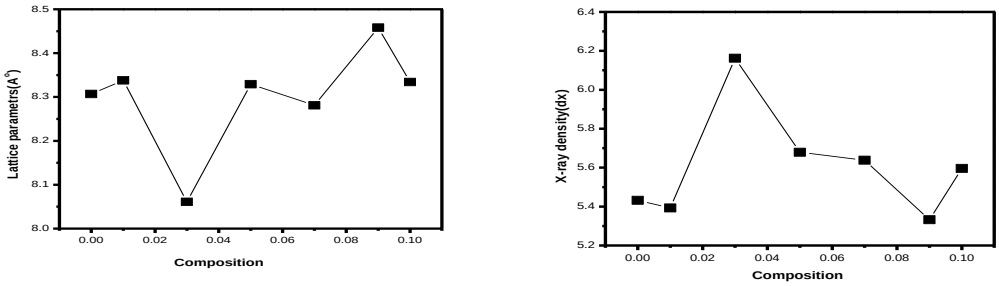

Fig; (3)) variation of lattice constant with Sm^{+3} content and figure (4) shows the X-ray density (d_x) vs Sm^{+} concentration

The **figure (4**) shows the X-ray density (d_x) vs concentration, The X-ray density (d_x) is depend on the lattice parameter and molecular weight of the sample. From the table one can observe that molecular weight of the sample is increases with Samarium concentration and lattice parameter is also increases with the increase of Sm compositions. This may due to the grater atomic weight of sm 150.36gm/mol and lesser atomic weight of Fe-55.845gm/mol(8) shown in figure[4, 5].

Samarium was very small .the calculated values of the lattice constant tabulated in table:1 show that there has been no structural distortion for the various ratios. The fact that samarium goes as substitution into the cubic spinel lattice evident from the absence of any extra peaks in the XRD spectrum

3.2. Morphology by SEM: studied microscope (prepared samples by Citrate- Gel Auto combustion method was using scanning electron SEM) where the secondary electron images were taken at different magnifications to study the synthesized samples were shown in **figure (5)**.

The sem images of Ni-Sm ferrite are shown in the Fig the images show that the particles have an almost homogeneous distribution ,and some of the samples are agglomerated form .it evidenced by SEM images that the agglomeration of particles lies in nano region.the particles were observed as uniform grain (in different SEM images) sizes[9]

X=0.0 X=0.010 X=0.030

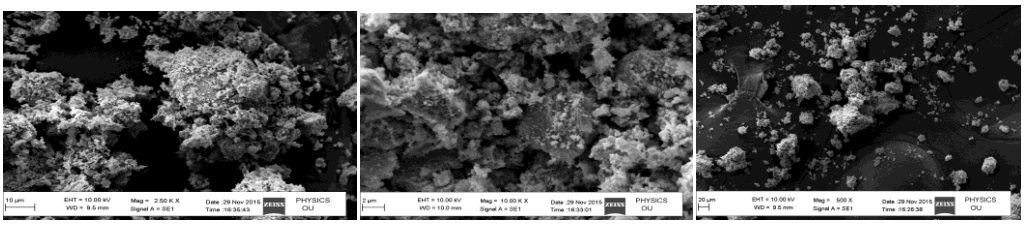

X=0.050 X=0.070 X=0.090

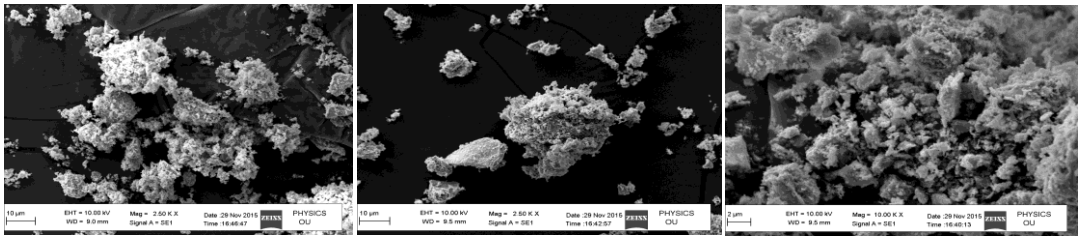

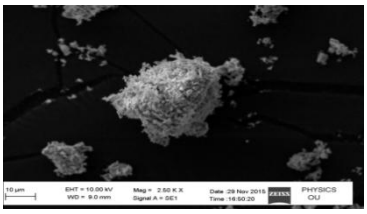

X=0.1

Fig(5) : SEM micrographs of compositions of Ni-Sm nano ferrites

3.3. Elemental Analysis by EDS:

The EDS spectra give information about the chemical composition of the elements present from the surface to the interior of the solids, and they are used to confirm the homogeneity of the investigated samples.

The spectra indicated the presence of O, Fe, Ni, and Sm as the major elements in the synthesized material with no impurities are observed along with elemental mapping. The EDX spectra of the samples are shown in figure (6)

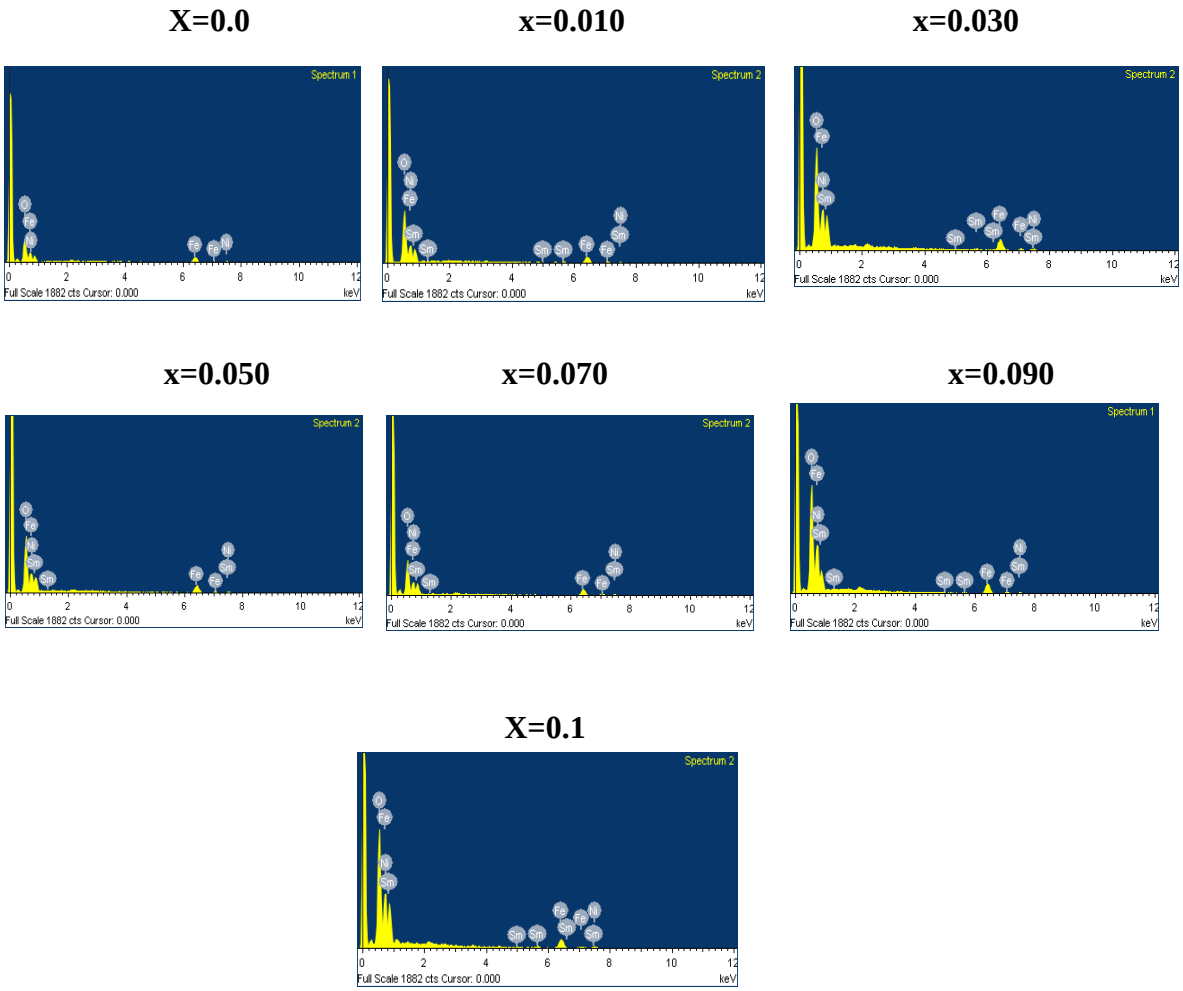

Fig(6) : EDS micrographs of compositions of Ni-Sm nano ferrites

4. Conclusion:

- Citrate Gel Auto Combustion technique is a convenient way for obtaining a homogeneous nano sized mixed ferrites, it is very simple and economical method where no specific heating or cooling rate is required .
- X-ray diffraction pattern confirms the formation of single phase cubic spinel structure. From standard data JCPDS.
- The crystalline size of the various NiSm ferrites was in the range of 28 to 39 nm.
- The Lattice parameter has increased with the increase of Sm concentration in Ni-Sm ferrites which indicate that the mixed Ni-Sm ferrite system obey the vegard's law

- SEM micrographs of various compositions indicate the morphology of particles is similar .they reveal that largely agglomerated.
- EDS data give the elemental % and atomic % in the mixed Ni-Sm ferrites and it shows the presence of Ni, Sm, Fe and O without precipitating cations.

5. Acknowledgements:

The authors are very grateful Prof.G.VenkateshwarluHead Department of Chemistry University college of science Osmania University Hyderabad, And thankful to Prof .M.Vithal Chairman board of studies .Department of Chemistry, University college of science O.U.Hyderabad for his support in characterization (XRD)one of the author Gopal Bodais thankful to**UGCNON- NET fellowship** for their financial assistance,

References:

[1] Smitha Thankachan,Binu P. Jacob, Sheena Xavier, E.M Mohammed 348 (2013) 140-145

[2] K.Kondo, T. Chiba, S. Yamada, Journal of Mag Mag mater **541,** 254(2003

[3] Cullity B D, Elements of X-ray diffraction (addition Wesley, Reading, Mass), 1959. P132.

[4] Mahmud ST, Akther Hossain AKM, Abdul Hakim AKM, Seki M, Kawai T. Tabata H (2006) j Magn Mater 305;269 doi; 1016/j.jmmm.2006.01.012.

[5] B.D. Cullity, Elements of X-ray diffraction, Wesely Pub,Co,.Massachusetts,1987,101-356

[6] B.P.Ladgaonkar, P.P.Bakare,S.R. Sainkar and A.S.Vaingankar, "Influence of Nd+3 substitution on permeability spectrum of Zn-Mg ferrite". Materials Chemistry and Physics, Volume 69,Issues 1- 3,March 1, 2001, pages 19-24.

[7] R.C.Kumbale. P.A.Shaikh, S.S. Kamble, Y.D.Kolekar J.Alloys Comp., 478(2009), p.599 doi:10.1016/j.jmmm.2005.03.007

[8] K.B.Modi, J.D.Gajera, M.P.Pandya,H.G.Vora, H.H.Joshi, Pramana Journal of Physics, Vol 62, No 5,May, 2004, pages 1173-1180

[9] M. Maria lumina Sonia, S. Pauline, Mary N. L ISSN-2319-8354(E).

Validation of Kinetic Modelling in Removal of Sulphonated Dye in Waste Water using Polyaniline/ZnO nanocomposites

[#]Neha V. Dambhare, Neha V. Nerkar, Subhash B. Kondawar*
Department of Physics, Rashtrasant Tukadoji Maharaj Nagpur University, Nagpur – 440033, India
*Corresponding Author E-mail: sbkondawar@yahoo.co.in
[#]Presenting Author E-mail: nehadambhare1994@gmail.com

ABSTRACT

Sulphonated dyes are some of the biggest contributors to water pollution and very harmful to environment for human health concerned. In this study, a method for the removal of cationic sulphonated methyl orange (MO) dye from aqueous solution using chemical interaction of dye molecule with PANI/ZnO nanocomposites are reported. PANI/ZnO nanocomposites have been prepared by in-situ polymerization. Morphological study using SEM revealed that PANI/ZnO was found to best promising candidate for adsorption of dyes due to more porosity compared to that of pure PANI. UV-Vis spectroscopy was done to study adsorption of MO dye. Percentage of removal of dye was then studied comparatively for PANI and PANI/ZnO nanocomposites. The percentage adsorption was found to be 79% for PANI/ZnO compared to that of 53% for pure PANI. In order to evaluate kinetic mechanism the pseudo first order model, pseudo second order model and intra particle diffusion model were tested the validity of the models were verified by the linear equation analysis. The second-order kinetic model was found to be the best linearity compared to other models which indicate that it is physical adsorption. The adsorption process was shown to be an efficient for dye removal from water solutions. The results clearly demonstrated that ZnO contributed to the adsorption mechanism through electrostatic interactions between sulphonic groups of the adsorbent (which are known as strong cation exchangers) and the cationic sites of methyl orange dye and it gives very novel and green method of removal of hazardous dye.

Keywords: Adsorption, conducting polymer, PANI/ZnO nanocomposites, UV-Vis spectroscopy, sulphonated dyes.

1. Introduction

Coloured wastewater is particularly associated with reactive dyes; these dyes make up approximately 30 % of total dye market. Reactive dyes are the most common dyes used due to their advantages, such as bright colours, excellent colour fastness and ease of application. Reactive dyes are highly soluble in water and the resultant change in the water colour is unattractive to the public. The characteristic structures of dyes, particularly reactive dyes, are very complex, chemically stable and difficult to degrade or eliminate. Moreover, the contamination of public streams with these dyes may present a risk to human beings since aquatic living creatures such as fish that can accumulate dyes in their tissues. And the toxicity of reactive dyes has been reported at concentration as low as 5.2 mg/l. Water pollution by high levels of pollutant dyes from textile industry is a serious problem owing to the toxicity effect of these compounds. Complete removal or at least decolourization of these compounds from the environment is therefore an important issue. The dyes from textile industries are major sources of environmental pollution because they are non-biodegradable. Many methods such as flocculation, reverse osmosis and activated carbon adsorption have been used in wastewater treatment. However, photocatalysis is often used as a technique to degrade dyes because it is simple and cost effective. Conventionally inorganic semiconductors are used as photocatalysts and TiO_2, doped TiO_2, and ZnO are extensively used for the degradation of dyes in waste water. Conducting polymers are becoming the most promising new materials for next-generation electronic devices [1]. Polyaniline (PANI) is one of the conducting polymers that generated a great interest over the past two decades because of its potential applications in many fields. Its high electrical and electronic properties, ease of preparation, and low costs render the polymer promising material for several technological applications. These applications include rechargeable batteries, sensors, separation membranes and corrosion inhibitor. Conducting polymers have band gaps in the same range as inorganic semiconductors. Further, the band gaps of these polymers can be tuned by chemical manipulation of the backbone. Therefore conducting polymers composites with suitable band gaps, could, in principle, act as photocatalysts for dye. Polyaniline (PANI) is a poly aromatic amine that can be

easily synthesised. It is one of the most potentially useful conducting polymers and has received considerable attention in recent years. Chemical polymerization of aniline in aqueous acidic media can be easily performed. The oxidation process is accompanied by the insertion of anions of acid electrolyte in order to maintain the charge neutrality of the final polymer product. Ammonium persulfate is a popular and frequently used chemical oxidant for polymerization of aniline in acidic aqueous solutions [2]. In this study, we report that polyaniline/zinc oxide composites can remove anionic (sulfonated) dyes with the application of UV and visible light through a chemical interaction with the sulfonated dyes. Thus, the objective of the article is to examine the use of polyaniline/ZnO composites for the removal of various sulfonated dyes from aqueous solutions and propose a mechanism of chemical interaction between the sulfonated dyes and PANI/ZnO. Methyl orange is intensely coloured compound used in dyeing and printing textiles. It is also known as C.I. acid orange 52. Chemist used methyl orange as an indicator of weak bases with strong acids. It is water soluble azo dye. It is carcinogenic and mutagenic in nature and hence it has bad impact on nature as well as human habitat [3, 4].

2. Experimental

Synthesis of Polyaniline/ZnO nanocomposites

ZnO nanoparticles were prepared by colloidal route method and 5 wt% of it sonicated with 0.2M aniline and 0.2M HCl solution in 100 ml water for half an hour. The mixture was stirred continuously and 0.2M ammonium persulphate was added drop wise. The colour was changed from colourless to blue and finally dark green. The mixture was kept overnight, filtered and washed with ethanol and distilled water. The precipitate was dried in vacuum oven at 80^{o}C [5]. Similarly, pure polyaniline was prepared with out the use of ZnO for comparison.

3. Result and Discussions

The SEM micrographs of PANI powder and PANI/ZnO are shown in **Fig. 1**(a) and (b), respectively. It can be seen that the surface morphology of PANI powder was composed of irregular agglomeration of particles. On the other hand, PANI/ZnO aggregates have regular diameter which merge tightly with each other to exhibit a

net like macro porous state. This macro porous structure of the immobilized PANI is expected to contribute to the efficient adsorption of adsorbents since it provides a path for the insertion and extraction of molecules or ions within the inner layer of the immobilized adsorbent. The thickness of the immobilized PANI would depend on the amount of PANI deposited on ZnO.

For adsorption experiments, the synthesized PANI and PANI/ZnO were added to methyl orange dye solution with concentration of 50 ppm. The chemical interaction of dye molecule with the PANI and PANI/ZnO provided the energy for chemical reaction between sulphonated dyes and charged backbone of PANI, leading to significant adsorption of the dyes. The solution was stirred for 1 hr. During this process, samples were collected from the reaction beaker at different time intervals, and the concentration of the dye was determined by UV-Vis absorption spectroscopy. The dye concentration was calibrated with the beer-Lambert law at λ_{max}. It was found that the polymer adsorbs the respective dye from the solution. After adsorption of the dye, the PANI and PANI/ZnO samples were washed with distilled water, dried and used for absorption spectroscopy [6]. **Fig. 2**(a) and 2(b) shows the variation of the dye concentration with time in the presence pure PANI and PANI/ZnO. All experiments were carried out for 1 hr., but after 40 min there was no significant adsorption after this time. The experiments were conducted with different initial concentrations of methyl orange in the presence of PANI and PANI/ZnO for 1 hr. When the initial concentration of the dye was less, the dye was completely adsorbed in solution. At higher concentrations of the dye, it was not completely adsorbed, indicating that there is a saturation limit for the polymer above which it does not remove the dye [7].

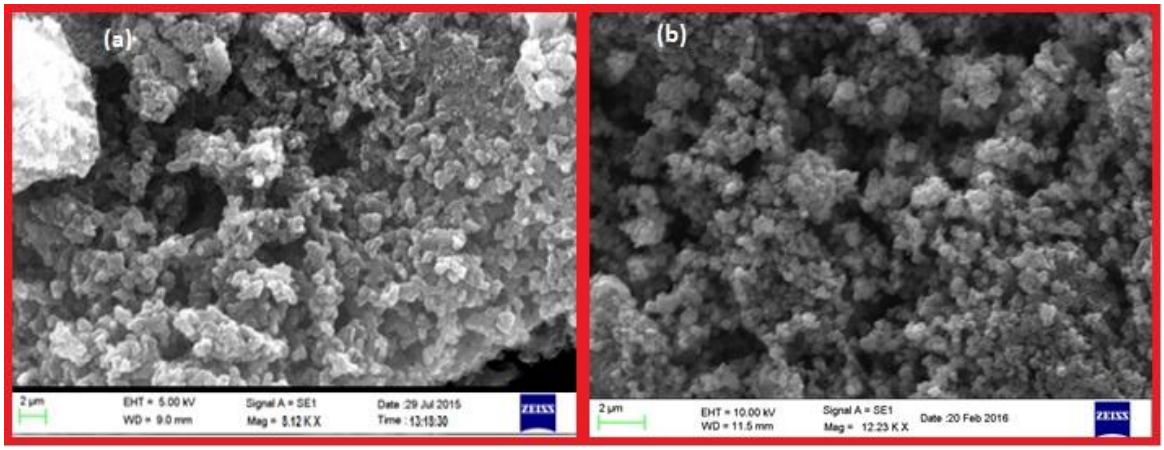

Fig. 1: SEM images of pure PANI and PANI-ZnO

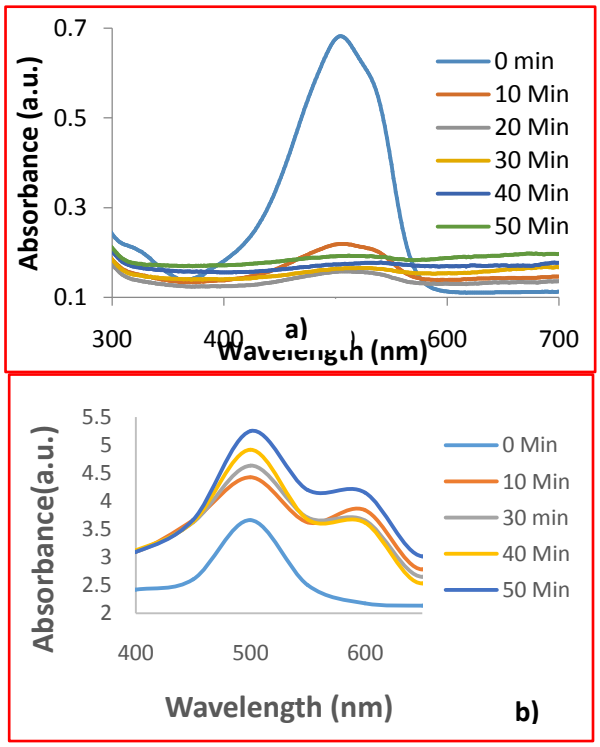

Fig. 2: Absorption spectra of PANI and PANI/ZnO in methyl orange dye of 50ppm

It is observed that adsorption amount increased in PANI/ZnO compared to that of pure PANI. The extent of MO dye adsorption onto PANI/ZnO composite is highly accessible as compared to pure PANI due to higher surface area and electronic interaction in PANI/ZnO composite. The binding sites of interactions available in PANI/ZnO composite would be larger hence more interactions with anionic dye MO occurred. Molecules containing π-electrons or non-bonding electrons (n-electrons) can absorb the energy in the form of ultraviolet or visible light to excite these

electrons to higher anti-bonding molecular orbital. The more easily excited the electrons (i.e. lower energy gap between the HOMO and the LUMO), the longer the wavelength of light it can absorb [8]. The characteristic peak of 507 nm assigned to the n-π* transition from the nonbonding nitrogen lone pair to the conduction band π*. This peak shows high absorbance with the presence of methyl orange in the solution. With respect to time, the absorbance was found to be decreased. PANI-ZnO absorbed more methyl orange compared to that of pure PANI [9]. It is well known that the degree of ionization of a dye molecule depends on the pH of the aqueous medium. Methyl orange contains one sulfonated group (-SO_3Na). In acidic aqueous solutions, the functional group of methyl orange (-SO_3Na) gets ionized, and the dye exists in anionic form. **Fig 3** shows the percentage removal of the methyl orange with dye concentrations. It is obvious that it is higher for lower concentration and lower for higher concentrations. In order to find kinetic mechanism pseudo first order model, pseudo second order model were tested and the validity of the models verified. The pseudo-first-order rate equation is given by equation (1)

$$Log(Q_e - Q_t) = logQ_e - \frac{k}{2.303}t \qquad (1)$$

Where Q_e and Q_t (mg g^{-1}) refer to the amount of dye adsorbed at equilibrium and time t (min), respectively, and k is the rate constant. **Fig. 4** shows the plot of the pseudo-first-order.

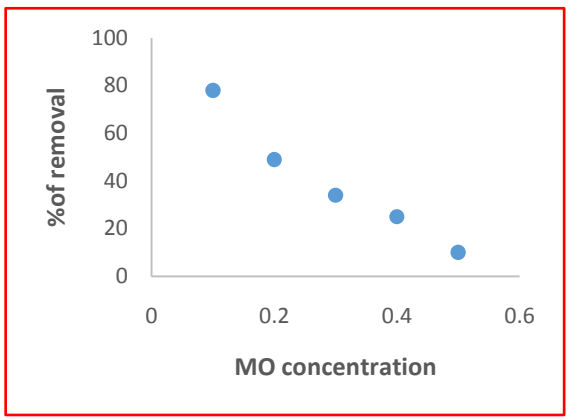

Fig. 3: % removal of dye

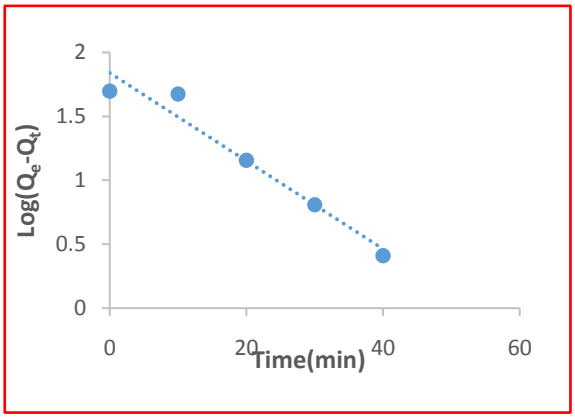

Fig. 4: Kinetic plot of MO adsorption onto PANI-ZnO composites (Pseudo first order reaction for 50mgL^{-1})

The pseudo-second-order model can be represented by equation (2);

$$\frac{t}{Q_t} = \frac{1}{k_2} Q_e^2 + \frac{t}{Q_e} \qquad (2)$$

Where, k_2 is the rate constant of the pseudo-second-order model. **Fig. 5** shows the curve-fitting plot of (t/Qt) vs. time. The third model is an Intraparticle diffusion model. Weber and Morris stated that if Intraparticle diffusion is the rate-controlling factor, uptake of the adsorbate varies with the square root of time. The root time dependence is expressed by (3);

$$Q_t = k_i t^{1/2} + C \qquad (3)$$

Where, k_i is an Intraparticle diffusion rate parameter. Figure 8 shows a plot of Q_t vs. $t^{1/2}$.

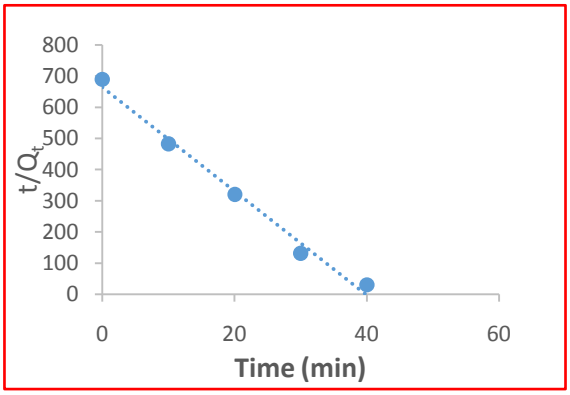

Fig. 5: Kinetic plot of MO adsorption onto PANI-ZnO (pseudo second order kinetic plot for dye concentration 50mgL^{-1})

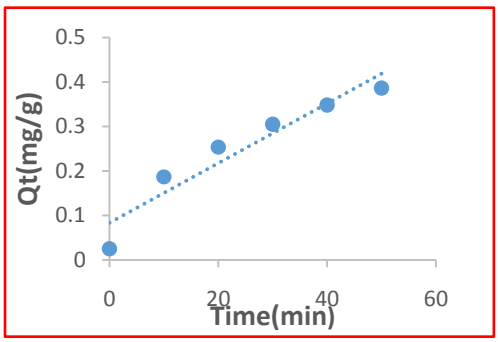

Fig. 6: Kinetic plot of MO adsorption onto PANI-ZnO (Intraparticle diffusion model for dye concentration 50mgL^{-1})

4. Conclusion

PANI/ZnO nanocomposites have been successfully prepared by in-situ polymerization. The adsorption of anionic sulfonated dye MO from aqueous solutions onto PANI/ZnO nanocomposite was studied. Percentage of removal of dye was studied comparatively for PANI and PANI/ZnO nanocomposites. It is concluded that the adsorption amount increased in the PANI/ZnO composites nearly about 79% which is much more than that of pure PANI, hence PANI/ZnO composite provides a more efficient adsorbent. The second-order kinetic model was found to be the best linearity compared to other models which indicate that it is physical adsorption.

References

1. Ozcan, A. S., Ozcan, A., *Journal of Colloid Interface and Science*, (2004), 276, 39–46.
2. Forgacs, E., Tibor, C., Gyula, O., *Environmental Monitoring*, (2004), 30, 953–971.
3. Annadurai, G., Chellapandian, M., Krishnan, M. R.V., *Environmental Monitoring* (1999), 59, 111–119.
4. Debajyoti, M., Giridhar, M., Radhakrishnan, S., Satish, P., *Journal of Physical Chemistry B*, (2009), 113, 2293–2299.
5. Mahanta, D., Giridhar, S., Madras, R., Patil, S., *Journal of Physical Chemistry B*, (2008), 112, 10153–10157.
6. Nerkar, N. V., Kargirwar, S. R., Kondawar, S. B., Burghate, D. V., Burghate, P. D., *International Symposium Ultrasonic*, (2015), 22(24), 195-198
7. Ayad, M., El-Nasr, A., *Journal Nanostructure Chemistry*, (2012), 3, 1-9.
8. Sharma, Y. C., Uma, S. N., Upadhyay, G. F., *Journal Applied Science and Environmental Sanitation*, (2009), 4, 21–24.
9. Kulkarni, M, Thakur, P, *Nepal Journal of Science and Technology*, (2014), 15(2), 105-110.

Synthesis and Photoluminescence of Tb^{3+} doped $Sr_3Y_2(BO_3)_4$ Phosphor

M.Srinivas
Department of Physics, Osmania University, Hyderabad, 500007, India
*Corresponding authot. E-mail: msrinivas.ou@gmail.com

ABSTRACT : Polycrystalline $Sr_3Y_2(BO_3)_4$ phosphor doped with Terbium ions (Tb^{3+}) were synthesized by conventional solid state reaction method. These samples are characterized by X-ray techniques (XRD), energy dispersive spectroscopy (EDS) and photoluminescence (PL) respectively. Strong photoluminescence spectrum was obtained at 543 nm. Emission spectra can be assigned to the emission lines of Terbium activators corresponding to 490, 543, 588 and 622 nm attributed to the $^5D_4 \rightarrow {}^7F_J$ (J = 3, 4, 5, 6) transitions of Tb^{3+} ions observed under UV excitation spectrum. PL peak intensity was found to increase with increase in the dopant concentration. These phosphors may provide a new kind of luminescent material for light emitting diodes under uv excitation.

Keywords: Phosphor, XRD, EDS, $Sr_3Y_2(BO_3)_4:Tb^{3+}$ and photoluminescence

1. Introduction

The study on luminescence properties of the rare earth elements hosted in numerous crystalline matrices such as oxides, silicates, aluminates, aluminoborates, aluminosilicates, nitrides, borates and inorganic materials are strongly intereting because of their potential application in solid-state lighting devices. [1]. Luminescence of several inorganic borate phosphors doped with rare earth ions, such as Eu^{+3}, Ce^{+3}, Tb^{+3} etc. have been studied. Owing to their simple and low-cost fabrication along with high thermal and chemical stability as well as transparency over a wide spectral range (beginning from UV and extending in to visible) borate hosts are considered as potential candidates for many optoelectronic applications [2]. The presence of sensitizer ions or activators, and the photoluminescence (PL) properties of the phosphor materials depend on the nature of host lattice, especially on the local geometry of the rare earth ion sites. Examples of these known borate phosphors are $M_3Al_6B_8O_{24}:Ce^{3+}$(M=Ca, Sr, Ba), $YCa_3(AlO)_3(BO_3)_4:Eu^{3+}$, $Sr_3Y_2(BO_3)_4:Eu^{3+}$, $Na_2Y_2B_2O_7:Eu^{3+}$, $Sr_2Mg(BO_3)_2:Ce^{3+}$ [3-6] have been reported in the

literature. The main aim of this work is to report the synthesis and photoluminescence (PL) of $Sr_3Y_2(BO_3)_4$: Tb^{+3} phosphor.

2 **Experimental**

The phosphors $Sr_3(Ya_{1-x}Tb_x)_2(BO_3)_4$ (x = 0, 0.01, 0.03 and 0.05) were synthesized by traditional solid-state reaction technique. The Stoichiometric amounts of starting materials are AR grade as $SrCO_3$ (99.99%), Y_2O_3 (99.99%), H_3BO_3 (99.9%) and Tb_2O_3 (99.99%), were mixed and then ground thoroughly in an agate mortar for 8 hours to give homogenous mixture. The resultant powders were initially dried at 80^0C and then kept in an alumina boat inside a tubular furnace made up of alumina tube and slowly heated to 1300^0C in air. These samples were kept at this temperature for 3 h and then annealed at 850^0C for 1 hour in air. These samples were rapidly cooled down to room temperature and were grinded to get fine powder for further studies.

In order to characterize the phase purity and structure of the as-prepared $Sr_3Y_2(BO3)_4$: Tb^{3+} samples have been studied by X-ray powder diffraction (XRD). The Powder X-ray diffractograms were recorded on Philips X'pert Analytical X-ray diffractometer using Nickel filtered Cu-K□ (λ = 1.5406 A^0) radiation. The operation voltage and current of the instrument were maintained at 40 kV and 30 mA respectively. All the compositions of as prepared samples were confirmed by energy dispersive spectroscopy (EDS) using a HITACHI S-3700N equipment. The photoluminescence spectra were measured using Spectrofluorophotometer (Shimadzu, RF 5301 PC) with a 150 w a xenon arc lamp. All measurements were recorded at room temperature. All measurements were carried out at room temperature.

3 Results and discussion

3.1. Powder XRD

The X-ray diffractograms of $Sr_3(Y_{1-x}Tb_x)_2(BO_3)_4$, (x = 0.01, 0.03 and 0.05) are shown in Fig.1 it is conformed that all the samples are shown in single phase diffraction peaks match very well with the reported values [7,8,9], which can be assigned to orthorhombic structures.

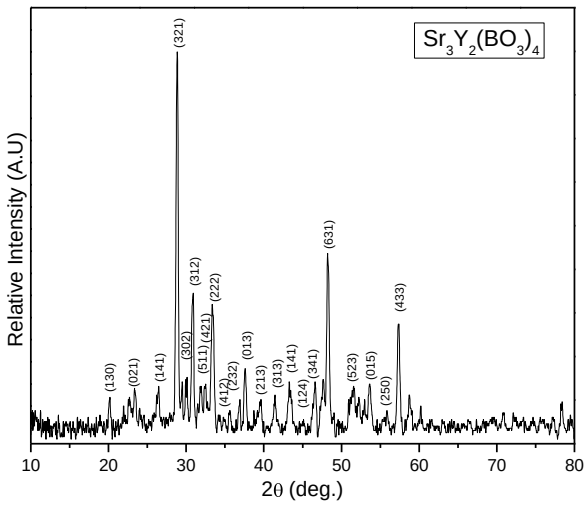

Fig 1 XRD of $Sr_3Y_{1.9}Tb_{0.1}(BO_3)_4$ phosphor

3. 2. EDS

The EDS spectrum of 0.1 mol % Tb^{3+} doped $Sr_3Y_2(BO_3)_4$ is shown in Fig.2. The results of the $Sr_3Y_2(BO_3)_4$: Tb^{3+} samples show peaks corresponding to Sr, Y, Tb and O. The EDS pattern confirms the presence of terbium in the $Sr_3Y_2(BO_3)_4$ powders and its wt% is nearly equal to the doped value of Tb in $Sr_3Y_2(BO_3)_4$.

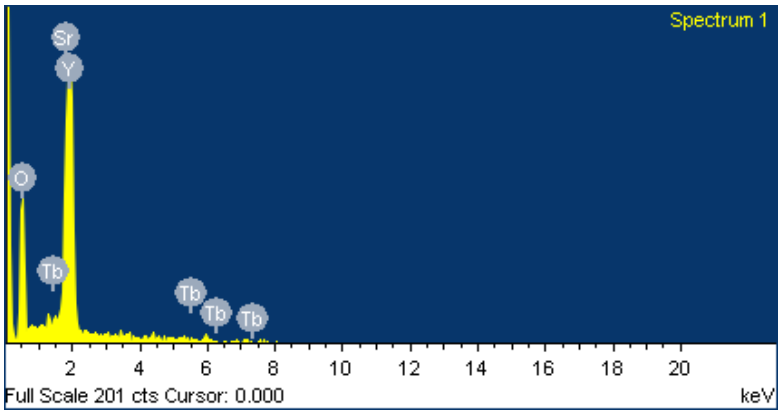

Fig.2 EDAX spectra of $Sr_3Y_2(BO_3)_4$ phosphor

3.3. Luminescence properties

The luminescence studies of Tb^{3+} activated $Sr_3Y_2(BO_3)_4$ phosphor which can efficiently emit under UV light excitation. The excitation and emission spectrum shown in figure 3(a) and (b)

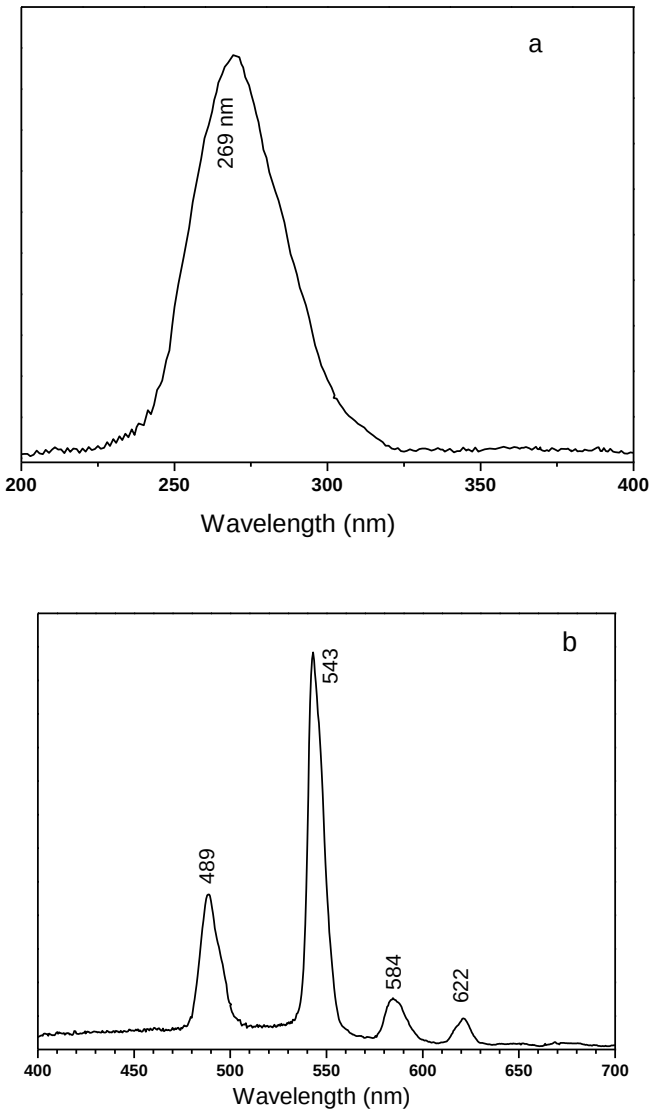

Fig.3 (a) Excitation and (b) Emission spectrum of $Sr_3Y_2(BO_3)_4$:Tb^{3+} phosphor for 0.1 concentration

The emission spectrum of $Sr_3Y_2(BO_3)_4$:Tb^{3+} phosphor recorded under the 269 nm excitation shown in fig.3. The emissions from Tb^{3+} ions confirm the presence of the RE ion into the cordierite matrices in the crystals. The sharp lines of Tb^{3+} ions were observed, which were attributed to the $^5D_4 \rightarrow {}^7F_J$ (J = 3, 4, 5 and 6) transitions of Tb^{3+} ions and were situated at 490, 543, 588 and 622 nm, when the samples were excited with wavelengths 269 nm. Among the emission lines from the $^5D_4$ state the dominant emission is observed at 543 nm, corresponding to the $^5D_4 \rightarrow {}^7F_J$ transition

of Tb^{3+} ions [8,9]. It is seen that the PL emission intensity are increased with the increase of dopant concentration.

4. Conclusions

$Sr_3Y_2(BO_3)_4$ were synthesized by conventional high temperature solid state reaction method and confirmed phase purity by XRD. The photoluminescence spectra indicate that the main emission peak at 543 nm under UV excitation due to $^5D_4 \rightarrow {}^7F_5$ transition of Tb^{3+} ions. PL peak intensity was found to increase with increase in the dopant concentration. These phosphors may provide a new kind of luminescent material as green light emitting diodes under ultraviolet excitation.

Acknowledgements:

The author acknowledge to the UGC, New Delhi for awarding MRP scheme to carried out this work.

References

[1] Bing Yan, Kun Zhou ,*J. Alloys.Compd.,398 (2005) 165-169.*

[2] Allu AmarnathReddy, Subrata Das, Ashtosh Geol, Rupam Sen, Renee Siegel, *AIP Advance **3**,022126(2013).*

[3] T.R.N.Kutty, Mater.Res.Bull., 1990, 25, 343.

[4] L.Wang and Y.Wang, Mater. Sci. Eng., B, 2007, 139, 232.

[5] Y.Zhang and Y.Li, J.Alloys Compd., 2004, 384, 88.

[6] H.Liang, H.Lin, G.Zhang, P.Dorenbos and Q.Su., J.Lumin.,2010

[7] A.Boultif, D.Louer, J App.Crystallogr.24 (1991) 987.

[8] Ling He, Yuhua Wang *J, Alloys.Compd., 431 (2007) 226-229.*

[9] Li Pan-Lai, Yang Zhi-ping,, WANG Zhi-jun, GUO Qing-lin,*Chinese Physics B, 17(5) 2008.*

[10] R. G. DeLosh, T. Y. Tien, F. F. Gibbon, P. J. Zacmanidis and H. L. Stadler, J. Chem. Phys. 53, 681 (1970).

[11] Lianhua Tian and Sun-il Mho, Byung-Yong Yu, Hong Lee Park, J of the Korean Physical Society, Vol. 47, No. 6, December 2005, pp. 1070

Highly Sensitive Hydrogen Gas Sensor Based on Polyaniline Coated SnO_2 Nanofibers

[#]Megha A. Salorkar, Hemlata J. Sharma, Subhash B. Kondawar*
Department of Physics, Rashtrasant Tukadoji Maharaj Nagpur University, Nagpur – 440033, India
*Corresponding Author Email: sbkondawar@yahoo.co.in
[#]Presenting Author Email: megisalorkar@gmail.com

ABSTRACT

Tin oxide (SnO_2) nanofibers were synthesized by using polyvinylpyrrolidone (PVP) as template through electrospinning technique and subsequent calcination at 300 °C for 4 hr to decomposition organic PVP and formation of SnO_2 from its hydroxide form. SnO_2-Polyaniline (SnO_2/PANI) heterostructure sensors have been developed for sensing hydrogen gas at room temperature with high specificity. SnO_2/PANI heterostructure has been prepared and the heterostructures have been optimized by chemical deposition of PANI on nanofibers of SnO_2 (size ~200 nm). The as-grown films were studied for some of the useful physicochemical properties by X-ray diffraction (XRD), scanning electron microscopy (SEM), UV/visible absorption spectroscopy (UV–vis) and Energy Dispersive X-ray spectroscopy (EDX). SEM micrograph revealed that pure SnO_2 nanofibers were ~200 nm and when PANI was coated then diameter increased to ~500 nm due to the micellar templates of PANI around them. XRD studies showed peak broadening and the peak positions shift from standard values, indicating the interaction of tin oxide nanoparticles with polyaniline. Optical absorbance spectra showed shifting of the characteristics peaks for PANI, which may be due to presence of tin oxide in PANI matrix. SnO_2/PANI composite sensor exhibited good sensitivity and much higher response magnitude towards H_2 gas. Space charge modulation occurring at various interfaces such as SnO_2/PANI interface and boundaries between the SnO_2 nanograins explains the high toxic gas sensitivity observed for the SnO_2/PANI heterostructured nanofibres sensor.

Keywords: Nanofibers; Polyaniline-SnO_2; Nanocomposites; Electrospinning; Gas Sensing.

1. Introduction

In recent years, gas sensors have seen fast development worldwide due to their wide applications in a large variety of fields such as environmental monitoring and protection, modern industrial and agricultural production, national defence, anti-terrorism and even disease diagnosis. Among the huge number of gas sensing materials investigated, SnO_2, which is a typical metal-oxide semiconductor, has received much attention owing to its fascinating gas sensing properties including highly sensitive and fast detection of a broad spectrum of species, such as H_2S, H_2, C_2H_5OH, CO, NH_3, volatile organic compounds, etc. However, hydrogen is colourless, odourless, and extremely flammable gas due to which there have been significant efforts to enhance the sensitivity of hydrogen sensors to be operated at low temperature [1]. By now, a great deal of work on H_2 sensors has been reported. Despite the great success of SnO_2 based gas sensors in both scientific research and practical applications, they generally have to work at high temperatures, which bring about the problems such as high power consumption and reduced working life. Additionally, their sensitivity and selectivity need further improvement. Moreover, greater efforts have been devoted to the nanocomposites of SnO_2 with conducting polymers, including polyaniline (PANI), since the nanocomposites are easy to prepare and could show much improved gas sensing characteristics than the constituent components at room temperature [2]. Electrospinning (ES) is a versatile method for the preparation of one-dimensional (1D) nanomaterials such as polymers, inorganic materials, or the composites. The preparation of nanostructured SnO_2 by ES generally involves high temperature calcination of electrospun nanofibers containing the precursor of tin salt for the removal of the polymer template and the conversion of the precursor to SnO_2. Moreover, the sensors based on nanocomposites of SnO_2 with conducting polymers are generally prepared by depositing nanostructured SnO_2 or the nanocomposite dispersions onto the substrates by dropping, dip coating or screen printing. In this work, a high-efficiency hydrogen sensor based on polyaniline-SnO_2 composite nanofibers has been demonstrated via electrospinning technique and calcination procedure [3].

2. Experimental

Materials

$SnCl_2 \cdot 2H_2O$, Aniline monomer (distilled under reduced pressure), ammonium peroxydisulphate (APS) and Polyvinyl pyrrolidone (PVP, Mw=1,300,000) were purchased from Aldrich. All supplement chemicals were of AR grade and used as received.

Preparation of SnO_2 nanofibers and SnO_2/PANI composite nanofibers

In a typical procedure, 0.4 g of $SnCl_2 \cdot 2H_2O$ was dissolved in 4.4 g of DMF and 4.4 g of ethanol under vigorous stirring for 10 min. Subsequently, 1.0 g PVP was added into the above solution under vigorous stirring for 30 min. The mixture was loaded into a glass syringe with a needle of 0.5 mm in diameter at the tip and was electrified using a high-voltage DC supply. Calcination (300˚C in air for 4 h) was performed to remove the organic constituents of PVP and crystallize the SnO_2. Electrospinning apparatus consists of a syringe pump, DC high voltage source and rotating or stationary collector. The spinning solution was kept in a vertical syringe with a stainless steel needle having an orifice of 0.5mm. The needle was electrically connected to a positive high voltage. 17 kV was provided between the tip of the spinning nozzle and the collector at a distance of 20 cm and the solution flow rate was kept at 0.4ml/h was maintained using computer control programmer. Thus, the nanofibers were prepared successfully. The SnO_2/PANI composite nanofibers were prepared by dipping SnO_2 nanofibers as substrate during chemical oxidative polymerization of 0.5 M aniline using 0.2 M camphor sulphonic acid (CSA) as a dopant and 0.2 M ammonium peroxidisulphate (APS) as an oxidizing agent.

3. Results and discussion

Fig. 1 shows the XRD pattern of composite nanofibers. All the strong diffraction peaks of SnO_2 present in composite can be perfectly indexed as the tetragonal rutile structure for SnO_2 (ICDD DATA CARD (41-1445) [4, 5]. The main dominant peaks of polyaniline-SnO_2 were identified at $2\theta = 26.66^\circ$ and 52.3°, which corresponding to the indices (1 1 0) and (2 1 1). The average diameter of composite nanofibers was found to be around 300 nm as conformed from SEM image (**Fig. 2**).

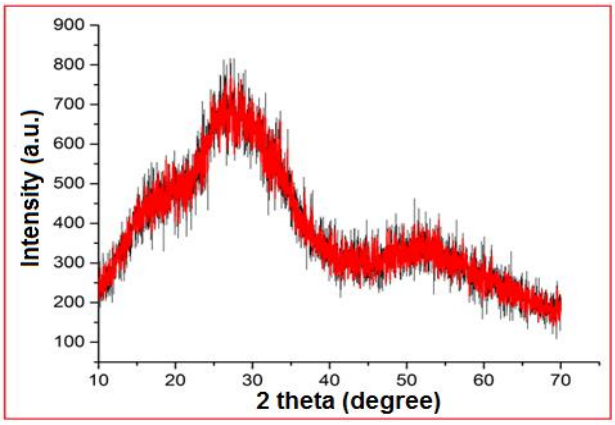

Fig. 1: XRD pattern of polyaniline-SnO_2 composite nanofibers

From SEM micrograph, it is revealed that diameter of as-synthesized SnO_2/PANI composite nanofibers increased due to encapsulation of PANI over SnO_2 nanofibers. Morphologically, composite nanofibers showed highly porous structure which favors SnO_2/PANI composite nanofibers for better sensing properties. EDX has been used to investigate the elemental compositions of composite nanofibers showing the presence of Sn, O, C, and N as illustrated in **Fig. 3**.

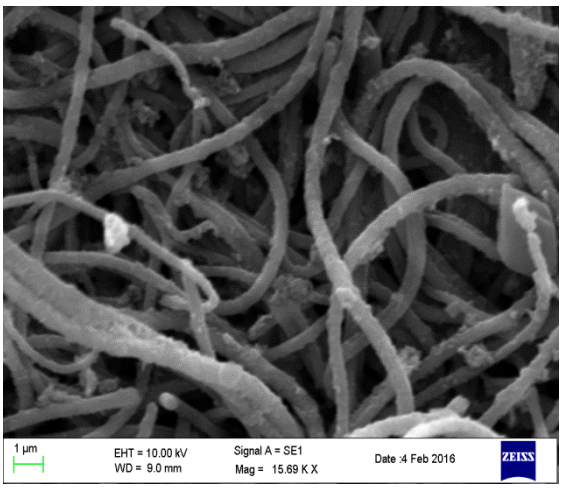

Fig. 2: SEM image of PANI-SnO_2 nanofibers

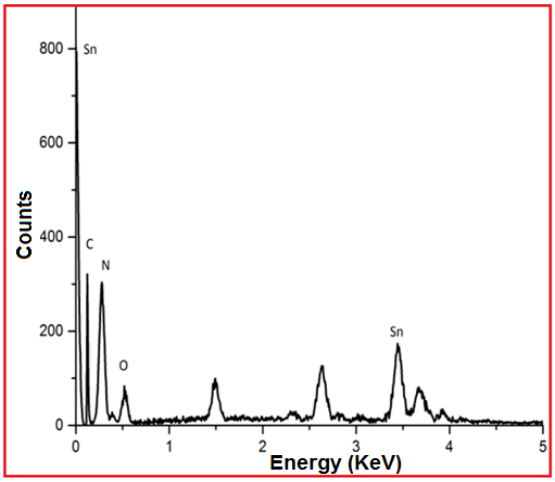

Fig.3: EDX spectrum of PANI-SnO_2 nanofibers

Hydrogen sensing mechanism

On exposure to H_2 gas, the composite film resistance changes from its original value, indicating that the electrical resistance of Polyaniline-SnO_2 composite film is a sensitive parameter in the presence of gas analyte. In presence of SnO_2 crystallites, the PANI matrix gets a modified structure electronically. On exposing the composite film with hydrogen (which can be permeated into the PANI matrix freely), some of the gas analyte molecules might reach into the depletion region, which is surrounding the SnO_2 crystallite and act as a dielectric between the PANI and SnO_2 border. The depletion region field might polarize the hydrogen molecules, and in turn provide a positive charge to PANI molecules, which can become mobile on its transfer to the central N atom of PANI molecule. This process creates some free holes on PANI molecules, which increase the hopping conductivity of the film, and therefore make the composite film relatively more conducting electrically.

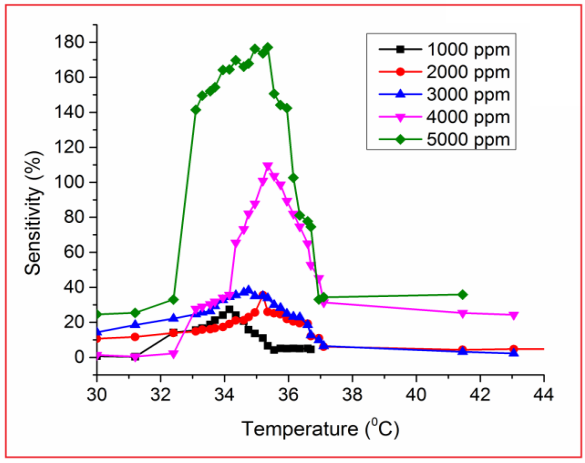

Fig.4: Sensitivity of PANI-SnO_2 nanofibers

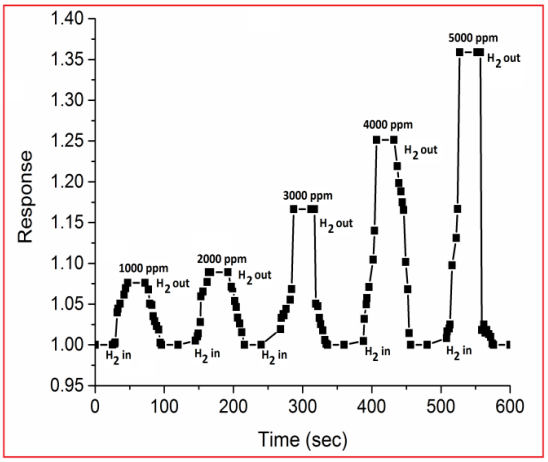

Fig.5: Response-Recovery of PANI-SnO_2 nanofibers

The Polyaniline-SnO_2 composite nanofibers showed a very high sensitivity to H_2 gas at room temperature and as the concentration of gas increases then sensitivity increases rapidly, as shown in **Fig. 4**. Sensitivity factor was monitored in terms of the % sensitivity calculated by % sensitivity = $\Delta R/R_0$. Where ΔR is the variation in resistance of composite films from baseline after exposure to gas analyte, Rg is the resistance of the sensor in presence of H_2 gas and R_0 is the initial baseline resistance of the sensor. **Fig. 5** shows the Response-Recovery Time graph for 1000-5000 ppm of H_2 gas at 35˚C [6-9]. From literature survey available in this regard, there is no appreciable change noticed in the nanofibers film resistance for the case of pure SnO_2, on exposure to different concentrations of H_2 gas and films remained insensitive to this gas near to room temperature. However, SnO_2/Polyaniline

composite nanofibers film showed appreciable sensitivity for 1000 ppm of H_2 gas. The sensitivity of composite nanofibers was found to be increased and reached its maximum around 35 ˚C for H_2 gas.

4. Conclusion

The nanofibers of polyaniline-SnO_2 composite were successfully fabricated using electrospinning technique. Presence of SnO_2 crystallites in the polyaniline-SnO_2 composite nanofibers drastically influenced the electronic property of PANI matrix. XRD study shows the interaction of SnO_2 nanoparticles with PANI. SEM image revealed the formation of fibers of average diameter in nanoscale regime (≤ 300 nm). The Polyaniline-SnO_2 composite nanofibers showed good sensitivity and response to H_2 gas at room temperature.

References

1. Rad, A. S., Nasimi, N., Jafari, M., Shabestari, D. S. and Gerami, E. *Sensors and Actuators B: Chemical*, (2015), 220 (1), 641–651.
2. Deshpande, N.G., Gudage,Y.G., Sharma, R., Vyas, J.C., Kim, J.B. and Lee, Y.P. *Sensors and Actuators B,* (2009), 138 (1), 76–84.
3. Sharma, H.J., Jamkar, D.V. and Kondawar, S.B. *Procedia Materials Science,* (2015), 10, 186 – 194.
4. Sharma, H.J., Sonwane, N.D. and Kondawar, S.B. *Fibers and Polymers*, (2015), 16(7), 1527-1532.
5. Kim, B.J., Oh, S.G., Han, M.G. and Im, S.S. *Synthetic Metals*, (2001), 122 (2), 297–304.
6. MacDiarmid, A.G. and A.J. Epstein. *Synthetic Metals*, (1994), 65(2-3), 103–116.
7. Monredon, S., Cellot, A., Ribot, F., Sanchez, C., Armelao, L., Gueneau, L. and Delattre, L., *Journal Materials Chemistry*, (2002), 12(8), 2396–2400.
8. Chang, S.J., Hsueh, T.J., Chen, I.C., Hsieh, S.F., Chang, S.P., Hsu, C.L., Lin, Y.R. and Huang, B.R. *IEEE Transactions on Nanotechnology*, (2008), 7(6), 754-759.
9. Zhang, H.N., Li, Z.Y., Liu, L., Wang, C., Wei, Y. and MacDiarmid, A., *Talanta*, (2009), 79 (3), 953-958.

Preparation and Characterization of Cadmium substituted Cobalt Nano ferrites by citrate-gel auto combustion method

Nehru boda[1], Gopal boda[2,], Abdul Gaffoor, D. Ravinder[1*], A. Panasa Reddy[2*,]
1. Department of physics, Osmania university, Hyderabad, , 500007,Telangana, India.
2. Department of chemistry, college of Engineering, Osmania university, Hyderabad, 500007, Telangana, India.
[*]Correspondence Author;D. Ravinder; email: ravindergupta28@rediffmail.com

ABSTRACT: Co-Cd Nano Ferrites with chemical formula $Co_{1-x}Cd_xFe_2O_4$(x=0.1, 0.2, 0.3, 0.4, 0.5, 0.6) were synthesized by the citrate-gel auto combustion method. Synthesized powders were sintered at 500^0C for four hours in air and characterized by XRD, FTIR. XRD analysis showed cubic spinel structure of the ferrites and the values of lattice parameter (a) and X-ray density (dx) increased with the increase of Cd content. The FTIR spectra shows the two significant absorption bands in the wave numbers range of 400-600cm^{-1} arising due to the inter-atomic vibrations in the tetrahedral and octahedral coordination compounds. The observed results can be explained on the basis of composition.

KEY WORDS:- Co-Cd Nano ferrites, citrate-gel auto combustion Technique, XRD,FTIR.

Introduction:

The study of nano ferrites has interested to attention of the scientific and technological advances. The ability to prepare nano structures with defined morphologies and sizes in large scale is an essential requirement for applications in nono materials.

Spinel ferrites have been studied extensively because they play a vital role in the technological application. Ferrites have good electric and magnetic properties and a large number of applications

The interest in ferrites nanoparticles is due to their important physical chemical properties and potential for various technological applications such as high capability data storage, electric and microwave devices, sensors, magnetically guided drug delivery etc.

These are of tremendous academic interest as these are considered as potential tools for developing our understanding about the fundamentals of nano magnetism [1]. Among these, spinel ferrites having the general formula MFe_2O_4, Properties of ferrites are highly sensitive to the substitution of different metal ions in its tetrahedral and octahedral sites [2].

The properties of ferrites are dependent on several factors, chemical composition, method of preparation, grain size, sintering temperature and atmosphere [3]. Various chemical technique have been used the synthesis of spinel ferrites [4] several researchers have reported the synthesis of Co-Cd ferrites using different techniques like co-precipitation method [5], ceramic method [6], combustion method [7]. so in the present work we reported the results of synthesis and structural and morphology of Co-Cd ferrites by Citrate Gel Auto Combustion method

2. Experimental Details:

The Cobalt- Cadmium nano ferrites having the chemical formula $Cd_x\ Co_{1-x}Fe_2O_4$ were synthesized by citrate gel auto combustion method using the below raw materials.

2.1 Raw Materials:

Cadmium Nitrate- 99% pure (AR Grade) ($CdNo_3$), Cobalt Nitrate- 99% Pure(AR Grade) ($CoNo_3$)

Ferric Nitrate-99%pure(AR Grade) ($Fe(No_3)_3\ 9H_2O$), Citric acid-99.5% Pure (AR Grade) ($C_6H_8O_7.H_2O$).

Ammonia solution-99% Pure (AR Grade) (NH_3).

2.2 The flow chart of the synthesis of Co- Cd nano ferrites:

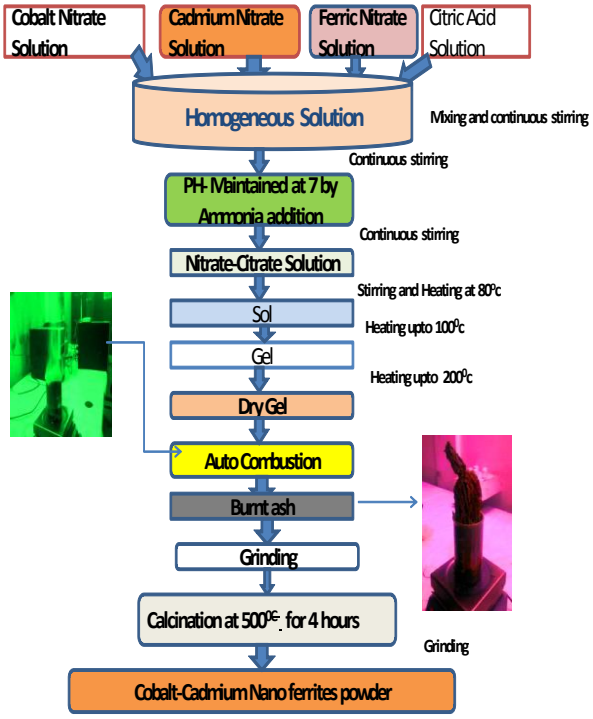

Fig (1): The flow chart of synthesis

The calculated quantities of metal nitrates were dissolved in minimum amount of distilled water to get clear homogeneous solution. An aqueous solution of citric acid was added to the metal nitrate solution. The molar ratio of citric acid to the total moles of nitrate ions was adjusted to1:1. The flow chart shown in fig; (1)

2.3 Structural Characterization by XRD:

The structural characterization was done by X-Ray Diffractmeter Philips x-pert pro system with diffracted monochromatic beam with Cu-Kα radiation of wavelength (1.5405A^0). The diffraction pattern of Co-Cd between the Bragg Angles 10º to 80º in the steps of 0.04º/sec. nano ferrites particles Were shown in fig.

The crystalline size was calculated for the sample using the high intensity 311 peak and using Debay Scherrer formula **[8]** while taking into account the intensity broadening [9].

Crystalline size of the sample $\boldsymbol{D = \frac{0.91\lambda}{\beta \cos\theta}}$

Where λthe wavelength of X-ray is used [10]. β is the width of diffraction peak i,e. full width Half Maximum(FWHM) , θ is the peak position .

Lattice parameter (a) of the sample was calculated by the formula. $\boldsymbol{a = d * \sqrt{h^2 + k^2 + l^2}}$ [11] Where a=Lattice constant, (h k l) are the Miller indices, d is the inter planner space The X-ray density of the prepared sample was calculated using the relation $\boldsymbol{dx = \frac{8M}{a^3 N}}$ (g/cm^3) [12] where **M**= molecular weight of the sample, **a** is the lattice parameter and **N** is the Avogadro number.

The Volume of the Unit cell $\mathbf{V=a^3}$

The distance between the magnetic ions (hoping length) on A-site(Tetrahedral) and B site (Octahedral) is calculated according to the following relations

$\mathbf{d_A = 0.25a\sqrt{3}}$ **and** $\mathbf{d_B = 0.25a\sqrt{2}}$ **[13]**

3. Result and Discussion;-

3.1. XRD Analysis:

A phase analysis using X-ray diffraction technique was performed to confirm the formation of single-phase cubic spinel structure as shown in **fig-(2)** . With n o extra lines corresponding to any other crystallographic phase. The results obtained from XRD pattern for all the samples of Cd_xCo_{1-x} Fe_2O_4 with the (hkl) values corresponding to the diffraction peaks of different planes (220), (311), (400), (422), (511), and (440) are spinel cubic phase

The calculated values of crystalline size for the different compositions are given in the table (1).

It can be seen from the table that the values of the crystal size varies from 11nm to 17nm of the various Cd concentrations

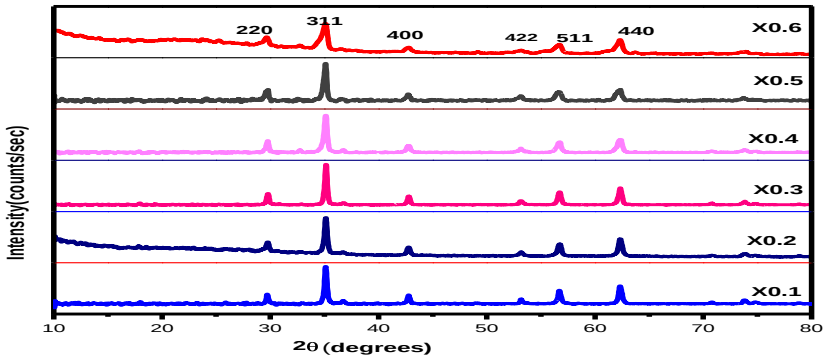

Fig (2): XRD pattern of Co-Cd Nano ferrites

The lattice parameter values of all the composition of Cadmium doped Cobalt ferrites have been calculated from the d- spacing and are given in the above table. A plot is drawn between the lattice parameter vs Cadmium composition is shown in **fig (3).**

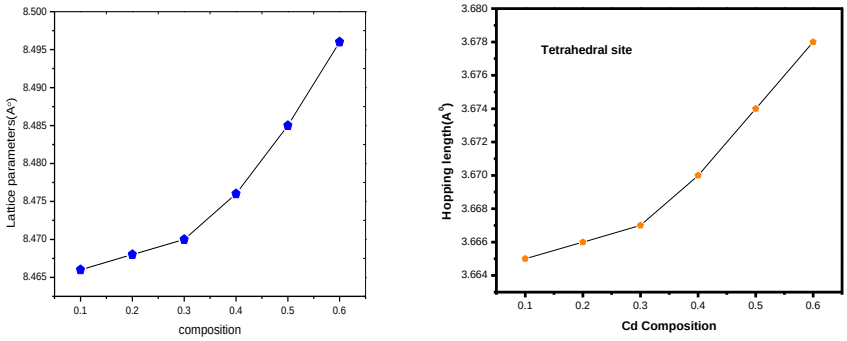

(a) **(b)**

Fig (3): a. Variation of lattice constant vs Cd composition 3.b. Variation of hopping length vs Cd composition

Ferrite composition	**Lattice Constant (A°)**	**Crystalline Size(nm)**	**Volume $(A°)^3$**	**Hoping length A-site(d_A)**	**Hoping length B-site(d_B)**
$Cd_{0.1}Co_{0.9}Fe_2O_4$	8.466	11.12	606.784	3.665	2.992
$Cd_{0.2}Co_{0.8}Fe_2O_4$	8.468	14	607.215	3.666	2.993
$Cd_{0.3}Co_{0.7}Fe_2O_4$	8.470	14.62	607.645	3.667	2.994
$Cd_{0.4}Co_{0.6}Fe_2O_4$	8.476	14.62	608.937	3.670	2.996
$Cd_{0.5}Co_{0.5}Fe_2O_4$	8.485	14.62	610.879	3.674	2.999
$Cd_{0.6}Co_{0.4}Fe_2O_4$	8.496	17.82	613.258	3.678	3.003

Figure (3) variation of lattice constant with Cd^{2+} content in $Co_{1-x}Cd_xFe_2O_4$ (x=0.1, 0.2, 0.3, 0.4, 0.5, 0.6), is observed that the Lattice parameter increases with increase in Cd content. This is attributed to replacement of smaller ionic radii Co(0.78A°) by larger ionic radii Cd^{2+} (0.99A°) ions. This linear variation indicates that the Co-Cd ferrite system obeys vegard's law [14]

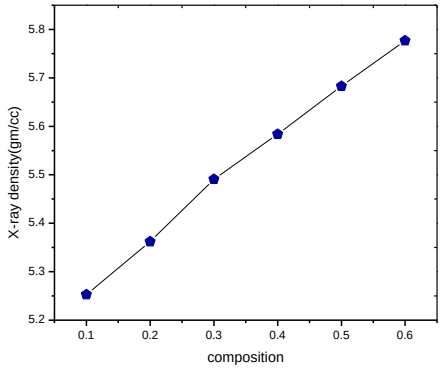

Fig(4): X-ray density vs Cd concentration

The **figure (4**) shows the X-ray density (dx) vs Cd concentration, The X-ray density (dx) is depend on the lattice parameter and molecular weight of the sample. From the table one can observe that molecular weight of the sample is increases with Cadmium concentration and lattice parameter is also increases with the increase of Cd compositions. This may due to the grater atomic weight of Cd-112.411gm/mol and lesser atomic weight of Co-55.845gm/mol(15) shown in below figure

SNO	**Ferrite composition**	**X-ray Density(gm/cc)**	ϑ_1**(cm^{-1})**	ϑ_2**(cm^{-1})**
01	$\mathbf{Cd_{0.1}Co_{0.9}Fe_2O_4}$	5.253	576.73	410.85
02	$\mathbf{Cd_{0.2}Co_{0.8}Fe_2O_4}$	5.362	580.59	412.78
03	$\mathbf{Cd_{0.3}Co_{0.7}Fe_2O_4}$	5.491	582.52	418.56
04	$\mathbf{Cd_{0.4}Co_{0.6}Fe_2O_4}$	5.584	576.73	418.57
05	$\mathbf{Cd_{0.5}Co_{0.5}Fe_2O_4}$	5.683	570.94	418.56
06	$\mathbf{Cd_{0.6}Co_{0.4}Fe_2O_4}$	5.777	574.80	418.57

FTIR Spectral analysis

Fig.(5) shows FTIR spectra of the ferrite samples in the range of wave numbers from 350 to 650 cm^{-1}. The two absorption bands Observed at 582 cm^{-1} (ϑ_1) and 410 cm^{-1} (ϑ_2) corresponds to vibrations of tetrahedral and octahedral complexes

respectively, and According to Waldron which confirms the formation of single phase cubic spinel structure of ferrites [16, 17]. From the figures it is to be noted that the shifting of band position (600 cm^{-1}) ϑ_1 towards lower wavelength region is due to the increase of Cd^{2+} ion in ferrite And preferably occupies the tetrahedral (A-site) [18, 19]. However,Co^{2+} ions occupy the octahedral(B-site) [20],

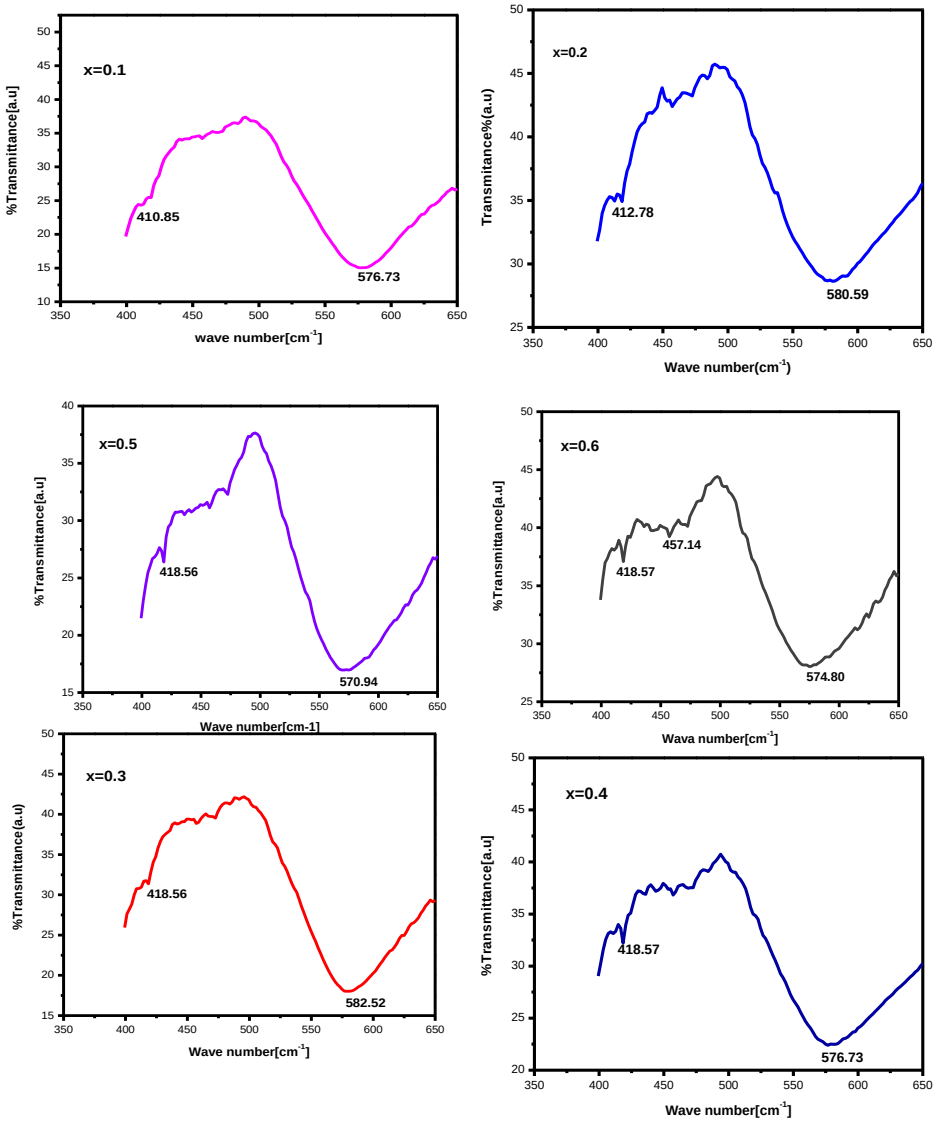

Fig.5.FTIR absorption spectra of the Cd_x $Co_{1-x}Fe_2O_4$ ferrite samples

But Fe^{3+} ions occupy both tetrahedral and octahedral sites. Substitution of Cd^{2+} ion in the system decreases the amount of $Co^{+2}$and increases the amount of Cd^{+2} ions in the octahedral B-site and shifts band position at (410 cm^{-1}) ϑ_2 towards lower wavelength.

4. Conclusion:

- Citrate Gel Auto Combustion technique is a convenient way for obtaining a homogeneous nano sized mixed ferrites, it is very simple and economical method where no specific heating or cooling rate is required.
- X-ray diffraction pattern confirms the formation of single phase cubic spinel structure. From standard data JCPDS.
- The crystalline size of the various Co-Cd ferrites was in the range of 11 to17 nm.
- The Lattice parameter has increased with the increase of Cd concentration in Co-Cd ferrites which indicate that the mixed Co-Cd ferrite system obay the vegard's law
- The FTIR spectra of the ferrite samples in the range of wave numbers from 350 to 650 cm^{-1}.
- The two absorption bands Observed at 582 cm^{-1} (ϑ_1) and 410 cm^{-1} (ϑ_2) corresponds to vibrations of tetrahedral and octahedral complexes respectively

5. Acknowledgements:

The authors are very grateful to **Prof. D. Suresh Babu** , Head, Department of physics, and **Prof. J. Shiva Kumar**, Chairmen Board of studies in physics, University college of science Osmania University Hyderabad, One of the author Nehru Boda is very thankful to **UGC, BSR-section** New Delhi, for their financial assistance.

References:

[1] y. Qi, Y . Yang, X. Liu, P. Wu, Particuology 8(2010) 207-211.

[2] Y. Koseoglu, F . Gozuak, A. Baykal, H. Kavas, Structural and magnetic properties of CoxZn1_xFe2O4 nanoparticles synthesized by microwave method, Polyhe- drone 28(2009)2887–2892.

[3] K.Kondo, T. Chiba, S. Yamada, Journal of Mag Mag mater **541,** 254(2003

[4] P.K.Roy and J.Bera, J Magn Magn mater 298,38,(2006)

[5] ch. Venkata Reddy, chan Byon, B. Narender, D. Basker, G.Srinivas,Jaesool shim, S. V. Prabhakar Vattikuti 82(2015) 165-173.

[6] S.E. Jacobo, s,Duhalde and H.R.Bertorello " Rare earth influencre on the structural and magnetic proper ties of Ni-Zn Ferrites" J of Mag and Mag Matrels Vol 272-276 N0 3, 2004pp 2254Doi:10.1016/j.jmmm.2003.12.564

[7] S.A.Morrison, C.L.Cahill, E.E.Carpenter,S.Calvin, R.Swaminnathon, M.E.McHenryand V G Harris Magnetic And Structrural Properties of Ni-Zn Ferrite nano particles synthesised by At room temperatureJ of Applied physics, Vol95,no 11 2004, pp.6392-6395doi 10.1063/1.171513

[8] Cullity B D, Elements of X-ray diffraction (addition Wesley, Reading, Mass), 1959. P132.

[9] Mahmud ST, Akther Hossain AKM, Abdul Hakim AKM, Seki M, Kawai T. Tabata H (2006) j Magn Mater 305;269 doi; 1016/j.jmmm.2006.01.012.

[10] B.D. Cullity, Elements of X-ray diffraction, Wesely Pub, Co,. Massachusetts, 1987,101- 356

[11] B.P.Ladgaonkar, P.P.Bakare,S.R. Sainkar and A.S.Vaingankar, "Influence of Nd+3 substitution on permeability spectrum of Zn-Mg ferrite". Materials Chemistry and Physics, Volume 69,Issues 1-3,March 1, 2001, pages 19-24.

[12] B. Vishvanathan, V. R.K. Murthy, Ferrite Materials Science and Technology, narosa Public House, New Delhi(1990).

[13] R.C.Kumbale. P.A.Shaikh, S.S. Kamble,Y.D.Kolekar J.Alloys Comp., 478(2009), p.599 doi:10.1016/j.jmmm.2005.03.007

[14] L. Vegard, "The Constitution of Mixed Crystals and the Space Occupied by Atoms," *Zeitsch rift fiir Physics*, Vol. 5, No. 17, 1921, pp.17-23

[15] K.B.Modi, J.D.Gajera, M.P.Pandya,H.G.Vora, H.H.Joshi, Pramana Journal of Physics, Vol 62, No 5,May, 2004, pages 1173-1180

[16] B.P. Ladgaonkar, C.B. Kolekar, A.S. Vaingankar, Bull. Mater. Sci. 25 (4) (2002)351.

[17] R.D. Waldron, Phys. Rev. 99 (1955) 1727

[18] S.A. Patil, V.C. Mahajan, A.K. Gatge, S.D. Lotake, Mater. Chem. Phys. 57 (1998)86.

[19] O.M. Hemeda, M.M. Barakat, J. Magn. Magn. Mater. 223 (2001) 127.

[20] G.K. Joshi, A.Y. Khot, S.R. Savant, Solid State Commun. 65 (1988) 1593.

Electrochemical Performance of Polyaniline/Nickel Ferrite/Carbon Nanotubes Ternary Nanocomposites

[#]Pooja A. Zingare, Zeenat Parveen, Subhash B. Kondawar*
Department of Physics, Rashtrasant Tukadoji Maharaj Nagpur University, Nagpur – 440033, India
*Corresponding Author Email: sbkondawar@yahoo.co.in
[#]Presenting Author Email: pooz11071994@gmail.com

ABSTRACT

The synthesis process of polyaniline/nickel ferrite/carbon nanotubes (PANI/$NiFe_2O_4$/CNT) nanocomposite electrodes via simplest in-situ oxidative chemical polymerization is reported. Nanocrystalline $NiFe_2O_4$ was prepared by simple approach of co-precipitation method. The morphology and chemical structure of PANI/$NiFe_2O_4$/CNT was characterized by means of scanning electron microscopy (SEM), energy dispersive X-ray spectroscopy (EDX), Fourier transform infrared (FTIR) and X-ray diffraction (XRD) analysis. The electrochemical performance of as-synthesized PANI/$NiFe_2O_4$/CNT electrode was studied by cyclic voltammetry (CV) in an aqueous solution at different scan rate using three electrodes electrochemical cell. The CV curve of PANI/$NiFe_2O_4$/CNT electrode compared with that of the PANI/$NiFe_2O_4$ and PANI/CNT binary nanocomposites. The improved electrochemical performance of PANI/$NiFe_2O_4$/CNT film is due to interaction between carbon nanotubes, $NiFe_2O_4$ nanoparticles and conducting polymers because the nitrogen atoms of polymers can bond to the metal ions of $NiFe_2O_4$ through their lone pairs and encapsulates the carbon nanotubes. Due to the synergistic effect of pseudo capacitance generated by polyaniline, nickel ferrite and electric double layer capacitance generated by carbon nanotubes at the interface between electrode and electrolyte, the specific capacitance of the ternary nanocomposite was found to be increased compared to that of binary nanocomposites. This improvement in electrochemical performance suggests that PANI/$NiFe_2O_4$/CNT electrodes are promising for the next generation high performance electrochemical capacitors.

Keywords: Nanocomposites, Nickel ferrite, Polyaniline, Carbon nanotubes, Cyclic voltammetry.

1. Introduction

The flexible and environmentally friendly energy storage devices have attracted much attention for sustainable energy and portable electronics. As intermediate systems between batteries and traditional dielectric capacitors, supercapacitors exhibit the desirable properties, e.g. high power density, high specific capacitance, long cycle life (>100,000 cycles), and rapid charging/discharging rates, thus they are probably one of the most important next-generation energy storage devices [1, 2]. According to the energy storage mechanism, supercapacitors are generally classified into electrochemical double layer capacitors (EDLC), using carbon-active materials (CNT, graphene) based on the surface area of the electrode materials, and pseudocapacitors, using redox-active materials based on the fast and reversible Faradic reactions. The specific capacitance just from the electrical charges at the electrode-electrolyte interface of EDLC is lower than pseudocapacitance based on conducting polymers and transition metal oxides. While poor cycle ability due to structural degradation through the redox process limits the applications of pseudocapacitors [3]. Combining the advantages of EDLC and pseudocapacitors has attracted vast interests due to the synergistic effect. On the basis of this point, it is apparent that the electrochemical performances can be enhanced by incorporating carbon materials with pseudocapacitive materials. However, the electrochemical properties of electrodes play a crucial role in determining the performance of supercapacitors. To overcome this obstacle, most of recent studies are urgent to develop excellent electrode materials for supercapacitors. It is well known that transition metal oxides possess multiple oxidation states/structures that enable rich redox reactions for pseudocapacitance generation [4]. But, simple metal oxides exhibit low specific capacitance, particularly at higher charge/ discharge rates. Therefore, it is of great interest to design complex metal oxide-based systems having high specific capacitance and low cost. Recently, spinel transition metal oxides (AB_2O_4) with two metal elements provide the feasibility to tune the energy density and working voltage by varying the metal content. Spinel ferrites (MFe_2O_4, M = Fe, Co, Ni, Cu, Mn) have been conceived as a promising cost-effective and scalable alternative for supercapacitors due to their greater electronic conductivity and

electrochemical activity than single component metal oxides [5, 6]. Pure ferrites only exhibited very less capacitance and hence a prospective way to enhance the electrochemical performance is designing novel ferrite-based hybrids. Over the past decades, conducting polymer, carbon nanotubes and graphene sheets have emerged as important materials in the development of new generations of energy storage and conversion devices [7]. Ternary hierarchical systems composed of carbon nanomaterials, conducting polymers and transition metal oxides have been explored. These novel ternary hybrids exhibited much higher specific capacitance than the individual components or the binary carbon nanomaterials (or conducting polymers)/transition metal oxides composites [8]. Therefore, it is interesting to design novel ternary nanocomposites, which may exhibit enhanced electrochemical capacitance performance compared with its individual components. Among numerous kinds of conducting polymer, polyaniline (PANI) has been considered as one of the most promising materials for electrode materials in pseudocapacitors because of its low cost, ease of synthesis, simple acid-doping/base-dedoping chemistry, and relatively high pseudocapacitance. Nickel ferrite ($NiFe_2O_4$), an inverse spinel in which Ni^{2+} occupies the octahedral site and half of the Fe^{3+} ions occupy the tetrahedral sites, has been reported as a pseudocapacitive candidate combined with carbon based materials. Herein, we present the fabrication of ternary polyaniline/nickel ferrite/carbon nanotubes (PNC) nanocomposites as electrode materials for supercapacitor.

2. Experimental

$NiFe_2O_4$ particles were synthesized by solution combustion technique. In a typical process, 0.372 g of $Ni(NO_3)_2.6H_2O$ and 1.035 g of $Fe(NO_3)_3.9H_2O$ were added to 10 ml of absolute ethanol with constant stirring for 30 min. 10 g of urea was dissolved in above solution and stirred for 30 min. The resulting mixture was transferred into Teflon-lined stainless steel autoclave and heated to 180 ^oC for 18 hr. It was then allowed to cool to room temperature. $NiFe_2O_4$ particles were obtained by filtered, washed and then dried in vacuum oven.

PANI particles were synthesized by chemical oxidative polymerization in acidic aqueous medium using ammonium persulphate (APS) as oxidant. For the typical

synthesis, aniline monomer 0.2 M was dissolved in 40 ml of 1 M H_2SO_4. 0.2 M of APS was dissolved in 50 ml of double distilled water. After that, APS solution was added drop wise into the monomer-solution which is maintained under constant stirring for 2 h. The polymerization process was identified by the change of colorless solution into green color. The collected sample was washed with double distilled water and methanol for several times. Finally, the sample was dried in vacuum oven at 80^{o}C.

Ternary PNC nanocomposite was synthesized via in situ polymerization of aniline monomer in the presence of as-synthesized nickel ferrite and functionalized carbon nanotubes (f-CNT). 10 wt% NF and f-CNT were ultrasonicated and then mixed with aniline solution under constant stirring and drop wise addition of APS turned to PNC nanocomposites after washing and drying in vacuum oven. Similarly, binary PN nanocomposite was prepared with out using CNTs.

To prepare working electrode, 80 wt.% of the prepared material (40 mg), 15 wt.% of carbon black (7.5 mg) and 5 wt.% of PVDF (2.5 mg) were dissolved in 0.2 ml of N-methyl 2-pyrrolidinone and made into slurry form. Then, slurry was placed on the carbon electrode. The electrochemical studies were performed with three electrode cell configurations. An active material coated electrode as working electrode, Pt wire as counter electrode and Ag/AgCl as reference electrode were used. 1M KCl aqueous solution was used as electrolyte.

3. Results and discussion

The morphology and microstructure of nickel ferrite (NF), polyaniline/nickel ferrite (PN) and polyaniline/nickel ferrite/carbon nanotubes (PNC) nanocomposites were confirmed by SEM images as shown in **Fig.** 1(a), (b) and (c). As can be seen from Fig. 1(a), NF particles show the roughly uniformity spherical-like morphology quite separated from each other. Fig. 1(b) and (c) shows the SEM images of PN and PNC nanocomposites. It can be clearly seen that highly agglomerated granular-like morphology was observed for PN composite, indicates that ferrite particles are surrounded by polymer chains of PANI. In other words, the polymer is coated on the surface of NF particles due to in situ polymerization. For PNC nanocomposite, it is seen that the CNTs are uniformly coated by NF and PANI due to which the average

diameter of the coated CNTs increased as shown in Fig. 1(c). The morphology of PN composite represents embedment of NF particles into the PANI matrix. In contrast to Fig. 1(c), a thin PANI film covering on the surface of NF-CNT is also recognized clearly, revealing the PNC composites were fabricated successfully. However, the NF nanoparticles and PANI also can hold back the aggregation of CNTs, and thereby improve the electrochemical properties, which can be approved by XRD and electrochemical tests. Moreover, the elemental mapping of PNC for carbon, nitrogen, iron, nickel and oxygen (**Fig. 2**), reveals that the various elements are homogenously distributed in the PNC nanocomposite, confirming the existence of NF and PANI on the surface of CNTs.

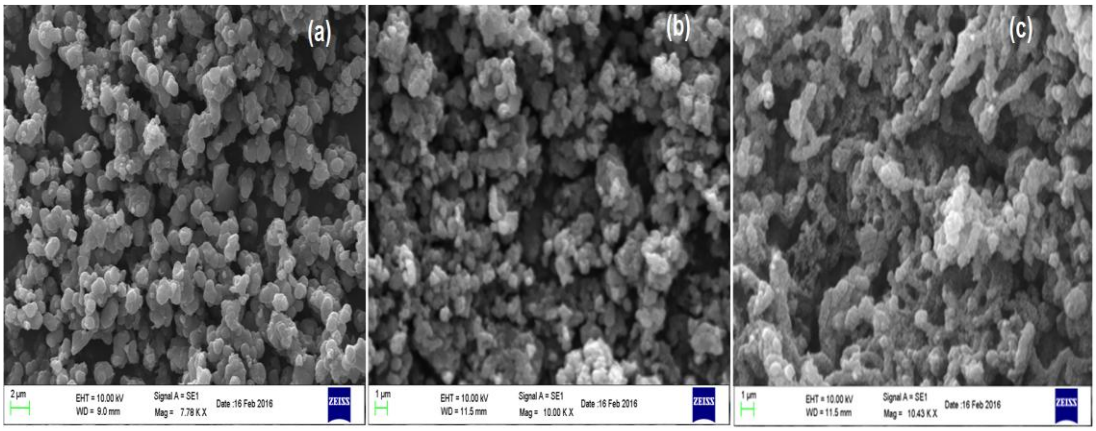

Fig. 1: SEM images of (a) NF, (b) PN and (c) PNC.

XRD diffraction patterns of the as-prepared NF, PANI and PNC are demonstrated in **Fig. 3**. In the pattern of PANI, a broad peak was observed at 26^{o} which is due to the periodicity perpendicular to the PANI chains and there are no sharp peaks observed which indicates the amorphous nature and emaraldine salt form of the prepared PANI. NF represents sharp diffraction peaks at 30.3, 35.7, 43.4, 57.4, 63.0 and 75.2^{o} which correspond to (hkl) plane of (220), (311), (400), (511), (440) and (622), respectively. The observed peaks elucidate the single phase formation and spinel group of NF and are in good agreement with the JCPDS (44-1485) file [9]. The XRD pattern of PNC showed the characteristic peaks related to the peaks of NF and that of CNTs peaks at 2θ = 43.6, 50.1^{o} corresponding to the planes (111) and (200) respectively [10], indicating the interaction of NF, PANI and CNT in ternary nanocomposites.

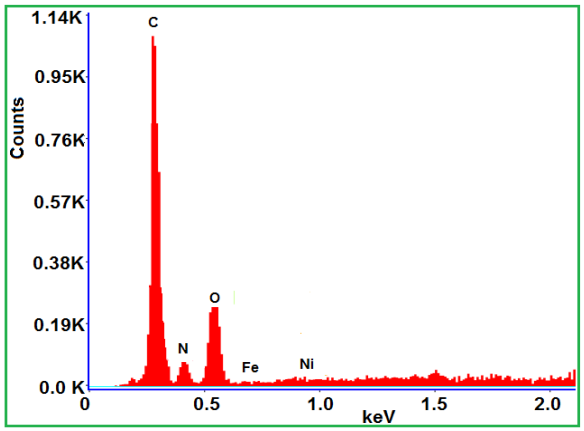

Fig. 2: EDX spectrum of PNC nanocomposite

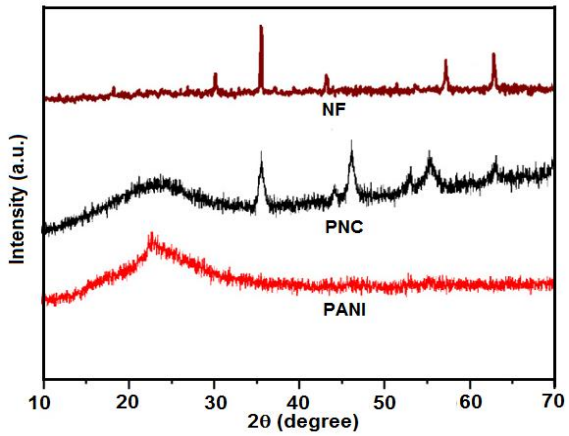

Fig. 3: XRD patterns of NF, PANI and PNC

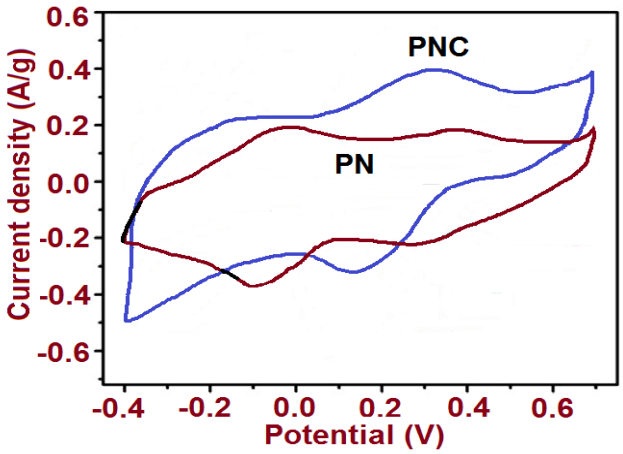

Fig. 4: CV curves of PN and PNC recorded at 1 mV/s

Electrochemical measurements were performed with a three electrode system from -0.4 to 0.7 V in 1 M KCl solution to evaluate the electrochemical performance as

supercapacitor electrode materials. **Fig. 4** shows the CV curves of PN and PNC recorded at 1 mV/s, revealing that the ternary PNC electrodes have the best electrochemical properties because of the largest current density responses. The electrochemical behaviour of PNC is distinctly improved owing to the combined effects between EDLC and pseudocapacitors. CV for PN evidently shows the redox peaks, indicating that PN has main pseudocapacitive performance coming from PANI. Therefore, the roles of NF and PANI are to enhance the specific capacitance, especially pseudocapacitance. The result further implies that the synergetic effect among three components leads to the additional capacitance produced. PNC nanocomposites achieved maximum specific capacitance value of 409.09 F/g, on the other hand PN showed specific capacitance value of 272.72 F/g at 1 mV/s scan rate. The achievement of such highest specific capacitance of the PNC nanocomposite may be due to the presence of highly accessible surface area of the CNTs in nanocomposites enhances the specific capacitance and the strong interaction among the π-bonded CNTs surface with the conjugated structure of polymer improves the specific capacitance of PNC [11].

4. Conclusion

We have successfully synthesized the ternary nanocomposites by in-situ chemical oxidative polymerization technique. Morphological analysis confirmed the uniform coating of NF and PANI over CNTs surface. The PNC nanocomposite showed highest specific capacitance than that of binary PN nanocomposite makes it superior for high electrochemical performance for supercapacitor application.

References

1. Wang, G., Zhang, L., Zhang, J., Chem. Soc. Rev. (2012), 41, 797–828.
2. Devadas, A., Baranton, S., Napporn, T. W., Coutanceau, C., J. Power Sources, (2011), 196, 4044–4053.
3. Chabi, S., Peng, C., Hu, D., Zhu, Y., Advance Mater. (2014), 26(15) 2440-2445.

4. Wei, T.Y., Chen, C.H., Chien, H.C., Lu, S.Y., Hu, C.C., Advance Mater. (2010), 22 (3), 347-351.
5. Zhu, M., Meng, D., Wang, C., Diao, G., ACS Appl. Mater. Interfaces (2013), 5(13), 6030-6037.
6. Wang, L., Ji, H., Wang, S., Kong, L., Jiang, X., Yang, G., Nanoscale (2013), 5, 3793-3799.
7. Yan, J., Wei, T., Fan, Z., Qian, W., Zhang, M., Shen, X., Wei, F., Journal of Power Sources(2010), 195, 3041–3045.
8. Jiang, H., Dai, Y., Hu, Y., Chen, W., Li, C., ACS Sustainable Chem. Eng. (2014), 2(1), 70-74.
9. Du, X., Wang, C., Chen, M., Jiao, Y., Wang, J., J. Phys. Chem. C (2009), 113, 2643–2646.
10. Chauhan, N., Narang, J., Rawal, R., Pundir, C.S., Synth. Met. (2011), 161, 2427– 2433.
11. Patil, D. S., Shaikh, J.S., Dalavi, D.D., Karanjkar, M.M., Devan, R.S., Ma, Y.R., Patil, P.S., J. Electrochem. Soc.(2011) 158 A653–A657.

Thermoluminescence studies of Eu^{3+} doped Calcium Lanthanum borate phosphor

M.Srinivas
Department of Physics, Osmania University, Hyderabad, 500007, India
*Corresponding authot. E-mail: msrinivas.ou@gmail.com

ABSTRACT: $Ca_3La_2(BO_3)_4$ phosphor doped with Eu^{3+} have been synthesized by high temperature solid-state reaction method. The crystalline structure and elemental analysis of these phosphors are carried out by using X-ray powder diffraction (XRD) and Energy dispersive X-ray spectroscopy (EDS) techniques. The thermoluminescence (TL) properties have been investigated. For TL studies, samples were γ-irradiated with 1320 Gy dose rates using ^{60}Co source. TL of these phosphors showed a sharp glow peak with maxima at 394 K. Incorporation of europium activator in $Ca_3La_2(BO_3)_4$ phosphor resulted in the increase of peak intensity. The trap parameters viz., order of kinetics (b), activation energy (E) and frequency factor (S) associated with the most intensive glow peak of $Ca_3La_2(BO_3)_4:Eu^{3+}$ phosphor were determined using glow curve shape (Chen's) method.

Keywords: Phosphor, XRD, EDS, $Ca_3La_2(BO_3)_4:Eu^{3+}$, Thermoluminescence

1 Introduction

The study of new thermoluminescent (TL) materials to be used as TL dosimeters has made necessary to have a deeper knowledge of the trapping energy as well as of the average time the electron stays in its trap. This information can be obtained from the glow curve analysis which is obtained after exposing the material to ionizing radiation in order to excite the electrons from the valence band to the conduction band and back to metastable states in the forbidden band over the Fermi level. Then, by heating, those electrons can be released from their traps and recombine with trapped holes emitting light. Hence, TL is considered as a thermally stimulated process [1]. The glow curve can exhibit various peaks (maximum intensity) originated from different trapping states. There are many different methods for determining the trapping parameters [2] (i.e., the activation energy or trap depth, the kinetic order and the frequency factor). Most of the existing methods of obtaining the frequency factors make use of the determination of the trap depth (activation energy) relaying on

some assumptions about the order of the kinetics. This causes inconsistencies in the reported values of the trapping parameters due to appreciable differences in the activation energy obtained by different methods. Then, it is necessary to use a method independent of the determination of the trap depth.

The TL characteristics of borate compounds have been reported such as un-doped and Ce-doped BaB_4O_7 [3], Tb^{3+}-doped $Ba_2Ca(BO_3)_2$ [4], un-doped and Cu- and Mn-doped $K_2B_4O_7$ [5], MgB_4O_7:Dy,Na [6], SrB_4O_7:Dy [7], rare-earth-doped $Sr_2Mg(BO_3)_2$ [8], $Li_2B_4O_7$:Cu,In [9,10] and BaB_4O_7: Dy [11] these results provide useful information concerning the defects and trap structure that are helpful in the search for new borate TLD materials. In this paper, we report the method making use of isothermal decay of the TL was studied to determine the trapping parameters of $Ca_3La_2(BO_3)_4$:Eu^{3+} phosphor by using the glow curve shape method.

2 Experimental

The Phosphor materials of composition $Ca_3La_2(BO_3)_4$ [CLB] doped with europium were synthesized by the solid state reaction method. Stoichiometric amounts of AR grade $CaCO_3$, La_2O_3, Eu_2O_3 and H_3BO_3 were thoroughly mixed and ground together with ethanol in an agate mortar for 5 hours to give homogenous mixture. The resultant powders were initially dried at 100^oC for 1 h, kept in an alumina boat and heated at 1200^oC in air for 3 hrs. Later, the temperature is brought down to 950^oC and the samples were held at that temperature for 1 hour in air. These samples were rapidly cooled down to room temperature and were grinded to get fine powder for further studies.

The phase purity of the as synthesized phosphor were characterized using X-ray diffraction (XRD) patterns with Cu-Kα radiation of wave length 1.5406 A^o in the 2θ range of $10 \sim 80^0$ with a step size of 0.04 ^{o}/ sec. The operation voltage and current of the instrument were maintained at 40 kV and 30 mA respectively. The compositions of the phosphor samples were obtained from energy dispersive spectrum (EDS). The EDS was attached to the HITACHI S-3700N model instrument. All measurements were recorded at room temperature. Thermoluminescence Analyzer system (type 1007) supplied by Nucleonix Systems Private Ltd., Hyderabad, India. offering an irradiation volume approximately 1000

cc had 2370 curies ^{60}Co source, used for γ-irradiation. The glow curves were recorded by heating the sample at a uniform rate of 2 K Sec-1 with the help of a temperature controller.

3. Result and Discussions

3.1. Powder XRD

The powder X-ray diffractograms of CLB are shown in fig.1 and the observed d-lines are indexed for higher concentration of Eu^{3+} shown in fig.2. The CLB belongs to the orthorhombic system with space group *Pnam*, and unit cell parameters are show as following: a = 7.279 Å, b = 16.417 Å, c = 8.654 Å. All the compounds are very close to that of reported values for CLB [12]. It is indicated that the doping Eu^{3+} ions do not form new phases in the synthesis process.

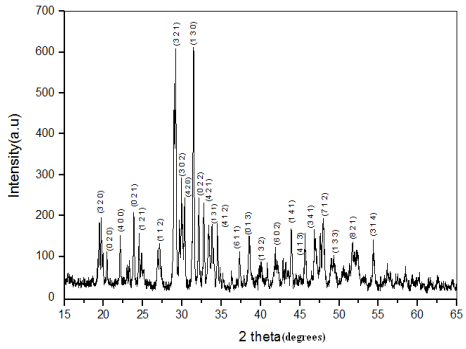

Fig 1 XRD of $Ca_3La_{1.9}Eu_{0.1}(BO_3)_4$ phosphor

3.2. Energy Dispersive Spectrum

The energy dispersive spectrum analysis of 0.1 mol % Eu^{3+} doped CLB sample peaks shown in Fig.2 corresponding to Ca, La, Eu, B and O. The EDS pattern confirms the presence of europium in the CLB powders and its wt% is nearly equal to the doped value of Eu in CLB.

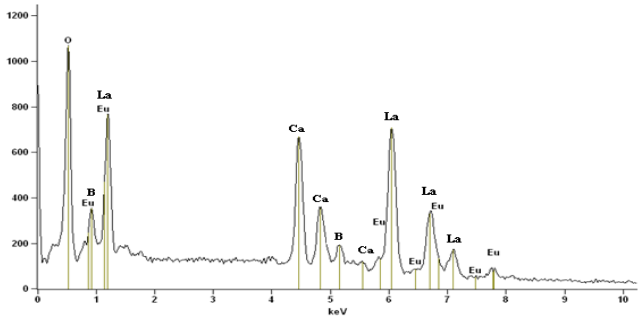

Fig 2 EDS of $Ca_3La_{1.9}Eu_{0.1}(BO_3)_4$ phosphor

3.3.1 Thermoluminescence of $Ca_3La_2(BO_3)_4$: Eu^{3+}

The observation of Eu^{3+} afterglow in the $Ca_3La(BO_3)_4$ host, it is necessary to take the TL spectrum into consideration. Fig. 3 represents the TL glow curve of $Ca_3La_{1.9}Eu_{0.1}$ $(BO_3)_4$ phosphor. During this study, glow curves of Eu^{3+} doped $Ca_3La(BO_3)_4$ samples were recorded at dose rate of γ-irradiation (1320 Gy) at room temperature. A strong TSL glow peak is observed at 394 K. It is observed that the intensity of this glow peak is found to increase with the increase of Eu concentration.

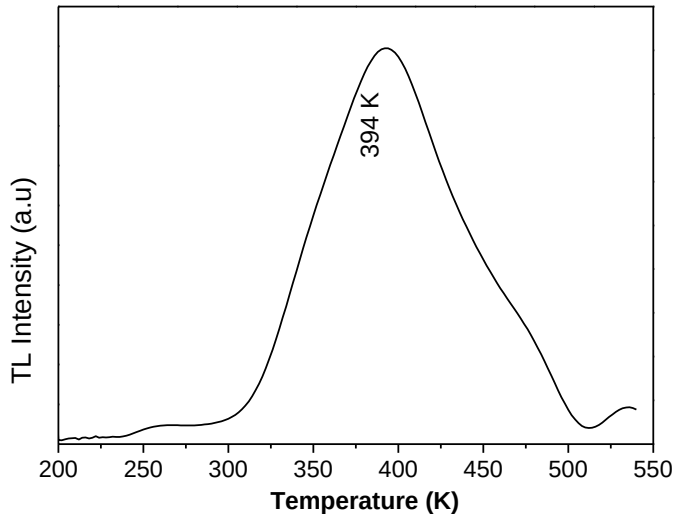

Fig 3 TL glow curve of $Ca_3La_{1.9}Eu_{0.1}$ $(BO_3)_4$ phosphor

3.3.2. Glow curve shape method

The method based on the shape of glow curve proposed by Chen was used to verify the trapping parameters. To determine these parameters the following shape parameters were determined: the total half intensity width ($\omega = T_2 - T_1$), the high temperature half width ($\delta = T_2 - T_m$), the low temperature half width ($\tau = T_m - T_1$), where Tm is the peak temperature and T_1 and T_2 are temperature on either side of T_m corresponding to half peak intensity. In order to calculate the trapping parameters associated with the 394°C glow peak by glow curve shape method using chen's method [13,14] and given in Table 1.

Sample	Dose (Gy)	T_m ±2K	τ (K)	δ (K)	Ω (K)	μ_g	Activation Energy (eV)				S (Sec^{-1})
							E_τ	E_δ	E_ω	E_{av}	
$Ca_3La_2(BO_3)_4$	1320	394	32	44	76	0.579	0.677	0.648	0.659	0.661	2.704×10^7
$Ca_3La_{1.9}Eu_{0.10}(BO_3)_4$		394	35	46	81	0.568	0.596	0.596	0.596	0.596	3.523×10^6
$Ca_3La_{1.9}\ Eu_{0.10}\ BO_3)_4$		394	31	42	73	0.575	0.700	0.671	0.683	0.684	5.522×10^7
$Ca_3La_{1.9}Eu_{0.10}\ (BO_3)_4$		394	35	49	84	0.583	0.609	0.591	0.598	0.599	3.860×10^6

4.0 Conclusions

In this work, we report the chemical synthesis of a new $Ca_3La_2(BO_3)_4$ thermoluminescent phosphor. The experimental evidence presented shows that these novel materials exhibit very good thermoluminescence properties, as to be considered for the development of new dosimeter phosphor materials.

5 Acknowledgements

The author gratefully acknowledge to the UGC, New Delhi for finance assistance under MRP scheme to carried out this work.

Reference

[1] J. Azorin, Luminescence Dosimetry: Theory and Applications, Ediciones Te´cnico-Cientı´ficas, Me´xico D.F., 1990.

[2] J. Azorin, Int. J. Radiat. Appl. Instrum. Part D: Nucl. Tracks 11 (1986) 159.

[3] A.N. Yazici, M. Dogan, V.E. Kafadar, H. Toktamis, Nucl. Instrum. Methods B 246 (2006) 402.

[4] L.Y. Liu, Y.L. Zhang, J.Q. Hao, C.Y. Li, Q. Tang, C.X. Zhang, Q. Su, Phys. Stat. Sol. (a) 202 (2005) 2800.

[5] J. Manam, S.K. Sharma, Nucl. Instrum. Methods B 217 (2004) 314.

[6] C. Furetta, G. Kitis, P.S. Weng, T.C. Chu, Nucl. Instrum. Methods A 420 (1999) 441.

[7] J. Li, J.Q. Hao, C.Y. Li, C.X. Zhang, Q. Tang, Y.L. Zhang, Q. Su, S.B. Wang, Radiat. Meas. 39 (2005) 229.

[8] L.Y. Liu, Y.L. Zhang, J.Q. Hao, C.Y. Li, Q. Tang, C.X. Zhang, Q. Su, Mater. Lett. 60 (2006) 639.

[9] C. Furetta, M. Prokic, R. Salamon, V. Prokic, G. Kitis, Nucl. Instrum. Methods A 456 (2001) 411.

[10] M. Prokic, Radiat. Meas. 33 (2001) 393.

[11] J. Li, J.Q. Hao, C.X. Zhang, Q. Tang, Y.L. Zhang, Q. Su, S. Wang, Nucl. Instrum. Methods B 222 (2004) 577.

[12] J. Azorin, Luminescence Dosimetry: Theory and Applications, Ediciones Te´cnico-Cientı´ficas, Me´xico D.F., 1990.

[13] R. Chen, S.W.S. McKeever, Theory of Thermoluminescence and Related Phenomena, World Scientific, Singapore, 1997.

[14] H.Nagabhushana,.N.Lakshminarasappa, and Fouran Singh, J. Radiat.Meas. Vol.43, (2008), pp. S651.

Synthesis and Magnetic properties of $CoFe_2O_4$ and Mg Fe_2O_4 spinel nano ferrites

M. Raghasudha[1*], D. Ravinder[2], P. Veerasomaiah[1], Shyamsunder goud[1], G. Satyanarayana Goud[3], B. Rambabu[1], N. Venkatesh[1]
1. Department of Chemistry, Osmania University, Hyderabad-500007
2. Department of Physics, Osmania University, Hyderabad-500007
3. Department of Chemistry, M.V.S. Govt Degree College, Mahabubnagar-509001

ABSTRACT

Crystalline, magnetic $CoFe_2O_4$ and $MgFe_2O_4$ nano particles were prepared by citrate-gel auto combustion method . The synthesized samples were subjected to calcinations at 500^0C for 4our hours. XRD analysis of the prepared ferrites confirmed the formation of single phased cubic spinel structure with a low particle size of 7nm for $CoFe_2O_4$ and 23nm for $MgFe_2O_4$. Room temperature magnetic measurements were carried out using Vibrating Sample Magnetometer. The hysteresis loops obtained for the synthesized ferrites revealed that $MgFe_2O_4$ nano particles are soft magnetic materials with very small area inside the loop. $CoFe_2O_4$ nano particles are hard magnetic materials with large area inside the loop when compared to the $MgFe_2O_4$. Due to soft magnetic properties of $MgFe_2O_4$ they are desirable for their utility in transformers, inductor cores, recording heads, microwave devices, and magnetic shielding. Due to excellent magnetic properties of nanocrystalline $CoFe_2O_4$ they can be used in high frequency devices, memory cores, recording media, and in biomedical field.

Keywords: Nano ferrites, Citrate-gel method, XRD, VSM

1.Introduction

Among the materials, Ferrites have attracted immense attention of the scientific community because of their novel properties and technological applications especially when the size of the particles approaches to nanometer scale [1]. As magnetic materials, nano-sized ferrites cannot be replaced by any other magnetic material because they are relatively inexpensive,

stable, and have a wide range of technological applications [2]. Among ferrites, the spinel ferrites have remarkable magnetic and electrical properties. The magnetic

properties of the nanosized ferrites are entirely different from those of their bulk counterparts. Nanosized ferrites with uniform particle size and narrow size distribution are desirable for a variety of applications like targeted drug delivery, medical imaging, magnetic data storage and other biomedical applications, etc. **[3]**.

Magnesium nano ferrites are the potential materials for various applications due to their high electrical resistivity, low magnetic and dielectric losses [4]. On the other hand, $CoFe_2O_4$ is also interesting because of its perfect chemical properties, thermal stability, high electrical resistivity, and excellent magnetic properties [5]. Nanocrystalline $CoFe_2O_4$ with such properties has potential applications in high frequency devices, memory cores, recording media, and in biomedical field [6]. The author is interested in comparing the magnetic properties of Magnesium and Cobalt ferrites for their potential applications.

Among Various methods used to prepare nano-sized ferrites such as co-precipitation method, micro-emulsion procedures, microwave plasma, mechanical milling and sol-gel auto-combustion method, the sol–gel auto combustion method is most suitable for the synthesis of nano-sized ferrite materials. This is because of its advantages such as good stoichiometric control and the production of ultrafine particles with a narrow size distribution in a relatively short processing time at a very low temperature. The present work reports the synthesis of nanocrystalline $MgFe_2O_4$ and $CoFe_2O_4$ and the study of their magnetic properties.

2. Materials and methods

The nanocrystalline $MgFe_2O_4$ and $CoFe_2O_4$ were prepared using Citrate-Gel auto combustion method. The following chemicals are used as starting materials for the synthesis.

Magnesium Nitrate - $Mg(NO_3)_26H_2O$
Cobalt Nitrate-Co $(NO_3)_26H_2O$
Ferric Nitrate -$Fe(NO_3)_29H_2O$,
Citric acid ($C_6H_8O_7{\cdot}H_2O$)
Ammonia (NH_3) (all 99% pure).

Calculated quantities of metal nitrates were dissolved together in a minimum amount of distilled water to get clear solution. An aqueous solution of Citric Acid was then added to the metal nitrate solution. The mixture was stirred to obtain a homogeneous solution and then was slowly heated to 80°C. pH of the solution was adjusted to 7 by adding Ammonia (NH_3) solution. The resulting solution was evaporated to dryness by heating at about 150°C on a hot plate with continuous stirring which has started to form a viscous gel. When finally all water molecules were removed from the mixture by increasing the temperature to 200°C, the viscous gel began frothing. The gel has undergone a flameless auto combustion reaction with the evolution of large amounts of gases. The reaction was completed in a minute giving rise to dark grey voluminous product with a structure similar to Branched tree. Finally the burnt powder was ground and was calcined in air at temperature 500°C for four hours to obtain a spinel phase.

The resultant powder was subjected X-ray Diffraction analysis with Cuk$_\alpha$ (λ = 1.54 Å) to study the single phase nature and nano-phase formation of the ferrites under investigation at room temperature by continuous scanning in the range of 2°C to 85°C. The magnetic measurements of prepared ferrites were measured by using Vibrating Sample Magnetometer at room temperature in the range of 15 kOe.

3. Results and discussion

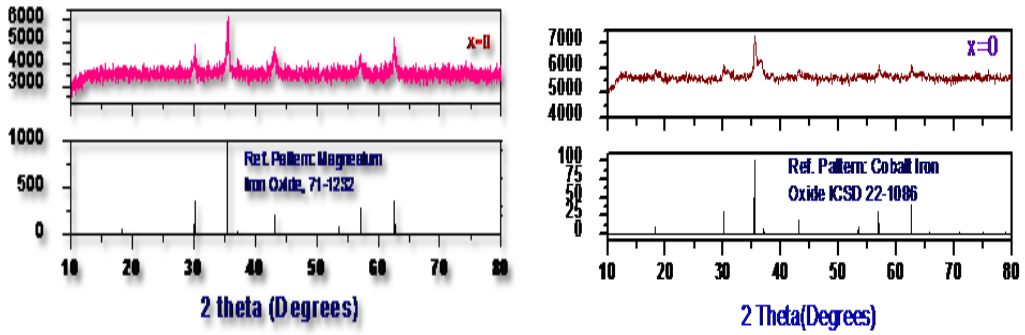

(a) (b)

Fig.1. XRD patterns of (a) $MgFe_2O_4$ and (b) $CoFe_2O_4$

Figure 1 (a) and (b) shows the x-ray diffraction patterns of Magnesium and Cobalt ferrites and reference data of magnesium iron oxide and cobalt iron oxide respectively. The figure showed a homogeneous single phased cubic spinel belonging to the space group Fd3m. All the Braggs re-flections have been indexed as (111), (220), (311), (400), (511) and (440) which confirmed the formation of a well defined single phase cubic spinel structure without any impurity peaks. All the peaks are allowed peaks. The strongest reflection is from (311) plane that indicates spinel phase. Crystallite size (D) of prepared ferrites was calculated from Scherrers Formula [7] mentioned below by using high intensity peak (311).

$$D = \frac{0.91\lambda}{\beta \cos\theta}$$

where λ = Wavelength of X-ray,

β = Full width and Half Maxima in radians,

θ= Bragg's angle at the peak position.

The crystallite size was found to be 23nm for magnesium ferrite and 7 nm for Cobalt ferrite. Figure 2 show the magnetic hysteresis loops for the Magnesium and cobalt ferrite samples obtained from Vibrating Sample Magnetometer measurements at room temperature in the range of 15Koe.

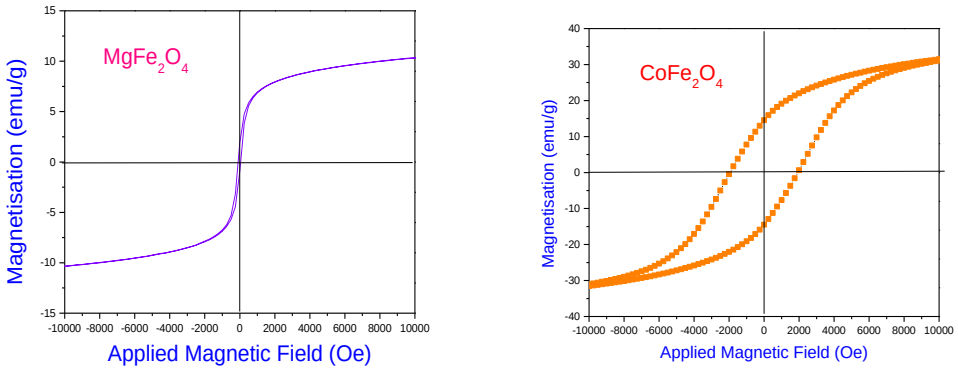

Figure 2. Magnetic Hysteresis loops of $MgFe_2O_4$ and $CoFe_2O_4$

The relation between the Magnetization (M) and the applied field (H) is given by Hysteresis loops. Various magnetic parameters extracted from the hysteresis loops

are Saturation Magnetization-Ms (maximum value of magnetization), Remanence Magnetization-Mr (magnetization at zero field), Coercivity-$H\ c$ (magnetic field required to reduce the magnetization of that material to zero after the magnetization of the sample has been driven to saturation), Remanence ratio or Squareness ratio (Mr/Ms). The magnetic parameters calculated for both the samples were tabulated in table 1.

Table 1. Magnetic parameters of Magnesium and Cobalt nano ferrites

Composition	Saturation magnetization Ms (emu/g)	Coercivity Hc (Oe)	Remanent Magnetization Mr (emu/g)	Remanence ratio $=Mr/Ms$
MgFe2O4	11.08	1.794	97.06	0.16
CoFe2O4	33.8448	14.540	1,954.66	0.4296

From the data it is clear that area inside the hysteresis loop for $MgFe_2O_4$ is very less where as it is more for $CoFe_2O_4$ which is a measure of magnetic property of a material. Due to the smaller area of the loop, $MgFe_2O_4$ is a magnetically soft material whereas $CoFe_2O_4$ is a hard magnetic material due to its larger loop area. Hence Magnesium ferrites are desirable for their utility in transformers, inductor cores, recording heads, microwave devices, and magnetic shielding.

Cobalt ferrites are desirable in high frequency devices, memory cores, magnetic storage systems such as magnetic tape for recorders and for recording heads. Magnetic storage is also widely used in some specific applications, such as bank cheques and credit/debit cards.

4. Conclusions

$MgFe_2O_4$ and $CoFe_2O_4$ nano ferrites were successfully synthesized through citrate-gel method with a particle size 23nm and 7 nm respectively. X-ray diffraction analysis confirmed the formation of single phased cubic spinel structure of the prepared ferrites. Magnetic measurements using VSM revealed that Magnesium nano ferrites are magnetically soft materials and Cobalt nanoferrites are magnetically hard materials. Hence, $MgFe_2O_4$ find applications in transformers, inductor cores, recording heads, microwave devices, and magnetic shielding and

$CoFe_2O_4$ are used in high frequency devices, memory cores and magnetic storage systems.

References

1. Subhash, C, Srivastava, BK, Anjali, K: Indian J. Pur. Appl. Phy 42, 366–367, (2004)
2. Costa, MM, GFM, PJ, Sombra, ASB: Int. J. Mater. Chem. Phy. 123, 35–39, (2010).
3. Kaur, Balwinder.; Arora, Manju.; Shankar, Ajay.; Srivastava, Avanish Kumar.; Pant, Rajendra Prasad. Adv. Matt. Lett., 3(5), 399, (2012)
4. C. Chen, Magnetism and Metallurgy of Soft Magnetic Materials, Dover, New York, NY, USA, 1986.
5. Muzquiz-Ramos, EM, Cortes-Hernandez, DA, Herrera-Romero, OA, Escobedo-Bocardo, J.C.: Mater Sci Forum 644, 39–42, (2010)
6. Pervaiz, E, Gul, IH:. J. Magn. Magn. Mater. 324, 3696–3703, (2012)
7. B. D. Cullity, "Elements of XR-Diffraction," Addison Wesley Publishing, Reading, 1959, p. 132.

Impedance spectroscopic studies on PMN-PT

UshaPraveena V.J, N. V. Prasad*, G. Prasad and G. S. Kumar
Department of Physics, Materials research Laboratory
Osmania University, Hyderabad 500007.

ABSTRACT

Impedance spectroscopic studies are done on PMN-PT (lead magnesium niobate-lead titanate) ceramic. The maxima of the impedance as wellas modulus are found to shift towards higher frequencies with increasing temperature, indicating a deviation from Debye behaviour. Cole-Cole plots show two-depressed semicircles, confirming grain and grain-boundary contributions. Double logarithmicspectroscopic plots, as a function of frequency, in the range of 1 kHz to 1 MHz, were used as a tool to study the electrical behavior of the sample. The results are corroborated to the new Euryod's conduction model.

Key words: PMN-PT, Impedance, conductivity, hopping mechanism

*Corresponding author's Email: nvp_phy@osmania.ac.in

1. Introduction

Lead magnesium niobate(abbrivated as PMN) with general formula $Pb(Mg_{1/3}Nb_{2/3})O_3$ is known for its specific properties like high dielectric permittivity, near-zero hysteresis, a diffuse phase transition, and high electrostrictive coefficients [1-5]. Smolenskii [1] was first to explainthe relaxor characteristics of PMN, based on the compositional fluctuations on a microscopic scaleglobally. In addition, Cross et al [2] reported that ferroelectric(polar) and paraelectric(non-polar) micro-regions exist simultaneouslyin the PMN material overa broader temperature interval. Lead titanate(abbreviated as PT)is a normal ferroelectric (different form PMN), where the dielectric maximum is sharp and it is independent of frequency.

It is a known fact that PMN forms a solid solution with PT, near morphotropic phase boundary (MPB)[3]. Keeping this in view, the chemical composition of PMN-PT (70/30) was prepared in the present investigation.

Impedance analysis helps us in studying the dielectric behavior of crystalline, polycrystalline, and amorphous materials [6]. This technique is often used to separate the contributions of grains and grain boundaries to the dielectric properties. The main objective of the study is to investigate the electrical properties of PMN-PT solid solutions near the MPB.

2. Experimental

The specimens under the investigation were prepared according to the chemical composition PMN-PT (70/30). The starting raw materials wereAR grade (99.9%) pure.The specimens were prepared by the columbite precursor method [2,5,8]. A detailed preparation of PMN-PT is summarized in the following flow chart. The procedure and XRD results would be presented elsewhere [9].

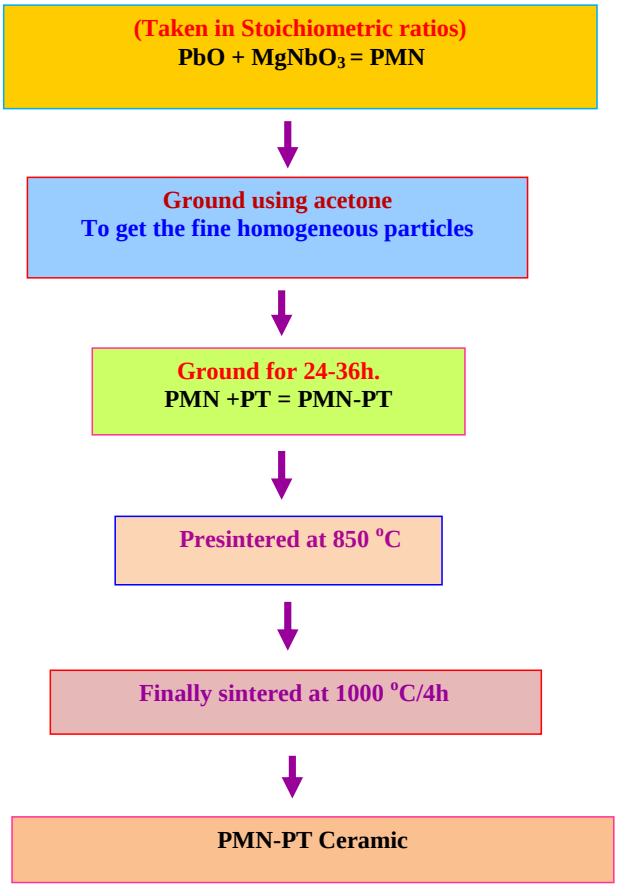

Fig 1.Flow chart for PMN-PT preparation

Prior to the impedance measurements, the sintered circular pellets were coated with silver paste. Impedance measurementswere doneat different temperatures,using HP 4192A impedance analyzer over a wide frequency range (100 Hz to 1 MHz). The dielectric data was extracted from the impedance data.

3. Results and Discussion

In our earlier results, the variation of imaginary part of impedance (Z") and modulus (M") for the PMN-PT with frequency showed non-Debye behavior. This behavior generally observed in the lead based perovskite materials. This is prompted us in relooking into the data.

Fig 2a show the complex impedance plot, drawn between Z" and Z' for a particular temperatures. The depressed two-semicircles indicate adeviation from Debye behavior. Each semi-circle is the representation of a relaxation mechanism, and the semicircle drawn at lower as well as higher frequency region represents grain-boundary and grain relaxation process.

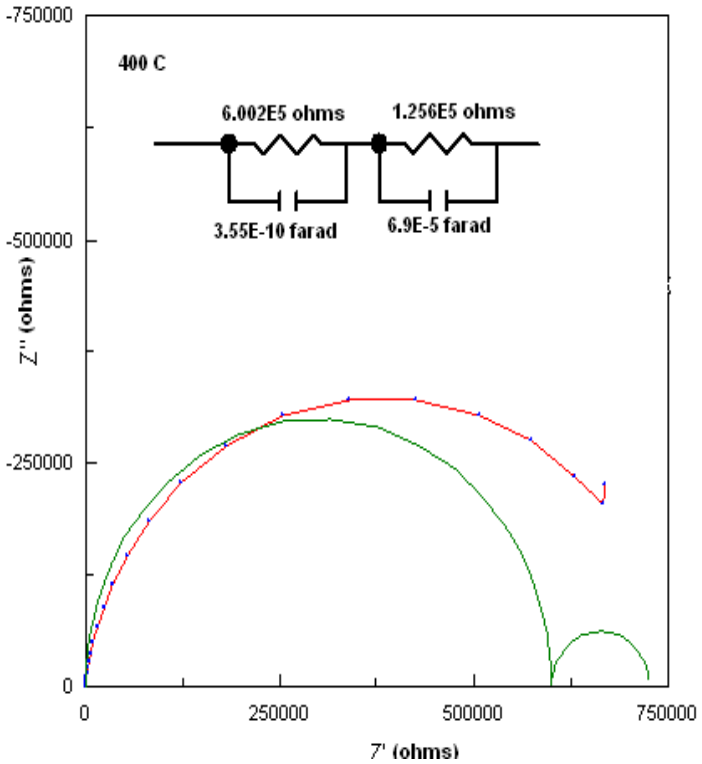

Fig 2 a Cole-Cole plot (Z" vs, Z')

The complex modulus plot is shown in the fig 2b, where the modulus data can be treated as complimentary to the impedance data. Each semicircle can be represented by a parallel combination of resistance (R) and capacitance (C) of a circuit component, and the simplest appropriate equivalent circuit is a series combination of parallel RC elements. Here, the R and C values were calculated by using the Z-view software, depicted in the plot.

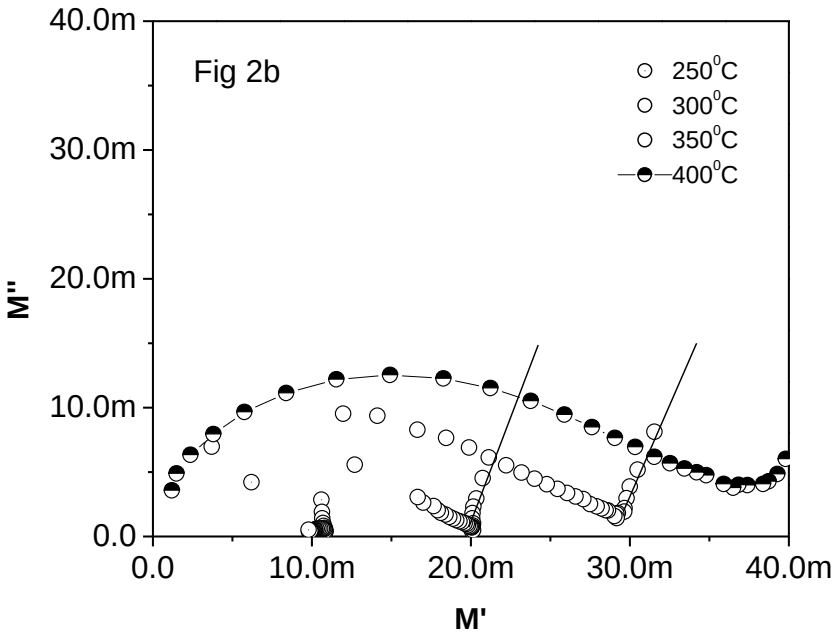

Fig 2b. M" vs. M'

However, the vertical spikes observed in the present case (shown as lines in the plot) at higher frequencies are mainly due to the migration of defects or ions. More aspect of this mechanism is explained in the following double logarithmic plots. The spikes observed in the modulus plot cannot ascribe certainly due to blocking of electrode-effects. If blocking electrodes were present, then vertical spikes could be observed in the lower frequency region of complex impedance plot.

Figs. 3 (a-d) show the dependence of the conductance and permittivity on frequency at different labeled temperatures. The conductance plots (fig 3b) show a slope change at a certain frequency called the hopping frequency of the charged species. The hopping frequency is a temperature dependent. Almost temperature independent nature of real conductance (fig 3a) indicates the presence of hopping-

conduction by electron. The linear nature observed in real respond plots can be described by the exponential relation ($\epsilon \alpha\epsilon^{n-1}$) with the frequency. The dispersion observed in the lower frequency of conductance plot (fig 3b) is ascribed to the continuous jumps or hopping type mechanism of non-Debye materials [10]. The overall behavior could be described by the multiple ionic migrations or transportation.

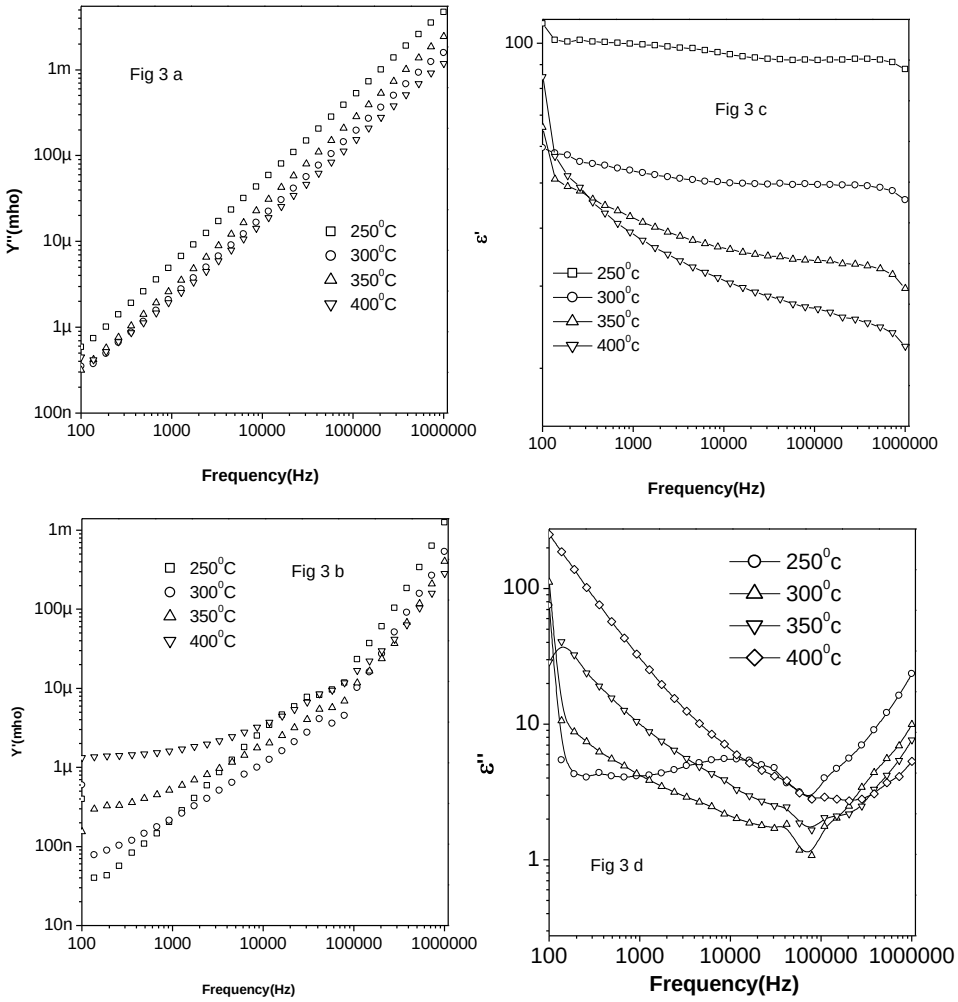

Fig 3 (a) Y' vs. frequency (b) Y" vs. frequency (c) □ ' vs. frequency (d) □ " vs. frequency

The results are consistent with Eyraud's [11] model, where Pb-based ceramics have fully ionizes cation and anion vacancies. The following exchange reaction, proposed by Eyraud [11] is seems to be more adequate. The terms V'_{Pb},

V_o' and V_o" indicates lead vacancy, single ionized vacancy and double ionized vacancies respectively.

$$V_{Pb} \rightarrow V'_{Pb} + e' \quad ; V_{o"} \rightarrow V_{o'} + e'$$

$$V"_{Pb} \rightarrow V'_{Pb} + e' \quad ; V_{o'} \rightarrow V_{o"} + e$$

4. Conclusions

(i) Spectroscopic plots as well as depressed semicircular Cole-Cole plots reveals the non-Debye behavior.

(ii) Double logarithmicplots of conductivity and permittivity indicate hopping between neighboring donor sites. Imaginary part of conductance and permittivity shows temperature dependent.

(iii) Real part of conductivity vs. frequency showed that the conduction is through hopping of electrons at extrinsic region and migration of oxygen vacancies at intrinsic region. An increasing of e" at higher frequency indicates the migration of both V_o' (single ionized) and V_o" (double ionized vacancies). However, the migration of V_o" predominates over Vo'. The results are consistent with our earlier results [9] as well as Euryod's conduction model.

(iv) Based on the double logarithmic plots and our earlier results [9], it is concluded that electron hopping is easier between double ionized and single ionized vacancies of both lead as well as oxygen vacancies. Finally, both single and double ionized oxygen and lead vacancies contribute in the conduction mechanism.

Acknowledgements: One of the authors UshaPraveena V.J. thanks the management of St. Francis College for women,Hyderabad for constant encouragement and support.

References

1. G.A.Smolenskii and A.I.Agronovskaya, Dielectric polarization of a number of complex compounds, sov. Phys.Tech. Phys. A3 (1958) 1380
2. L.E.Cross,Relaxor ferro electrics, Ferroelectrics 76, (1987) 241
3. V.K.Wadhawan, Introduction to ferric materials, Gordon & Breach, UK (2000)
4. K.Uchino , Ferroelctric Devices, Marcel Dekker Inc, NY (2000)
5. B.Jaffe , W.R.Cook and H.Jaffe, Piezoelectric Ceramic, Acadamic Press, London (1971)
6. J.R.Mac Donald, Impedance spectroscopy, Wiley, NY(1987)
7. M.E Lines and AM Glass , principles and application of ferroelectric and related materials, Clarendon press, Oxford (1977).
8. S.W. Choice , T.R.Shrout, S.J.Jang and A.S.Bhalla, Dielectric and pyro electric properties in the $Pb(Mg_{1/3}\ Nb_{2/3})O_3$-$PbTiO_3$ system, Ferroelectrics 100 (1989) 29
9. N.V.Prasad, M.ChandraSekar and G.S.Kumar, Ferroelectrics, 366 (2008) 55
10. A.K.Jonscher, Dielelctric relaxation in solids, Chelsa Dielelctrics, London (1983); Universal Realaxation law ,Chelsa Dielelctrics, London (1996)
11. L.Eyraud, B. Guiffard, L.Lebruen and D.Guyomar, Ferroelectrics 330 (2006) 51.

Resistive Switching Property of Nickel-Zinc Thin Film Synthesized By Sol Gel Route

K. Rama Krishna [1] K. Vijaya Kumar[2] D. Ravinder[3]

1. Department of Physics, Malla Reddy College of Engineering & Technology, Secunderabad – 500 014. A.P. India.
2. Department of Physics, Jawaharlal Nehru Technological University Hyderabad, College of Engineering, Nachupally (Kondagattu), Karimnagar-Dist., 505 501, A.P., India
3. Department of Physics, Osmania University, Hyderabad – 500 007. A.P. India
**Corresponding author email id: ramu521@gmail.com*

ABSTRACT : $Ni_{0.8}Zn_{0.2}Fe_2O_4$ nano thin films were synthesized using spin coating chemical process, by depositing a solution of iron (III) nitrate, nickel acetate, zinc chloride and ethylene glycol solutions on a glass Substrate. This substrate is subjected to pre and post annealing at 350^0 C &550^0C for 30 & 60 min which results the formation of nano thin film. The conformation of single phase formation and structural analysis were carried by employing X-ray diffraction technique and Atomic force micro scope (AFM). The I-V measurements of the sample is were done using Keithley 4200 Semiconductor Characterization System (SCS)

Key words: Ni-Zn nano ferrite thin film, Spin coating method, topography. I-V measurements

1. INTRODUCTION

Ferrites, which are magnetic oxides, are best examples for very good electrical materials because of their high resistivity and low loss behavior hence they have vast technological applications over a wide range of frequencies [1 2]. Ni-Zn ferrite is a significant magnetic material for practical applications because of its better properties at high frequency and high resistivity.

2. EXPERIMENTAL

A precursor solution of $Ni_{0.8}Zn_{0.2}Fe_2O_4$ was prepared from iron (III) nitrate, nickel acetate, zinc chloride and dissolved in anhydrous 2-mithoxyethanol. The mixture obtained in such a manner was stirred in a magnetic stirrer for about 4 hrs. at room temperature. It was observed that the solubility of nickel acetate, zinc chloride

wasn't as good in ethanol. Due to this, the associated acetate forms colloids and a solution is obtained. The technique stabilizers were added to the respective solutions to eliminate/minimize the turbidity and precipitates. In some cases the solution was kept in the ultrasonic bath to promote the reaction. Among various stabilizers, mono-ethanolamine (MEA) is widely used as effective capping agent, to not only control the crystallite size but also to obtain oriented films. The solution was hydrolyzed with water per mole of metal by adding water dissolved in 2-mithoxyethanol at 20 wt. % drop-wise, along with roughly 2 wt. % MEA in order to remove turbidity and precipitates completely. Clear, transparent, and homogenous solution with no precipitations used for deposition.

Double size polished soda lime glass, SiO_2 (quartz) of size 15 x 10 x 1 mm squares were used as substrates, after being thoroughly cleaned in an ultrasonic cleaner (PCI corporation, Mumbai, frequency of 33 kHz) in following sequence : double distilled water → acetone →distilled water for a total duration of 40 minutes. The substrates were rinsed with deionized water for 5 min and then dried in air atmosphere. The cleaned substrates were spin coated at rpm of 4000 to 4500 for 20 seconds at room temperature. Films were very slowly dried at 250 °C for 30min. This cycle was repeated 5-6 times until the desired thickness was obtained. The thickness of the films was in the range of some nm. The deposited films were annealed in air at temperature of 550°C for 60 min. The Schematic flow chart of CSD route of $Ni_{1-x}Zn_xFe_2O_4$ thin films is as shown in the fig 1.

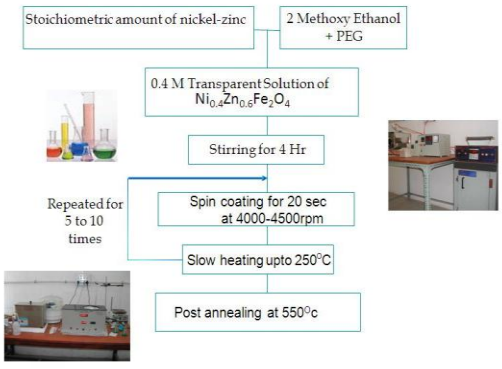

Fig 1.1 Flow chart

3. RESULTS AND DISCUSSION

$Ni_{0.8}Zn_{0.2}Fe_2O_4$ thin film is characterized by X-ray diffraction confirms the single phase formation of ferrite to cubic structure and corresponding X-rd is as shown in the fig 2.

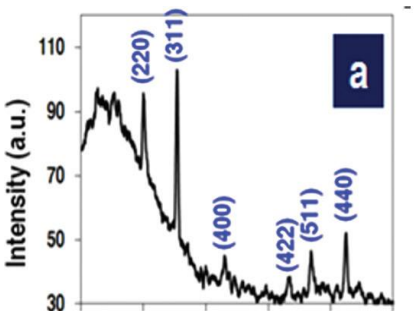

Fig. 2 X-rd of $Ni_{0.8}Zn_{0.2}Fe_2O_4$

3.1 Lattice parameter

The hin film is calculated by using the following equation [3] and it was found to be 8.42 A^o, different researchers found that the lattice parameter is in the same order [4].

$$a=d\,(h^2+K^2+l^2)^{1/2}$$

Where, a=lattice constant

d= inter planar distance &

(h, k, l) are the Miller indices

3.2 Particle Size:

The particle size of the samples are calculated by using Sherrer's formula [5] by using the following equation and the particle size is found to be 20 nm

$$d_{hkl} = \frac{0.91\lambda}{\beta Cos\theta}$$

Where

d_{hkl} is the crystalline size perpendicular to (h k l) pane,

λ --- The wave length of X-ray used,

β --- Width of diffraction peak i.e., Full Width Half Maxima (FWHM)

θ --- The peak position.

3.3 X-ray density:

X- ray density (dx) was determined using the following equation and it was found to be 5.20 gm/cm^3

$$d_x=ZM/Na^3$$

Where 'Z 'is the number of molecules per unit cell (Z=8), 'M' is the molecular weight and 'N' is Avogadro number.

3.4 AFM MEASUREMENTS

The AFM measurements (NANO SURF 2.0, VERSION 1.6) of the film annealed at 550 C as shown in the figure 3below displays a particle size of the film to be around to 20 nm, and an rms roughness of around 5.2 nm

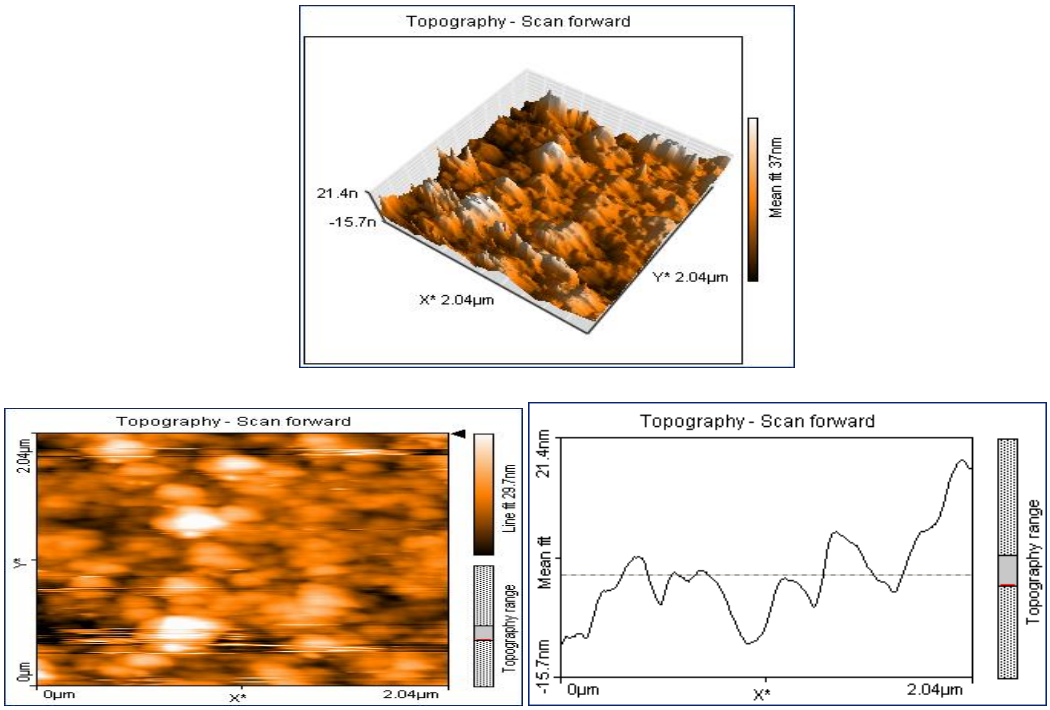

Fig 3 AFM images of samples

Film annealed at 550 ^{0}C

AFM Particle Size – 20 nm

Film roughness – 5.2 nm

3.5 ELECTRICAL PROPERTIES

For electrical measurements, stripe shaped, 3 mm long electrodes of Ag were prepared by using silver paste to form planner Ag/$Ni_{1-x}Zn_xFe_2O_4$/Ag structures and copper probes were pressed directly on the films to use as electrodes. Typical current voltage (log I vs. V) characteristics of Ag/ $Ni_{0.8}Zn_{0.2}Fe_2O_4$ /Ag planar structure are shown in fig 4.

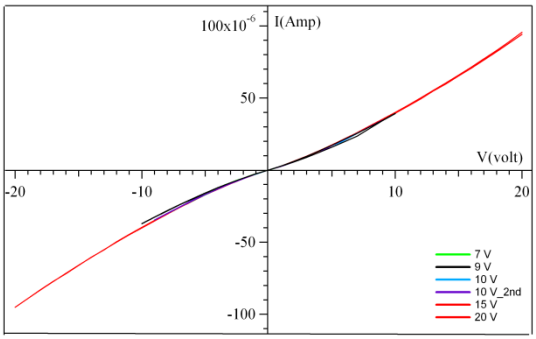

Fig 4 I-V characteristics of $Ni_{0.8}Zn_{0.2}Fe_2O_4$

The inset shows the I-V properties at low voltages. A continuous voltage sweep with a sequence -20V→0V→+20V→0V was applied through outer terminals and current was measured at the inner points. Current values for several voltage sweep cycles were recorded over a span of three to four hours to reproducibility of the results and even by reversing the polarity. The I-V of the film displays diode like dynamic characteristics [6] . It shows a nonlinear behavior that indicates different resistance at different bias. This behavior needs further investigation.

CONCLUSIONS

$Ni_{0.8}Zn_{0.2}Fe_2O_4$ nano thin film is successful prepared by spin coating method with particle size 20 nm. This ferrite is subjected I-V characteristics, from this characteristics we can concluded that this ferrite is not suggestible for switching property

References

1. M. G. Patil , V. C. Mahajan, A. K. Ghatage , and S. A. Patil, Indian J. Pure Appl.Phys.34, 166(1996).
2. M.Ul-Islam, M.Ashraf Chaccdhry, T. Abbas, and M. Umar, Mater. Chem..phys. 48, 227 (1997).
3. Iqbal MJ, Siddiquah MRJ Magn Magn Mater 320(2008) p 487
4. SS Bellad BK Chougule - Materials research bulletin, 33 1998, p.1165–1173
5. Cullity B D, Elements of X-ray diffraction Addition Wesley, Reading, Mass),1959, p132
6. Yamashiro T Jpn. J. Appl. Phys. 1973 12, 148

Excluded Energy and Relative Encircled Energy an important role in the Optical Imaging Systems with amplitude and apodised Parameters

B. Sambaiah* and D. KarunaSagar¶

Optics Research Group, Department of Physics, University College of Science, O. U., Hyderabad – 500 007, India*
Professor, Department of Physics, University College of Science, (O.U.), Hyderabad – 500 007, India¶
Email: sam.bokkala@gmail.com

ABSTRACT

Encircled Energy Factor (EE), Excluded Energy and Relative Encircled Energy are important corollaries of the Point Spread Function (PSF) of an optical system. In this paper, we have studied the Excluded Energy, Relative Encircled energy to understand their role as Point Image quality assessment parameters of Optical systems with amplitude apodised rotational symmetric filter functions.

Key-words: Mathematical Optics, Apodisation, Encircled Excluded Energy Factor, Relative Encircled Energy, Pupil Function etc..

1. Introduction

Encircled energy is an important parameter which can be studied as a measure of image quality. According to Wetherill1, "Excluded energy" is the energy difference between total energy and the energy concentrated within a specified circle of radius δ . It is denoted with Ex [δ] and is also useful to study the structure of a specified ring in detail. It is also known as the "Dispersion Factor", as designated by Dossier2, higher value of this factor indicates better functioning of the pupil function. The most desirable pupil function is that which can minimize the excluded energy and maximize the encircled energy. Surender3 has remarked on the importance of the excluded energy as follows. "The contrast at the centre of the image of a black disc, seen against a uniform incoherent background is what can be interpreted as the physical significance of Ex(δ)". If the energy in the outer rings of the diffraction pattern is to be examined in details, it is convenient to focus more on the excluded energy rather the encircled energy. This aspect has made the study on Ex(δ) more

useful, in various techniques of apodisation, to change the ring structures in a pre-determined way. The study of Ex(δ) is also useful in several photometric analysis. Relative encircled energy the most important corollary of the Point Spread Function (PSF) is the "Relative Encircled Energy". It measures the fraction of the total energy in the PSF, which lies within a specified radius 'δ' in the plane of observation or detection. We will designate this important parameter by the symbol REE(δ). Lord Rayleigh4 was the first to point out the importance of the encircled energy factor to find the illuminations in the various rings of the diffraction pattern and presented a formula for calculating the

same. When a converging spherical wave is diffracted by a circular aperture the classical theory of focusing predicts that light energy is highly concentrated in the geometrical focal plane. It means that there is a maximum amount of energy within a receiving circle of a given radius centered at the aperture axis and placed in the geometrical focal plane which contains more energy per unit area than any other plane parallel to it. Thus, it comes out that the EE() is the primary corollary of the and is the factor, which describes the integrated behavior of the point source diffraction image. It is a sensible image quality evaluation parameter of an optical system, with this phenomena Excluded energy Factor, Relative Encircled energy are very close to Encircled energy we have studied in this paper these two parameters. Murthy5 was investigated the PSF Based corollaries viz Encircled energy Excluded energy and energy increment in the presence of defocusing by employing co-sinusoidal amplitude filters. Karunasagar6 has studied the Encircled energy Relative encircled energy and Excluded energy, Displaced energy and zonal increment for rotationally symmetric Ratnam7 similar studies have been carried out for multiple coded apertures and complimentary multiple annuli coded apertures Steal8 and Mehatha9 have studied the encircled energy in the Fraunhoper diffraction pattern with circular apertures with triangular apodisation filters Surender, Seshagiri Rao and Mondal10 have studied the encircled energy and its complimentary quantity, Excluded energy using Lanczos apodisation filters. Keshavulu11 was investigated the encircled energy in the presence of individual and the combined effects of defocusing and primary spherical aberration in the case of optical systems apodised

by shaded aperture systems. V.N Mahajan12 have obtained a closed form solution for the excluded power, using the well known recurrence relations of Bessel functions of the first kind. In our investigation we are using filter function f $f\ r\ = Cos\ \pi\beta r$ and get results for Excluded energy Factor, Relative encircled energy, we have discussed the results with figures and tabular. This paper organized as fallows.

2. mathematical formulations:

Excluded Energy can be represented mathematically as Excluded Energy and Relative-Encircled Energy apodisation Parameters. According to WETHERELL (1980) excluded energy is the energy difference between total energy and energy concentrated within a specified circle of radiusδ. It can be represented a

$$XE\ (\delta) = 1 - EE\ (\delta) \qquad (2.1)$$

It is an important quality factor to examine the performance of the pupil function and also to study the structure of a specified ring in detail. Minimum value of this factor indicates well functioning of the pupil function. The best pupil is that which can minimize the excluded energy and maximize the encircled energy. The above equation (3.11) can be expressed in terms of intensity as,

$$XE\ (\delta) = \frac{\int_{\delta}^{\infty} |\ G_F\ (0, Z)|^2\ Z\ dz}{\int_{0}^{\infty} |\ G_F\ (0, Z)|^2\ Z\ dz} \qquad (2.2)$$

Where G(0, z) is the amplitude in the image plane at a point z, it is defined14 as

$$G_F\ (0, Z) = 2 \int_{0}^{1} f\ (r)\ J_0\ (Zr)\ r\ dr \qquad (2.3)$$

Where f (r) is the pupil function which defines the nature of transmission over the pupil of the aperture of the optical system the pupil-function f(r) can be mathematically represented as

$$f\ r\ = Cos\ \pi\beta r \qquad (2.4)$$

Where β is the apodisation parameter which controls the amplitude transmission of the pupil and r is the normalized distance of a point on the pupil from its centre and J_0 (Zr) 0 is the Bessel function of the first kind with zero order for the argument (Zr) finally from equation (2.1) and (2.2) we get the mathematical expression for Ex[δ]. Relative Encircled energy is defined as the ratio of the light energy within a specified circle of radius δ centered on the diffraction head due to the non-airy pupil to the total light energy in the diffraction pattern due to the Airy-pupil. Mathematically, it can be represented as:

$$EE_{rel}(\delta) = \frac{\int_0^{\delta} |G_F(0,Z)|^2 Z\,dZ}{\int_0^{\infty} |G_A(0,Z)|^2 Z\,dZ} \qquad (2.5)$$

where the subscripts A and F stand for Airy filtered and non-airy pupils respectively. It has been observed that for rotationally symmetric pupil functions, For Airy pupil function the apodisation parameter β values are difference from zero, Non-airy pupil function the apodisation parameter β values are equal to zero in this case the numerator function GF (0, z) is defined as below,

$$G_F(0,Z) = 2\int_0^1 J_0(Zr)\,r\,dr \qquad (2.6)$$

Substituting amplitude functions in both cases airy pupil and non-airy pupil in equation (2.5) then we get corresponding results for Relative Encircled energy.

3. Results and Discussions

The results from the amplitude studies made on the effects of apodisation and defect-of-focus, when the optical imaging system is under the influence of primary spherical aberration and primary coma are presented in the following sections. WOLFRAM MATHEMATICA-7.0 has been used to evaluate the relevant expressions for the corollaries of point spread function. The apodisation parameter β is varied from 0 to 1 in steps of 0.25.

i. Excluded Energy [xe (δ)]:

Expression (2.2) has been employed in evaluating the excluded energy values for various values of δ raging from 0.2 to 12 in steps of 0.2 when the apodisation parameter (β) is varied from 0 to 1.0 in increment of 0.25. Excluded energy (XE (δ)) represents the fraction of the total energy in the diffraction pattern present in the outer specified ring. The desirable energy distribution is one, which corresponds to the greatest concentration of energy in the near vicinity of the center of the diffraction pattern. Hence, the minimization of this factor and consequent maximization of the encircled energy have a greater influence in mitigating the degrading effects and resulting in enhanced quality of the imaging system. The variations of excluded energy with δ for various amounts of apodisation are presented in Table 1. Figs.1 and 2 gives the distribution of excluded energy for defect-of-focus $\phi_d = \pi$ and primary spherical aberration $\varphi_s = \pi$. It is clear that the excluded energy decreases rapidly for values of δ up to 3.8 for β = 0.50 which in terms of results in the enhancement of the encircled energy for β = 0.50.

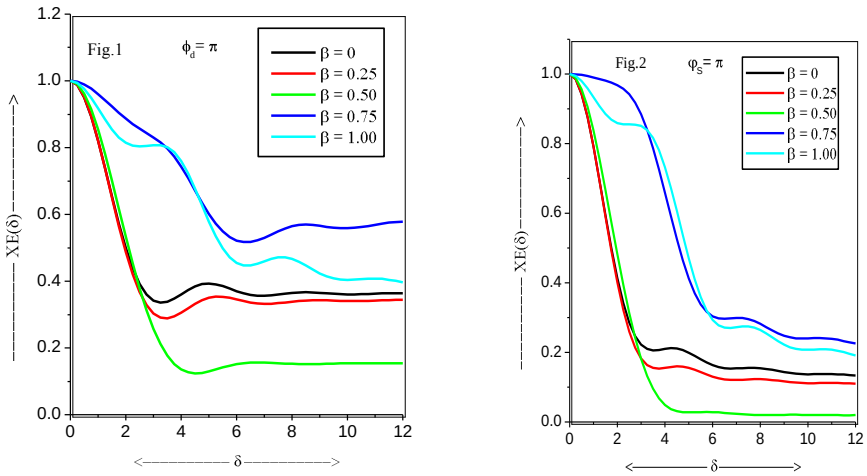

Fig.1 & 2 Excluded Energy with δ various values of β

TABLE 1 Excluded Energy

	$\phi_d = \pi$						$\varphi_S = 2\pi$					
δ = 0.25	β = 0	β = 0.25	β = 0.5	β = 0.75	β = 1.0		δ = 0.25	β = 0	β = 0.25	β = 0.5	β = 0.75	β = 1.0
0.25	0.0166	0.0182	0.0077	0.0081	0.0101	0.0131	0.25	0.0137	0.0205	0.0099	0.0118	
0.50	0.0645	0.0708	0.0301	0.0310	0.0387	0.0507	0.50	0.0531	0.0794	0.0389	0.0456	
0.75	0.1378	0.1516	0.0657	0.0650	0.0818	0.1080	0.75	0.1128	0.1692	0.0850	0.0968	
1.00	0.2282	0.2520	0.1119	0.1050	0.1330	0.1779	1.00	0.1851	0.2789	0.1453	0.1584	
1.25	0.3256	0.3611	0.1657	0.1450	0.1855	0.2520	1.25	0.2612	0.3957	0.2159	0.2226	
1.50	0.4201	0.4685	0.2235	0.1800	0.2327	0.3226	1.50	0.3324	0.5071	0.2928	0.2820	
1.75	0.5034	0.5649	0.2818	0.2060	0.2700	0.3832	1.75	0.3917	0.6025	0.3717	0.3309	
2.00	0.5695	0.6436	0.3376	0.2214	0.2949	0.4296	2.00	0.4343	0.6742	0.4485	0.3660	
2.25	0.6155	0.7008	0.3882	0.2261	0.3079	0.4606	2.25	0.4581	0.7178	0.5198	0.3870	
2.50	0.6419	0.7362	0.4318	0.2214	0.3120	0.4773	2.50	0.4629	0.7315	0.5827	0.3963	
2.75	0.6515	0.7519	0.4670	0.2096	0.3121	0.4828	2.75	0.4504	0.7158	0.6350	0.3983	
3.00	0.6489	0.7522	0.4937	0.1943	0.3139	0.4811	3.00	0.4234	0.6725	0.6753	0.3986	
3.25	0.6399	0.7424	0.5120	0.1817	0.3226	0.4764	3.25	0.3870	0.6056	0.7028	0.4024	
3.50	0.6303	0.7284	0.5227	0.1824	0.3421	0.4723	3.50	0.3503	0.5236	0.7171	0.4137	
3.75	0.6255	0.7161	0.5270	0.2061	0.3742	0.4712	3.75	0.3280	0.4439	0.7187	0.4346	
4.00	0.6299	0.7103	0.5263	0.2531	0.4183	0.4742	4.00	0.3372	0.3981	0.7083	0.4645	
4.25	0.6456	0.7146	0.5221	0.3144	0.4714	0.4808	4.25	0.3838	0.4200	0.6875	0.5010	
4.50	0.6718	0.7298	0.5157	0.3799	0.5288	0.4893	4.50	0.4570	0.5070	0.6580	0.5400	
4.75	0.7052	0.7540	0.5087	0.4406	0.5849	0.4972	4.75	0.5406	0.6261	0.6220	0.5770	

5.00	0.7410	0.7834	0.5020	0.4905	0.6345	0.5024	0.6079	5.00	0.6206 0.7480 0.5824
5.25	0.7742	0.8131	0.4964	0.5261	0.6738	0.5039	0.6296	5.25	0.6880 0.8547 0.5419
5.50	0.8011	0.8390	0.4926	0.5468	0.7007	0.5021	0.6410	5.50	0.7375 0.9364 0.5036
5.75	0.8198	0.8583	0.4904	0.5548	0.7154	0.4992	0.6427	5.75	0.7675 0.9895 0.4703
6.00	0.8300	0.8703	0.4899	0.5543	0.7199	0.4984	0.6375	6.00	0.7791 1.0145 0.4442
6.25	0.8334	0.8754	0.4905	0.5507	0.7181	0.5032	0.6293	6.25	0.7761 1.0157 0.4268
6.50	0.8326	0.8756	0.4919	0.5496	0.7143	0.5166	0.6230	6.50	0.7635 0.9995 0.4182
6.75	0.8305	0.8734	0.4934	0.5560	0.7130	0.5401	0.6234	6.75	0.7474 0.9740 0.4170
7.00	0.8301	0.8715	0.4948	0.5731	0.7176	0.5733	0.6342	7.00	0.7345 0.9484 0.4212
7.25	0.8336	0.8720	0.4958	0.6018	0.7302	0.6144	0.6572	7.25	0.7304 0.9318 0.4285
7.50	0.8423	0.8765	0.4963	0.6401	0.7510	0.6598	0.6912	7.50	0.7389 0.9311 0.4364
7.75	0.8560	0.8854	0.4962	0.6842	0.7781	0.7052	0.7329	7.75	0.7606 0.9495 0.4433
8.00	0.8733	0.8981	0.4957	0.7290	0.8086	0.7463	0.7773	8.00	0.7924 0.9847 0.4479
8.25	0.8921	0.9129	0.4949	0.7695	0.8387	0.7796	0.8191	8.25	0.8290 1.0301 0.4498
8.50	0.9100	0.9279	0.4940	0.8019	0.8651	0.8027	0.8541	8.50	0.8646 1.0774 0.4489
8.75	0.9250	0.9412	0.4932	0.8243	0.8854	0.8153	0.8795	8.75	0.8943 1.1193 0.4457
9.00	0.9357	0.9513	0.4926	0.8366	0.8987	0.8187	0.8943	9.00	0.9152 1.1506 0.4408
9.25	0.9419	0.9577	0.4923	0.8410	0.9053	0.8161	0.8995	9.25	0.9264 1.1692 0.4351
9.50	0.9442	0.9605	0.4923	0.8408	0.9069	0.8114	0.8975	9.50	0.9289 1.1755 0.4295
9.75	0.9440	0.9608	0.4925	0.8398	0.9061	0.8091	0.8918	9.75	0.9252 1.1721 0.4247
10.00	0.9431	0.9599	0.4928	0.8419	0.9055	0.8130	0.8860	10.00	0.9188 1.1633 0.4212

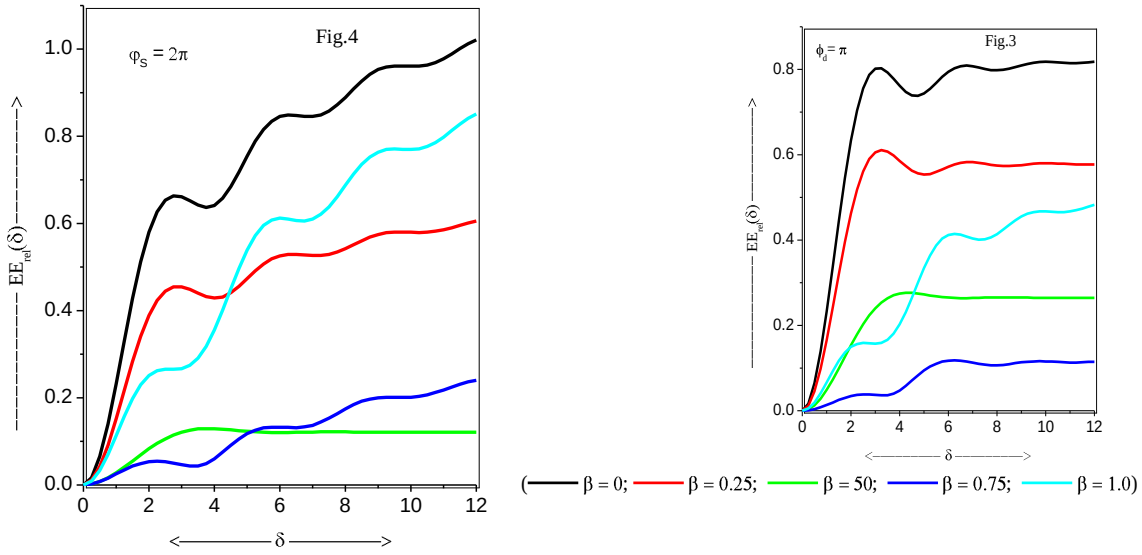

ii. Relative Encircled Energy REE(δ):

We used the equation (2.5) For evaluating the Relative Encircled energy, the results have been shown in figures 3and 4 the table 2.The case of the optical system with defocusing $\phi_d = \pi$ and primary spherical aberration $\varphi_s = 2\pi$. The graphical representation has been given as relative encircled energy curves in For non-Airy Pupil function that is apodisation parameter β=0 for various values of δ gives same value of Relative Encircled Energy, for high value of δ that is δ=12 with various values of δ then the Relative Encircled energy become identical it is evident for convergence. For lover values of δ in the range 1≤ δ ≤ 2 the Relative Encircled energy increases 2.26. For higher value of δ in the range 3 ≤ δ≤ 12 then the Relative Encircled energy increases and instantly small decreasing after that Relative encircle energy become identical and it goes to infinite.

4. Conclusions

The pupil function $f\ r\ = Cos\ \pi\beta r$ is rotationally symmetric. For higher values of β with various values of δ then the Excluded energy factor and Relative encircled energy both increases monotonically and becomes identical it happens with the effect of our consideration filter function and Bessel function.

Table 2 Relative encircled energy

$\varphi_S = 2\pi$						$\phi_d = \pi$			
δ	β = 0	β = 0.25	β = 0.5	β = 0.75	β = 1.0	δ	β = 0	β = 0.25	β = 0.5	β = 0.75	β = 1.0
0.25	0.0103	0.0076	0.0027	0.0011	0.0030	0.25	0.0046	0.0036	0.0017	0.0004	0.0004
0.50	0.0402	0.0297	0.0108	0.0042	0.0115	0.50	0.0179	0.0143	0.0067	0.0015	0.0015
0.75	0.0872	0.0645	0.0237	0.0091	0.0245	0.75	0.0392	0.0313	0.0147	0.0035	0.0032
1.00	0.1472	0.1093	0.0409	0.0153	0.0401	1.00	0.0671	0.0536	0.0255	0.0061	0.0052
1.25	0.2153	0.1607	0.0613	0.0224	0.0564	1.25	0.0996	0.0799	0.0385	0.0094	0.0074
1.50	0.2862	0.2149	0.0840	0.0298	0.0715	1.50	0.1350	0.1087	0.0532	0.0134	0.0094
1.75	0.3550	0.2684	0.1079	0.0371	0.0839	1.75	0.1713	0.1385	0.0689	0.0179	0.0112
2.00	0.4174	0.3182	0.1319	0.0439	0.0927	2.00	0.2065	0.1678	0.0852	0.0230	0.0124
2.25	0.4702	0.3616	0.1552	0.0498	0.0979	2.25	0.2391	0.1954	0.1015	0.0285	0.0131
2.50	0.5114	0.3969	0.1768	0.0547	0.0998	2.50	0.2679	0.2204	0.1171	0.0345	0.0131
2.75	0.5400	0.4234	0.1962	0.0585	0.0996	2.75	0.2921	0.2419	0.1317	0.0408	0.0123
3.00	0.5562	0.4408	0.2129	0.0612	0.0984	3.00	0.3114	0.2596	0.1450	0.0474	0.0106
3.25	0.5611	0.4495	0.2266	0.0630	0.0976	3.25	0.3256	0.2733	0.1567	0.0542	0.0080
3.50	0.5562	0.4506	0.2374	0.0641	0.0986	3.50	0.3352	0.2833	0.1667	0.0611	0.0042
3.75	0.5436	0.4453	0.2453	0.0649	0.1027	3.75	0.3407	0.2898	0.1750	0.0679	0.0015
4.00	0.5261	0.4353	0.2506	0.0658	0.1106	4.00	0.3427	0.2934	0.1815	0.0746	0.0074
4.25	0.5064	0.4225	0.2537	0.0673	0.1226	4.25	0.3421	0.2945	0.1865	0.0810	0.0148
4.50	0.4875	0.4088	0.2549	0.0695	0.1379	4.50	0.3397	0.2939	0.1900	0.0870	0.0231
4.75	0.4720	0.3962	0.2547	0.0726	0.1550	4.75	0.3363	0.2921	0.1924	0.0925	0.0319
5.00	0.4619	0.3860	0.2536	0.0762	0.1722	5.00	0.3326	0.2896	0.1937	0.0975	0.0410
5.25	0.4577	0.3794	0.2520	0.0800	0.1878	5.25	0.3291	0.2870	0.1943	0.1017	0.0498

5.50	0.4591	0.3766	0.2502	0.0837	0.2005	5.50	0.3262	0.2846	0.1943
	0.1053	0.0580							
5.75	0.4644	0.3770	0.2486	0.0870	0.2092	5.75	0.3243	0.2827	0.1940
	0.1082	0.0653							
6.00	0.4717	0.3798	0.2473	0.0897	0.2138	6.00	0.3232	0.2814	0.1935
	0.1104	0.0715							
6.25	0.4790	0.3838	0.2464	0.0914	0.2142	6.25	0.3229	0.2806	0.1929
	0.1120	0.0765							
6.50	0.4847	0.3877	0.2460	0.0921	0.2113	6.50	0.3232	0.2804	0.1923
	0.1130	0.0801							
6.75	0.4878	0.3906	0.2460	0.0917	0.2059	6.75	0.3239	0.2805	0.1918
	0.1135	0.0825							
7.00	0.4878	0.3920	0.2463	0.0902	0.1994	7.00	0.3247	0.2809	0.1914
	0.1136	0.0839							
7.25	0.4847	0.3915	0.2468	0.0878	0.1930	7.25	0.3254	0.2814	0.1912
	0.1133	0.0843							
7.50	0.4793	0.3892	0.2474	0.0847	0.1882	7.50	0.3259	0.2818	0.1911
	0.1129	0.0839							
7.75	0.4723	0.3856	0.2479	0.0813	0.1860	7.75	0.3262	0.2821	0.1911
	0.1123	0.0831							
8.00	0.4649	0.3812	0.2482	0.0780	0.1867	8.00	0.3263	0.2823	0.1912
	0.1117	0.0820							
8.25	0.4581	0.3766	0.2484	0.0751	0.1902	8.25	0.3261	0.2823	0.1913
	0.1112	0.0808							
8.50	0.4528	0.3725	0.2484	0.0729	0.1956	8.50	0.3257	0.2822	0.1914
	0.1107	0.0797							
8.75	0.4496	0.3694	0.2483	0.0716	0.2018	8.75	0.3253	0.2820	0.1915
	0.1103	0.0789							
9.00	0.4484	0.3675	0.2480	0.0712	0.2077	9.00	0.3249	0.2818	0.1916
	0.1101	0.0783							
9.25	0.4490	0.3668	0.2477	0.0714	0.2123	9.25	0.3246	0.2816	0.1916
	0.1100	0.0780							
9.50	0.4506	0.3670	0.2473	0.0720	0.2154	9.50	0.3243	0.2814	0.1917
	0.1100	0.0780							
9.75	0.4525	0.3678	0.2470	0.0726	0.2166	9.75	0.3242	0.2813	0.1917
	0.1101	0.0781							
10.00	0.4540	0.3688	0.2468	0.0730	0.2162	10.00	0.3241	0.2812	0.1917
	0.1102	0.0784							

5. References

1. Wetherell, W.B., In “Applied Optics and Optical engineering”, Vol. VIII Academic, Press, New York, Editors. R.R. Shamon, and, J.C. Wyant). p.212, 272,215,202,207, 209, (1980).
2. Dossier, B., Rev. Opt., 33, 57, 147 and 267 (1954).
3. Surendar, K., Ph. D Thesis, Osmania University, Hyderabad, India (1986).
4. Rayleigh Lord, Phil. Mag. 8, 261 (1879).

5. Murty, P.V.V.S., P.32, in Thesis entitled “Studies On Diffracted Field and Imaging Charecteristics of Optical Systems with Cosinusidal Apodisation Filters” presentedto Osmania University, for Ph.D (1992).
6. Karunasagar, D., P. 62, Ph.D, Thesis” Studies on the Performance of Optical Systems apodised with generalized Hanning amplitude filters (2003).
7. C.V. Ratnam, “Fourier Analytical Investigations on The performance of Multiple- Annuli coded Apertures in Multiplexed Tomography”, Ph.D. Thesis Thesis, Osmania University, Hyderabad, India, (2005).
8. Steel,.W.H., Opt. Acta. 3, 65 (1956).
9. Mehta, B.L., Atti Fond. G. Ronchi, 30, 17 (1975).
10. Surendar, Sheshagiri Rao., Mondal, P.K., Acta Cienca Indica 18, p.6134 (1992).
11. Keshavulu, Ph.D. Thesis Osmania University. India (2001).
12. V.N. Mahajan, “Diffraction Theory of Optical Images and Aberrations”, Part-II, SPIE Press, Massachusetts, U.S.A. (2004).
13. P. Thirupathi, Vol. 3 (6). Pp.3935-3943., Advances in applied science And research (2012).

Structural and Magnetic properties of Mg Ferrite

D.Ravi Kumar[a], B.Kiran Kumar[a], Ch.Abraham Lincoln[a*], D.Ravinder[b]
a. Dept of chemistry, University College of science, Osmania University Hyderabad-7, India.
b. Dept of Physics, University College of science, Osmania University Hyderabad-7, India.
*Corresponding author email: chal_lincoln@yahoo.com.

ABSTRACT:

Mg Nano ferrite has been synthesized by the citrate gel auto combustion method, in this method citric acid used as chelating agent. Synthesized powder were calcinated at 500^{o}C for four hours in the air and characterized by XRD, SEM and EDS. XRD analysis shows that the cubic spinal structure of the spinel ferrite and the crystalline size (D) were found 34 nm. Scanning Electron Microscopy (SEM) studies revealed that the Nano nature of the compound. An elemental composition of the sample was studied by using Energy Dispersive Spectroscopy (EDS). FTIR studies reveal that the tetrahedral and octahedral of the sample it has the spinel structure of the sample. Magnetization measurements were obtained at room temperature by using pulse field hysteresis loop technique, which showed that the calcinated sample exhibited super paramagnetic behavior.

Keywords: Citrate gel auto combustion method, XRD, SEM, EDS, FTIR, VSM.

Introduction

Spinel ferrites with the general formula AFe2O4 (A = Mn,Co, Ni, Mg, or Zn) are very important magnetic materials because of their interesting magnetic and electrical properties with chemical and thermal stabilities [1]. Magnesium ferrite (MgFe2O4) is one of the most important ferrites. It

has a cubic structure of normal spinel-type and is a soft magnetic n-type semiconducting aterial, which finds a number of applications in heterogeneous catalysis, adsorption, sensors, and in magnetic technologies [2]The ordered magnetic materials such as nanorods and nanowires have

Currently attracted a great interest due to their enhanced magnetic property [3,4] Spinel magnesium ferrite possesses many attractive properties like high catalytic

activity, high magnetic permeability, humidity and gas sensing characteristics. Moreover, Mg ferrite has high resistivity, high Curie temperature, and environmental stability makes it most suitable candidate for wide range of sensing applications [5, 6].

Experimental method

Mg ferrite nanoparticles were prepared by citrate gel auto combustion method using a nitrates of $Mg(NO_3)_26H_2O$,$Fe(NO_3)_29H_2O$ and citric acid used as chelating agent, all these are dissolved in double distilled water, P^H maintained 7 with ammonia solution. Obtained powder was calcinated at 500^0C. Further the powder was characterized to XRD SEM EDS FTIR and magnetic properties.

Chemical Reaction:

$Mg(NO_3)_26H_2O + 2Fe(NO_3)_29H_2O + C_6H_8O_7H_2O$ ------>$MgFe_2O_4 + 29H_2O + 4N_2 + 6CO_2 + 5.5O_2$

Synthesis flow chart:

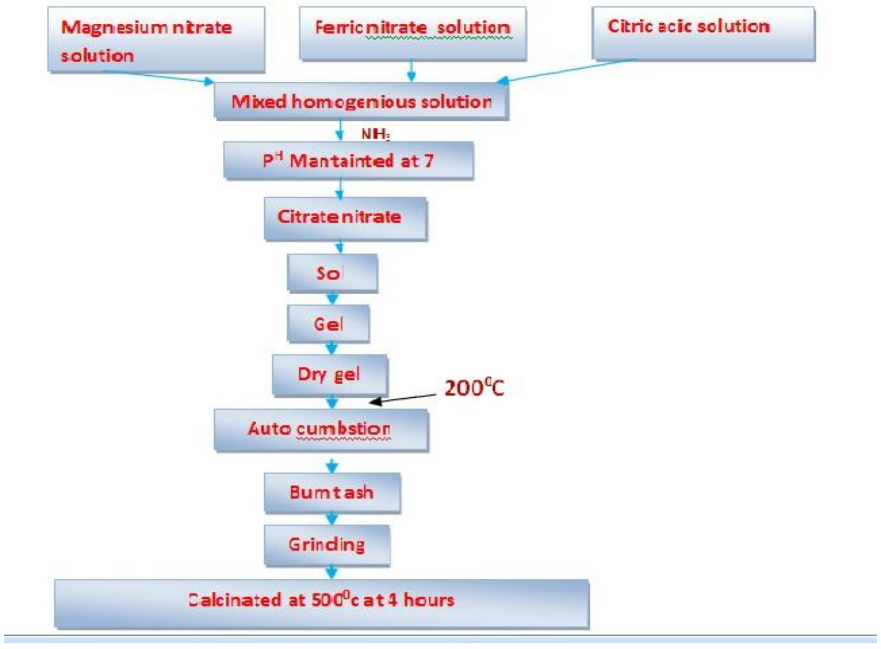

Figure 1.Flow chart of citrate gel auto combustion.

Results and Discussions:

XRD studies:

The powder x-ray diffraction of the prepared sample has been recorded to identify the crystalline phases present in the sample. From the XRD patterns the lattice parameter, particle size, x-ray density and unit cell of $MgFe_2O_4$ has been determined. The crystallite size (D) was calculated for all the composition using maximum intensity peak from Scherrer's formula [7].

Crystallite size $D = 0.91\lambda/\beta Cos\theta$

Where λ = wavelength of X-Ray;

β = Full width half maximum (radians);

θ = Bragg's angle at the peak position

Crystalline size is 34.54 nm.

Lattice parameter (a) of the individual composition was calculated by using the following formula

$a = d * \sqrt{h^2 + k^2 + l^2}$

Where a = lattice parameters*; d* = inter planar spacing and h k l are the miller indices lattice parameter is 8.35 nm.

The X-Ray density (dx) is calculated using the following formula [8]

X-Ray density $(dx) = 8M / Na^3 (gm/cc)$

Where M = molecular weight of the sample , N = Avogadro's number, a = lattice parameter, X ray density is 4.52 gm/cm3.

The Volume of the unit cell is calculated as $V=a^3$ unit cell is 583.438 A^o.

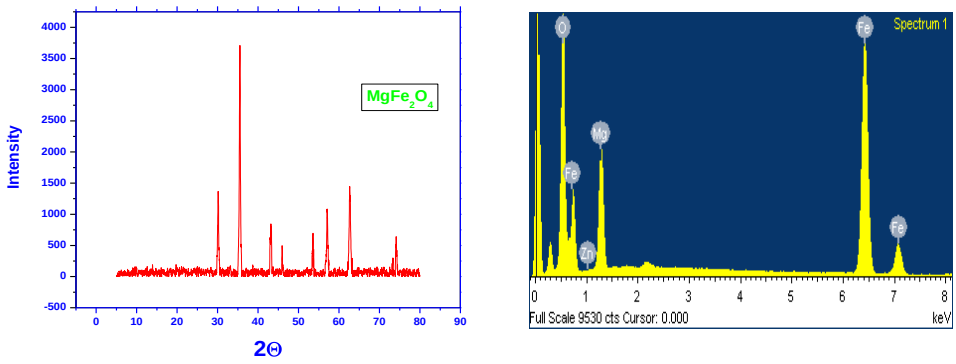

Figure 2.XRD patterns of MgFe2O4 .

SEM And EDS

SEM technique was used to study the morphology of the $MgFe_2O_4$ samples. SEM images of the Magnesium ferrite sample have given in below Fig 3. The micrographs show the presence of particles that are agglomerated together. A close inspection would reveal the presence of particles showing cubic faces. The distribution of particles is uniform and it can be seen that the particles are well below the size of 100 nm, which supports our prediction of grain size determined using Scherrer's formula

The composition of the MgFe2O4 has been determined by the EDS and the patterns obtained are shown in Fig 3. The specimen shows the presence of Mg, Fe, and O in the sample and did not contain any other elements.

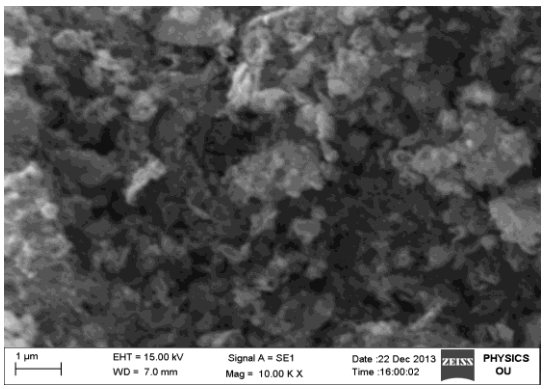

Figure 3.SEM and EDS pattern of MgFe2O4 .

FTIR

The FTIR spectra of the prepared sample are shown in bellow fig. the inspection of FTIR spectra shows two absorption bands as a common feature of the spinel ferrites. The band position is V1 and V2. The high frequency band V1 is assigned to intrinsic vibration of the tetrahedral groups and low frequency band V2 is assigned to the octahedral (10-11). The difference in the band position is expected because of the difference in the Fe^{+3} O^{-2} distance from octahedral and tetrahedral complexes.

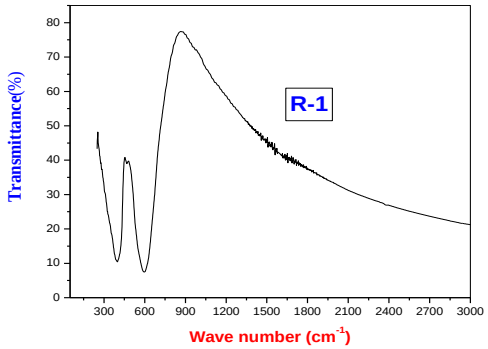

Figure 4.FTIR patterns of MgFe2O4.

Magnetic properties:

To understand the magnetic properties of nano ferrite, it is characterized using vibrating sample magnetometer (VSM). The hysteresis loop traced at room temperature for $MgFe_2O_4$ is shown in Fig. 5. The values of the saturation magnetization (Ms), coercivity (Hc) and remnant magnetization (Mr) are obtained. Figure 5. shows the characteristic hysteresis loop of the typical sample of $MgFe_2O_4$ sample recorded at room temperature. saturation magnetization (Ms) is a 79.59 (emu/g), coercive force[Hc] is a 137.09 (Oe), remnant magnetization (Mr) is a 19.09 (emu/g). The hysteresis loop explains the soft ferri magnetic nature of the synthesized $MgFe_2O_4$.

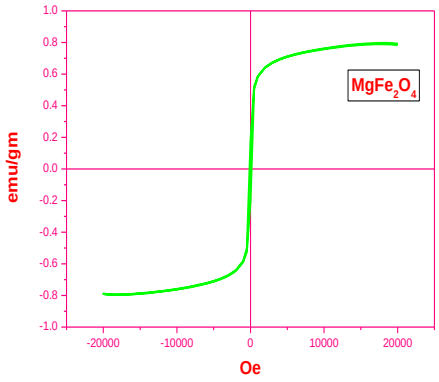

Figure 5.VSM patterns of $MgFe_2O_4$.

Conclusions:

- Nano structures of MgFe2O4 have been successfully synthesized by citrate gel auto combustion method.
- In fact, XRD measurements display the formation of magnesium ferrite, MgFe2O4, as a single phase.
- SEM micrographs of the composition indicate the morphology of the particles is similar. They reveal largely agglomerated, well defined nano particles of the sample powder within homogeneous broader grain size distribution.
- EDS data give the elemental % and atomic % in the magnesium ferrites and it shows the presence of Mg, Fe and O without precipitating cations.
- FTIR studies reveal that tetrahedral and octahedral of the spinel ferrites characterization.
- Vibrating sample magnetization studies reveal that the ferromagnetic materials.
- We believe that the $MgFe_2O_4$ could have potential in some new applications as ferromagnetic for nano composites, separation, anodic material in lithium ion batteries, catalysts, and as electronic material for nano devices and storage devices.

Acknowledgement

Authors thankful to Prof. G.Venkateswarlu, Head, Dept of Chemistry, and Prof M.vittal, BOS, University College of Science, for their support & encouragement to carry out this research work and to the characterization of XRD facilities to the lab.

References

1. R. Valenzuela, Magnetic Ceramics (Cambridge University Press, Cambridge, 1994)
2. R.J. Willey, P. Noirclerc, G. Busca, Chem. Eng. Commun. 123, 1 (1993). doi:10.1080/00986449308936161
3. Z.H. Hua, R.S. Chen, C.L. Li, S.G. Yang, M. Lu, X.B. Gu, Y.W.Du, J. Alloys Compd. 427, 199 (2007). doi:10.1016/j.jallcom. 2006.02.048
4. G. Ji, S. Tang, B. Xu, B. Gu, C. Du, Chem. Phys. Lett. 379, 484(2003). doi:10.1016/j.cplett.2003.08.090
5. S.A. Oliver, R.J. Willey, H.H. Hamdeh, G. Oliveri, G. Busca, *Scr. Mater.* 33 (1995)1695.
6. G. Busca, E. Finocchio, V. Lorenzelli, M. Trombetta, S.A. Rossini, J. Chem. Soc. Faraday, Trans. 92 (1996) 4687.
7. M.J. Iqbal; m.N. Ashiq; P. Hernandez-Gomezb; J.M. Munoz, *J. Magn. Magn. Mater.*2008, 320, 881.Doi:10.1016/j.jmmm.2007.09.005
8. B.Viswanatham; V.R.K. Murthy; Ferrie Materials: Science and Technology, Narosa Publishing House, 1990,4.
10. R.D.Waldron, phys.Rev.99(1955) 1727
11. S.T.Hafner Z.Fur.Krist.115(1961) 331

A study on Infrared Spectroscopy of Human Blood

U. Vijaya Ushasree, Kaleem Ahmed Jaleeli & Adeel Ahmad
Biophysics Reasearch Laboratory, Department of Physics, Nizam College (Autonomous), Osmania University, Hyderabad – 500 001, India
e. mail: dr_adeelahmad@yahoo.com sunilusha999@gmail.com

ABSTRACT

The paper reports IR spectroscopic data on human blood and its constituents. IR analysis has been made on whole blood, plasma and serum. The characteristic spectral bands pertaining to fibrinogen, hemoglobin, erythrocyte membrane lipids and other plasma proteins are identified. The paper explores the possibility of disease analysis by IR spectroscopy.

Key words: FTIR spectroscopy; Human blood; Plasma; Blood Serum.

1. Introduction

In recent past, mid infrared and UV - Visible spectroscopic methods were efficiently used in the fields of biological sciences [1, 2]. Implementation of these techniques reduces time, resources and cuts cost. IR spectroscopy is emerging as a potential diagnostic tool in the medical and pharmacological fields to provide information about the different chemical structures of healthy and pathological tissues [3]. Blood being the chief circulatory medium of our body, reflects the physiological and pathological changes that take place in the tissues, which leads to the changes in the various plasma, serum and cellular constituents. In view of this, an attempt is made to analyse human blood spectroscopically in the IR range.

2. Materials and Methods

2.1. Sample collection

Collection and handling of a sample is an integral part of obtaining valid results. Here a disposable plastic syringe was used to collect venous blood. Blood samples were collected from healthy volunteers. Blood collection tubes with anticoagulant (EDTA- Ethylene Diamine Tetra Acetate) were inverted gently as soon after collection as possible to prevent clotting. The blood samples were brought to the

laboratory in siliconized bottles, keeping them in ice cooled thermos. The samples were kept in refrigerator at 4^0C until used. Investigations were done within two to three hours after collection.

2.2. Preparation of sample

First, spectral grade pure KBr powder was dried in an oven upto 60^0c for 24 hours. Then 1 gm powder was taken in an agate motor and was ground until it becomes fine powder. The ground powder was mixed with blood sample and transferred into the cylinder bore so that it was distributed across the polished face of lower plate. The polished face of the second plate towards the powder was inserted in to the bore by a plunger. The die assembly was connected to a vacuum pump and was kept under vacuum for approximately 2 min so as to remove air from the sample disk. The die was dismantled and the KBr disk was removed without touching its faces. Here, FTIR spectrometer of make *Bruker Optics* and model *Tensor 27* was used.

3. Results and Discussion

Fig.1.presents FTIR spectrum of Human blood, which reveals a series of bands with different intensities and the spectral data is shown in Table 1. For the systematic analysis, IR spectrum is divided into three regions. Region I is from 4000 to 3000 cm^{-1}, concerned with water and hydroxyl group. This region is of considerable interest, because it reveals the nature of hydrogen bonding. Region II is 3000 to 1500 cm^{-1}, wherein bands for functional groups are observed. In this region, major IR absorption pertaining to fibrinogen occurs. Region III is 1500 – 200 cm^{-1}, which has significant importance in the context of biological minerals and their combinations.

The spectra of human blood indicate the presence of bands characteristics of water molecule and also of some functional groups concerned with proteins and lipids. The IR band at wave numbers 3294 cm^{-1} and 3065 cm^{-1} are related to Amide A and Amide B respectively. The dominating band at 1396 cm^{-1} may be originated due to the important protein of blood Fibrinogen. This band is related to the stretching C=O symmetric stretching vibrations of COO^-. A band around 2960 cm^{-1} is due to the -C-H asymmetric stretching of $–CH_3$ in Fatty acids, Phospholipids,

Cholesterol esters. The band at 1106 cm^{-1} is related to HbO_2, exhibits $\nu_{(O2)}$ bond. The two most intensive bands are centered at 1652 cm^{-1} and 1547 cm^{-1} in the FTIR spectrum of human blood. They correspond to the Amide I and Amide II. Both bands are representative of secondary structures of proteins. Amide I peak arises from C=O hydrogen bonded stretching vibrations, and Amide II is attributed to C-N stretching; NH and CH_2 bending modes. Amide I and Amide II absorption bands are associated also with specific secondary sub- structures, such as α-helix, β-sheet, β-turn and random coil. The bands at 1307 $cm^{-1}$and 1248 cm^{-1} are related to Amide III bond components of proteins (C-N). The band at 1170 cm^{-1} corresponds to C-O-C asymmetric stretching vibrations of phospholipids. The bands at 1106 cm^{-1}, 1170 $cm^{-1}$and 1248 cm^{-1} are associated with triglycerides of human blood. The band at 2936 cm^{-1} is related to platelets due to -C-H symmetric stretching of $–CH_2$

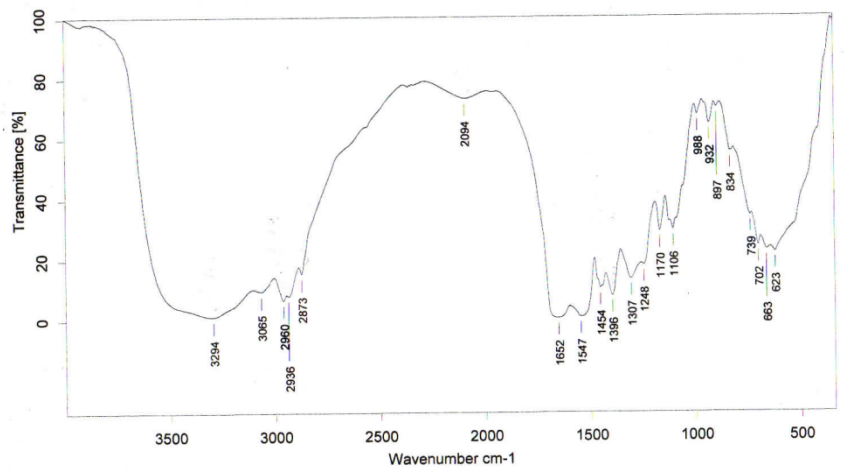

Fig. 1. FTIR spectra of human blood

Table 1 FTIR spectral data of human blood

Wave Number (cm^{-1})	*Characteristic vibrations of functional groups*
3294	Amide A, N-H stretching of proteins
3065	Amide B, N-H stretching
2960	-C-H asymmetric stretching of $–CH_3$ in **Fatty acids**, **Phospholipids**, **Cholesterol esters**
2936	-C-H symmetric stretching of $–CH_2$, **Platelets**
2873	-C-H symmetric stretching of $–CH_3$
2094	
1652	Amide I. – helical structures (C=O)

1547; 1454	Amide II Peak region – Protein (NH, C-N) CH_2 bend
1396	C=O symmetric stretching vibrations of COO^-, **Fibrinogen**
1307, 1248	Amide III band components of proteins (C-N)
1170	C-O-C asymmetric stretching vibrations of phospholipids
1106,	HbO_2 exhibits $\nu_{(O2)}$ band, **Oxy hemoglobin**
1106, 1170, 1248	Triglycerides

References

[1] Sylwia Olsztyńska-Janus, Katarzyna Szymborska-Małek, Marlena Gąsior-Głogowska, Tomasz Walski, Małgorzata Komorowska, Wojciech Witkiewicz, Celina Pezowicz, Magdalena Kobielarz, Sylwia Szotek, Acta of Bioengineering and Biomechanics,Vol. 14, No. 3(2012), pp. 101 – 115.

[2] A. Barth, Infrared Spectroscopy of Proteins, Biochim. Biophys. Acta, Vol. 1767(2007), pp. 1073–1101.

[3] M. Polakovs, N. Mironova-Ulmane, A. Pavlenko, E. Reinholds, M. Gavare and M. Grube, Spectroscopy: An International Journal, Vol. 27, No. No. 5-6 (2012), pp. 367-371

Electrical Studies In Silver Doped Gallium Oxide Glasses

K. Veerabadra Rao, C. Anuradha, G.Aravind
Department of Physics, Methodist College of Engineering & Technology, Hyderabad

ABSTRACT: The glasses of composition xAgI-(100-x)[0.02Ga_2O_3-0.49Ag_2O-0.49B_2O_3] where x=5 to 30 in steps of 5 weight% are prepared by melt quenching technique. XRD, FTIR and DSC investigations are carried out on all glasses to understand physical characteristics of the prepared glasses. Electrical characterization is done in terms of DC and AC conductivities.DC conductivity at room temperature increased from $10^{-4}$to 10^{-2} Scm^{-1} with increasing concentration of AgI. DC activation energy (E_{dc}) is found to decreasefrom 0.36 to 0.19eV with increasing concentration of AgI.From the Impedance spectroscopy real and imaginary parts of impedances (Z', Z'') plotsplotted, and by using Z-View equivalent software R-C circuit parameters are obtained from Cole-Cole plots and relaxation times also calculated. The quantitative analysis of these results indicates that the electrical conductivity of these glasses is enhanced by addition of AgI.

Keywords: Electrical properties, oxide; Ga_2O_3 , Ag_2O, XRD

1. Introduction

Portable electronic devices, omnipresent nowadays, requiresmall-size power sources which should be more efficient,durable, reliable and safer for the environment than those availablenow. To meet growing and urgent needs for such powersources it is vital to carry out the research on many prospectiveideas: miniaturized fuel cells, rechargeable microbatteries,etc. One of specific tasks in this research is the development ofsolid electrolytes (polycrystalline, amorphous or composite) forrechargeable silver microbatteries [1,2].Though the ionic conductivity of many silver glasses, especiallythose with high contents of AgI, can be suitable for batteryapplications at moderate temperatures, some disadvantages ofthose glasses such as, e.g. their brittleness or low thermal stabilitythreshold, limit the prospects of their practical use. One ofpossible solutions to circumvent the drawbacks of glassy electrolytesis to produce composites based on these glasses. Therehave been already explored several interesting approaches toprepare composites based on AgI and

other components, e.g.confining AgI particles in pores of porous alumina [3], elaborating systems containing AgI and Al_2O_3 xerogels and aerogels [4] or 'sintered' mixtures of AgI and alumina powder [5].

Several electrical studies on glassy materials revealed that glasses under certain circumstances can be super ionic conductors [1–3]. These glassy materials are of technological interest in view of their applications such as biosensors, storage batteries and fuel cells etc.,. The conductivity depends on the nature and content of the modifier oxide and also glass former compositions [4, 5]. The incorporation of alkali halides or metal halides in to the mixed glass formers [6, 7] is considered to be predominant factor playing the role of enhancing the conductivity of the conventional glasses to reach the values of super ionic materials.The nature of the interaction between metal ions (Ag^+) and amorphous molecules is usually studied by different techniques. The structure and the electrical properties of silver ion-conducting borate-based glasses have been reported in the literature [8, 9]. Borate glasses exhibit well-known and unique structural features. The fast ion conducting glasses are characterized by greater freedom of movement of Ag^+ ions. The mobility of Ag^+ ions associated with an iodide environment is considered to be higher and based on the fact that increase in the percentage of AgI in the glass gives rise to higher conductivities [10-12]. One of the most widely used glass formers for the synthesis of super ionic conducting glass is B_2O_3.

It has been observed that in many cases the conductivity can be enhanced by mixing two different glass formers [10-15] with different coordination polyhedrons. But such mixtures have a strong tendency to phase separation at low modifier oxide molar ratio. Therefore, the complete substitution of one network former by another one has not always been possible [11].Electrical conductivity investigation on AgI–Ag_2O–Ga_2O_3–B_2O_3glass systems have been started recently. They also exhibit high ionic conductivity on suitable modifications of the network [16-18]. Correlation between structural properties and electrical behavior and electrical transport mechanisms is scanty in literature. So an attempt is made to fill the gap.

The present study aims to investigate the conductivity of the glasses containing high conducting electrolyte material such as AgI and Ag_2O by changing

the concentrations of AgI (dopant salt) with [$0.02Ag_2O–0.49Ga_2O_3–0.49B_2O_3$]. Silver oxide has been chosen as a network modifying oxide, since silver ions possess high ionic conductivity compared to alkali modifying cations such as Li^+ ion. The DC and AC conductivity studies provide significant information on the transport mechanism of the materials at room temperature as well higher temperatures, which in turn are aimed to correlate with the battery characteristics in future. AC conductivity is one of the common methods to characterize the bulk resistance of glasses. In the present investigation complex impedance measurements are used to study AC conductivity.

2. Experimental

2.1. Sample Preparation

xAgI-(100-x)[$0.02Ga_2O_3$-$0.49Ag_2O$-$0.49B_2O_3$] where x=5 to 30 in steps of 5 weight% are prepared by melt quenching technique. Sample with x=5 is termed as Ga-1 and sample with x=10 is termed as Ga-2 and so on. Starting compounds AgI, Ag_2O, B_2O_3 and Ga_2O_3 are taken according to their molecular weight percentage (mol.wt.%) and mixed thoroughly in a porcelain crucible. This mixture is heated gradually to 850°C and maintained at that temperature for about 30 min. The melt was poured onto a stainless steel plate and pressed with another plate to obtain a thin disc (0.1–0.15 cm in thickness). For XRD, FTIR and DSC studies the obtained glasses are crushed into fine powders using pestle and mortar. All the samples are characterized by using XRD, FTIR, DSC and electrical characterization is done by impedance spectroscopy over a frequency range of 20Hz-3MHz and between room temperature (RT) and 573K.In the present investigation, X-ray diffraction measurements were carried out for all the samples using Philpsx'pert pro with Cu K_α-radiation of wavelength λ =1.5418Å between $10^\circ$and $90^\circ$of 2θ. The FTIR spectra for all the samples are recorded on BRUKER (**Model:** TENSOR 27) FTIR spectrometer. Pellets made with the mixture of Ga powder and KBr are used to record FTIR spectra in the range of 400–4000 cm^{-1} with 4 cm^{-1} resolution. All Ga samples were also characterized by differential scanning calorimeter (DSC-Q20) of Mettler make with a heating rate of $10Kmin^{-1}$.

2.2. Electrical Characterization

For DC and AC characterization pellets of the glass samples (dia=1cm, thickness=1.5 mm approximately) both sides painted with silver for better electrode contact were used. For DC conductivity measurement the pellets were sandwiched between two spring loaded stainless steel blocking electrodes of surface area 3.14 cm^2. The sample holder is placed in a thermostat controlled furnace and temperature is varied from 30^0C to 300^0C (573K). DC conductivity measurements were carried out using Keithly 6485 pico ammeter in the temperature range of 303-573K for all Ga samples.

For AC electrical conductivity, impedance measurements were carried out by Waynekerr LCR-6440B impedance analyzer from 20 Hz to 3MHz over the temperature range of 303–573K for all Ga samples. The impedance data was analyzed by nonlinear curve fit method, and from those curves AC conductivity, activation energy, RC values and relaxation values were calculated.

3. Results and Discussions

3.1. XRD

The structural studies of the samples were analyzed using X-ray diffraction. XRD is extensively employed as a powerful characterization for determination of crystallographic structure of the materials. It gives the information regarding the lattice parameters, crystal structure and orientation, defects and ctrystallite size of the nanoparticles. In this investigation, PHILIPS Xpert X-ray diffractometer with CuK_α radiation source was used for determining the amorphous nature of the samples. Fig. 1 shows the XRD spectra of all the compositions of Ga glasses prepared by melt quench technique and the absence of any sharp peak confirms that all the samples are amorphous in nature.

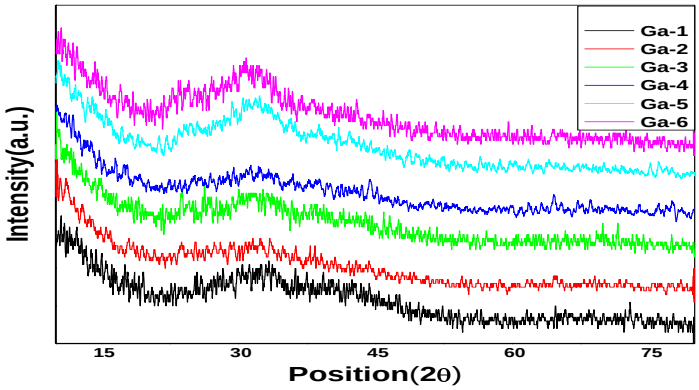

Fig. 1.XRD patterns of Ga glasses

3.2. Differential Scanning Calorimetry (DSC)

DSC thermo grams of different samples are shown in Fig.2. Glass transition temperature (T_g) is identified from DSC curves of each former composition of Ga samples andthese values are observed to decrease from 380^0C to 352^0C with increasing the concentration of AgI.

The glass transition is a measure of strength of the glass, the observed fact that the glass transition temperature (T_g) decreases with the increasing AgI content in Ga system may be due to the fact that more and more number of bonds are destroyed within the glassy network, in order to allow its rearrangement to form a thermodynamically stable phase. This addition of AgI made samples more and more amorphous.this is observed and shown in Fig 3.

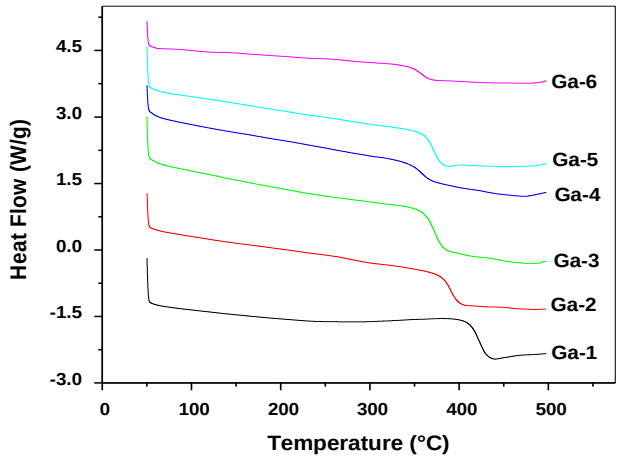

Fig. 2.DSC Curves of the all samples Temperature vs Heat Flow

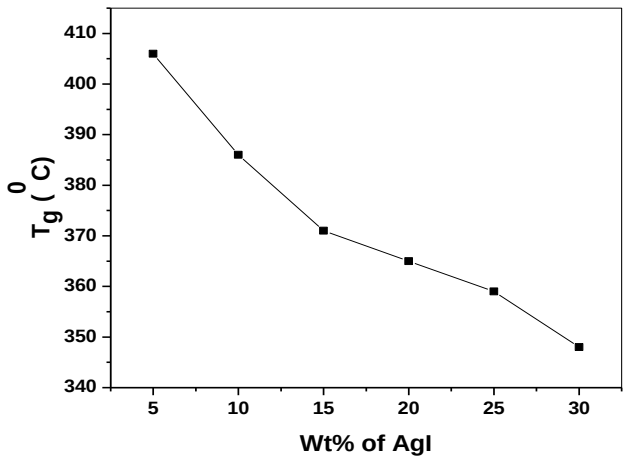

Fig. 3. Variation of glass transition temperature with AgI wt.%

3.3. Density

Table-1.AC conductivities and activation energies for all samples at room temperature

SNo.	Sample Name	Density
1	Ga-1	4.6024
2	Ga-2	5.2380
3	Ga-3	5.5097
4	Ga-4	5.7333
5	Ga-5	6.1546
6	Ga-6	6.3073

From the above table we conclude that as increase the concentration of dopant salt density increases, this indicates that strengthening of the glass increases.

3.5. ACConductivity

Impedance spectroscopic technique utilizes alternating current (AC) with variable frequency and when measurements are carried out as a function of frequency and temperature, it is possible to determine the activation energies of the conduction and dielectric relaxation process. Variation of real part of impedance (Z') with imaginary part of impedance (Z'') at different temperatures for Ga-1, Ga-6 samples is represented in Fig.5(a) & (b) respectively. From these plots it is observed that the intercept of the semi-circle with the real axis at lower frequency shifts towards the higher frequency with increase in temperature. The intercept of the semi-circle at lower frequency with the real axis gives the equivalent DC resistance (bulk resistance-R_b) for each composition and at each temperature. DC resistance decreases with increase in temperature.

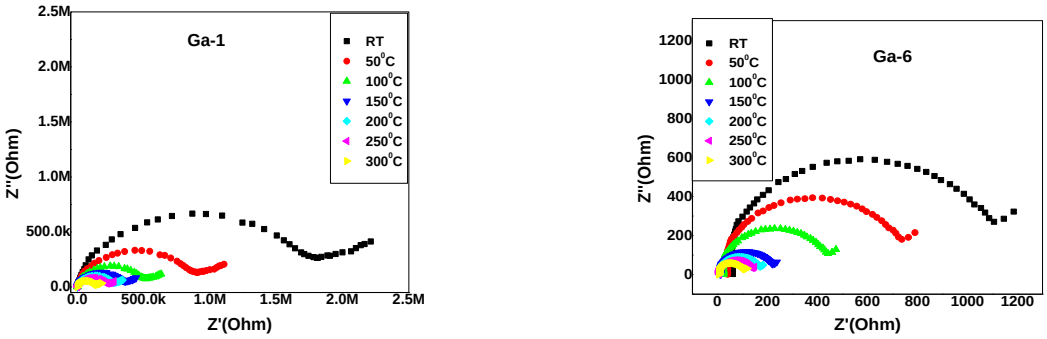

Fig. 5 (a) & (b). Cole-Cole plots of Ga-1 and Ga-6 samples at different temperatures

Variation of real part of impedance (Z') with frequency at different temperatures for Ga-1, Ga-6 samples is represented in Fig.6(a) & (b) respectively. It is observed that real part of impedance (Z') is both frequency and temperature independent up to about 300 kHz.

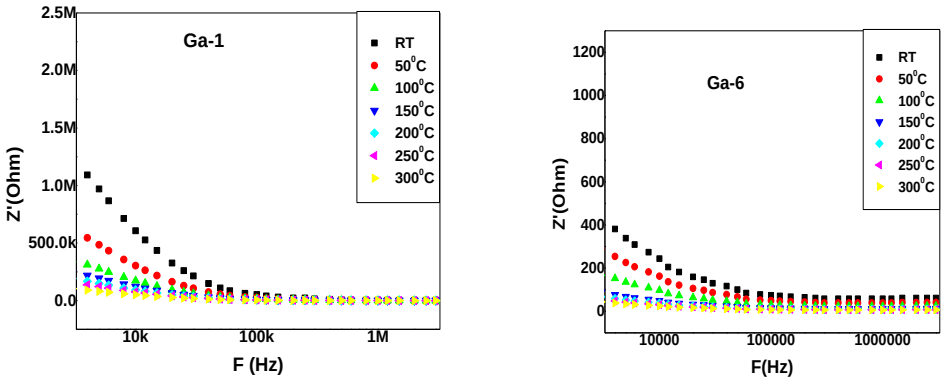

Fig. 6 (a) & (b). Cole-Cole plots of Ga-1 and Ga-6 samples at different temperatures

Variations of value of Imaginary impedance (Z") with frequency at different temperatures for Ga-1, Ga-6 samples are represented in Fig. 7(a) & (b). It is observed that imaginary part of conductivity increases with the increasing the temperature at higher frequency region, and merged at lower frequencies for all temperatures.

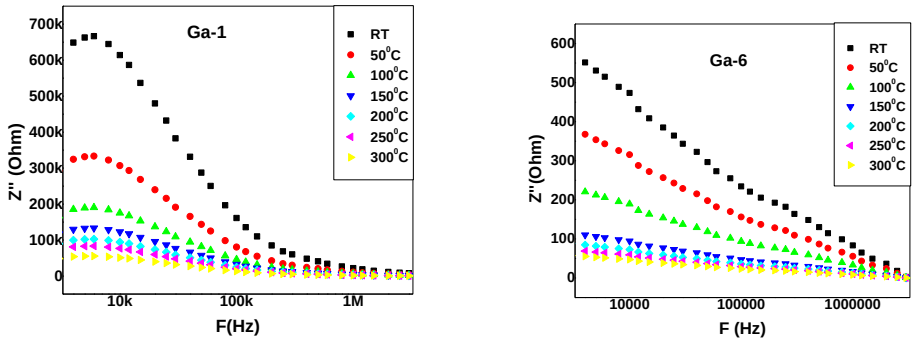

Fig. 7(a) & (b). Cole-Cole plots of Ga-1 and Ga-6 samples at different temperatures

DC conductivity values are found to vary between 10^{-5} Scm^{-1} (Ga-1) to 10^{-3} Scm^{-1} (Ga-6) at room temperature. It is observed from Fig. 8(a) the AC conductivity increased with increase of temperature. Higher temperatures favour the conduction in Ga glasses. DC conductivity increases with increasing AgI concentration, hence this favour the conduction in Ga glasses. Activation energies were calculated from Arrhenius equation. From Fig. 7(b) it is observed that AC activation energy decreases with increasing AgI concentration from 0.86 to 0.29eV. These values are

given in Table 2. Decrease in AC activation energy depends on increase in temperature at selected frequency. This behaviour is a characteristic of conductors with hopping charge carriers.

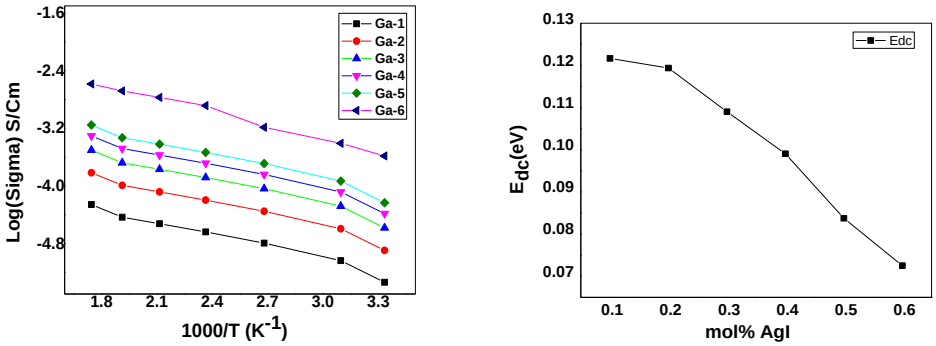

Fig.8 (a) & (b). Cole-Cole plots of Ga-1 and Ga-6 samples at different temperatures

Table-2.DC conductivities and activation energies for all samples at room temperature

SNo.	Sample	σ_{dc}(S/Cm) RT(303K)	E_{dc} (eV)
1	Ga-1	$5.80x10^{-5}$	0.86
2	Ga-2	$6.80x10^{-5}$	0.77
3	Ga-3	$2.80x10^{-4}$	0.72
4	Ga-4	$8.30x10^{-4}$	0.68
5	Ga-5	$6.94x10^{-4}$	0.59
6	Ga-6	$1.23x10^{-3}$	0.53

The migration of mobile ions is described by the relaxation times. These values are tabulated in Table 2. We can observe from the table, relaxation time decreases with increase in temperature means that the relaxation frequencies are increasing.Observation of semi-circle in these plots indicates thatthe samples are parallel combination of a resistance and a capacitance, which are respectively, the bulk resistance R_b and the bulk capacitance C_b of the solid electrolyte [19-20]. The straight line observed as a tail at the low frequency region represent a capacitance effect at the electrode and electrolyte interface and it is called double layer capacitance (C_{dl}). Further the inclination of this tail in the low frequency region is due to the presence of the asymmetric nature of the distributed elements in the

electrode and electrolyte interface. Relaxation time τ of the distributed elements at the interface is not a single valued, but it is distributed continuously around a mean value [20]. The amount of the inclination in the low frequency straight line is related to the width of the relaxation time distribution.

Table -3. Variation of Resistance, Capacitance and relaxation time values with temperature for Ga-1, Ga-6 samples

Temperature	Ga-1			Ga-6		
	R_b(ohm)	C_b(nf)	τ(ms)	R_b(ohm)	C_b(nf)	τ(ms)
303K	396597	0.671	0.13	31120	6.39	0.13
323K	278721	0.762	0.098	20754	7.67	0.099
373K	157842	1.445	0.072	7788	17.05	0.073
423K	76245	2.023	0.056	4447	23.87	0.057
473K	30487	3.145	0.042	2784	33.42	0.042
523K	10784	4.864	0.027	1435	42.12	0.037
573K	5872	5.735	0.011	874	48.17	0.017

3.6. Cole-Cole plots of all samples at room temperature and at higher temperature

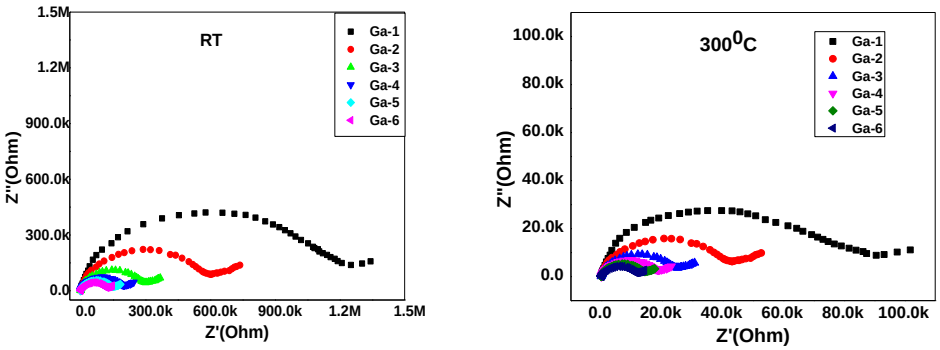

Fig.8 (a) & (b). Cole-Cole plots of Ga-1 and Ga-6 samples at different temperatures

From above plots we can observed that the conductivity is maximum for Ga-6 which is highest dopant of AgI at room temperature and at highest temperature and the conductivity increases with increasing temperature and with concentration also and in below graphs we presented varitaion of frequency with imaginary impedance for all samples at room temperature and at (300^0C) 573K.

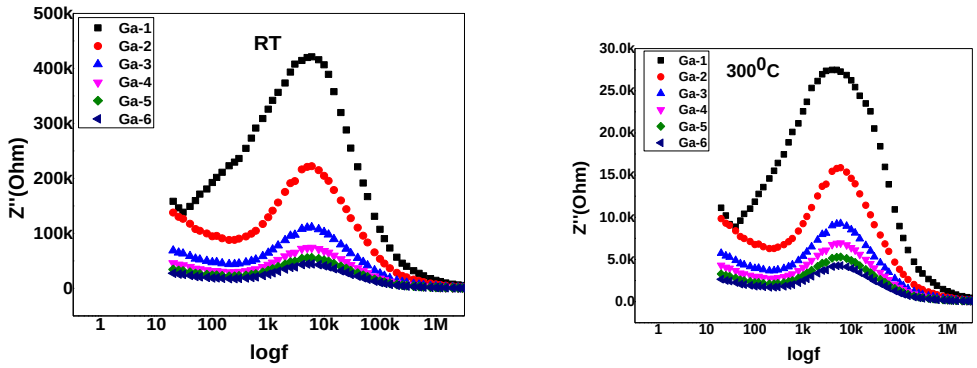

Fig. 9 (a) & (b). Cole-Cole plots of Ga-1 and Ga-6 samples at different temperatures

Conclusions

The glassy nature of all former compositions of prepared Ga samples by melt quenching method is confirmed from X-ray diffractogram spectra. Peak assignments obtained from FTIR spectra. DSC spectra confirm the glassy nature.The decrease in glass transition temperature indicates the strengthening the glass increases with increasing dopant salt. Similar nature is observed in density. AC conductivity plots show the presence of relaxation.Impedance spectroscopy also reflects the involvement of conducting ions. This confirms hopping of charges between the coordinating sites, local structural relaxation and segmental motion of chains. Even the FTIR, DSC results supports that increase of AgIconcentration favor better amorphous network in Ga glasses.

The fast ion conducting glasses are characterized by greater freedom of movement of Ag^+ ions because these ions are not held in the lattice sites or anion cages firmly. Hence addition of network modifier such as AgI introduces ionic bonds usually associating non-bridging oxygen ions with modifying cations.

REFERENCES

1. N. Baskaran, G. Govindaraj, A. Narayanasamy, J. Power Sources 55 (1995) 153–157.
2. Y.-G. Guo, Y.-S.Hu, J.-S. Lee, J. Maier, Electrochem. Commun. 8 (2006) 1179–1184.
3. M. Nagai, T. Nishino, J. Mater. Synth.Process. 6 (1998) 197–201.
4. K. Tadanaga, K. Imai, M. Tatsumisago, T. Minami, J. Electrochem. Soc.147 (2000) 4061–4064.
5. N.F. Uvarov, P. Vanek, M. Savinov, V. Zelezny, V. Studnicka, J. Petzelt, Solid State Ionics 127 (2000) 253–267.
6. El-Damrawi G, (1994) J Non-Cryst Solids 176:91
7. Stangrennec MK, Elliott SR (1994) Solid State Ionics 73:199
8. Saunders GA, Metcalfe RD (1996) Phys Rev B 53:53
9. Ingram MD (1987) PhysChem Glasses 28:215
10. Magistris A (1993) In: Scrosati B, Magistris A, Mari CM, and Mariatto G (eds) Proceedings of the Nato advanced research workshop on fast ion transport in solids. Kluwer Academic Publishers, Netherlands, p 213
11. El-Damrawi G, Hassan AK, Meikail MS (1996) PhysChem Glasses 37:101
12. El-Damrawi G (1995) J PhysCondens Matter 8:1557
13. Chiodelli G, Vigano GC, Magistris A, Villa M (1983) Solid State Ionics 8:311
14. Chiodelli G, Magistris A, Villa M, Bjorkstam JL (1982)Mater Res Bull 17:1
15. Magistris A, Chiodelli G (1983) Solid State Ionics 9 & 10:611
16. Coppo D, Duclot JJ, Souquet JL (1996) Solid State Ionics 90:111
17. Shastry MCR, Rao KJ (1989) Solid State Ionics 37:17
18. Lefterova ED, Angelov PV, Dimitriev YB (2000) PhysChem Glasses 41:362
19. Jayasinghe GDLK, Bandaranayaka PWSK, DissanayakeMAKL, Gunawardane RP (1995)
20. Solid State Ionics 78:199
21. Rodrigues ACM, Duclot MJ (1988) Solid State Ionics.
22. El-Damrawi G, Abd-El-Maksoud S (2000) PhysChem
23. Rossignol S, Reau JM, Janguy B, Videau JJ, Portier J (1993) J Non-Cryst Solids 55:77

24. Jayasinghe GDLK, Coppo D, Bandaranayake PWSK, SouquetJL (1995) Solid State Ionics 76:297
25. R.J. Grant, M.D. Ingram, L.D.S. Turner, C.A. Vincent, J. Phys.Chem. 82 (1978) 2838.
26. M. Venkateswarlu , N. Satyanarayana J .Materials Science and Engineering B54(1998) 189-195.

Biosynthesis and Characterization of Silver Nanoparticles using young leaves extract of *Gymnosporia emarginata* and their antimicrobial activity

P. Shivakumar Singh[1], D.S.R. Rajender Singh[2], G.M. Vidyasagar*[3]

[1]Department of Botany, Palamuru University, Mahabubnagar-509001, Telangana,
[2]SV Govt. UG & PG College, Palem, Mahabubnagar Dist, Telangana, India.
[*3]Medicinal Plants and Microbiology Research Laboratory, Department of Post-Graduate Studies and Research in Botany, Gulbarga University, Gulbarga – 585 106, Karnataka, India.

ABSTRACT

The enlargement of eco-friendly and trustworthy processes for the biosynthesis of nanoparticles has engrossed extensive attention in nanotechnology because of its incredible impetus in modulating metals into nanosized to their impending use for human profit. In the present report the young leaves extract of *Gymnosporia emarginata* was subjected for biosynthesis of silver nanoparticles (AgNPs), the manifestation, size, and shape of the silver nanoparticles are inherent by UV-visible spectroscopy, Transmission Electron Microscopy. The X-ray diffraction studies, energy dispersive X-ray analysis indicate that particles are crystalline in nature. Fourier transform infrared spectroscopy analysis revealed that the nanoparticles are covered with bio-moieties on their surface. The biosynthesised AgNPs were screened against *Fusarium oxysporum, Fusarium semitectum, Colletotrichum gloeosporioides, Aspergillus niger, E. coli, Bacillus subtilis.* As can be seen from the present report results, the bio functionalized silver nanoparticles thus produced have shown splendid antimicrobial effect. The synthesis prescription implicated is eco-friendly, graceful and hence high range manufacture of the same can be considered for using them in many bio-pharma applications.

Keywords: *Gymnosporia emarginata* (Celestraceae), AgNPs, UV, TEM, FTIR, Phyto-pathogens.

INTRODUCTION

Remedial plants and wild edible fruits play a chief role in the originality of novel beneficial agents for drug development. *Gymnosporia emarginata* is a shrub or small tree with medicinal properties belonging to the family Celestraceae. It is

commonly known as Dantha chettu in Telugu. *Gymnosporia emarginata* is an imperative plant as its leaves have been used in wound healing [1], anthelmintic activity [2] and other pharmaceutical purposes. However, the present plant young leaves is not being used in the synthesis of silver nanoparticles and their antibacterial activity have not been under taken in research anywhere in literature. Hence, taking into account all these facts the present search has been intended to optimise the young leaves extract concentration of *Gymnosporia emarginata* for the synthesis of AgNPs and their antibacterial activity. In this study, we show that young leaves extract of *Gymnosporia emarginata*, placed in a concentrated aqueous solution of $AgNO_3$, resulted in the reduction of the silver ions and formation of silver nanoparticles, and that an extract in aqueous solution of $AgNO_3$ resulted in the reduction of the silver ions and formation of silver nanoparticles. UV-visible (UV-vis) spectroscopy, transmission electron microscopy (TEM), scanning electron microscopy (SEM), energy dispersive X-ray analysis and Fourier transform infra-red spectroscopy (FTIR) were used to examine size and shape of silver nanoparticles in aqueous extract of *Gymnosporia emarginata.*

MATERIALS AND METHODS

Collection of source material

Fresh young leaves of *Gymnosporia emarginata* were collected from Palamuru university campus, Mahabubnagar District. Silver nitrate ($AgNO_3$) is procured from High Media Laboratories. Solutions were prepared with triply distilled water.

Preparation of the young leaves extract

Weighing 25 g of *Gymnosporia emarginata* young leaves were thoroughly washed in distilled water, cut into fine pieces and was smashed into 100 ml sterile distilled water and boil plant extract 5 to 6 min& filtered through Whatman No.1 filter paper (pore size 0.45 μm) and was further filtered through 0.22 μm sized filters. The extract was stored at 4^0C for further experiments.

Synthesis of Silver nanoparticles from *Gymnosporia emarginata* young leaves extract

The aqueous solution of 1mM silver nitrate ($AgNO_3$) was prepared and used for the synthesis of silver nanoparticles. 10 ml of *Gymnosporia emarginata* young leaves extract was added into 90 ml of aqueous solution of 1 mM silver nitrate for reduction into Ag+ ions and kept for incubation period of 90min at room temperature. Here the filtrate acts as reducing and stabilizing agent for 1mM of $AgNO_3$.

Characterization

The formation of AgNP is verified by using UV–visible 5704SS ECIL spectrophotometer operated at with 1 nm resolution with optical length of 10 mm. UV–visible analysis of the reaction mixture was observed for a period of 300s. For the study of crystallinity, films of colloidal AgNP formed on Si(III) substrates by drop coating were used for X-ray-diffraction (XRD) study. The data were obtained using Ricago X-Ray Diffractrometer (Japan), operated at 30 kV and 20 mA current with Cu Ka(I = 1.54 A °). The transmission electron microscopy (TEM) images were obtained using Technai-20 Philips instrument operated at 190 keV. Sample for this analysis were prepared by Rapid Biosynthesis of Silver Nanoparticles Using *Cordia dichtoma young leaves* 109 coating of aqueous AgNPs drops on carbon coated copper grids, kept for 5 min; the extra solution was removed using blotting paper. The film of TEM grid is exposed to IR light for drying. The powder sample of AgNP was prepared by centrifuging the synthesized AgNP solution at 10,000 rpm for 20 min. The solid residue formed is then washed with deionized water to remove any unattached biological moieties to the surface of the nano particles, which are not responsible for biofunctionalization and capping. The resultant residue is then dried completely and the powder obtained is used for FTIR measurements carried out on a Nicolet iS5 FTIR with diamond ATR.

Antimicrobial activity of AgNPs synthesised from *Gymnosporia emarginata* young leaves extract

Test microorganisms

Three fungi *Fusarium oxysporum, Fusarium semitectum, Colletotrichum gloeosporioides, Aspergillus niger, three bacterial strains Staphylococcus aureus, Escherichia coli, Bacillus subtilis* were used in the present study, all the tested strains were obtained from Chandighar, sample centres, India. These test cultures were grown in PDA & nutrient broth (Himedia, M002) at 37ºC and maintained on nutrient and potato agar slants at 4ºC.

Agar-well diffusion technique

The assay was conducted by agar well diffusion method. About 15 to20 ml of potato dextrose agar medium was poured in the sterilized petri dishes and allowed to solidify. The bacterial strains were suspended in a saline solution (0.85% NaCl) and adjusted to a turbidity of 0.5 Mac Farland standards (108 CFU/ml). 1 ml of fungal strains were spread over the medium using a sterilized glass spreader. Using flamed sterile borer, wells of 4 mm diameter were punctured in the culture medium. Required concentrations (40 mg^{-1}, 20 mg^{-1}, 10 mg^{-1},5 mg^{-1}) were added to the wells. The plates thus prepared were left for diffusion of extracts into media for one hour in the refrigerator and then incubated at 37^{o}C. After incubation for 48h, the plates were observed for zones of inhibition. The diameter zone of inhibition was measured and expressed in millimetres. 1mM $AgNo_3$ solution and aqueous plant extract was used negative control. Whereas positive control used ketokonazole, streptomycene against fungi and bacteria (500 μg/ml conc.). The experiments were conducted in triplicates. The same method was followed for testing antibacterial activity using nutrient agar medium incubated at 37^{o}C for 18h.

RESULTS AND DISCUSSION

Green synthesis of AgNPs from young leaves aqueous extract (slight yellowish) of *Gymnosporia emarginata* was approved out and reported in this research work. 01 ml of *Gymnosporia emarginata* young leaves aqueous extract was added to 250 ml of 1mM $AgNO_3$ solution. The appearance of the retort

concoction subsequent to 20 minutes at room temperature changes transparent to thick yellowish colour and this surveillance is strapping signal for the formation of AgNPs is exposed in Fig. 2.

Fig. 2 Synthesis of silver nanoparticles using *Gymnosporia emarginata* young leaves extract treating with AgNO3 solution at room temperature

A) Formation of AgNPs ,B) silver nitrate($AgNO_3$) solution, C) *Gymnosporia emarginata* aqueous young leaves extract.

The AgNPs formation and constancy of the condensed in the ordeal solution was examined by using UV–vis spectral analysis. The UV–vis range recorded from reaction mixture is shown in Fig. 3.

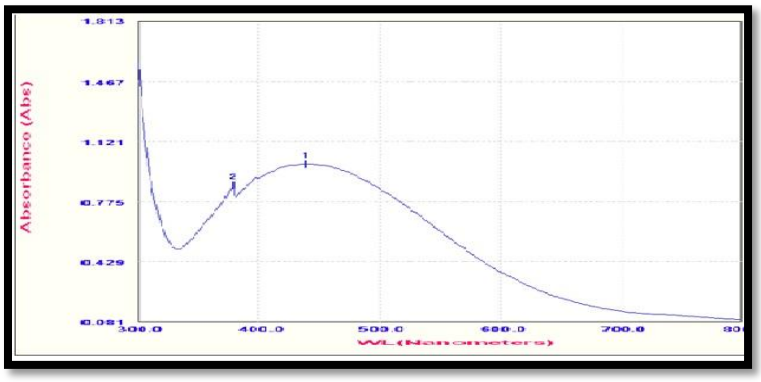

Fig. 3 UV–visa spectrum of bio functionalized AgNPs showing surface plasmon peak at 440 nm

The exterior plasmon height experimental at 440 nm is auxiliary confirmation of occurrence of AgNPs in the ordeal solution [25, 26]. The XRD results of AgNPs which advocate that the particles are of crystalline in nature. The dynamic diffraction peaks like (220), and (311), (380) observed. The recorded peaks competition well with the standard JCPDS file 04-0783 of silver shown in figure 4.

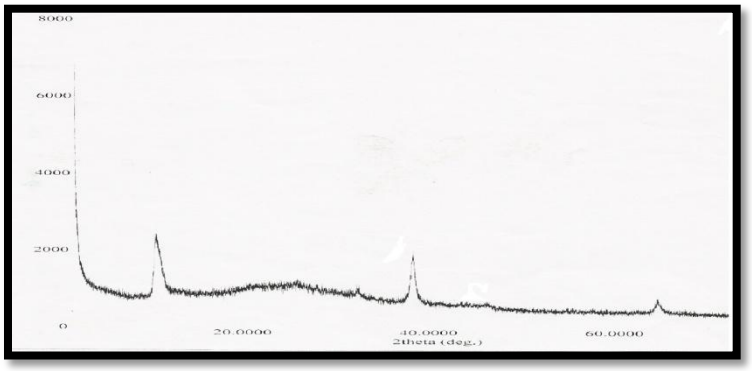

Fig. 4 XRD patterns of bio functionalized AgNPs

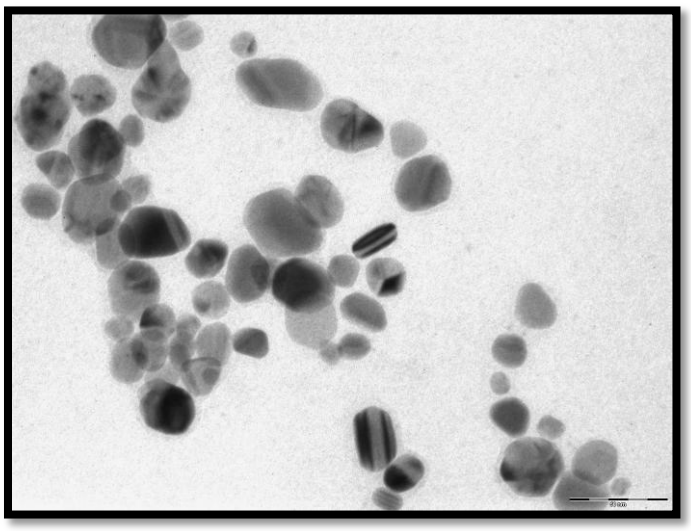

Fig. 5. TEM image of bio functionalized AgNPs, B. size pattern

By the TEM results the size and shape of AgNPs was clarified. A classic TEM image of green synthesized AgNPs, which suggests that the particles are uneven in shape. Some are round, spherical and triangular twisted particles with a altering size of 18.14–75.84 nm shown in figure 5.

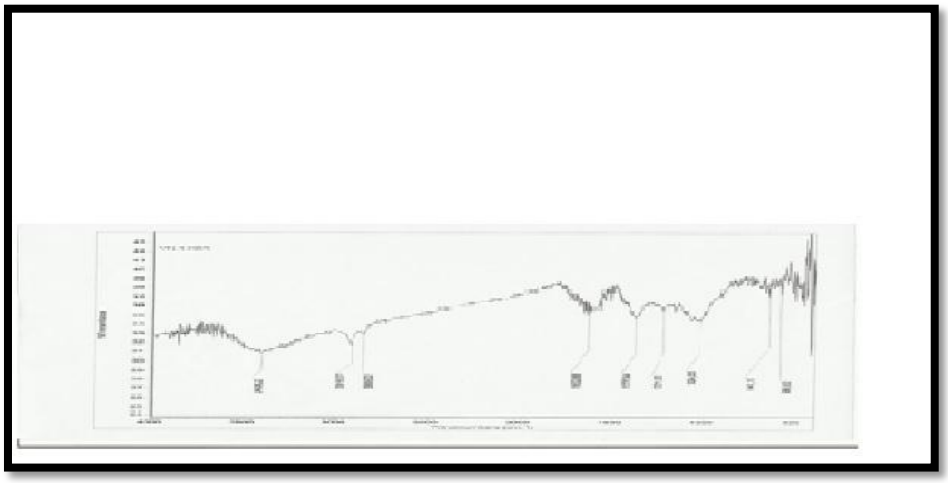

Fig 7. FTIR spectrum of bio functionalized AgNPs

The FTIR spectroscopy is a helpful method to study the middle–shield morphology of AgNPs is as shown in Fig. 6. The strong band at _1650, 53 was observed.

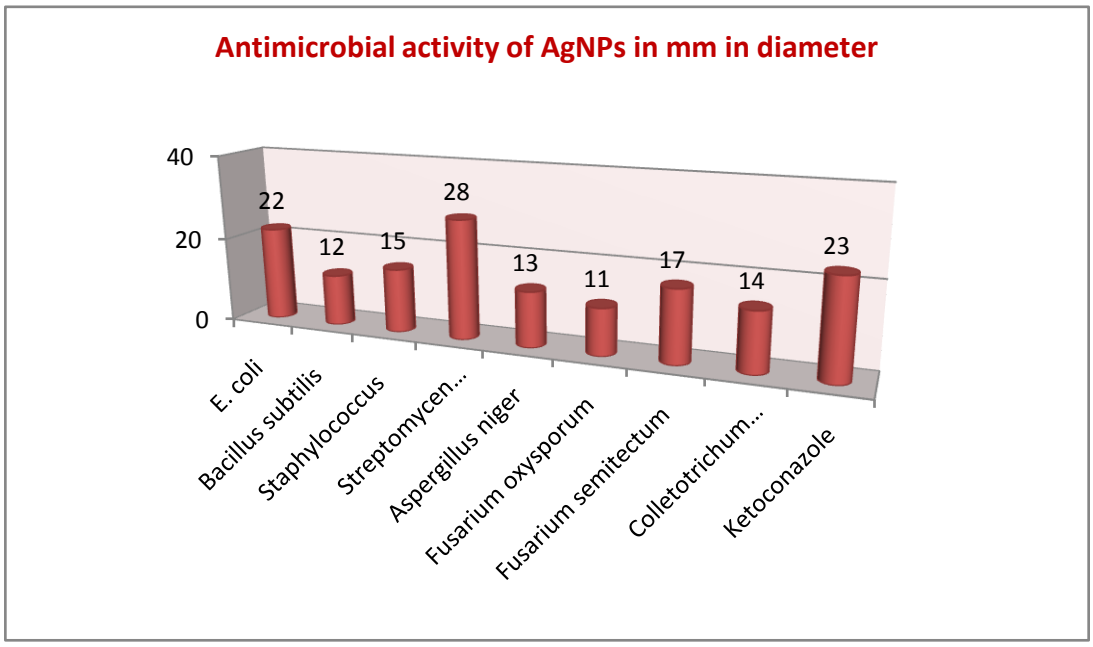

Graph 1: Antimicrobial activity of AgNPs of *Gymnosporia emarginata*

Via young leaves extract of *Gymnosporia emarginata* based AgNPs antimicrobial activity at 80 μl/well showed maximum antifungal activity against *Fusarium semitectum* 17.00 mm followed by *Colletotrichum gloeosporioides* 14.00 mmAspergillus niger 13 and the least 11.00 mm diameter zone of inhibition showed by *Fusarium oxysporum.* Similarly, against bacteria the maximum activity of 22.00

mm was recorded against *E. Coli* followed by *S. aureus* 15.00mm and *B. Subtilis* 15.00 mm. The antimicrobial activity was straight relative to the meditation of AgNPs. Two negative controls i.e., $AgNo_3$ solution showed activity 06-07mm and plant aqueous extract have not showed activity due to their low concentration. Streptomycin sulphate and Ketoconazole used as standards alongside test organisms showed the inhibition zones of 23.00mm & 28.00mm, respectively (Graph.1).

Conclusion

The biosynthesis of silver nanoparticles from *Gymnosporia emarginata* young leaves was shown to be brisk and produce particles of varing crystallographic shapes. The synthesis method eco-friendly in nature. The synthesized particles showed antimicrobial activity was detected. The present upshot suggests that they are helpful in applications as antimicrobial agent.

ACKNOWLEDGMENTS

Authors are contented to thank IIT Mumbai for TEM analysis, JNTU Hyderabad for FTIR analysis, Dept of Physics Gulbarga University for XRD analysis, and Gulbarga University for providing the lab facilities.

REFERENCE

1. Santapan H and Henry AN. Council of Scientific & Industrial Research. New-Delhi, India; 1983 (reprint).
2. Kirtikar KR and Basu BD. Indian Medicinal Plants. Vol.1. Allahabad, India: Lalit Mohan Basu ; 1933. pp 577.
3. W.R. Rajesh, R.L. Jaya, S.K. Niranjan, D.M. Vijay, and B.K. Sahebrao, "Phytosynthesis of Silver Nanoparticle Using *Gliricidia sepium*," *Current Nanoscience*, Vol. 5, pp. 117- 122, 2009.
4. S. Arulkumar and M. Sabesan, "Biosynthesis and characterization of gold nanoparticle using antiparkinsonian drug *mucuna pruriens* plant extract," *International Journal of Research in Pharmaceutical Sciences*, Vol. 4, pp. 417- 420, 2010.

5. V. Arya, S. Yadav, S. Kumar and J.P. Yadav, "Antimicrobial Activity of *Cassia occidentalis* L (Leaf) against various Human Pathogenic Microbes," *Life Sciences and Medicine Research,* Vol. 9, pp. 1-11, 2010.

6. A. Bankar, B. Joshi, A.R. Kumar and S. Zinjarde, "Banana peel extract mediated synthesis of gold Nanoparticle," *Colloids and Surfaces B: Biointerfaces,* Vol. 80, pp. 45 – 50, 2010.

7. S.S. Shankar, A. Rai, A. Ahmad and M. Sastry, "Rapid synthesis of Au, Ag, and bimetallic Au core–Ag shell Nanoparticle using Neem(*Azadirachta indica*) leaf broth," *Journal of Colloid and Interface Science,* Vol. 2, pp. 275- 496, 2004.

8. S.P. Chandran, M. Chaudhary, R. Pasricha, A. Ahmad and M. Sastry, "Synthesis of gold nanotriangles and silver nanotriangles using Aloe vera plant extract," *Biotechnolgy Progress,* Vol. 22, pp. 577-579, 2006.

9. B. Amkamwar, C. Damle, A. Ahmad and M. Sastry, "Biosynthesis of gold and silver nanoparticles using *Emblica officinalis* fruit extract, their phase transfer and transmetallation in an organic solution," *Journal of Nanoscience and Nanotechnology,* Vol. 5, pp. 1665-1671, 2005.

10. S. Li, L. Qui, Y. Shen, A. Xie, X. Yu, L. Zhang and Q. Zhang, "Green synthesis of silver nanoparticles using *Capsicum annum* L. Extract," *Green Chemistry,*Vol. 9, pp. 852-858, 2007.

11. J. Huang, C. Chen, N. He, J. Hong, Y. Lu, L. Qingbiao, W. Shao, D. Sun, Y. Wang, X.H. Wang and X. Yiang, "Biosynthesis of silver and gold nanoparticles by novel sun dried *Cinnamomum camphora* leaf," *Nanotechnology,* Vol. 18, pp. 105-106, 2007.

12. R.W. Raut, J.R. Lakkakula, N.S. Kolekar, V.D. Mendhulkar and S.B. Kashid, "Phytosynthesis of silver nanoparticle using *Gliricidia sepium* (Jacq.)," *Current Nanoscience,* Vol. 5, pp. 117-122, 2009.

13. N. Mude, A. Ingle, A. Gade and M. Rai, "Synthesis of silver nanoparticles using callus extract of *Carica papaya*-A first report," *Journal of Pantl*

Biochemistry and Biotechnology, Vol. 18, pp. 83-86, 2009.

14. A.K. Gade, S.C. Gaikwad, V. Tiwari, A. Yadav, A.P. Ingle, M.K. Rai, "Biofabrication of silver nanoparticles by *Opuntia ficus-indica*: In vitro antibacterial activity and study of the mechanism involved in the synthesis," *Current Nanoscience,* Vol. 6, pp. 370-375, 2010.

15. S.R. Bonde, D.P. Rathod, A.P. Ingle, R.B. Ade, A.K. Gade, M.K. Rai, "First report of Murraya koenigii mediated synthesis of silver nanoparticles and its activity against three human pathogenic bacteria," *Nanoscience Methods,* Vol. 1, pp. 25-36, 2012.

16. K. Mallikarjun, G. Narsimha, G.R. Dillip, B. Praveen, B. Shreedhar, S. Lakshmi, V.S. Reddy and D.P. Raju, Green synthesis of silver nanoparticles using *Ocimum* leaf extract and their characterization. *Digest Journal of Nanomaterials and Biostructures,* 6 (1): 181-186, 2012.

17. P. C. Nagajyoti, T. N. Prasad, V. M. Shreekanth, K. D. Lee, "Biofabrication of silver nanoparticles using leaf of *Saururus chinenis*," *Digest Journal of Nanomaterials and Biostructures,* Vol. 6, No. 1, pp. 121-133, 2011.

18. A. Ingle, A. Gade, S. Pierrat, C. Sonnichsen and M. Rai, "Mycosynthesis of silver nanoparticles using the fungus Fusarium acuminatum and its activity against some human pathogenic bacteria," *Current Nanoscience,* Vol. 4, pp. 141-144, 2008.

19. A.K. Gade, P. Bonde, A.P. Ingle, P.D. Marcato, N. Duran, M.K. Rai, "Exploitation of *Aspergillus niger* for synthesis of silver nanoparticles," *Journal of Biobased Matetrials Bioengineer,* Vol. 2, pp. 243-247, 2008.

20. N. Duran, P.D. Marcarto, G.I.H. De Souza, O.L. Alves and E. Esposito, "Antibacterial effect of silver nanoparticles produced by fungal process on textile fabrics and their effluent treatment," *Journal of Biomedical Nanotechnology,* Vol. 3, pp. 203-208, 2007.

21. L.P. Li, Q.W. Song and E Newton, "Antimicrobial effects of surgical masks coated with 869 nanoparticles," *Journal of Hospital Infection,* Vol. 62, pp. 58-

63, 2006.

22. K.M. Nadkarni, "*Indian Materia Medica,"* Mumbai, India: Popular Prakashan; 2002.

23. S. Basavaraja, S. D. Balaji, A. Lagashetty, A. H. Rajasab, and A. Venkataraman *Materials Research Bulletin*, Vol. 43, pp. 1164, 2008.

24. Ravishankar Bhat, Sharanabasava Ganachari, Raghunandan Deshpande, G. Ravindra, A. Venkatraman, "Rapid Biosynthesis of Silver Nanoparticles Using Areca Nut (Areca catechu) Extract Under Microwave-Assistance," *Journal of Cluster Science,* Vol. 24, pp. 107–114, 2013.

Optical Properties of Pure and TICI Doped Poly (Vinyl Alcohol) Polymer Electrolyte Films

C. Anuradha, K.Veerabadra Rao, G.Aravind

Department of physics, Methodist College of Engineering & Technology, Abids, Hyderabad

ABSTRACT: Poly vinyl alcohol (PVA) is a water-soluble amorphous/crystalline polymer that is widely used in protective coating, biomedical and optical materials, orbents and membranes. In the present investigation, an attempt has been made to characterize the polymer electrolytes based on Poly(vinyl alcohol) (PVA) complexed with thallium chloride(TlCl) at different weight percentage ratio. Solid polymer electrolyte films based on poly(vinyl alcohol) complexed with TlCl were prepared using solution cast technique. The structural properties of these films were examined by XRD. The XRD results show that the amorphous domains of PVA matrix increased in the composite films. In FTIR spectra, changes are noticed in the C-H stretching vibrational mode at 2900 cm^{-1} of PVA along with disappearance of few bands and the appearance of new bands. Morphological studies show that as the percentage of TlCl concentration exceeds that of host concentration, the TlCl gets aggregates on the surface of the film, increasing the surface roughness. The optical parameters including the energy band gaps (direct and indirect) and absorption edge are investigated. It is observed that direct and indirect band gaps (Direct band gap from 5.12-4.80 eV and indirect band gap from 4.82-4.67 eV) show a decreasing trend on complexing.

Keywords: Poly vinyl alcohol, thallium chloride, XRD, FTIR, SEM, Optical absorption.

1.INTRODUCTION

Polymers have gained much experimental attention due to their unique properties, such as low density, ability to form intricate shapes, versatile electric properties and low manufacturing cost [1]. The physical properties of these polymer materials can be enhanced by incorporating filler into its matrix, because dispersed filler will improve various physical properties of the host polymer [2]. Poly (vinyl alcohol) (PVA) is a water-soluble amorphous/crystalline polymer that is widely used in protective coatings, biomedical and optical materials, orbents and membranes [3]. In the present investigation, an attempt has been made to characterize the polymer electrolytes based on Poly (vinyl alcohol) (PVA) complexed with thallium chloride (TlCl) at

different weight percentage ratio.

II.MATERIALS AND METHOD

Films of pure PVA and various compositions of complexed films of PVA with TlCl salt were prepared in weight percent ratios (80:20), (60:40) and (40:60) by solution cast technique using double distilled water as solvent. The solution was stirred for 12hrs to get homogeneous mixture and then casted on polypropylene dishes and kept in hot air oven for 12hrs at a temperature of 40^{o}C. The films thus formed were stored in desiccators. The XRD pattern of the films was recorded with a 'X' pert x-ray diffractometer at room temperature. The FITR spectra of these films were recorded using Bruker tensor-27 spectrometer with a resolution of 4 cm^{-1}. The measurements were taken over a wave number range 400-4000 cm^{-1}. The surface morphology of these polymer electrolyte films have been observed using JEOL JSM 840A scanning electron microscope. The optical absorption spectra of the present samples were recorded at room temperature using Shimadzu UV-VIS-NIR in the wavelength range 300-900nm with a spectral width of 3nm.

III. RESULTS AND DISCUSSION

A.XRD Analysis

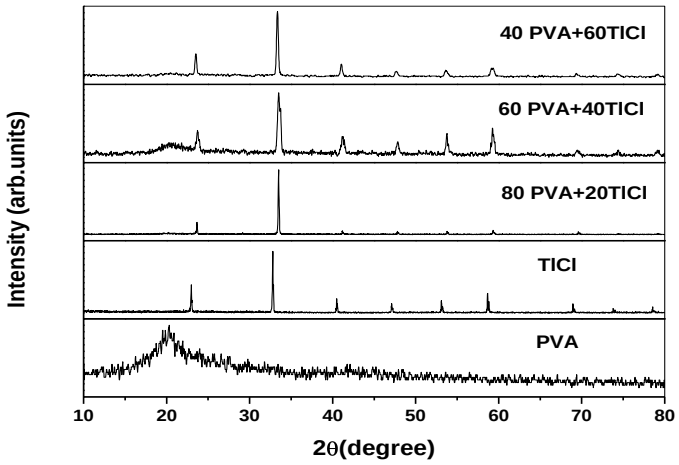

Fig 1. XRD pattern of Pure PVA and PVA/TlCl films

The X-ray diffraction pattern of pure PVA, TlCl salt and PVA complexed with TlCl are shown in Fig.1. The XRD pattern of pure PVA reveal that a broad peak is appearing at scattering angle $19^{o} < 2\theta < 20^{o}$, corresponding to a 'd' spacing of 0.457 nm. The pure PVA characteristic peak becomes less intense as the TlCl content in the composite is increased. This could be due to

disruption of PVA crystalline structure by TlCl. The diffraction peaks associated with PVA has disappeared in 80:20 composite and reappeared again when TlCl present is increased in PVA films. This shows a decrease in the degree of crystallinity of the polymer after the addition of higher concentrations of TlCl. The increase in the composition of TlCl in PVA, results in increase in the amorphous nature of the composite films. Higher and broader peaks are obtained in the case of 60:40 compositions indicating greater accumulation of atoms at lattice sites, creating greater lattice distortion.

B. FTIR Studies

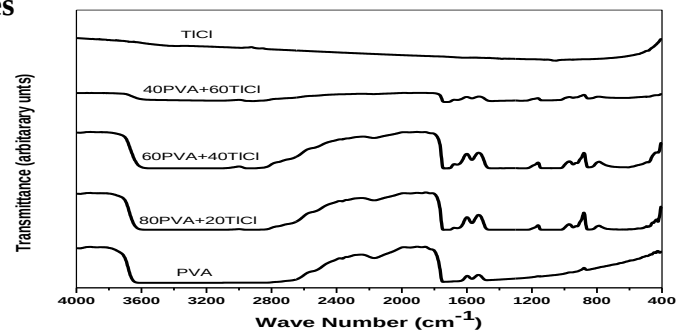

Fig. 2: FTIR spectra of Pure PVA, TlCl salt and PVA/ TlCl polymer films.

The FTIR spectra for pure PVA, TlCl and PVA : TlCl composites of different compositions are shown in the fig2. The following changes in the spectral features have been observed after comparing the spectrum of PVA : TlCl composites. Changes are noticed in the C-H stretching vibrational mode at 2900 cm^{-1} of PVA along with disappearance of few bands and the appearance of new bands. The inter molecular hydrogen bonded O-H stretching frequency of PVA appearing in the range of 3590 cm^{-1} is shifted to 3507 cm^{-1}. In PVA : TlCl (60:40) composition and at higher compositions of PVA : TlCl (40:60), this band appears at 3175 cm^{-1}. The C-H bonding of CH_2 in pure PVA exhibits absorption at 1474cm^{-1} and is shifted to 1418$cm^{-1}$and 1439^{-1} in (80:20) and (40:60) compositions respectively.

C. SEM Analysis

Fig 3 (a,b,c) shows the SEM pictures of the surface of PVA : TlCl(80:20); PVA : TlCl (60;40)and PVA : TlCl (40:60) films of different magnification respectively. These pictures show not many aggregates on the surface of the films.The increase in degree of roughness with increased TlCl concentration, indicates, the presence of the dopant which is completly complexd with the polymer. As the percentage of TlCl exceeds that of the host concentration the TlCl gets aggregates on the surface of the film increasing the surface roughness

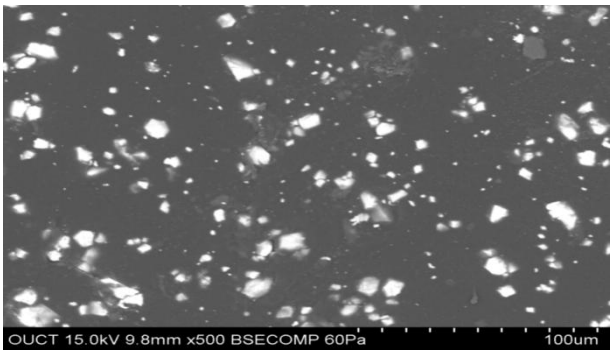

Fig 3 (a): SEM picture of PVA/TlCl (80:20)

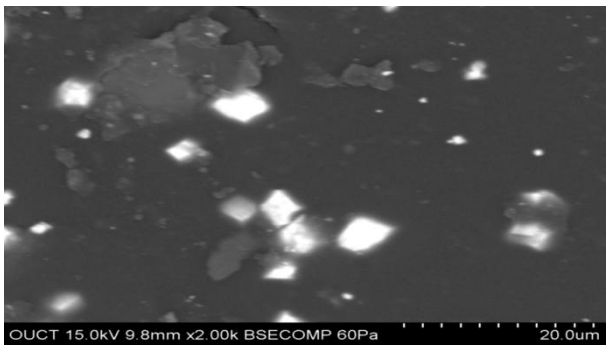

Fig 3 (b): SEM picture of PVA/TlCl (60:40)

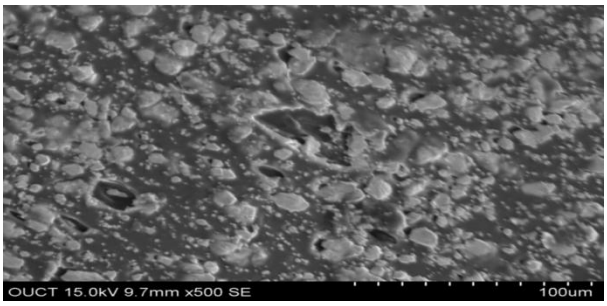

Fig 3 (c): SEM picture of PVA/TlCl (40:60)

D.Optical Absorption Studies

The optical absorption (OA) studies are very interesting because it provides important information about the absorbance, transmittance and reflectance of the observed polymeric films [4].The optical absorption and especially the absorption edge presents a useful method for the investigating optically induced transitions and for getting information about the band structure, the band tail and energy gap of the polymeric materials under consideration [5]. By studying the optical absorption spectrum, one can clearly identify its band structure [6-8]. The

absorption coefficient α(ν) can be estimated from the optical absorption spectrum from the following equation [9].

$$\alpha(\nu) = 2.303 \ X \ A/d \qquad .....(1)$$

Where „d is the film thickness in cm and 'A' is defined by $\log(I/I_o)$ where I_o and I are the intensities of the incident and transmitted beams respectively.

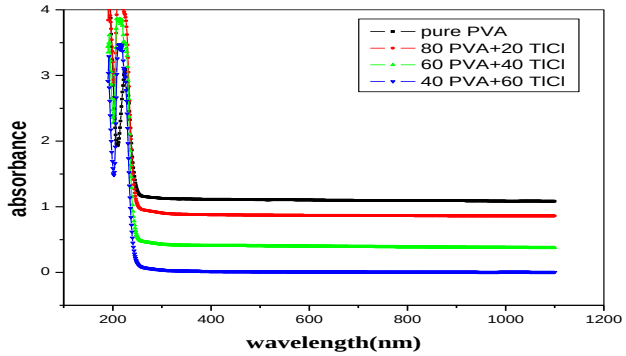

Fig. 4: OA spectra of Pure and TlCl complexed PVA films

Regarding the optical transitions resulting from photons of energy $h\nu > E_{opt}$, the present optical data is studied according to the following relationship for near edge optical absorption [10].

$$\alpha(\nu)h\nu = B\,(h\nu - E_{opt})^r \qquad .....(2)$$

where α is the absorption coefficient , ν is the frequency, B is the constant, h is the Planck's constant, E_{opt} is the optical energy band gap between the valence and conduction bands and r is the power that characterizes the transition process. Here 'r' takes the values of 1/2, 3/2, 2 and 3 for transitions designated as direct allowed, direct forbidden, indirect allowed and indirect forbidden respectively [5]. The determination of the value of the optical energy band gap E_{opt} is done by plotting $(\alpha h\nu)^{1/r}$ against hν.

The OA spectrum of pure PVA, PVA complexed with different concentrations of TlCl are shown in fig.4. The OA spectrum of pure PVA is characterized by an absorption peak at wavelength 283nm as well as unresolved shoulder at 330nm. No absorption peaks are noticed at higher wavelengths. The absorption peak at 283nm can be attributed to the absorption by simple carbonyl groups along the polymer chains. On the other hand shoulder can be assigned to the appearance of the $-CO-(CH=CH)_3-$groups (5)

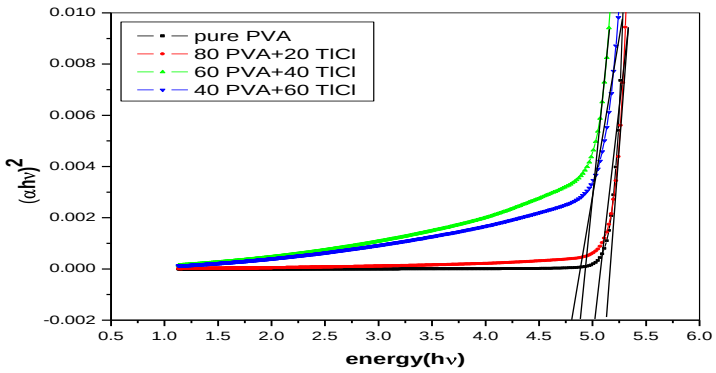

Fig. 5(a): Plot of (αhν)2 versus photon energy (hν) for PVA:TlCl

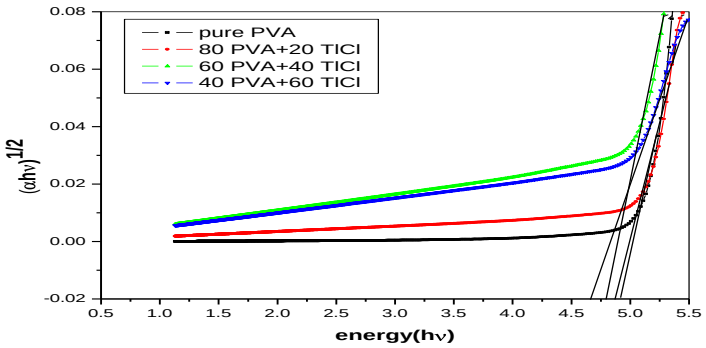

Fig. 5(b): (αhν)½ versus photon energy (hν) for PVA:TlCl

Polymer	Absorption edge (ev)	Band gap (eV)	
		Direct	Indirect
PVA	5.02(247)	5.12	4.82
80PVA+ 20TlCl	4.94 (251)	5.02	4.79
60PVA+ 40TlCl	4.77 (260)	4.85	4.71
40PVA+ 60TlCl	4.65 (267)	4.80	4.67

The addition of TlCl to PVA matrix shows no substantial change in 283 nm peak but the shoulder which appeared in pure PVA has disappeared on addition of TlCl. There is a decrease in UV absorption in the case of PVA/TlCl films. The fundamental band edge, both direct and indirect transitions can be observed by plotting $(\alpha h\nu)^{2}$ and $(\alpha h\nu)^{1/2}$ versus photon energy hν. These plots are shown in fig 5.

These plots present experimental data near the absorption edge and give a linear fit in the high

energy range. The intercept on the energy axis on extrapolating the linear portion of the curves to zero absorption value may be interpreted as the value of band gap. The values of experimental band gaps of pure PVA and PVA complexed with TlCl are listed in table 1.

It is clearly evident from the table that both the direct and indirect band gap show decreasing trend on complexing. The decrease in optical band gap energies with increase in the TlCl concentrations respectively explains the fact that the addition of TlCl increases the disorder of these films. The increase in the degree of the disorder causes the band tail to increase. The decrease in band gap on increasing the TlCl content in PVA matrix also indicates that there are charge transfer complexes which arise between the PVA and TlCl molecule.

IV.CONCLUSIONS

The complexation of the salt with polymer is confirmed by X D and FTIR studies. The morphological studies of pure PVA and (PVA:TlCl) polymer electrolyte at different weight percentage is done using SEM. The optical band gap is evaluated and its dependence on filling was investigated. The decreasing trend of the optical band gap with increase in TlCl concentration is attributed to the charge transfer complexes.

REFERENCES

[1]. A.El-Khodary, A.h.Oraby and M.M.AbdelnabyJournal of magnetism and magnetic materials 320,1739-1746 (2008).

[2]. V.Raja, A.K.Sarma and V.V.R.Narsimha Rao, "Optical properties of pure doped PMMA-Co-P4VPNO polymer films", 57 (30), 4678-4683 (2003).

.M.E.Rozenberg, Polyvinyl Acetate based polymers [in Russia], Khimiya,

Leningrad (1983).

.P.Balaji Bhargav, V.Madhu Mohan, A.K.sharma and V.V.R.Narsimha Rao,

nternational Journal of Polymer materials, 56, 579 (2007).

.A.El.Khodary, Phsica B:Condensed Matter, 405(16) , 4301 (2010)

.M.Tabata, M.Satoh, K.Kaneto and Yoshino, J.Phys.Soc.Japn, 55, 1305 (1986).

.S.Proneanu, S.Torcu, M.Brie and Mihileasan, Mater.Sci.Fourum 191 (1995).

.W.A.Jabbar, N.F.Habubi and S.S.Chiad, J.Arkansas Academy of Sci, 64, 101(2010)

.J.Ballato and S.Foulger, "Optical properties of Perfluocydobutyl polymers",Journal of Optical Society of America B, 20(9), 1838-1843 (2003).

].J.Tauc, A.Menith and D.N.Wood, Physical review letters, 25(11), 749 (1970).

Structural Properties of $Mg_{1-x}Zn_xFe_2O_4$ Nano-Ferrites Synthesized by citrate Gel Autocombustion method

Shyamsunder Goud[1], Nakiraboina Venkatesh[1], Nama Hari Kumar[2], B. Rambabu[1], B.Shankar[1],P.Naresh[2]M.Raghasudha[1], P. Veera Somaiah[1]*
[1]Department of chemistry, Osmania University, Hyderabad, 500007- India.
[2]Department of Physics, Osmania University, Hyderabad, 500007- India.
Corresponding author Email: vs_puppala@rediffmail .com Ph (+91)9247562742

ABSTRACT:

In this work, the Mg1-xZnxFe2O4 Nanoferrites (where x = 0.0, 0.2, 0.4, 0.6 and 0.8) was synthesized using citrate Gel Auto combustion method. The investigation of structural and optical properties was carried out for the synthesized samples using X-ray diffraction (XRD), Fourier transform infrared spectroscopy (FTIR) and Ultraviolet visible spectrophotometer (UV-Vis). XRD revealed that the structure of these nanoparticles is spinel with space group Fd3m and crystallite size lies in the range 21.0 - 42.8 nm. Lattice parameter was found to increases with Zn concentration and this may be due to the larger ionic radius of the Zn^{2+} ion. FTIR spectroscopy confirmed the formation of spinel ferrite and showed the characteristics absorption bands around 612, 1146, 1404, 1649 and 3245 cm^{-1}. The energy band gap was calculated for samples with different ratio and was found to be 4.77, 4.82, 4.86, 4.87 and 4.95 eV. The substitution was resulted in slight increased in the lattice constant and that sequentially may lead to the slightly decreased in the energy gap.

Keywords: Citrate Gel Auto combustion Method, Ferrite Nanoparticles, Spinel Structure,

1. Introduction

Nanotechnology is one of the leading scientific fields today since it combines knowledge from the fields of Physics, Chemistry, Biology, Medicine and Engineering. The application and use of nanomaterials are extensive such as in electronic and mechanical devices, optical magnetic components, tissue engineering magnetic storage systems and magnetic resonance imaging [1] [2]. Nanotechnology and material technology are new techniques for synthesis and processing

manipulation and assembly using natures own building blocks (atoms, molecules or macromolecules) for the intelligent design of functional materials, components and systems with attractive qualities and functions [3] [4].

Ferrites are well known magnetic nanomaterials intensively studied as a recording media due to their superior physical properties. These properties make ferrites an ideal candidate for technical applications such as magnetic resonance imaging enhancement, catalysis, sensors and pigments [5]. Mixed spinel ferrites have been studied intensively over the last few years due to their potential applications. Spinel ferrites have the chemical formula MFe_2O_4 in which M can be any divalent metal cations. In spinel ferrite, oxygen forms face centre cubic (FCC) lattice with divalent cations at tetrahedral (A) and/or octahedral (B) sites. Magnesium ferrite ($MgFe_2O_4$) has an inverse spinel structure with the preference of Mg^{2+} cations mainly on octahedral sites [6]- [9], while Zinc ferrite ($ZnFe_2O_4$) has normal spinel structure, in which Zn^{2+} cations mainly occupy tetrahedral sites [6] [10].

The small scale size of the well known spinel ferrites has opened up the door for intensive research to utilize their properties for biomedical applications [11]-[13] . Numerous methods were reported in literature showing the possibilities of producing particle with size in the range of 2 - 100 nm. Among these methods are co-precipitation, hydrothermal and citrate gel Methods [14] [15], which were reported to be fast and producing high quality nanoparticles.

In this work, $Mg_{1-x}Zn_xFe_2O_4$ nanoferrites where x = 0.0, 0.2, 0.4, 0.6 and 0.8) were synthesized using co-precipitation methods. X-ray diffraction (XRD) was used in order to investigate the structural of Zn substituted magnesium nanoferrites and to determine the lattice parameters and the space group symmetry. Ultraviolet visible spectrometer (UV vis) and Fourier Transform Infrared Spectroscopy (FTIR) were used to investigate the structural properties of crystallite nanoparticles.

2. Material and Method

Mg Zn ferrite ($Mg_{1-x}Zn_xFe_2O_4$) nanoparticles with composition (x = 0.0, 0.2, 0.4, 0.6 and 0.8) was prepared by the citrate gel auto combustion Method. Stoichiometric amounts from pure raw materials of $Fe(NO_3)_3 \cdot 9H_2O$, $Mg(NO_3)_2 \cdot 6H$

$_2O$, $Zn(NO_3)_2 \cdot 6H_2O$, and NaOH were used to prepare the required solutions with required molarities. The solution of $Fe(NO_3)_3 \cdot 9H_2O$, 0.4 M (25 ml), $Mg(NO_3)_2 \cdot 6H_2O$ 0.2M (25 ml) and $Zn(NO_3)_2 \cdot 6H_2O$ Calculated quantities of metal nitrates and citric acid were dissolved in minimum amount of distilled water to get clear solution. Here citric acid acts as a chelating agent and helps in the homogenous distribution of metal ions. The above mixture was stirred to get homogenous clear solution which is heated to 80^0C using a hot plate magnetic stirrer. Then the pH of the solution is adjusted at 7 by addition of ammonia. A sol is formed. The resulting solution was evaporated to dryness heating at about 180^0C on a hot plate with continuous stirring. The gel gave a fast flameless auto combustion reaction with the evolution of large amount of gases which results a burned powder. The burned powder was grinding using Agate Mortar and pestle to get a fine ferrite powder. Finally the grinded powder was calcinated in air at 500^0C for 4 hours and cooled to room temperature. The XRD analysis was carried out to confirm the purity of the synthesize materials using Shimadzu 6000 X-ray diffractometer with Cu-kα radiation of a wavelength λ = 1.5406 Å source. FTIR measurements were performed using (Mattson, model 960m0016) spectra, while the absorption of solution with different concentration was calculated using UV min 1240 spectrometer Shimadzy.

3. Results and Discussion

3.1. Crystal Analysis

Determination of the crystal structure, the lattice parameters and the space group symmetry are importance in the study of structural, electrical and optical properties of the nanoparticle ferrites. The information of single phase $Mg_{1-x}Zn_xFe_2O_4$ is confirmed after analyzing the x-ray diffraction pattern by MDI Jade 5.0, ORIGAN and FULLPROF. The crystal structure is found to be cubic with space group Fd3m. The X-ray diffraction (XRD) is carried out at room temperature. Figure1 shows the X -ray diffraction patterns for the sample $MgFe_2O_4$ nanoparticles with x = 0.0, while Figure2 shows the X -ray diffraction patterns for the samples $Mg_{1-x}Zn_xFe_2O_4$ nanoparticles with different composition (x = 0.2, 0.4, 0.6 and 0.8) . The peaks were indexed as (111), (220), (311), (222), (400), (422), (511), (440), and (533). The crystallite size, lattice constants, volume and densities are listed in **Table**

1. The crystal size is calculated using the Debye-Scherer's equation [18]:

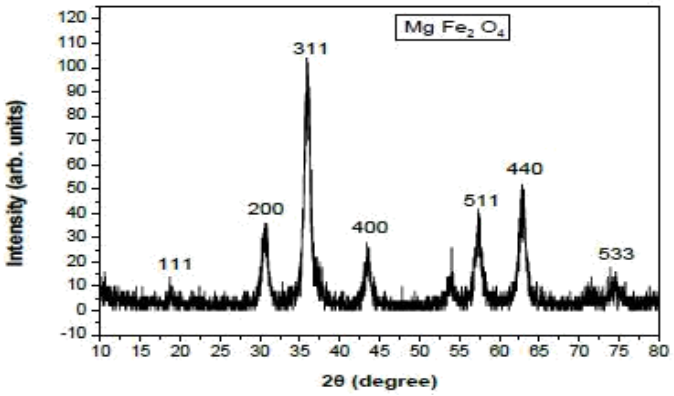

Figure 1. XRD patterns of Mg_1- xZn xFe2O4 nanoferrites for x = 0

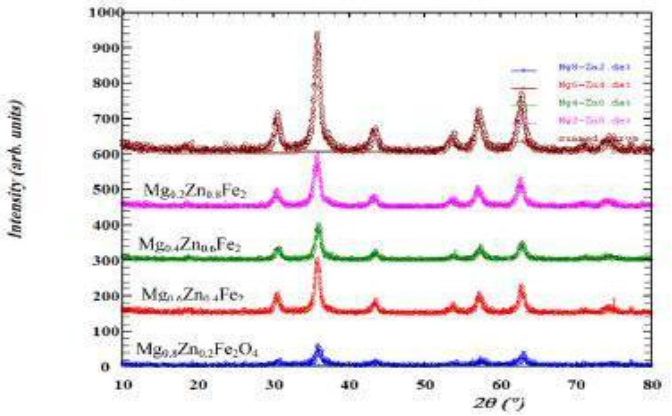

Figure 2. XRD patterns of Mg_1- xZn xFe2O4 nanoferrites for x = 0.2, 0.4, 0.6 and 0.8.

Table 1. Particle size (D), Lattice constant (a), Volume and Density of $Mg_{1-x}Zn_xFe_2O_4$ nano-ferrites.

No.	Samples	Crystal size (nm)	Lattice constant (Å)	Volume (nm^{-3})	Density (g/cm^3)
1	MgFe2O4	42.8	8.09	529.5	5.175
2	Mg0.8Zn0.2Fe2O4	26.6	8.38	587.4	4.522
3	Mg0.6Zn0.4Fe2O4	24.1	8.39	590.0	4.502
4	Mg0.4Zn0.6Fe2O4	21.0	8.40	591.9	5.176
5	Mg0.2Zn0.8Fe2O4	23.2	8.44	601.5	5.070

where *D* is the average crystallite size, θ is the diffraction angle, λ is the wavelength of incident X-ray and β is the full width at half maximum (FWHM) of the (XRD) peak in units of radians. The crystallite size vs. Zn concentration is plotted in Figure3 and the crystallite size is found to scattered in the range 21 - 42.8 nm for different compositions. In the obtained diffraction pattern the lattice constants are found to increase from (8.09 - 8.44 Å) as the Zn concentration increased. The particle size of the nanocrystalline samples, calculated from the XRD data using Equation (1), is remained within the range (21.0 - 42.8 nm). The increased in lattice constant with Zn concentration may be due to the fact that Zn^{2+} ions (0.82 Å) is larger than that of the Mg^{2+} ions (0.72 Å). Addition of Zn^{2+} at the expense of Mg^{2+} in the ferrite is expected to increase the lattice constant. The lattice pa-rameter (*a*) is estimated using lattice spacing (*d*) values and respective miller indices (*hkl*). The lattice constant (*a*) was calculated by MDI Jade 5.0 program and using the equation [19]:

$$a = \frac{d}{\left(h^2 + k^2 + l^2\right)^{1/2}}$$

where *a* is the lattice parameter, *d* is the lattice spacing and *h*, *k*, *l* are the miller indices. The lattice parameter is obtained using XRD data lies in the range of 8.1 - 8.4 Å for different Zn concentration as shown in Figure 4. It increases with increasing Zn concentration due to the larger ionic radius of Zn^{2+} (0.08 nm) Cation as compared to ionic radius of Mg^{2+} (0.06 nm) Cation [20] [21].

3.2. FTIR Analysis

In order to investigate the chemical functional groups on the the synthesized $Mg_{1-x}Zn_xFe_2O_4$, FTIR spectroscopy are performed. The FTIR of nanocrystals powders (as pellets in KBr) in the range of 400 cm^{-1} to 4000 cm^{-1} is shown in Figure 5 for pure sample where x = 0. The FTIR of $Mg_{1-x}Zn_xFe_2O_4$ nano ferrites powders for samples where x = 0.2, 0.4, 0.6 and 0.8 is plotted and shown in Figure 6. The bands (υ_1, υ_2) for the samples are found to be in range 3148 - 3450 cm^{-1} and 1644 - 1649 cm^{-1}, respectively. These observed bands maybe are due to the O-H

stretching vibration of the free absorbed water and indicates the existence of hydroxyl groups in the synthesized ferrites, which is observed in previous experiments [22] [23]. The band (υ_3) for the samples are observed around 1404 cm^{-1} and is attributed to the C=O stretching vibration of the carboxyl group. In range 1107 - 1147 cm^{-1}, the band (υ_4) is observed and is related to the stretching vibration due to nitrate group [24] [25]. In the range of 800 - 400 cm^{-1}, two main absorption bands with very low intensity are observed around 400 and 600 cm^{-1} and may be is caused by metal oxygen vibration in the octahedral side. The υ_1, υ_2, υ_3, υ_4 and υ_5 are absorption bands around 3148 - 3450, 1644 - 1649, 1404, 1107 - 1147 and 612 - 663 cm^{-1}, respectively for the samples with different compositions and are attributed to the vibration of the tetrahedral and octahedral met-al-oxygen (M-O) bands in the lattices of the synthesized nanocrystals. The FTIR frequency bands for various Zn and Mg contents are listed in **Table 2**.

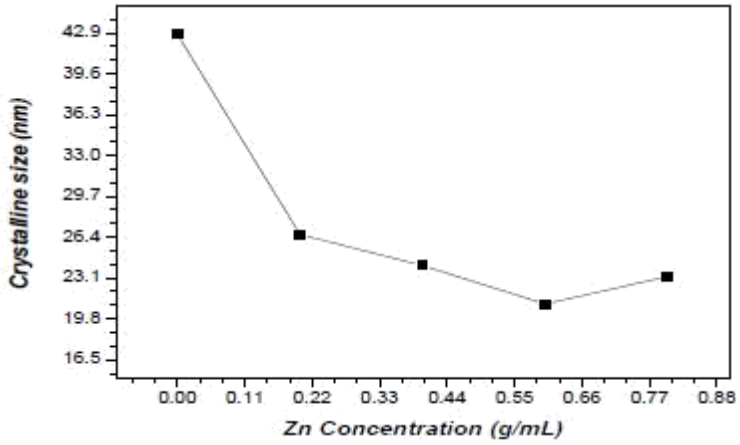

Figure 3. Particle size as a function of Zn concentration of $Mg_{1-x}Zn_xFe_2O_4$ nanoferrites.

3.3. UV Visible Analysis

The absorption as a function of wavelength for sample $Mg_{0.6}Zn_{0.4}Fe_2O_4$ is shown in Figure 7. Maximum absorption for the sample is observed at wavelength 232.4 nm. Several models are used to determine the optical properties of nanoferrites. The most widespread is the Tauc model which allows the derive of the band gap energy E_g from $(\alpha h\upsilon)^2$ as function of the incident energy ($h\upsilon$). The Tauc

$$(\alpha h\upsilon) = A\left(h\upsilon - E_g\right)^n$$

optical gap associated with the $Mg_{1-x}Zn_xFe_2O_4$ nanoferrites is determine through an extrapolation of the linear trend observed in the spectral

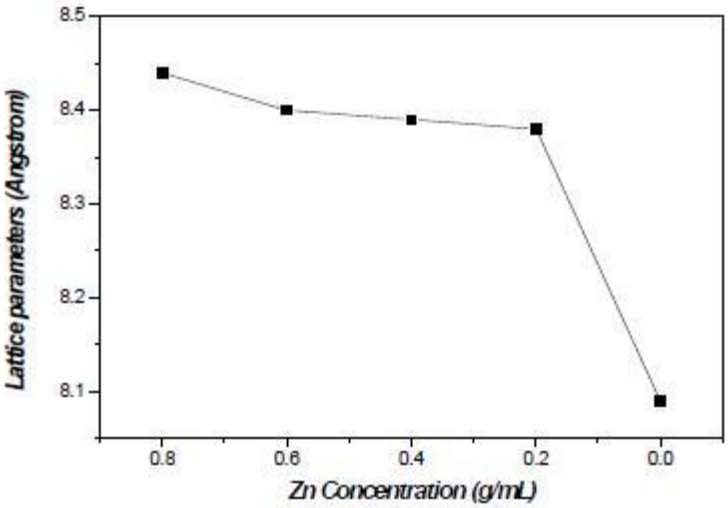

Figure 4. Lattice parameter as a function of Zn concentration of Mg1- xZnxFe2O4 nanoferrites.

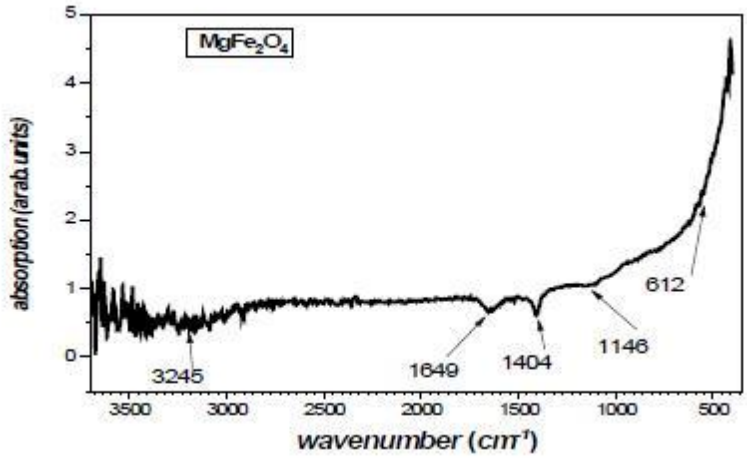

Figure 5. The FTIR spectrum of Mg1-xZnxFe2O4 nanoferrites for x = 0.

Dependence of $(\alpha h\upsilon)^2$ over a limited range of photon energies $h\upsilon$. The Tauc optical gap is defined as occurring at the intercept of this linear extrapolation with Y axis. The absorption coefficient α near the band edge in many

Nano ferrites shows an exponential upon photon energy usually obeying the relation [26]: where, α is the absorption coefficient and A is known as edge width parameter, E_g is the energy band gap, n = (1/2, 1, 2) is the a constant dependent on the degree of

transition, ($h\upsilon$) is incident photon energy. The band gap is

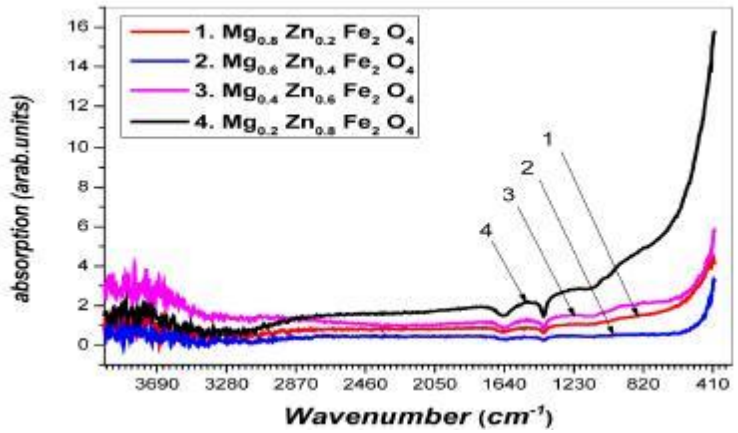

Figure 6. The FTIR spectrum of Mg1-xZnxFe2O4 nanoferrites for x = 0.2, 0.4, 0.6 and 0.8.

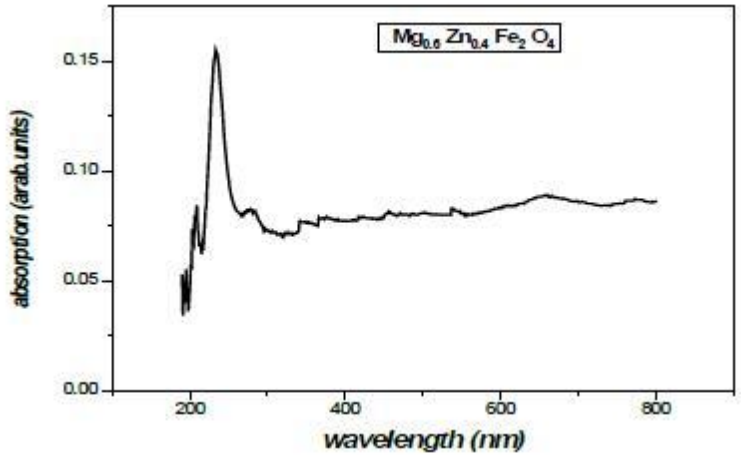

Figure 7. Absorption as a function of wavelength for sample of Mg0.6Zn0.4Fe2O4 composition.

Table 2. Wave numbers, wavelength, and energy band gaps of $Mg_{1-x}Zn_xFe_2O_4$ nanoferrites.

No.	Samples	υ1	υ2	υ3	υ4	υ5	Energy gap *Eg* (eV)
1	MgFe2O4	3245	1649	1404	1146	612	4.77
2	Mg0.8Zn0.2Fe2O4	3245	1649	1404	1146	612	4.82
3	Mg0.6Zn0.4Fe2O4	3450	1649	1404	1107	663	4.86
4	Mg0.4Zn0.6Fe2O4	3148	1644	1404	1140	612	4.87
5	Mg0.2Zn0.8Fe2O4	3419	1649	1404	1120	613	4.95

then evaluated by plotting ($h\upsilon$) versus $(\alpha h\upsilon)^2$ and extrapolating the tangent on the X-axis (Tauc plots) . Figure 8 shows Tauc plot method for sample of $MgFe_2O_4$, and the energy band gap are found to be 4.77, 4.82, 4.86, 4.87 and 4.95 eV for samples with different concentration (x = 0.2, 0.4, 0.6 and 0.8), respectively.

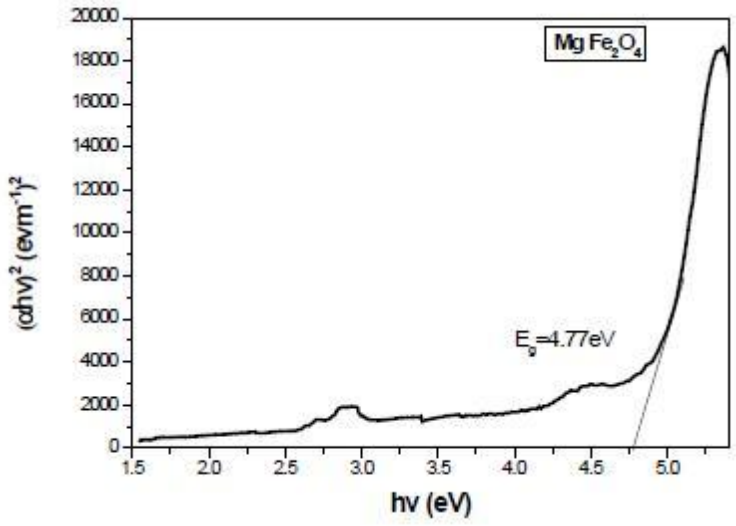

Figure 8. Plot of $(\alpha h\nu)^2$ versus hv for MgFe2O4 nanoferrites.

4. Conclusion

$Mg_{1-x}Zn_xFe_2O_4$ nanparticles was prepared successfully using co-precipitation method. The formation of single phase crystallite structure with size in the range 21.0 - 42.8 nm was confirmed by X-ray diffraction. Lattice parameter was found to increase with Zn concentration and this may be due to the larger ionic radius of the Zn^{2+} ion. FTIR spectrum exhibited expected main absorption bands, thereby confirming the spinel structure. Optical band gap energy Mg_{1-x} $Zn_xFe_2O_4$ nanoferrite was found to be in the range 4.77 to 4.95 eV for samples with different ratio of Mg Zn. The synthesized nanoferrites are expected to be useful in several technological applications such as soft magnets and magnetic fluids for hyperthermia. The structural properties of spinel ferrites depend upon the method of preparation, the nature of substitutional element and the concentration of the substitution element. Attempts can be made to prepare the samples by different methods to get desired properties and crystallite size.

References

a) Flores-Acosta, M., Sotelo-Lerma, M., Arizpe-Chavez, H., Castillon-Barraza, F.F. and Ramirez-Bon, R.J. (2003) A. *Solid State Communications*, **128**, 407-411. http://dx.doi.org/10.1016/j.ssc.2003.09.008

b) Pulisova, P., Kovac, J., Voigtd, A. and Raschman, P. (2013). *Journal of Magnetism and Magnetic Materials*, **341**, 93-99. http://dx.doi.org/10.1016/j.jmmm.2013.04.003

c) Lodhi, M.Y., Mahmood, K., Mahmood, A., Malika, H., Warsi, M.F., Shakir, I., Asghar, M. and Khan, M.A. (2014) New *Current Applied Physics*, **14**, 716-720. http://dx.doi.org/10.1016/j.cap.2014.02.021

d) Jan, L.S., Radiman, S., Siddig, M.A., Muniandy, S.V., Hamid, M.A. and Jamali, H.D. (2004) *A*: *Physico-chemical and Engineering Aspects*, **251**, 43-52. http://dx.doi.org/10.1016/j.colsurfa.2004.09.025

[5] Mathew, D.S. and Juaug, R.-S. (2007) An. *Chemical Engineering Journal*, **129**, 51-65. http://dx.doi.org/10.1016/j.cej.2006.11.001

[6] Rahman, S., Nadeem, K., Anis-ur-Rehman, M., Mumtaz, M., Naeem, S. and Letofsky-Papst, I. (2013) *Ceramics Interna-tional*, **39**, 5235-5239. http://dx.doi.org/10.1016/j.ceramint.2012.12.023

[7] Pradeep, A., Priyadharsini, P. and Chandrasekaran, G. (2008). *Journal of Magnetism and Magnetic Materials*, **320**, 2774-2779. http://dx.doi.org/10.1016/j.jmmm.2008.06.012

[8] Greenwood, N.N. and Earnshaw, A. (1984**)** Chemistry of the Elements; Pergamon Press Ltd., Oxford, 279.

[9] Ichiyanagi, Y., Kubota, M., Moritake, S., Kanazawa, Y., Yamada, T. and Uehashi, T. (2007) Magnetic Properties of Mg-Ferrite Nanoparticles. *Journal of Magnetism and Magnetic Materials*, **310**, 2378-2380. http://dx.doi.org/10.1016/j.jmmm.2006.10.737

[10] Thummer, K.P., Chhantbar, M.C., Modi, K.B., Baldha, G.J. and Joshi, H.H. (2004) Localized Canted Spin Behaviour in $Zn_xMg_{1.5-x}Mn_{0.5}FeO_4$ Spinel Ferrite System. *Journal of Magnetism and Magnetic Materials*, **280**, 23-30. http://dx.doi.org/10.1016/j.jmmm.2004.02.017

[11] Kumara, C.S.S.R. and Mohammad, F. (2011) Magnetic Nanomaterials for Hyperthermia-Based Therapy and Con-trolled Drug Delivery. *Advanced Drug Delivery Reviews*, **63**, 789-808. http://dx.doi.org/10.1016/j.addr.2011.03.008

Giri, J., Pradhan, P., Somani, V., Chelawat, H., Chhatre, S., Banerjee, R. and Bahadur, D. (2008) Synthesis and Char-acterizations of Water-Based Ferrofluids of Substituted Ferrites [$Fe_{1-x}B_xFe{=}O_4$, B=Mn, Co (x=0−1)] for

Biomedical Applications. *Journal of Magnetism and Magnetic Materials*, **320**, 724-730. http://dx.doi.org/10.1016/j.jmmm.2007.08.010

[12] Sharifi, I., Shokrollahi, H. and Amiri, S. (2012) Ferrite-Based Magnetic Nanofluids Used in Hyperthermia Applica-tions. *Journal of Magnetism and Magnetic Materials*, **324**, 903-915. http://dx.doi.org/10.1016/j.jmmm.2011.10.017

[13] Chen, Y., Ruan, M., Jiang, Y.F., Cheng, S.G. and Li, W. (2010) The Synthesis and Thermal Effect of $CoFe_2O_4$ Nanoparticles. *Journal of Alloys and Compounds*, **493**, L36-L38. http://dx.doi.org/10.1016/j.jallcom.2009.12.170

[14] Liu, Q., Sun, J.H., Long, H.R., Sun, X.Q., Zhong, X.J. and Xu, Z. (2008) Hydrothermal Synthesis of $CoFe_2O_4$ Nano-platelets and Nanoparticles. *Materials Chemistry and Physics*, **108**, 269-273. http://dx.doi.org/10.1016/j.matchemphys.2007.09.035

[15] Omer, M.I.M., Elbadawi, A.A. and Yassin, O.A. (2013) Synthesis and Structural Properties of $MgFe_2O_4$ Ferrite Na-no-Particle. *Journal of Applied and Industrial Sciences*, **1**, 20-23.

[16] Ali, R., Khan, M.A., Mahmood, A., Chughtai, A.H., Sultan, A., Shahide, M., Ishaq, M. and Wars, M.F. (2014) Struc-tural, Magnetic and Dielectric Behavior of $Mg_{1-x}Ca_xNi_yFe_{2-y}O_4$ Nano-Ferrites Synthesized by the Micro-Emulsion Method. *Ceramics International*, **40**, 3841-3846. http://dx.doi.org/10. 1016/j.ceramint.2013.08.024

[17] Ahmed, M.A., Rady, K.E.S., El-Shokrofy, K.M., Arais, A.A. and Shams, M.S. (2014) The Influence of Zn^{2+} Ions Substitution on the Microstructure and Transport Properties of Mn-Zn Nanoferrites. *Materials Sciences and Applica-tions*, **5**, 932-942. http://dx.doi.org/10.4236/msa.2014.513095

[18] Mittal, V.K., Chandramohan, P., Santanu, B., Srinivasan, M.P., Velmurugan, S. and Narasimhan, S.V. (2006) Cation Distribution in $Ni_xMg_{1-x}Fe_2O_4$ Studied by XPS and Mössbauer Spectroscopy. *Solid State Communications*, **137**, 6-10. http://dx.doi.org/10.1016/j.ssc.2005.10.019

[19] Ladgaonkar, B.P., Vasambekar, P.N. and Vaingankar, A.S. (2000) Cation Distribution and Magnetisation Study of Nd^{+3} Substituted Zn-Mg Ferrites. *Journal of Magnetism and Magnetic Materials*, **210**, 289-294. http://dx.doi.org/10.1016/S0304-8853(99)00468-0

[20] Maensiri, S., Masingboon, C., Boonchom, B. and Seraphin, S. (2007) A Simple Route to Synthesize Nikel Ferrite ($NiFe_2O_4$) Nanoparticles Using Egg White. *Scripta Materialia*, **56**, 797-800. http://dx.doi.org/10.1016/j.scriptamat.2006.09.033

[21] Dey, S., Roy, A., Das, D. and Ghose, J. (2004) Preparation and Characterization of Nanocrystalline Disordered Li-thium Ferrite by Citrate Precursor Method. *Journal of Magnetism and Magnetic Materials*, **270**, 224-229. http://dx.doi.org/10.1016/j.jmmm.2003.08.024

[22] Priyadharsini, P., Pradeep, A., Sambasiva, P. and Chandrasekaran, G. (2009) Structural, Spectroscopic and Magnetic Study of Nanocrystalline Ni-Zn Ferrites. *Materials Chemistry and Physics*, **116**, 207-213. http://dx.doi.org/10.1016/j.matchemphys.2009.03.011

[23] Hankare, P.P., Patil, R.P., Jadhav, A.V., Pandav, R.S., Garadkar, K.M., Sasikala, R. and Tripathi, A.K. (2011) Synthe-sis and Characterization of Nanocrystalline Ti-Substituted Zn Ferrite. *Journal of Alloys and Compounds*,

[24] Sánchez-Vergara, M.E., Alonso-Huitron, J.C., Rodriguez-Gómez, A. and Reider-Burstin, J.N. (2012) Determination of the Optical GAP in Thin Films of Amorphous Dilithium Phthalocyanine Using the Tauc and Cody Models. *Molecules*, **17**, 10000-10013. http://dx.doi.org/10.3390/molecules170910000

[25] Jan, L.S. and Siddig, M.A. (2011) *Chinese Journal of Polymer Science*, **29**, 181-190. http://dx.doi.org/10.1007/s10118-010-1016-4

Synthesis, Characterization of (1-x) $NaNO_3$-xAl_2O_3 Composite Solid Electrolytes

A.Vennela[1], A. Raju[1], A.Mallaiah[3], S.Narender Reddy[2], A. Sadananda Chary[1].
[1]Department of physics, University College of Science, Osmania University, Hyderabad-7, Telangana, India.
[2]Department of physics, University College of Engg, Osmania University, Hyderabad-7, Telangana, India.
[3]Department of physics, PG College, Secunderabad, Osmania University, Hyderabad-3 , Telangana, India.

ABSTRACT

Composite solid electrolyte system (1-x) $NaNO_3$- xAl_2O_3(with x=0.05, 0.1, 0.15, 0.2) is prepared by fast evaporation technique. The synthesis has been carried out at moderate temperatures and the samples were characterized by XRD and FTIR techniques. X-Ray diffractograms confirmed that there is no indication of any chemical reaction between $NaNO_3$ and Al_2O_3. The crystallite size estimated from all the XRD peaks using Debye Scherrer formula is about 50nm. The FTIR transmittance spectrum of $NaNO_3$ and Al_2O_3 recorded in the wave number range from 400 to 4000cm^{-1} revealed sharp peaks at 835cm^{-1}, 1381cm^{-1}, 1789cm^{-1} and 2430cm^{-1} for pure $NaNO_3$ and sharp peaks at 1633cm^{-1}, 3437$cm^{-1}$and 3550cm^{-1} for pure Al_2O_3.

Keywords: *Composite, XRD, FTIR, Crystallite size, Dispersoid.*

INTRODUCTION:

Composite solid electrolytes are a new class of fast ion conductors which have attracted wide spread interest in the recent years due to their possible technological applications in the solid state batteries,electrochromic display devices ,fuel cells etc. Sodium nitrate($NaNO_3$) has a low melting point and crytalizes with rhombohedral cacite structure at room temperature.Crystaline $NaNO_3$ undergoes a gradual phase transformation which sets in around 150^oC and ends at 275^oC.$NaNO_3$ exhibits Frenkel type disorder[1].

Literature survey indicates major work carried out in many dispersed systems in the recent past namely LiI-Al_2O_3,CuCl-Al_2O_3,Na_2SO_4-Al_2O_3,Li_2SO_4-

Al_2O_3,CsCl-Al_2O_3,$Sr(NO_3)_2$-Al_2O_3 ,Na_2SO_4-Al_2O_3[2].Earlier research work was carried out on $NaNO_3$-Al_2O_3, by P.S Anantha[1] et.al by melt quench method,$NaNO_3$-Al_2O_3 by M.V.Madhavarao[2] et.al by slow evaporation technique.Al_2O_3 was in micron size in their work . Size of the dispersoid plays a major role in physical properties of composite electrolyte system. Fast evaporation technique is one of the methods to obtain products in nanoform.the present study is an attempt to disperse $NaNO_3$ with fine insulating oxide nano powder Al_2O_3 to make it dispersed solid electrolyte system.

In this study, dispersed solid electrolyte (1-x)$NaNO_3$-xAl_2O_3 with (x=0.05,0.1,0. 15,0.2)is prepared by fast evaporation technique which is one of the wet chemical methods based on hydrolysis, condensation followed by drying[3] the solution.The obtained samples were characterized by XRD and FTIR techniques.

EXPERIMENTAL:

The synthesis of the system (1-x)$NaNO_3$-xAl_2O_3(with x =0.05,0.1,0.15,0.2)was explained followed by the flow chart shown in fig .1.

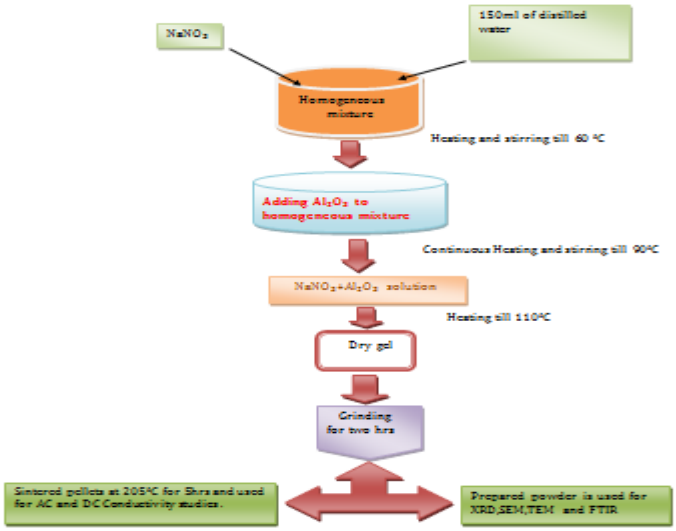

Fig.1. Flow Chart

The sodium nitrate of AR grade and Aluminium oxide of AR grade with particle size <50nm(TEM)were obtained from sigma Aldrich(USA).First host material is taken in a desired amount and was dissolved in double distilled water, heated on magnetic stirrer till 60^{O}C,after half an hour desired mole% of alumina was

introduced to initial solution and heated till 90°c with continuous stirring .then stopping the rpm count and heating till 110°C dry gel is obtained. The final product obtained was collected and grinded in agate mortar for 2hrs for XRD,FTIR studies.

RESULTS AND DISCUSSION:

XRD Analysis: XRD data of (1-x)NaNO3-xAl_2O_3 with (x=0.05,0.1,0.15,0.2)are shown in fig.2.

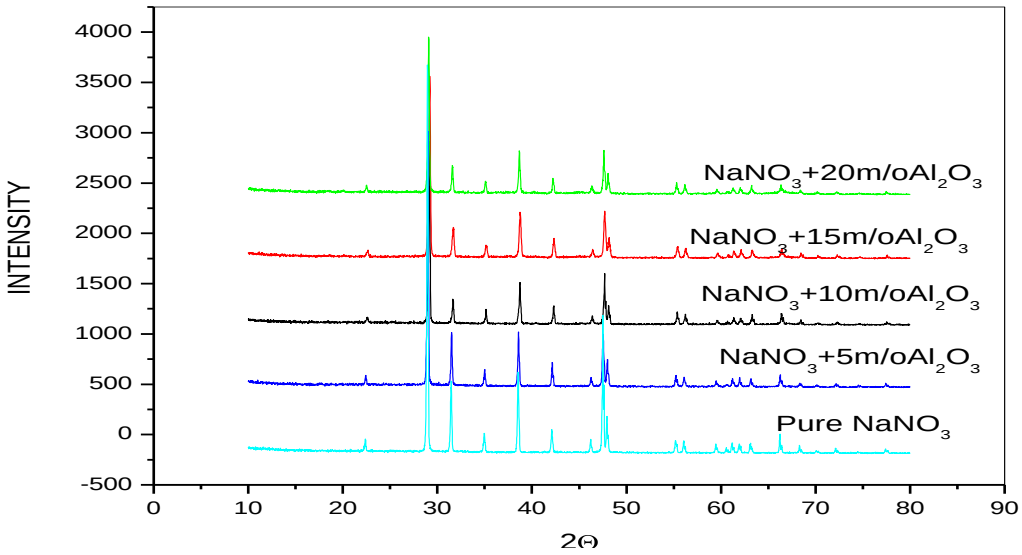

Fig.2. XRD of (1-x)NaNO3-xAl_2O_3

The XRD pattern of the pure $NaNO_3$ and pure Al_2O_3 shows crystalline and amorphous nature with predominant peaks at 2θ of 22.28,31,38,42,46 and 2θ of 40 and all the peaks obtained from XRDare matching with individual XRD pattern of pure $NaNO_3$ and pure Al_2O_3 according to JCPDS data[4].XRD peaks in the diffractogram reveal that there is no indication of any chemical reaction between $NaNO_3$ and Al_2O_3[1].It is observed from XRD that the host and dispersed system have distinct and high intense peaks indicating that it is in the crystalline form where as pure Al_2O_3 show broader peaks indicates that it is in the order of nano meter. The Crystallite size obtained from the XRD pattern of the system(1-x)$NaNO_3$-xAl_2O_3 is around 50nm using Debye Scherrer formula.

FTIR: The FTIR spectra of pure $NaNO_3$ and the composite samples with(x=0.05,0.1,0.15,0.2) in the wave number .range 4000-100cm^{-1} are presented in fig.4.

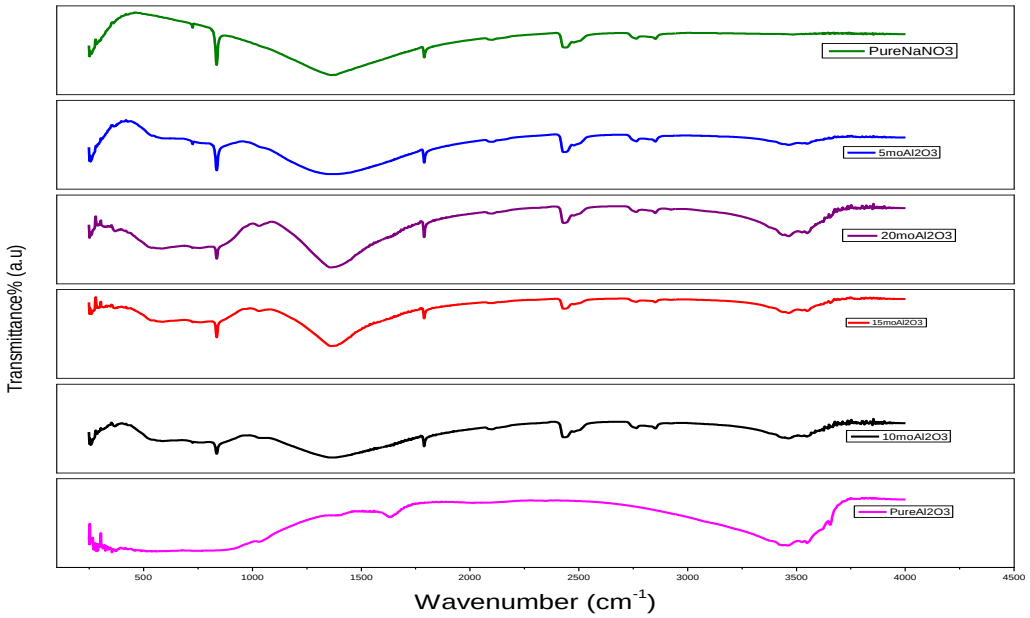

Fig.3. FT-IR spectrum of pure $NaNO_3$ and dispersed system

The FT-IR spectrum of pure $NaNO_3$shows a strong absorption band at 1361$cm^{-1}$and two medium bands at 835 and 1781cm^{-1}[5] .These bands are ascribed to symmetric N-O stretching(υ_3),out of plane deformation(υ_2)and anti symmetric stretch(υ_4) modes of NO^-_3ion respectively. These characteristic bands of the nitrate group are also observed in all of the composite samples(x=0.05, 0.1, 0.15,0.2) in fig .4.The spectrum of the pure Al_2O_3 shows a sharp peaks at 3437 and 3550cm^{-1}.These bands are ascribed to the O-H stretch(υ_1)H-bonded modes. Addition ofAl_2O_3 caused υ_1 mode to shift towards higher wave no of 3466cm^{-1} by an increase in the half-band width indicates the presence of an amorphous phase. The $\upsilon_1$mode shift can be observed in the composite samples with x=0.05,0.1,0.15,0.2 .

CONCLUSION :

XRD and FTIR studies on solid electrolyte system(1-x)$NaNO_3$-xAl_2O_3 reveal that there is no chemical reaction between $NaNO_3$and Al_2O_3 from XRD studies. From

the FTIR , it is observed that as the mole percent of dispersoid is increasing, there is an increase in shift towards a higher wave number of the composite system.

References:

[1]. P.S. Anantha , K. Hariharan , Journal of physics and chemistry of solids 64(2003) 1131-1137.

[2]. M.V. Madhav Rao , S.Narender reddy, A. Sadananda chary, physica. B362 (2005) 193-198.

[3]. Mazdida Sulaiman , N.A. Dzulkarnain , A.S. Rahman, N.S. Mohammad, Solid state sciences 14(2012) 127-132.

[4]. Vijaykumar,Swarnalatha, advances in applied science research 2012 3(5) : 2599-2604.

[5]. Mazdida Sulaiman, A.A Rahman &N.S.Mohammed Int.J.Electrochem. sci,8(2013) 6647-6655.

Doping effect on crystal structure and phase Properties of Chromium Doped Lithium Nano-Ferrites

D. Ravinder Nayak, G.Aravind, B.Neheru, D. Ravinder
Department of Physics, Osmania University, Hyderabad-500007
Corresponding Author email id:ravindergupta28@rediffmail.com

ABSTRACT:

Lithium based ferrites are potential applications.Single phase soft ferrite Nano crystallites could be synthesized by different methods. Out of various methods We have tried to synthesize Chromium doped Lithium Nano ferrites with a chemical formula $Li_{0.5}Cr_x Fe_{2.5-x} O_4$ (where x=0.0,0.2,0.4,0.6,0.8 and 1.0) using Citrate- Gel Auto Combustion Technique at low temperature (180^0C) to improve their properties. It is a unique combination of the combustion and the chemical gelation processes. They are obtained as dried gel after the successful chemical reaction of these compositions of respective metal nitrate solutions in the midst of citric acid as catalyst. X-ray diffraction (XRD) analysis reveals that all the samples possess a single phase cubic spinel structure particle size of 17nm-26nm. The surface morphology and particle size of the samples was observed by Scanning electron microscopy (SEM) and stoichiometric composition from EDAX andICPMS(Inductively coupled plasma mass spectroscopy) .

Keywrds: Li-Cr nano ferrites, Citrate- Gel Auto Combustion Technique, XRD, SEM,EDAX&ICPMS.

Introduction:

Ferrites have Technological Importance and further Nano ferrites play an important role in the miniaturization of several micro wave device applications.$Li_{0.5}Fe_{2.5} O_4$ has been extensive technical and fundamental studies both in pure and substituted form[1,2].Various physical properties of ferrites are highly influenced by the distribution of cation among the sub lattices nature of grain(shape,size & orientation) grain boundaries Voids, in homogeneities, surface layer and constants etc.

The properties of ferrites depend on several factors which include method of preparation,sintering temperature, time ,PH value ,amount and x>0 respectively, the general formula for ferrites . for lithium ferrites ,the conduction mechanism takes place between $fe^{+}2$&$fe^{+}3$ ions present in equivalent crystallographic sites in the structure of ferrite

$$\mathbf{Fe^{+3}+e-} \longrightarrow \mathbf{Fe^{+2}}$$

The chromium doped lithium ferrites are among the few systems exhibiting the effect of magnetic compensation and Gorter et al[3,4]were the first observe this phenomenon in $\mathbf{Cr_{1.25}Li_{0.5}Fe_{2.5}\ O_4}$.In ferrites the electrons transfer between the adjacent B sites in spinelstructure the properties of lithium ferrites can be enhanced by controlling the preparation method . a spinel type crystal structure (AB_2O_4, or $Li_{0.5}\ Fe_{2.5}\ O_4$) , the distribution of metal cation over the tetrahedral (A) and octahedral (B) voids also play an crucial role for exhibiting different physical properties. In lithium ferrite possesses a higher curie temperature than other spinel ferrites [5].In$Li_{0.5}\ Fe_{2.5}O_4$is an inverse spinel with Li^{+} ions and 3/5 of Fe^{+3} ions can occupy the octahedral B- sites[6]where as the remaining Fe+3 ions can occupy tetrahedral A-sites.The β-phase is a disordered phase where the Li+ and Fe3+ ions are randomlydistributed in the octahedral interstices and the space groupis Fd3m [7–9]. In the above mention facts,synthesis of single phase lithium ferrites has receive d considerable attention. Various synthesis routes have been employeed to synthesis ferrites which include, microwave hydrothermal high temp ceramic technique, flash combustion, co-precipitation ,sol-gel & citrate methods [10]. Among all these synthesis method ,citrate gel auto combustion method has more attracted and much attention since this process involves alow temp processing ,homogeneity distribution of reactants and the less time ,the ability to produce nano-size particles.Several investigations on the properties of the Li–Cd [11], Li–Zn [12], and Li–Mg [13].

2. Experimental details

2.1 Material

Lithium nitrate-Li(NO3) sigma aldrich 99% pure AR grade

Ferric Nitrate-(Fe(NO3)29H2O)(98% pure GR grade), ChromiumNitrate -(Cr(NO3)29H2O)(Otto ChemiePvt. Limited, 98%pure GR grade), Citric acid -(C6H8O7.H2O) (SDFCL-SdfineChem. Limited, 99% pure AR grade), Ammon ia -(NH3)(SDFCL-sd fine Chem. Limited, 99% pure AR grade) as starting materials for the synthesis .

2.2Synthesis of Chromium Doped lithium ferrites

The synthesis of lithium ferrites nanoparticles with chromium doped compositional formula solution were prepared by mixing the stoichiometric amount of metal salts into deionized water .the required molar ratio of metal nitrates and citric acid taken and prepared by citrate gel auto-combustion method. This method has inherent advantages like low temperature (200^{O}C),excellent stoichiometric control,homogeneous distribution of reactants and production of fine particles with narrow size distribution.In this citrate gel auto-combustion method, metal nitrates act as oxidizing agents and organic fuels as reducing agents(19,20).the various powder properties can be systematically tuned by altering the oxidant to fuel ratios.

The stoichiometric amounts of all the nitrates were weighed and dissolve it individually in add minimum amount of deionized water. All the individual solutions were adding in a way and mix with continuous stirring of upto one hour .

The structural characterization of the synthesized samples

was carried out by Philips X-ray diffractometer (Model3710) using Cu Kαradiation of wavelength 1.5405 ˚A at room temperature by continuous scanning in the range of Bragg's

Angles 10to 80degin steps of 0.04 ^{0}/sec to investigate the phase and crystalline size.

Theaverage crystalline size of the ferrites was determined from the measured using high intensity [3 1 1] peak width of their diffraction pattern using Debye Scherer's formula [14].

$D = 0.91\lambda / \beta\cos\theta$---------- (1)

Where is the wavelength of the X-ray used for diffraction

And is the full width half maximum (FWHM) in radians

The lattice constant was calculated using the followingrelation:

$2d \sin\theta = n\lambda$,---------- (2)

where$d = a/\sqrt{(h2+ k2+ l2)}$

The X-ray density (dx) has been calculated according to

the relation$dx = 8M/ Na^3$[gm/cm3] ------ (3) [15]

where$M$ = molecular weight of the sample. a is the lattice

Parameter and N is the Avogadro number. The volume of the unit cell $V = a^3$.

3. Results and Discussion:

The X-ray diffraction pattern of the prepared Cr substituted Lithium nano ferrites were shown in fig(1). The X-ray diffraction pattern of the prepared samples were confirmed the well-defined homogeneous single phase cubic spinel structure[16] belonging to the space group Fd3m.The average Crystallite size of the prepared nano samples measured from the X-ray analysis line width of most intense peak (311)was in the range 27-17nm by using Debye-Scherrer's formula.

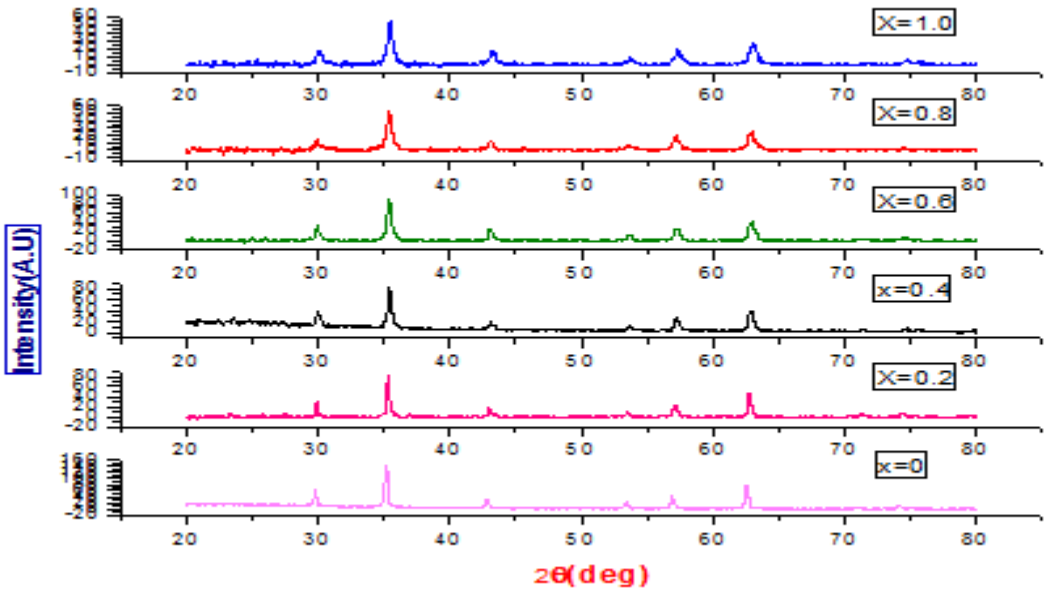

Fig (1) XRD pattern of the nano crystalline Li-Mg ferrites

Table1 The experimental density of the prepared sample of Li-Cr Nano ferrites

Cr composition	Mol.wt (gm/mole)	Crystallite size(nm)±0.2nm	Lattice parameter(A^0)± 0.002A^0	X-ray density (d_x)±0.02
X=0	207.091	27	8.433	4.760
X=0.2	206.321	21	8.414	4.600
X=0.4	205.551	26	8.401	4.611
X=0.6	204.781	21	8.400	4.587
X=0.8	204.001	21	8.397	4.575
X=1.0	203.241	17	8.381	4.565

Lattice parameter of the prepared samples was decreased with increasing the Cr composition [17,18] in the range 0.0<X<1.0 of Li-Crnano crystalline ferrites .A similar variation was also observed by West and Blankenship [19]in Li−Zn ferrites.In this study, we also observed thisphenomenon. Fig. 2 shows the dependence of the lattice constant on Cr-substituted concentration. The lattice constant decreased markedly with increasing concentration of chromium substitutionin the range of 0.0 <*x* < 0.4, and in the range of 0.5 <*x* < 1.0, the lattice constant gradually decreases as *x* increases. Generally, as the Crsubstituted. As the concentration increases, the lattice constant decreases.It is attributed to the fact that different radii of Fe3+ (0.64Å) and Cr3+ (0.62 Å) in an oxide solid solution with a spinel-type structure.In this study, we also observed this phenomenon. Fig. 2 shows the dependence of the lattice constanton Cr-substituted concentration.Cr compositions with lattice parameter and X-ray density experimentally which were shown in below fig (2a) & fig (2b) respectively.

When doped with smaller Cr3+ ions, the spinel lithium ferrite willshrink. Doping Cr3+ ions in a spinel-type structure will induce uniformstrain in the lattice as the material is elastically deformed. Thiseffect causes the lattice plane spacing to change

and the diffractionpeaks shift to a higher 2theataposition. Noticeably, the latticeparameter is nonlinearly dependent on Cr-substituted concentrationfor $Li_{0.5}Cr_xFe_{2.5-x}O_4$. Gorter's defined the chemical formulasof (Fe1.0)[Li0.5Fe1.5]O4 and (Fe1.0−*y*Li*y*)[Li0.5−*y*Fe1.5−*x*+*y*Cr*x*]O4 for $x=0$and $x > 0$, respectively. The formula for $x > 0$ indicates that Li+ ionspartially occupy the tetrahedral (A) site and that the distributionof Fe3+ ions occupying the tetrahedral (A) and octahedral (B) siteschanges. *Y* increases nonlinearly as *x* increases .Several authors have reported the lattice parameter of $\mathbf{Li_{0.5}Fe_{2.5-x}Cr_xO_4}$ [20-22]. The observednonlinear Cr-substituted concentration dependence of the latticeparameter may have resulted from the change of ion distributiondepending on the concentration of Cr substitution. The theoreticaldensity was calculated according to the formula: *Dx*=8*M*/*Na*3where*M*is the molecular mass, *N* is Avogadro's number, and *a* is thelattice parameter which was calculated from the X-ray diffractionpattern. The theoretical density is in the range of 4.76–4.56 gcm−3for $Li_{0.5}Cr_xFe_{2.5-x}O_4$ (x = 0–1.0). The lattice constant, theoreticaldensity, and mol.weight of the $Li_{0.5}Cr_xFe_{2.5-x}O_4$ system sinteredat 500 ◦C for 4 h are summarized in Table 1.

As the increasing the Cr composition experimental density is also decreases marakablyand there is slight increasing taking place.additionally,it was predicted that the lattice parameters of nanoparticles decrease with a decrease in the particle size[23].

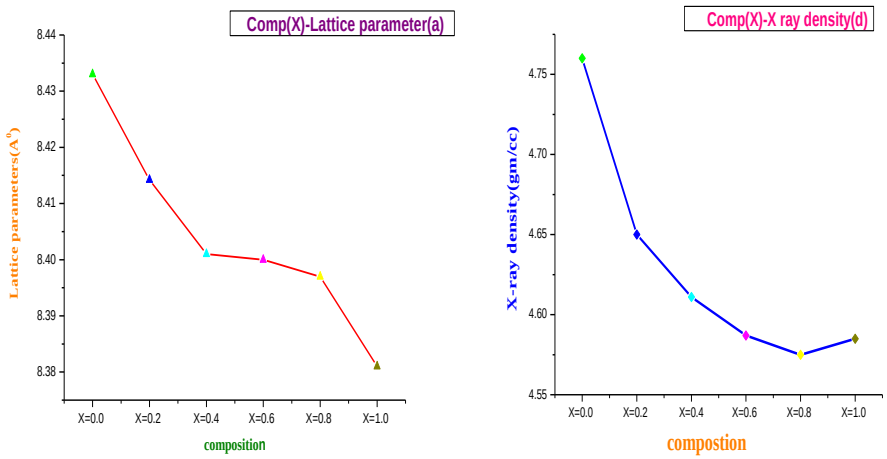

fig (2a) fig (2b)

3.2 **SEM ANALYSIS**

Electrical and magnetic properties are depending on the sensitively microstructure of ferrites.Grain diameter is more important parameter affecting the magnetic properties of ferrites. In SEM each grain consists of several particles[24]. The Scanning electron microscope (SEM) scan patterns of the specimen shows the surface morphology of the Li-Cr Nano ferrite particles sintered at 500^{o}C.The SEM images of the $Li_{0.5}Cr_xFe_{2.5-x}O_4$Nano ferrites shown in Figure (3).

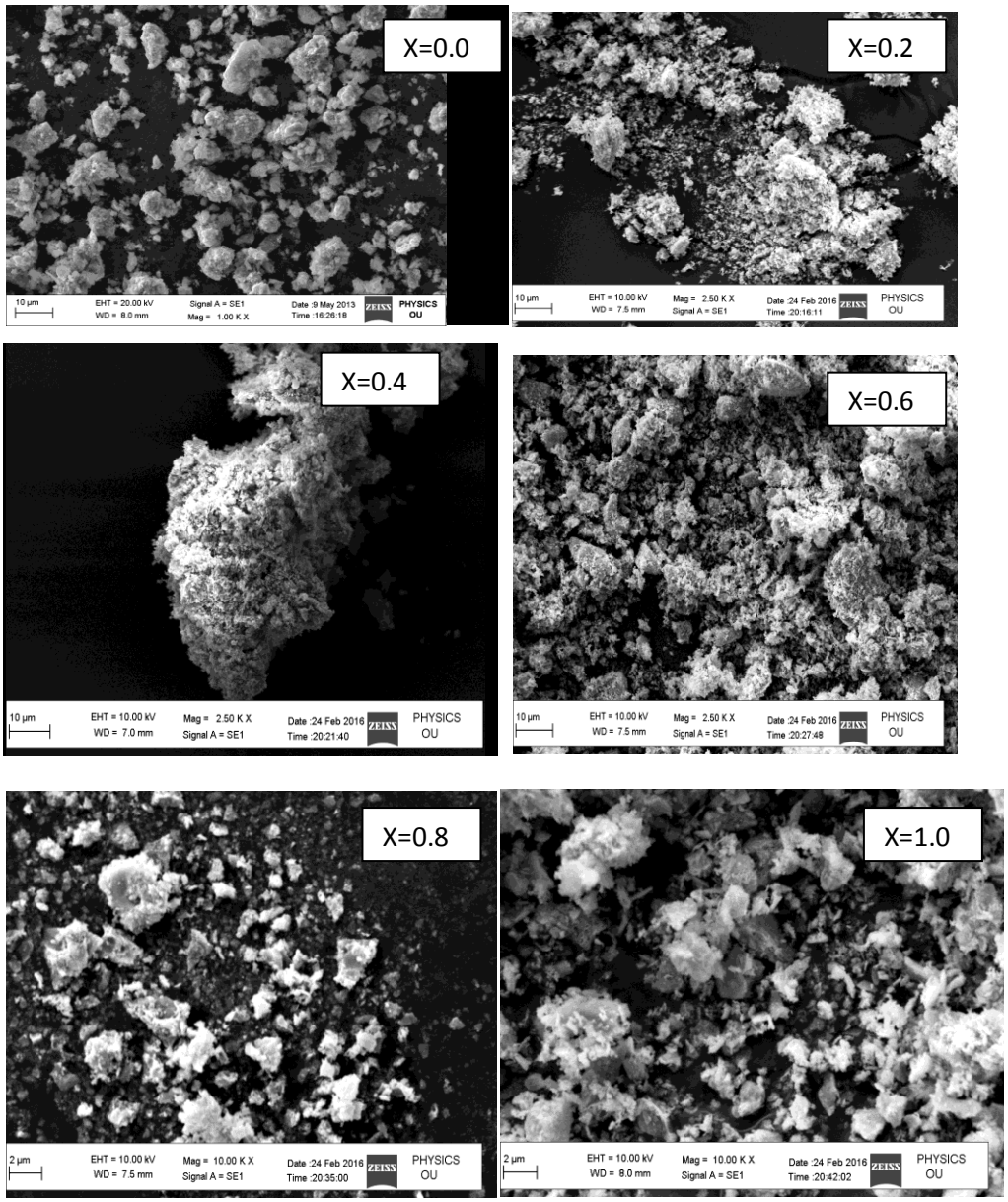

Figure (3).The SEM images of the $Li_{0.5}Cr_xFe_{2.5-x}O_4$Nano ferrites

The morphology and grain size of the sample s seem to be spherical shape anda narrow size distribution.In which some what agglomeration in the synthesized samples which is unavoidable. From the Observation of the image , one can observe the grain size is slightly affected by the doping the Cr composition.

ELEMENTAL ANALYSIS BY EDAX: The EDAX spectra fig.4.Energy dispersive Spectrometer was used for the elemental analysis of the prepared ferrites with different compositions. In EDAX spectra Cr substituted grains indicated in the presence of concentrated of Cr with energy range of up to 8 keV and seen at0.6keV,5.4keV and 5.9keV Fe was seen at the 0.8keVand 6.5keVand 7keV.In this Lithium low atomic element because of that can't detect elemental analysis in Few SEMs .

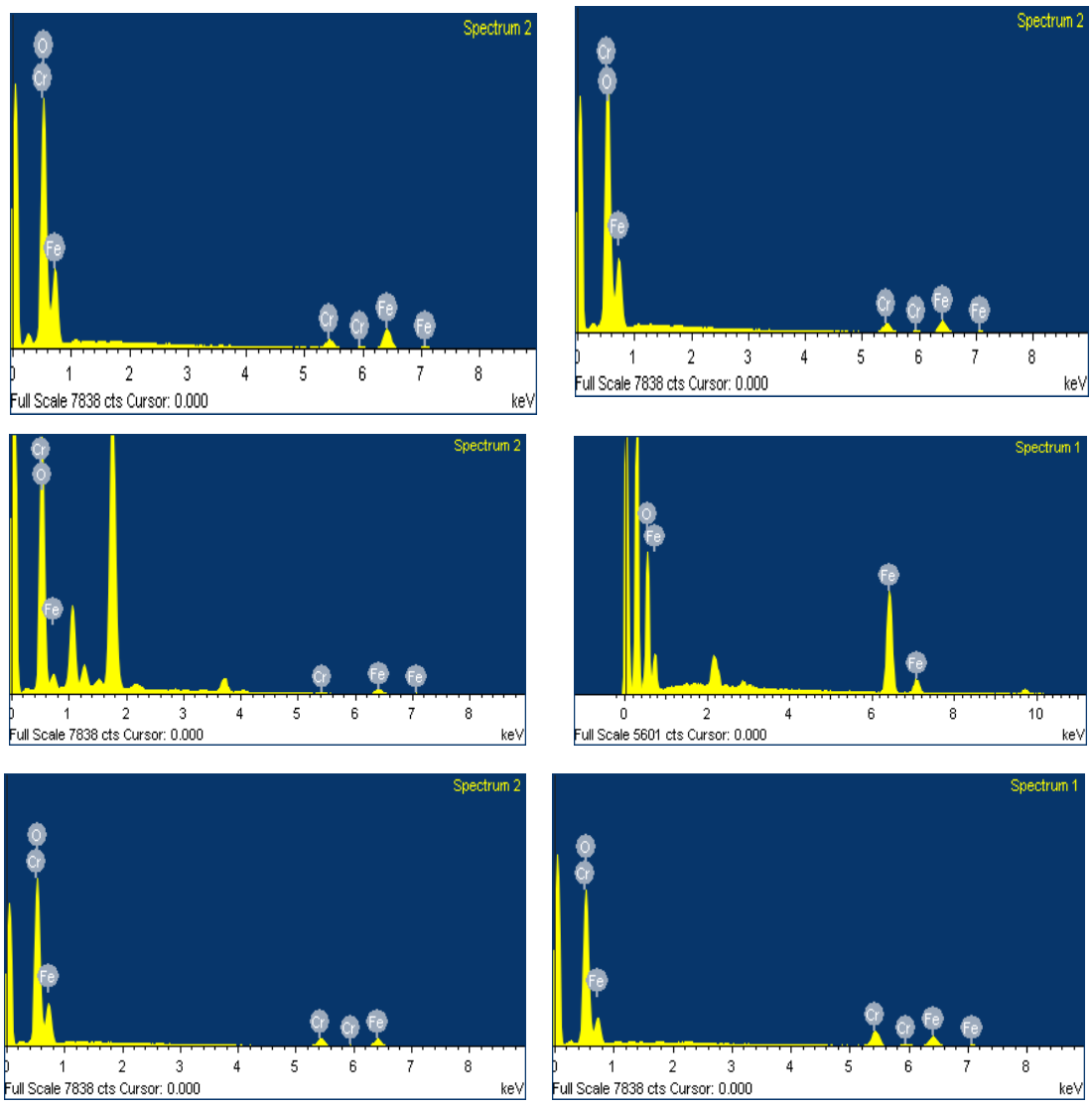

fig. 4 The EDAX spectra

ICPMS:

Inductively coupled plasma mass spectroscopy is used to conform the Li elemental compositional

presence in the Lithium Nano ferrite and To compensate for this, a matrix component is often used as aninternal standard. However, usingan internal standard prohibits theanalysis of all elements simultaneously in the sample compositions.by this conforming the Li is present in this sample.

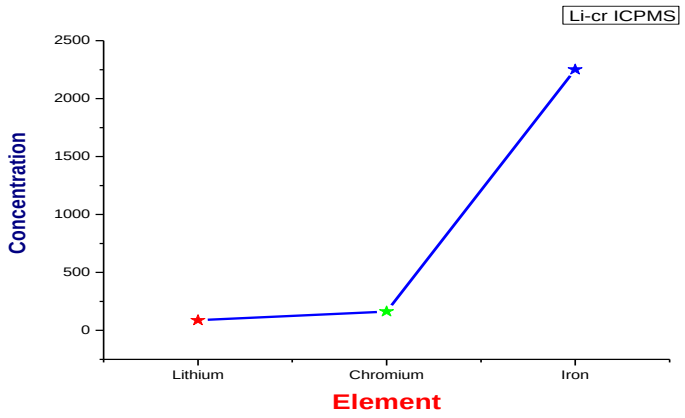

Conclusion

The Cr-substituted Nano-crystalline lithium ferrite samples were synthesized by sol–gel auto-combustion method.

Citrate gel auto- combustion methodwas a very suitabletechnique for the preparation of nano sized (27-17 nm) Cr substituted lithium ferrite at low sintering temperature.

X-ray diffraction studies confirm the cubic spinel structure formation.

The lattice constant and crystallite size decrease with increase in Cr content .

The EDAX spectra Energydispersive Spectrometer was used for the elemental analysis of the prepared ferrites with different compositions.

Inductively coupled plasma mass spectroscopy is used to conform the Li elemental compositional presence in the Lithium Nano ferrite

Acknowledgements:

The authors are very grateful to Prof.D.Suresh Babu, Head, Department of Physics,

Prof. J.Shiva Kumar, BOS, Department of physics , University College of Science, OsmaniaUniversity,Hyderabad.

References

[1] Dorman J.L,Rev.Phys.appl.1980,15,1113

[2] Krishnan R,Physica B1977,86-88,1457

[3] Gorter E.W. Philips Res.Rep.1954,9,295

[4] Gorter E.W and schulkes J.A Phy.Rev 1953,89,487

[5] Y.P. Fu, Mater. Res. Bull. 41 (2006) 809.

[6] S. Verma, P.A. Joy, J. Appl. Phys. 98 (2005) 124312.

[7] S. Verma, J. Karande, A. Patidar, P.A. Joy, Mater. Lett. 59 (2005) 2630–2633.

[8] A.Tomas,P. Laruelle, J.L. Dormann, M. Nogues, ActaCrystallogr. C 39 (1983)1615.

[9] S.J. Marin, K. O'Keefe, D.E. Partin, J. Solid State Chem. 113 (1994) 413.

[10] E.E.Sileo,RRoteldo S.E Jacobo J.Phy.B,320(2002),257-260

[11] S. S. Bellad, R. B. Pujar, and B. K. Chougule, *Materials Chemistry and Physics*, vol. 52, no. 2, pp. 166–169, 1998.

[12] D. Ravinder*Journal of Materials Science Letters*, vol. 11, no. 22, pp.1498–1500, 1992.

[13] Y. Purushotham, M. B. Reddy, P. Kishan, D. R. Sagar, and P. V. Reddy, *MaterialsLetters*, vol. 17, no. 6, pp. 341–345, 1993.

[14] Cullity B D,(addition Wesley,reading ,mass)1959,P132

[15] R.C.Kumbale,P.AShaik,S.SKamble,Y.D.KolekarJ.Alloys Comp.,478(2009),P.599

[16] S.A.Mazen,S.F. Mansour,H.M.ZakiCry.res.Technol.38.No 6,471-478(2003)

[17] P.P. Hankare, R.P. Patil, U.B. Sankpal , K.M. Garadkar, R. Sasikala , A.K.Tripathi, I.S. Mulla Journal of Magnetism and Magnetic Materials 322 (2010) 2629–2633

[18] R.G. West, A.C. Blankenship, J. Am. Ceram. Soc. 50 (1967) 343

[19] R.G. West, A.C. Blankenship, J. Am. Ceram. Soc. 50 (1967) 343.

[20] Y.P. Fu, Jpn. J. Appl. Phys. 46 (2007) 7314.

[21] M.V. Kuznetsov, Q.A. Pankhurst, I.P. Parkin, Physica D 31 (1998) 2886.

[22] L. Fernandez-Barquin, M.V. Kuznetsov, Y.G. Morozov, Q.A. Pankhurst, I.P. Parkin,Int. J. Inorg. Mater.1 (1999) 311.

[23] G.K. Shenoy, F.E. Wagner, Mössbauer Isomer Shifts, Amsterdam:North-Holland, 1978

[24] A.Dhahri,JDhahri,S.Zemni,M.Oumezzine,M.Said and H.Vincent journal of Alloys and Compounds,ol.450,no1-2,pp12-17,2008.

Thermo Electric Power studies of Li-Co nano ferro spinels

G.Aravind[1], V.Nathanial[2], A. Ranjith[2], Ch.Sumalatha[2], V.Ludhiya[3] D.Ravinder[3]

[1] Department of Physics Methodist College of Engg. & Technology, Abids, Hyd.
[2]Department of Physics, University College of Science, Saifabad, Osmania University Hyderabad-500007
[3]Department of Physics Osmania University Hyderabad-500007

ABSTRACT

Nanocrystalline lithium cobalt ferrites of compositions [Li0.5Fe0.5]1-x Cox Fe2O4 (where x = 0.0, 0.2,0.4, 0.6, 0.8, and, 1.0) were synthesized at lower processing temperature (180 ^{o}C) by non-conventional citrate gel auto ignition method using citric acid as a fuel and oxidant. Structural characterization of the sintered samples was carried out by X-ray diffraction (XRD) analysis. XRD studies of the prepared samples confirmed the homogeneous single-phase cubic spinel structure with the crystallite sizes ranging from 37 to 43 nm. Thermoelectric power (TEP) studies of the prepared samples were carried out from 200 to 600 ^{o}C using a differential method. The variation of Seebeck coefficient (S) with temperature indicated p-type semiconducting nature of the sample at lower temperature and n-type semiconducting nature at higher temperature indicating the conduction due to the electrons. The Curie temperature (Tc) of the prepared samples measured from TEP studies showed a decreasing trend with the increasing Cobalt concentration.

Keywords: XRD, Spinel ferrites and Thermo Electric Power (TEP)

1. Introduction:

The field of ferrites is well developed but due to its potential applications in various fields, and interesting physics involved in it, even after several decades of its first artificial synthesis, scientists and researchers are still interested in various types of synthesized methods by different preparative techniques, parameters and conditions in bulk, nano crystalline and thin film forms and in the study of structural, magnetic, electrical, properties as a function of composition, frequency, temperature etc. ferrites have a high magnetic permeability which is used to store stronger magnetic field than iron.

Ruiyun He et al. **[1]** observed the application of titanium doped lithium ferrites in circulators at 11 GHz operating frequency in the temperature range of 20-300 K. The saturation magnetization value and Curie temperature of samples decreased with increasing the Ti composition. Reddy et al. **[2-4]** studied the lithium titanium mixed ferrites. The saturation magnetization and Curie temperature also decreased with titanium content.

2. Experimental techniques

In the present communication we prepare Li-Co nano crystalline ferrites by auto-combustion method at low sintering temperature. The synthesis procedure was discussed in our earlier publication **[5].** X-ray diffraction analysis of the prepared ferrite powders were performed by using Philips X-ray diffractometer with Cu K_α radiation of wavelength 1.5405 A^o. For the thermo electric power measurements, the synthesized powders were made in the form of circular pellets (diameter – 13 mm and thickness – 2 mm) using 2% polyvinyl alcohol (PVA) as binder under a pressure of 5 tons for 1–2 min. These pellets were finally sintered at 500 °C for 4 h and then slowly cooled to room temperature. Pellets were then coated on either side with a thin layer of silver paste to have good electrical contact. Thermo electric power measurement studies on the prepared pellets were carried out by differential method from 320 K to well beyond Curie temperature..The thermo electric power or Seebeck coefficient (S or α) was calculated using the following relation.

$$S = \frac{\Delta E}{\Delta T}(\mu V/K)$$

where ΔE is the thermo electro motive force produced across the two ends of the sample which is measured by using a digital micro voltmeter and the ΔT is the temperature difference between the two surfaces of the pellet which is measured by two chromel-alumel thermocouples that were kept very close to the sample. For achieving good thermal stability, thermo emf values were measured while cooling.

3. Results and Discussions:

3.1 XRD analysis

The structural study is essential for optimizing the properties needed for various applications. The phase identification and structural parameter determination were performed on an x-ray diffraction analysis. The x-ray diffraction pattern of the $[Li_{0.5}Fe_{0.5}]_{1-x}\ Co_x\ Fe_2O_4$ (where x= 0.0 to 1.0 with step of 0.2) powder ferrite samples sintered at 500^{o}C for 4 hours are shown in **fig (1).** Analyzing the x-ray diffraction pattern one can observed that the positions of the peaks are comply with the reported values **[6-8].** From the **fig (1)** it can be seen that the location of the peaks in XRD pattern of all prepared samples are coincident, which indicate that there were no distinct differences in phase structure of Li-Co nano crystalline ferrites with different cobalt composition. On increasing the cobalt compositions, reflection peaks become sharp and reflection intensities of the pattern increases which reveal that cobalt composition is useful in the crystallization of the nano crystalline ferrites and use to promoting the grain growth. It was observed that cobalt ions were partly replaced by iron and lithium ions in the lattice and then increased the lattice constant.

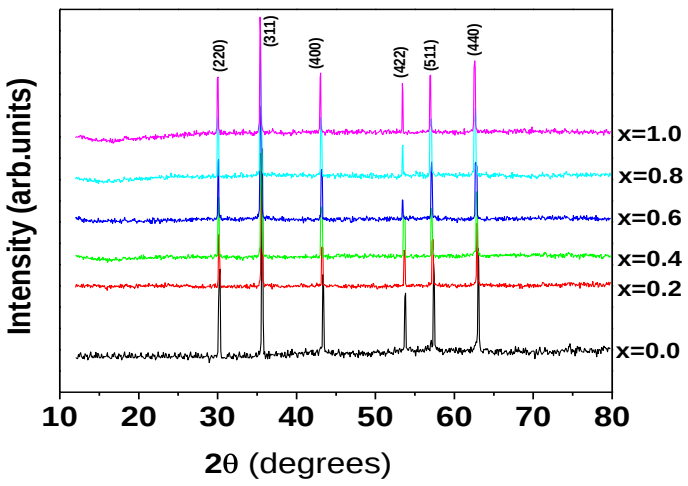

Fig (1) XRD pattern of the $[Li_{0.5}Fe_{0.5}]_{1-x}\ Co_x\ Fe_2O_4$ ferrite samples

The observed peaks at (220),(311),(400),(422),(511) and (440) confirmed the spinel structure of the prepared samples. This indicates that the synthesized ferrite compositions are of single phase cubic spinel since no ambiguous reflections other than the spinel structured are observed and also demonstrates the homogeneity of the prepared nano crystalline ferrite samplesThe x-ray diffraction analysis of the prepared Li-Co nano crystalline ferrite samples provides the estimation of the crystallographic lattice constant (a), crystalline size (D), x-ray density and experimental density etc are given in **table1**

The average crystallite size which are calculated from the Debye-Scherrer's formula were in the range of 36-43 nm which confirms the nano crystalline form. The lattice constant of the samplesincreases with cobalt composition which obeys the Vegard's law **[9].**

Table1

Structural parameters of the prepared Li-Co ferrite sample

composition	Mol.wt (gm/mol)	Crystallite Size (nm)	Lattice constant (A^o)	X-ray Density (d_x) (gm/cc)	Experimental Density (d_e) (gm/cc)	% of Porosity (P)
$Li_{0.5}Fe_{2.5}O_4$	207.079	41.90	8.35	4.71	4.28	9.00
$Li_{0.4}Co_{0.2}Fe_{2.4}O_4$	212.587	43.01	8.37	4.81	4.37	9.10
$Li_{0.3}Co_{0.4}Fe_{2.3}O_4$	218.095	38.44	8.37	4.93	4.38	11.00
$Li_{0.2}Co_{0.6}Fe_{2.2}O_4$	223.603	37.57	8.38	5.03	4.39	12.70
$Li_{0.1}Co_{0.8}Fe_{2.1}O_4$	229.111	37.06	8.39	5.14	4.58	10.90
$CoFe_2O_4$	234.619	36.90	8.40	5.25	4.68	10.70

3.2 Thermo Electric Power studies of $[Li_{0.5}Fe_{0.5}]_{1-x}\ Co_x\ Fe_2O_4$ nano ferrites

The thermo electric power studies of the prepared nano crystalline $Li_{0.5}Fe_{0.5}]_{1-x}\ Co_x\ Fe_2O_4$ ferrites were measured by differential method in the temperature range 200-600^{o}C. The thermo e.m.f of the samples measured during cooling cycle because during cooling the sample attains more thermal stability than heating. The values of the seebeck coefficient of mixed Li-Co nano ferrites were

calculated from the observed values of the thermo electro motive force and tabulaed in the **table2** Carrier concentration of the prepared samples was calculated at 500K. It can be seen from the table that among all the mixed Li-Co spinel ferrites, the composition $Li_{0.3}Co_{0.4}Fe_{2.3}O_4$ was having highest values of carrier concentration. From the table2 one can observed that Seebeck coefficient increases with increasing the Co concentration this may be attributed to the fact that by increasing the Co^{+2} ions in the lithium ferrites, more number of charge carriers are produced so that large energy was needed to transfer the charge carriers between the different cations. Hence large electro motive force produced, which enhances the thermo electric power. The addition of Co^{+2} ions in the Li-Co ferrites has an effect of decreasing the number of Fe^{+2} ions in the B-site so that seebeck coefficient increases. **Fig (2)** shows the variation of Seebeck coefficient with temperature for all prepared sample. It can be seen from the **fig (2)** that the sign of seebeck coefficient was positive at low temperature and increasing the temperature S became negative value for all ferrites under investigation.

Table2: Seebeck Coefficient, Curie point of the prepared Li-Co ferrite samples

Composition	**Seebeck Coeficient(S) (μV/K)@T_c**	**Curie Point (K)**	**Carrier concentration**
$Li_{0.5}Fe_{2.5}O_4$		>873	3.10 $X10^{22}$
$Li_{0.4}Co_{0.2}Fe_{2.4}O_4$	-3546	861	1.90 $X10^{22}$
$Li_{0.3}Co_{0.4}Fe_{2.3}O_4$	-4413	840	3.15 $X10^{22}$
$Li_{0.2}Co_{0.6}Fe_{2.2}O_4$	-4958	815	1.46 $X10^{22}$
$Li_{0.1}Co_{0.8}Fe_{2.1}O_4$	-5840	801	3.06 $X10^{22}$
$CoFe_2O_4$	-6140	790	2.98 $X10^{22}$

This indicates that at low temperature these prepared samples behave like a p-type semiconductor and increasing the temperature predominant conduction mechanism in these ferrites was due to the electrons and behaves like a n-type semiconductors. It can be seen that the values of the seebeck coefficient for all mixed nano crystalline Li-Co ferrites increases with increase of temperature which

indicates that more n-type charge carriers i,e electrons were released with an increase in temperature.

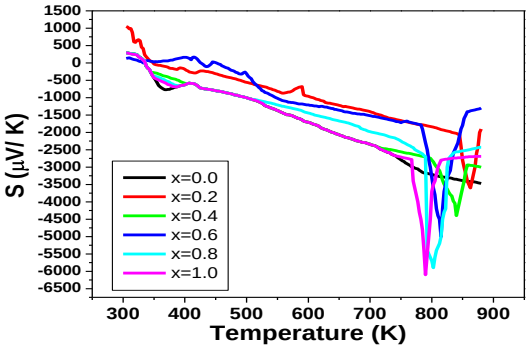

Fig (2) Variation of Seebeck coefficient (S) with temperature for Li-Co ferrites

Further increase in temperature results a decrease in seebeck coefficient which remains almost constant later on. This may be due to the transition at that temperature (Curie temperature). It was clear that in case of Li-Co nano ferrites the non magnetic property (thermo electric power) under study was exhibiting a well-defined transition at the Curie temperature, like the magnetic properties viz., susceptibility, permeability and spontaneous magnetization. The fact that the value of seebeck coefficient shows minimum values at Curie temperature indicates that the magnetic ordering has a marked influence on the thermo electric power of these ferrite samples under investigated. From the present study and considering the semiconducting behavior of investigated ferrites, the charge carriers are considered to be localized at ions or at vacant sites as a result of electron-phonon interaction **[10]**.

Conclusions

Citrate Gel auto combustion technique is a convenient way for obtaining a homogeneous nano sized mixed ferrites. The process involves no impurity pickup and material loss. It is a very simple and economical method where no specific heating or cooling rate is required. It is a low temperature processing technique and requires shorter sintering duration. X-ray diffraction pattern confirms the formation of cubic spinel structure in single phase without any impurity peak. It is in good agreement with the standard data from ICSD . In synthesized nano ferrite systems it

is observed that with increase in temperature, the value of thermoelectric power increases and shows maximum value at curie temperature Tc(K) beyond which it decreases.

References

[1] Raiyun He, MIngche Sun and Deqiong yu, IEEE trans, MAG-18, 1982,1622.

[2] M.Bhagavantha Reddy, V.Devender Reddy and P.Venugopal Reddy, Moder.Phys.Lett B.10,1996,29.

[3] S.A.Jadhav, Materials Chemistry and Physics,65,2000,120-123.

[4] PranKishan, D.R.Sagar and Premswasup, J.Less-common Met, 108, 1985,345.

[5] **G.Aravind**, M.Raghasudha, D.Ravinder, Abdul Gaffoor, V.Nathanial, J of Nanostruct Chem, **(Springer Publications) DOI.10.1007/s40097-014-0138-6**

[6] M.S.Ruiz, S.E.Jacobo, "Electromagnetic properties of Li-Zn ferrites doped with aluminum", Physica B 407 **(2012)** 3271-3277.

[7] Mamatha Maisnam, Sumitra Phanjoubam, " Frequency dependence of electrical and magnetic properties of Li-Ni-Mn-Co ferrites", Solid State Commun 152 **(2012)** 320-323.

[8] S.A.Saafan,S.T.Assar, B.M.Moharram, M.K.El Nimr, J of Magn and Magn Mater 322 **(2010)** 628-632.

[9] K.Wykpis,A.Budnoik,E.lagiewka,Mater,Science,Forum.636 **(2010)**1053-1058

[10] F.Habery,H.P.J.Wijn, Physica status Solidi,26 (1968) 231.